Numerical simulation of spatio-temporal behavior in high-density helicon discharge

諫山, 翔伍

https://doi.org/10.15017/1807094

出版情報：九州大学, 2016, 博士（理学）, 課程博士
バージョン：

Numerical simulation of spatio-temporal behavior in high-density helicon discharge

by

Shogo Isayama

A dissertation submitted in partial fulfillment of

the requirements for the degree of

Doctor of Philosophy

Interdisciplinary Graduate School of Engineering Sciences (IGSES),
Department of Earth System Science and Technology (ESST),

in Kyushu-University, 2016

ACKNOWLEDGEMENTS

I would first like to express deep appreciation to my supervisor, Prof. Tohru Hada for the profound scientific education and guidance throughout my years at ESST, Kyushu university. I could met my current exciting research subject owing to his broad knowledge and wide perspective, that allows me to conduct my research with great delight. I am very lucky to meet such a great supervisor.

I am very grateful to Profs. Shunjiro Shinohara and Takao Tanikawa for numerous fruitful discussions, advices, and suggestions, that enable me to conduct my research with considerations from experimental aspects. I am also obliged to Prof. Yuji Sugihara and Prof. Naoji Yamamoto for their critical reading of the manuscript and suitable suggestions for revision.

I am also very grateful to Prof. Shuichi Matsukiyo for his education about the simulation techniques, helpful assistance in performing PIC simulation, and discussions on various scientific topics.

I would like to thank Dr. Fumiko Otsuka for useful discussions and encouragement. I would also like to thank Profs. Hideyuki Usui, Yohei Miyake, and Yasuhiro Nariyuki for their useful discussions and comments.

I also greatly benefited from the discussions with Mrs. Kazuki Yamanokuchi and Masaru Nakanotani, and with other students of Hada laboratory.

Finally, I thank my brother, Keishiro Isayama, and my parents, Seiji Isayama and Tamaki Isayama for their encouragement and support in my private life.

TABLE OF CONTENTS

LIST OF FIGURES

Figure

ABSTRACT

Numerical simulation of spatio-temporal behavior in high-density helicon discharge

by

Shogo Isayama

In this thesis, we develop the self-consistent fluid model of the helicon discharge, that includes the excitation of the helicon and the Trivelpiece-Gould (TG) waves, mode conversion between these two waves, the wave dissipation via the collisional processes, the electron heating (Joule heating), ionization of neutrals, particle loss toward the wall, and the diffusion process of the background plasma. Results of our study will be useful for a variety of applications such as the plasma processing and the next generation spacecraft propulsion systems.

In section 1, after the review of the helicon study, we refer to the purpose of this thesis. In section 2, we review the theoretical treatment of the dispersion relation, the density jump observed in the experiment by Nisoa *et al* [1–3], and the mode conversion from the helicon wave to the TG wave.

In section 3, we discuss the so-called bulk mode conversion process. The bulk mode conversion is a classical type of the mode conversion that occurs near the mode conversion surface (MCS) where the perpendicular wave number of the helicon and the TG waves merge, that is considered to be a primary production mechanism of

the high-density helicon plasma. Assuming a plasma with a background density gradient, we numerically solve the linear coupling equations for the helicon wave and the Trivelpiece-Gould (TG) wave. We estimated the efficiency of the bulk mode conversion by calculating the energy fluxes of the helicon and the TG waves, and have shown that the efficiency of the bulk mode conversion strongly depends on the dissipation included in the plasma and that the bulk mode conversion is significant when the dissipation is small. Also, by evaluating the power absorption by the helicon and the TG waves, we investigated qualitatively the relative importance of the bulk mode conversion for the power absorption. We show that the TG wave which is excited by the bulk mode conversion plays crucial role on the power absorption when the collision frequency is small, and plays minor role when the collision frequency is large. When the collision frequency is large, the helicon wave dissipates directly and heats the core (high density region) plasma. That argument is remarkable fact since it has been believed that the helicon discharge is sustained mainly by the TG wave.

In section 4, motivated by experiments by Nisoa *et al*, a self-consistent discharge model is developed. We employ two methods to compute the evolution of the background plasma: the ambipolar diffusion model, that assumes the charge neutrality and the flux equality between the electrons flux and the ions flux, and the full-fluid model, that calculates the drift-diffusion momentum equation for electrons and the full momentum equation for ions. Using the results of the one-dimensional ambipolar diffusion model, we discuss the time evolution of profiles of the plasma density and the electron temperature and their peak values. We examine the temporal behavior of the plasma density and the electron temperature using the total power balance between the power absorption and the power loss. As a case study of this model, we investigate the dependence of the steady-state plasma density on the RF input power. Although we were able to determine the threshold RF input power for the density growth, the density jumps detected in Niosafs experiment were not reproduced in our

results. We show that the time scale of the classical ambipolar diffusion across the magnetic field is too long to explain the density profile that is peaked at the center as usually observed in experiments. We present some ideas to improve our model in the last chapter. In the two-dimensional model, we found that the low-density mode ($n \sim 10^{17}$ [1/m^3]) observed in the experiment can be generated by the TG wave. The low-density mode is considered to be generated by the antenna induction field in Niosafs and many other authors arguments, thus that low-density mode is called the Inductively Coupled Plasma (ICP) mode. However, at the low-density plasma ($n \sim 10^{17}$ [1/m^3]), the excited wave profiles are the superpositions of the TG wave and the purely imaginary (non-propagating) helicon wave (not the antenna induction field). We also show that the TG wave can play a dominant role in the power absorption at the low-density mode. Finally, we compare the results obtained by the ambipolar diffusion model and the full fluid model. We show that the axial heat transfer is much enhanced in the full fluid model, and this indicates the existence of a fast heat transfer (non-ambipolar) mechanism in the axial direction. We investigate this axial fast heat transfer mechanism in more detail by diffusion tests using the ambipolar diffusion model, the full fluid model, and the Prticle-In-Cell Monte Carlo Collision (PIC-MCC) model. Then we found that the thermal energetic electrons can move freely along the magnetic field line, but the charge neutrality is conserved by adjusting the number of charged particles between the hot plasma region and the background cold plasma region.

In section 5, after the summarize of this thesis is given, some ideas to improve our model and make better demonstration of the experimental results are introduced. In the final of this chapter, the most outstanding issues to improve our model is also introduced.

CHAPTER I

Introduction

1.1 Review of the helicon wave studies

1.1.1 Early studies of the helicon plasma

In 1960, Aigrain called the helical wave (the counter-clockwise polarized) propagating in a solid state laboratory plasma "helicon wave" [4]. The dispersion property of the helicon wave in solid state plasma was first investigated by Bowers, Legendy, and Rose [5], and its property was extended to a magneto-plasma by Legendy [6,7] and Klozenberg, McNamara, and Thonemann [8](hereafter referred to as K. M. T.). K. M. T. theory presented the dispersion relation and the attenuation of the helicon wave in a uniform cylindrical plasma bounded by a vacuum. The helicon wave propagation in a partially ionized cylindrical plasma was studied by Lehane and Thonemann [9], while Facey and Harding investigated the standing helicon waves in a cylinder of indium [10]. The predictions of the K. M. T. theory were in good agreement with the observations of the phase velocity, the attenuation, and the structure of the plasma magnetic fields in these above two experiments [9, 10].

In 1970, Boswell made a small helicon plasma source with a new type of antenna that is now called the Boswell antenna (Fig. 1.1) [11]. The antenna produced the transverse radio frequency (RF) magnetic field which excites the standing helicon

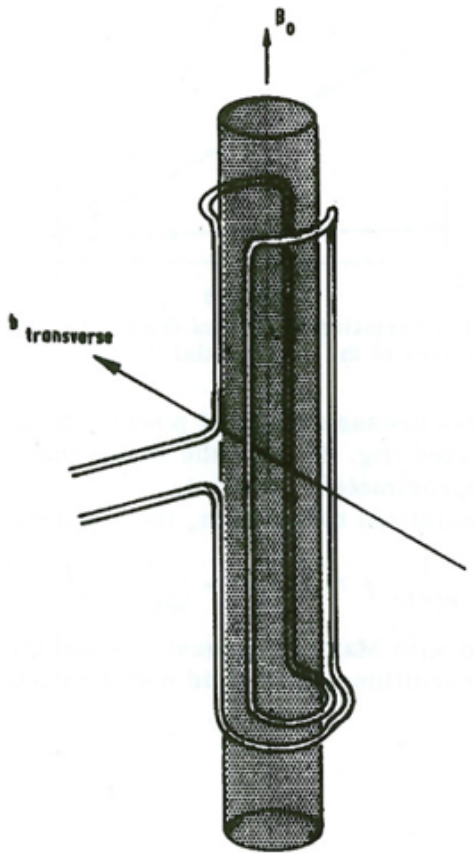

Figure 1.1: Boswell antenna, the rf current produces the transverse rf field across the plasma [11].

wave by coupling into the radial component of the magnetic field. Since the helicon waves have frequencies between the lower hybrid frequency, $(\omega_{ce}\omega_{ci})^{1/2}$, and the ion cyclotron frequency, ω_{ci}, which are both much lower than the electron cyclotron frequency, ω_{ce}, most of initial studies neglected the contribution of electron dynamics. The dispersion relation of the bounded helicon wave, that satisfies the radial boundary conditions (both of insulating and conducting walls), represents the linear dependence of the plasma density on the magnetic field (the linear $B-n$ dependence) [11,12]. Figure 1.2 is the radial density profile observed in Boswells experiment [11], that shows the increasing of the density with the increasing of applied magnetic field. However, Chen *et al* [13] found that there are threshold values of the magnetic field and the

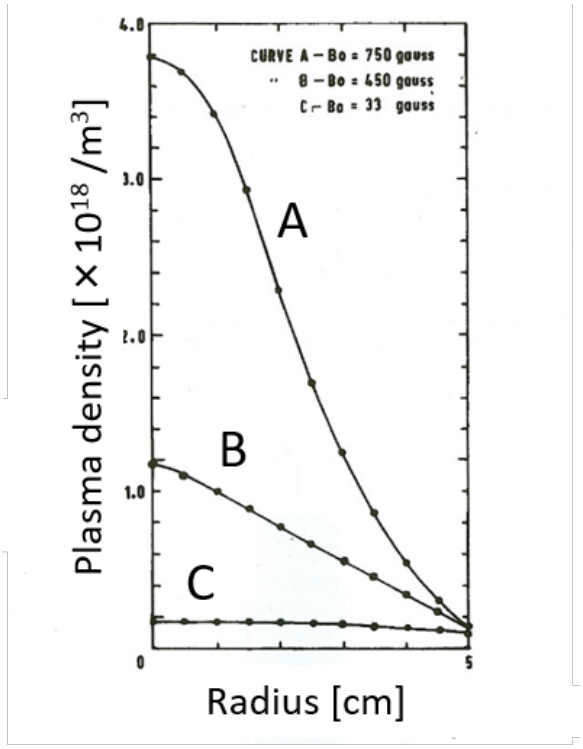

Figure 1.2: Radial variation of plasma density for different values of the steady axial B_0 [11].

RF input power for the linear $B - n$ dependence. As seen in Fig. 1.3, the linear dependence of the plasma density on the magnetic field is not established unless the magnetic field is above 400-500 [G] and the RF power above 400-500 [W] [13]. These threshold values are also found in the density jumps as the magnetic field and the RF input power are increased [14, 15].

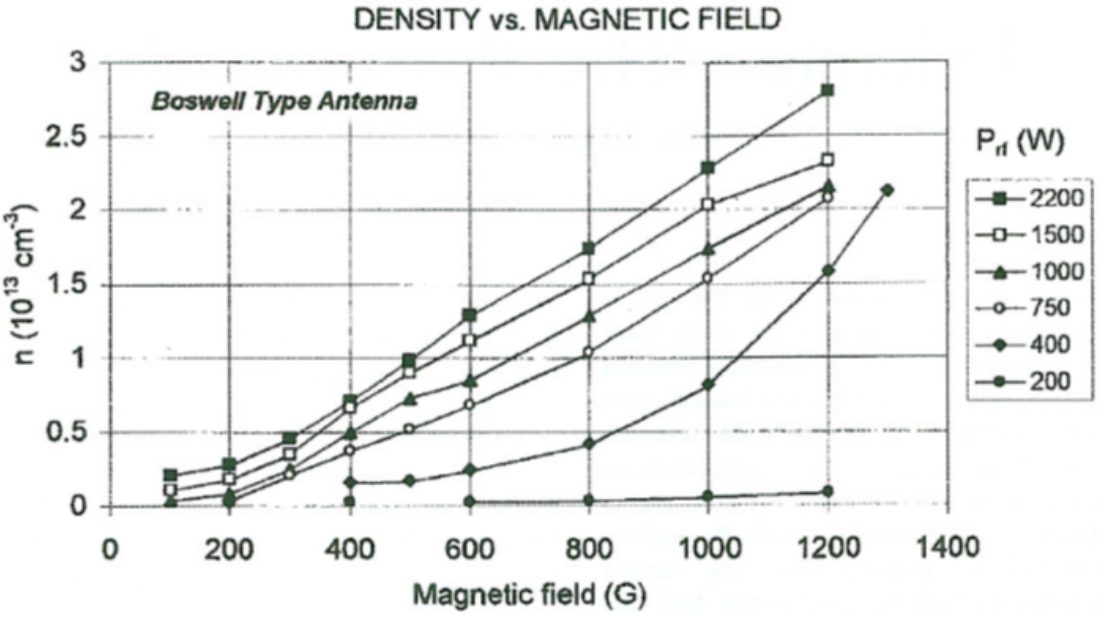

Figure 1.3: Linear relationship between the plasma density and the magnetic field [13].

1.1.2 Dissipation of the helicon wave

The damping length of the helicon wave was estimated in early work [9]. In Boswell's experiment, however, he found the collision rate, which is determined from the electron-neutral collision frequency, is much too low to explain the efficient ionization observed. Moreover, the measured wave profiles were consistent with theory only if the collision rate were 1000 times larger than the classical one. In 1991, Chen suggested that Landau damping could be the cause of the efficient energy absorption [12, 16]. This mechanism was adopted by numerous authors [17, 18] and was supported by detection of fast electrons by Ellingboe *et al* [19] using RF-modulated emission of Ar^+ light. However, Molvik *et al* [20] and Chen and Blackwell [21] showed by experiments using gridded energy analyzers that the number of fast electrons was insufficient to provide all the ionization in a helicon discharge. Thus, the role of the Landau damping for efficient ionization in considered to be unimportant.

1.1.3 Effect of the electron inertia

The importance of the electron inertial term in the generalized Ohm's law [22] has been shown by Davis [23] to be important in low density laboratory plasmas even if the wave frequency is much lower than the electron cyclotron frequency. Boswell discussed the effect of electron inertia on the dispersion relation of helicon waves, and recognized that the Trivelpiece-Gould (TG) wave, which was found theoretically and its features are verified by Trivelpiece and Gould [24], would exist when it was included [25]. The TG mode is an electrostatic cyclotron wave typically localized near the plasma edge (radial boundary), propagating oppositely directed phase and group velocities (backward waves). Since the TG wave has much shorter radial wavelength than the helicon wave, it is strongly damped by collisions and therefore is localized near the boundary. The RF energy is often absorbed more by the TG wave than by the helicon wave. Its relation to the helicon mode has been treated theoretically by

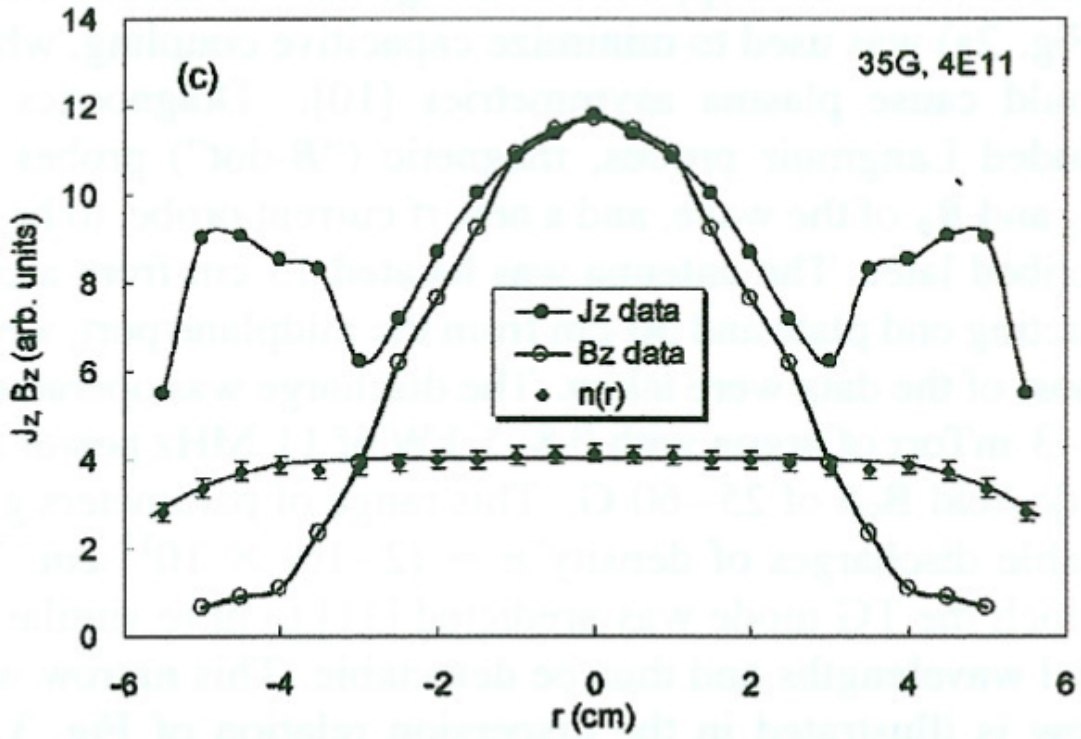

Figure 1.4: Typical radial profiles of measured $|B_z|$ and $|J_z|$ profiles at $n \sim 4.0 \times 10^{17}$ [1/m^3] and $B_0 = 35$ [G] [29].

Shamrai and Taranov [26], Boswell [27], Chen and Arnush [28], and numerous other authors. The presence of the TG mode was first detected by Blackwell *et al* [29], as shown in Fig. 1.4, where the TG mode structure can be seen in the current profile $J_z(r)$ more than in the magnetic field profile $B_z(r)$. The amplitude peaks of the TG mode can be seen in $J_z(r)$ profile at the edge of plasma column ($r \sim \pm 5$ [cm] in Fig. 1.4) [29] although the density is low. It is widely recognized that the TG mode plays main contribution to collisional power absorption in the helicon plasma.

1.1.4 Density jump observed in the experiments

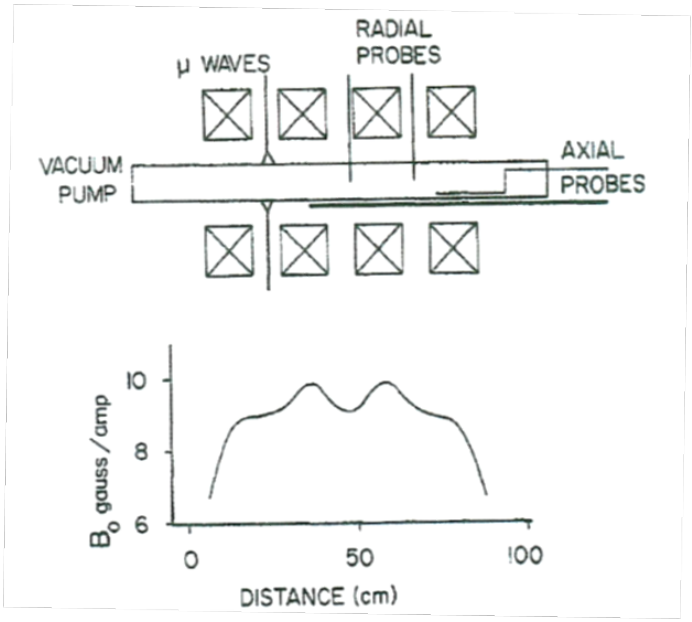

Figure 1.5: The layout of helicon device and measured magnetic field strength in Boswell's experiment [14].

In 1984, a helicon device with 10 [cm] in diameter and 120 [cm] in length was built by Boswell [14]. The layout of the apparatus is shown in Fig. 1.5. In this experiment, the input power of 180 [W] was used to generate a plasma of high density ($\sim 10^{18}$ [1/m^3]). Boswell detected the wave form and measured the relation between the plasma density n and the magnetic field amplitude B_0 as shown in Fig. 1.6. An interesting point of this observation is that the plasma density remains approximately constant ($\sim 10^{17}$ [1/m^3]) (the discharge color is light pink due to ArI lines in the red part of the spectrum) until B_0 is increased to 500 [G], at which point the plasma switches suddenly into a new mode, in which the electron density is five times greater and the color of the plasma turns to light blue due to emission of ArII lines. As B_0 is further increased the measured wavelength slowly decreases and the density increases until at 750 [G] the density again suddenly increases by a factor of two accompanied by further changes in the wave fields and wavelength.

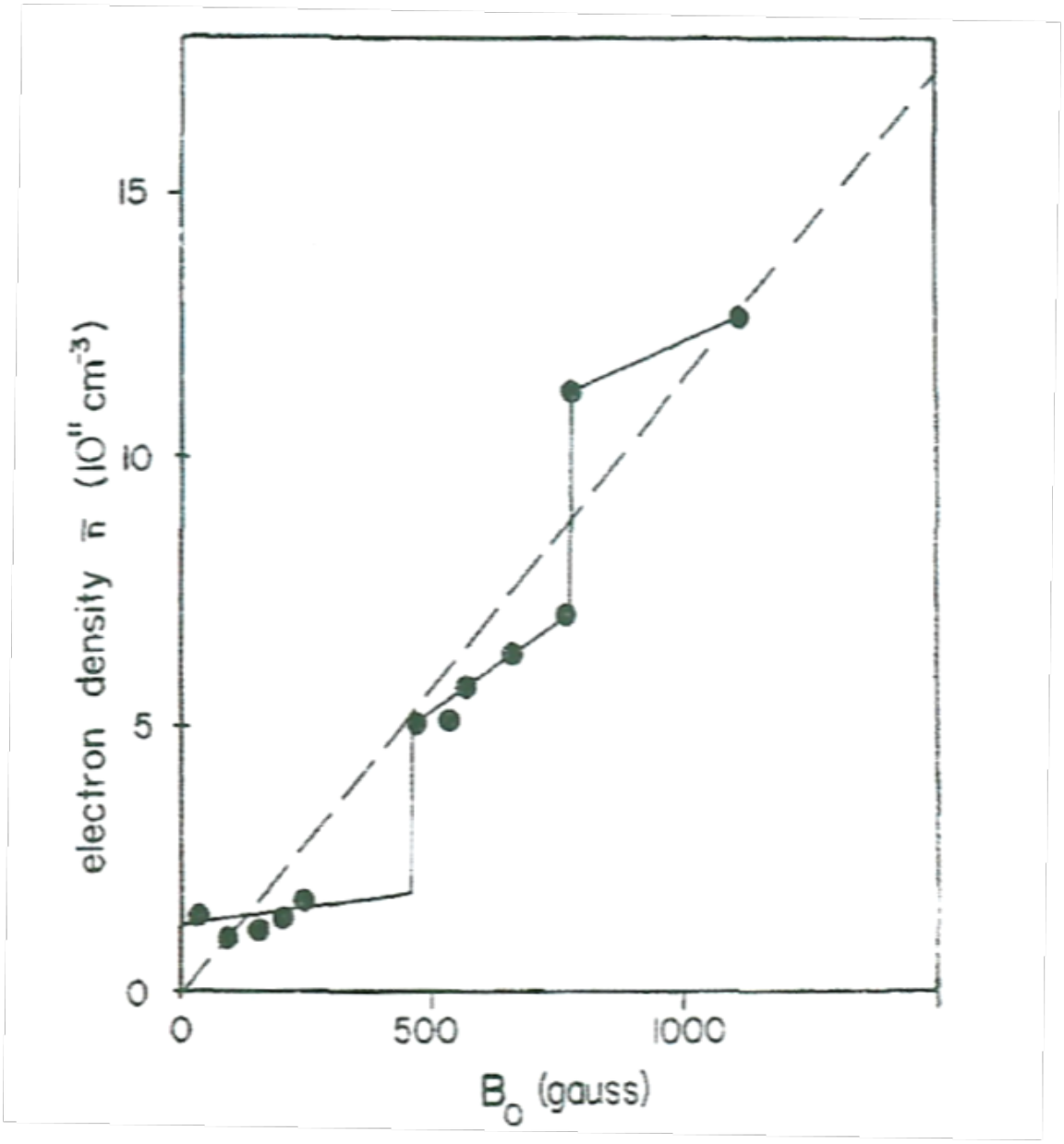

Figure 1.6: Variation of the average electron density $\bar{n}$ and the magnetic field B_0. The solid line is fitted to the experimental points and the broken line is given according to the linear dispersion relation for plane wave whistler propagation [14].

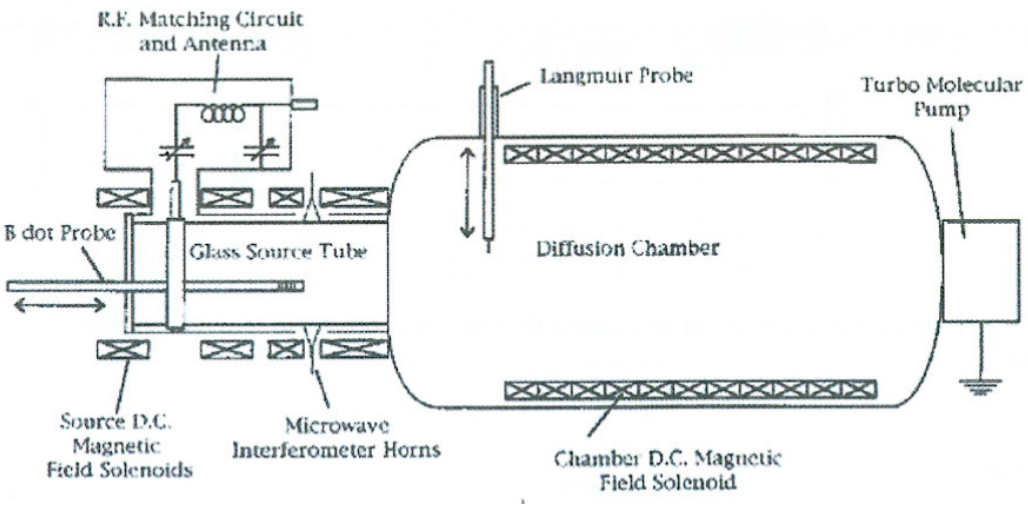

Figure 1.7: The Australian WOMBAT machine [15].

The WOMBAT machine [15], shown in Fig. 1.7 had a helicon source of 18 [cm] in diameter and 50 [cm] long, injecting the plasma into a large chamber 90 [cm] in diameter and 200 [cm] long. Chi *et al* [30] showed the RF discharge mode transition from the capacitive (E mode), to the inductive (H mode), and finally to the helicon discharge (W modes), as the RF input power is increased (Fig. 1.8). The successive W modes as seen in Fig. 1.8 correspond to helicon wave cavity resonances of the plasma-filled vacuum vessel. The first helicon discharge mode (W_1) has an $m = \pm 1$ azimuthal mode number (the predominantly B_z radial profile of the first order Bessel function J_1 was observed) and the second (W_2) and third (W_3) helicon modes have an $m = 0$ azimuthal symmetry (the axially peaked B_z radial profile of the zeroth order Bessel function J_0 was observed). Although they used the double saddle field (DSF) antenna which is designed to launch the $m = \pm 1$ azimuthal mode number waves, the antenna spectrum also contains the $m = 0$ component due to slight asymmetries of the antenna and the plasma, that may be exacerbated at higher densities [30].

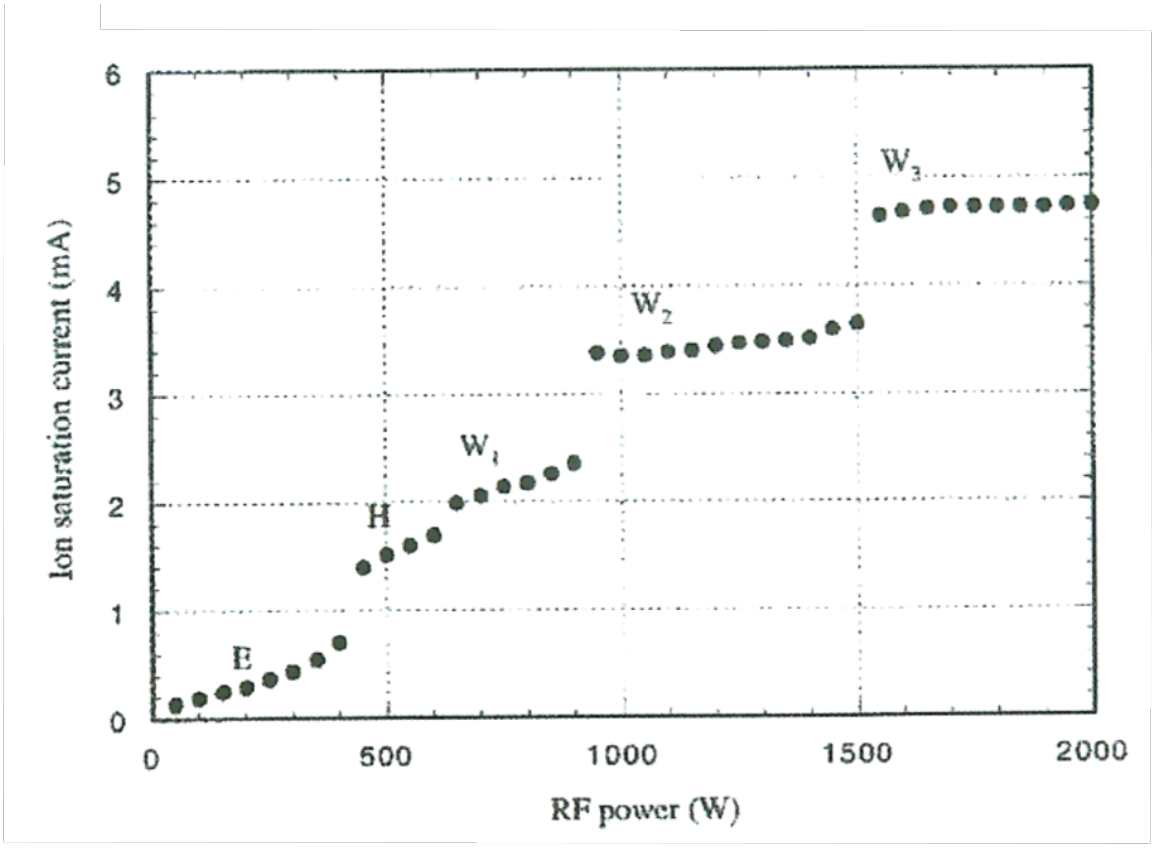

Figure 1.8: Density jumps versus RF power [30].

1.1.5 Theoretical studies of the density jump

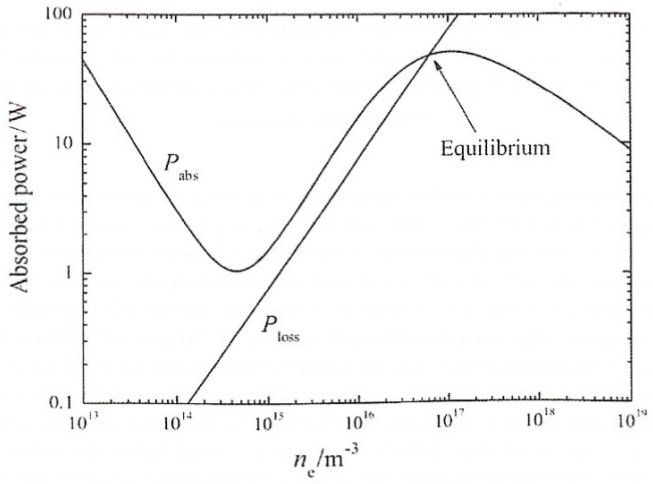

Figure 1.9: Absorbed power and power loss as a function of the electron density [35].

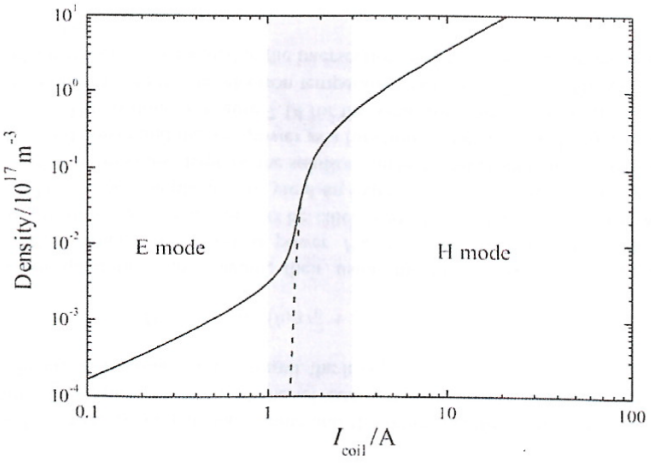

Figure 1.10: Electron density at the equilibrium as a function of the coil current for the inductive discharge with capacitive coupling. The dashed line is the density when capacitive coupling is reduced to zero. The region in gray, between 1A and 3A, corresponds to the CCP-ICP mode transition region [35].

As in any Inductively-Coupled-Plasma (ICP) discharge, the RF power is transferred to the plasma via both inductive and capacitive coupling [31]. At relatively low input power, the capacitive coupling normally dominates, and the discharge operates in the low density regime. As the input power gradually increases, the onset of induc-

tive coupling occurs as the jump of the discharge into the high density regime [32–34]. This mode transition from ICP to Capacitively-Coupled-Plasma (CCP) discharge is often explained by the global model, that solves the particle balance and the power balance in the spatial integrated form over the plasma volume. The absorbed power P_{abs} integrated over the plasma volume for an inductive discharge with capacitive coupling is plotted in Fig. 1.9 [35] for a fixed coil current $I_0 = 3$ [A] as a function of the electron density, where the parameters of five turn coil of radius $r_c = 0.08$ [m], the cylinder of inner radius 0.065 [m] and length $l = 0.3$ [m], the argon gas pressure $p = 1.33$ [Pa], and the RF antenna frequency 13.56 [MHz] are used. The loss power P_{loss} integrated over the plasma volume is plotted in Fig. 1.9 as a linear function of the plasma density. The equilibrium state solution of the plasma density can be found at the intersection of the two power curves where $P_{\text{abs}} = P_{\text{loss}}$. Using the same procedure and the same parameters, the equilibrium density can be followed while the coil current is scanned as shown in Fig. 1.10 [35]. One can clearly distinguish three regions. At low coil current, the discharge is in the CCP (E) -mode, that is the intersection between the absorbed power and the power loss curves occurs before the minimum of the absorbed power. At high coil current, the intersection occurs after the maximum of the absorbed power, i.e., in the inductive mode. In the region delimited in gray (between 1 [A] and 3 [A]), the intersection occurs between the minimum and the maximum of the absorbed power; this is the CCP(E) - ICP(H) transition region. Note that in this region the increase in the electron density is much faster than in the other two modes because the equilibrium intersection occurs in a region where the slopes of both lines in Fig 1.9 are positive and quite similar.

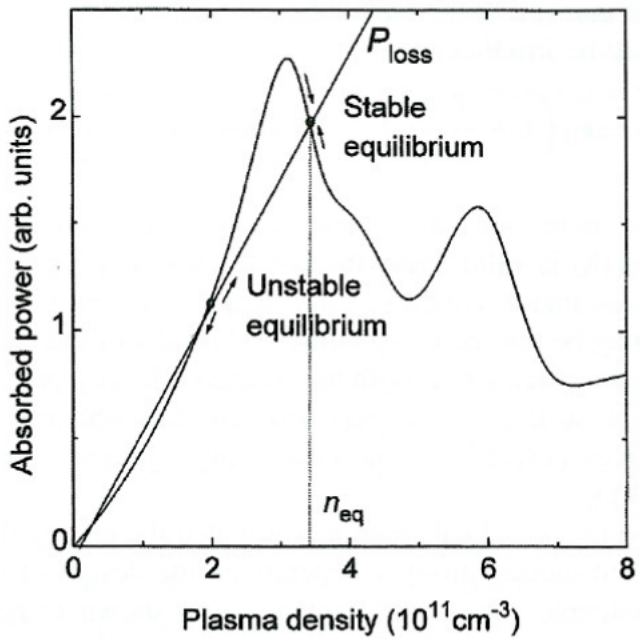

Figure 1.11: Absorbed power and loss power against plasma density at constant antenna current [37].

The same discussions have been made in the helicon discharge. The resonant cavity modes in the helicon source were first investigated by Shamrai [36], and Shamrai [37] and Arnush [38] described a non-monotonic variation of absorbed power as a function of the plasma density as shown in Fig. 1.11 [37]. Shamrai discussed the stability of the equilibrium, that the equilibrium state where the absorbed curve and the loss line intersect can be stable when the following condition is satisfied,

$$\frac{\partial P_{\rm abs}}{\partial n} < \frac{\partial P_{\rm loss}}{\partial n}. \tag{1.1}$$

The stability condition 1.1 fails at a critical equilibrium point of the following saddle type condition is satisfied,

$$\frac{\partial^2 P_{\rm abs}}{\partial n^2} > \frac{\partial^2 P_{\rm loss}}{\partial n^2}, \quad at \frac{\partial P_{\rm abs}}{\partial n} = \frac{\partial P_{\rm loss}}{\partial n}. \tag{1.2}$$

At this saddle type point, the density increases when the any sign of the density

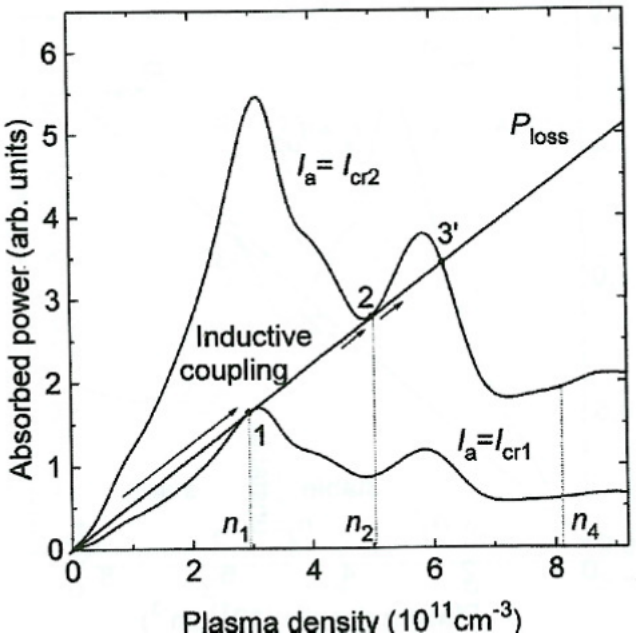

Figure 1.12: Absorption curves at different antenna currents [37].

fluctuation is given. Figure 1.12 [37] (non-monotonicity of the power absorption curves will be discussed in section 2.2.4) shows that inductive coupling starts provided that the antenna current exceeds some critical value, I_{cr1}. When this value of current is reached, the jump from a low-density (CCP mode) to a high-density (ICP mode) with plasma density n_1 has to happen (point 1 in Fig. 1.12). Since the capacitive coupled fields are ignored in this calculation, this jump looks in Fig. 1.12 like a transition starting from at zero density. If the antenna current increases above I_{cr1}, the height (but not the shape) of the absorption curve also increases. As a result, the equilibrium point moves to the right along the stable right slope of absorption curve, so that the plasma density grows. As seen in Fig. 1.12, the density increases continuously up to some value n_2, which corresponds to the antenna current I_{cr2}. The loss line touches the absorption curve from below at this point 2, which is the point of the type 1.2. The equilibrium at this is unstable against fluctuations increasing the plasma density, and what has to happen is a discontinuous jump of the discharge into the mode with higher density, that is the point 3' which is a stable equilibrium

point. Further increase of the antenna current above I_{cr2} is followed by a continuous increase of density until the next lower touching of the loss line to the absorption curve occurs near the next absorption minimum (n_4) and the second density jump happens. The comparison of experimental and theoretical results was made by Shinohara and Shamrai [39], and the agreement within 50% of the threshold input power at which the density jump occurs was obtained because of the quite simple model ignoring the effect of the plasma non-uniformity.

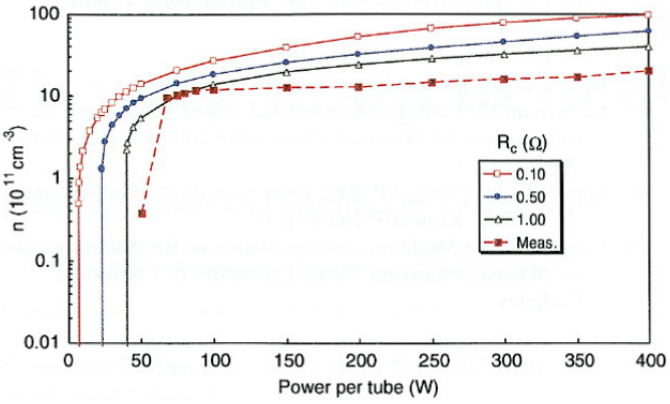

Figure 1.13: Density versus P_{RF} for three values of circuit resistance, showing the abrupt density jump in density as applied power is increased. The dashed curve shows density measured inside the discharge tube [41].

In the recent study, Chen showed the good agreement with experimental result in a threshold RF power at which a sudden density jump into a high density helicon mode by using the HELIC program [40] and including the circuit resistance in his calculation [41] (Fig. 1.13). However, this calculation do not predict a low density discharge at low power, but one is seen in experiment. He also pointed out that the mode transition from the low-density mode into the intermediate-density mode is not the transition from the ICP discharge but from the low-density helicon mode, since the finite magnetic field precludes the ICP mode in the helicon discharge system [41]. Moreover, calculations with $B = 0$ for same geometry showed that ICP operation suffers little comparison with low-field helicon mode [41]. The difference comes from the RF absorption mechanism, which in helicon discharge is dominated by coupling

to the radially damped TG modes, a magnetic field effect not available in ICPs. The detail of the mode transition is therefore unclear, and it is need to investigate the time evolution of the mode transition with the more realistic conditions such as non-uniformities of electron temperature and plasma density for the further understanding of mode transition.

1.1.6 Ion heating by the TG wave and parametric decay instability

The HELIX machine was built by West Virginia University research group led by Scime [42]. Using the HELIX machine, Kline *et al* [42, 43] measured the electron temperature in the downstream of the helicon source with an RF-compensated Langmuir probe [44] and microwave interferometry [45], and the ion temperature in the downstream and near the antenna with the Laser induced fluorescence [46]. They found the electron heating correlated with parametrically driven electrostatic waves generated downstream form the antenna in the helicon plasma source. They also found the anisotropic ion heating in the edge of downstream of the helicon source.

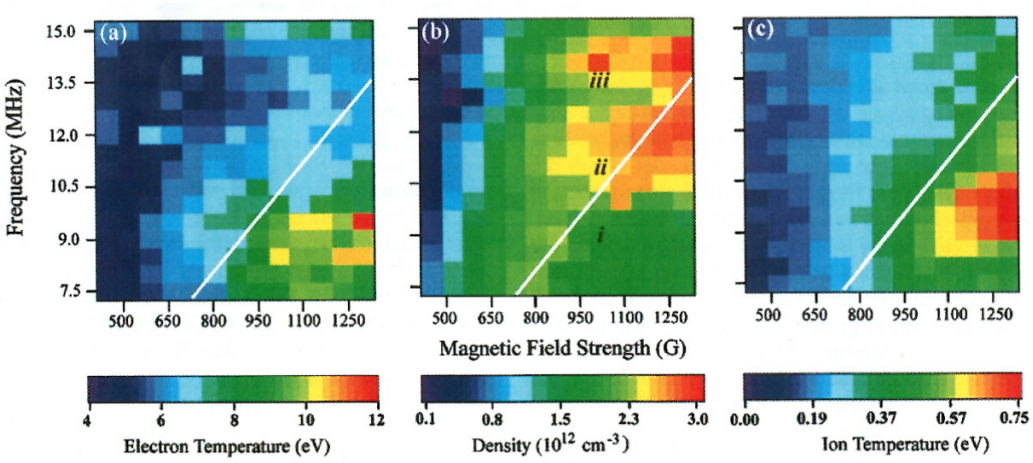

Figure 1.14: (a) Electron temperature, (b) Plasma density, and (c) Ion temperature versus RF frequency and magnetic field strength at the down stream of the helicon source. The white line indicates where the RF frequency equals the on-axis lower hybrid frequency [42].

Figure 1.14 shows the electron temperature, electron density, and perpendicular ion temperature measured at the downstream of the helicon source as a function of the RF frequency and the magnetic field strength. As seen in Fig. 1.14 (a), there is an increase in the electron temperature as the RF frequency approaches the lower hybrid frequency $\omega \sim \omega_{\mathrm{LH}}(0)$ (white line), where $\omega_{\mathrm{LH}}(0)$ is evaluated on axis $r = 0$. However, the continued increase in electron temperature in the $\omega < \omega_{\mathrm{LH}}(0)$ region (the lower right corner of Fig. 1.14 (a)) results from a net drift in the electron distribution function and not from a true increase in electron temperature (the electron temperature is overestimated when the ratio of the drifting speed V_d and thermal speed V_{th} is greater than $V_d/V_{th} > 0.1$) [47]. From Fig. 1.14 (b), one can see that the largest plasma densities occur for $\omega \sim \omega_{\mathrm{LH}}$. The dependence of the density peak at $\omega \sim \omega_{\mathrm{LH}}(0)$ on the RF frequency and the magnetic field suggests that eigenmode resonances may also play an important role in coupling the RF power to helicon sources.

The frequency spectrum of electrostatic waves measured by a single tip of the double probe is shown in Fig. 1.15 (a) for three RF frequencies and a magnetic field of 1 [kG] (parameters identified by *i*, *ii*, and *iii* in Fig. 1.14 (b)). All three spectra have typical features of kinetic parametric decay; distinct sidebands indicates a low-frequency "beat" wave such that $\omega_{\mathrm{low}} + \omega_{\mathrm{sideband}} = \omega_{\mathrm{rf}}$. The frequency spacing between the sidebands and the pump wave, the amplitude of the sidebands, and the amplitude of the broad spectral feature are greatest for the 11 [MHz] case, at which the RF frequency is closest to the lower hybrid frequency. Figure 1.15 (b) shows the frequency spectra as a function of radius. The amplitudes of the sidebands, the broad band feature, and the low-frequency beat wave all increases towards the center of discharge. The clear low-frequency beat wave appears in Fig. 1.15 (b) only on axis $r = 0$ [cm].

As seen from Fig. 1.14 (c), the perpendicular ion temperature peaks for $\omega <$

$\omega_{\mathrm{LH}}(0)$. Radial profiles of the perpendicular and parallel ion temperature at $\omega_{\mathrm{rf}} = 9.0$ [MHz] and $B = 1200$ [G] are shown in Fig. 1.16. The perpendicular ion temperature is constant across the inner portion of the discharge and increases at the edge. They concluded that enhanced ion heating near the plasma edge results from the ion-Landau damping of the slow waves (TG wave) in the edge region, and damping of the low-frequency beat waves is unlikely to be cause of the ion heating, since the low-frequency beat waves appear only near the center of the discharge as seen in Fig. 1.15 (b). When the RF wave frequency equals the local lower hybrid frequency, the slow wave (TG wave) becomes predominantly electrostatic and its phase velocity is low enough that ion-Landau damping can occur. Because of the low plasma densities near the plasma edge, the local lower hybrid frequency can drop below 8 [MHz] even though the lower hybrid frequency on axis $r = 0$ is 12 [MHz].

Lorenz and Krämer also measured the electrostatic fluctuations, and identified the fluctuations as ion sound and TG waves that originate from parametric decay of the helicon pump wave. They found that the growth rates and thresholds inferred from the evolution of the fluctuations in a wide range of helicon plasma parameters are in good agreement with predictions for the parametric decay instability that takes into account realistic damping rates for the decay waves [48, 49]. Although the detail of parametric interaction were measured in the above experiments, its importance for the power absorption in the helicon discharge is still under the discussion [50].

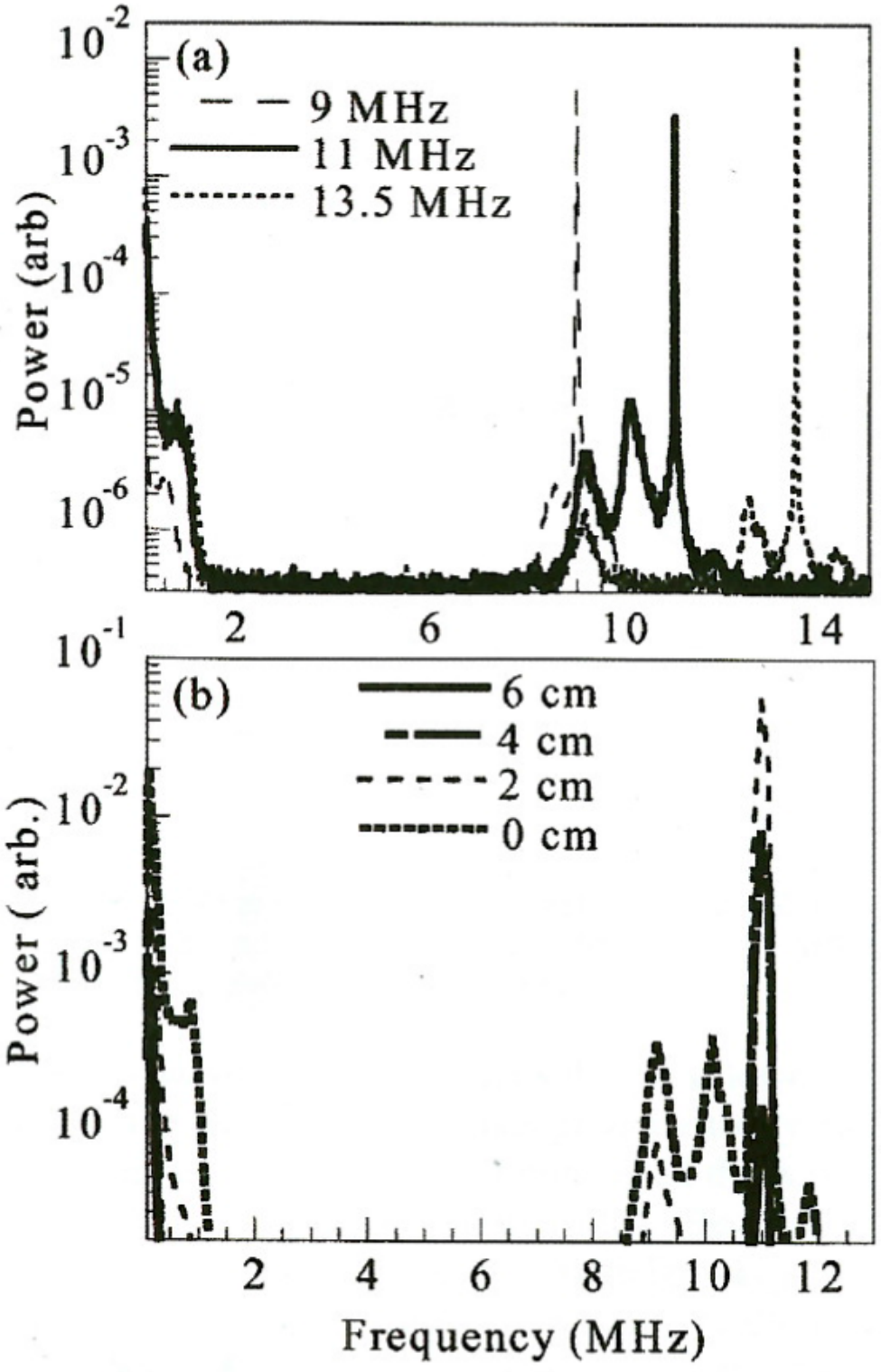

Figure 1.15: (a) Power spectrum of electrostatic fluctuations for three different RF frequencies. (b) Power spectrum of electrostatic fluctuations versus radius for the RF frequency of 11 [MHz] and the magnetic field of 737 [G] [42].

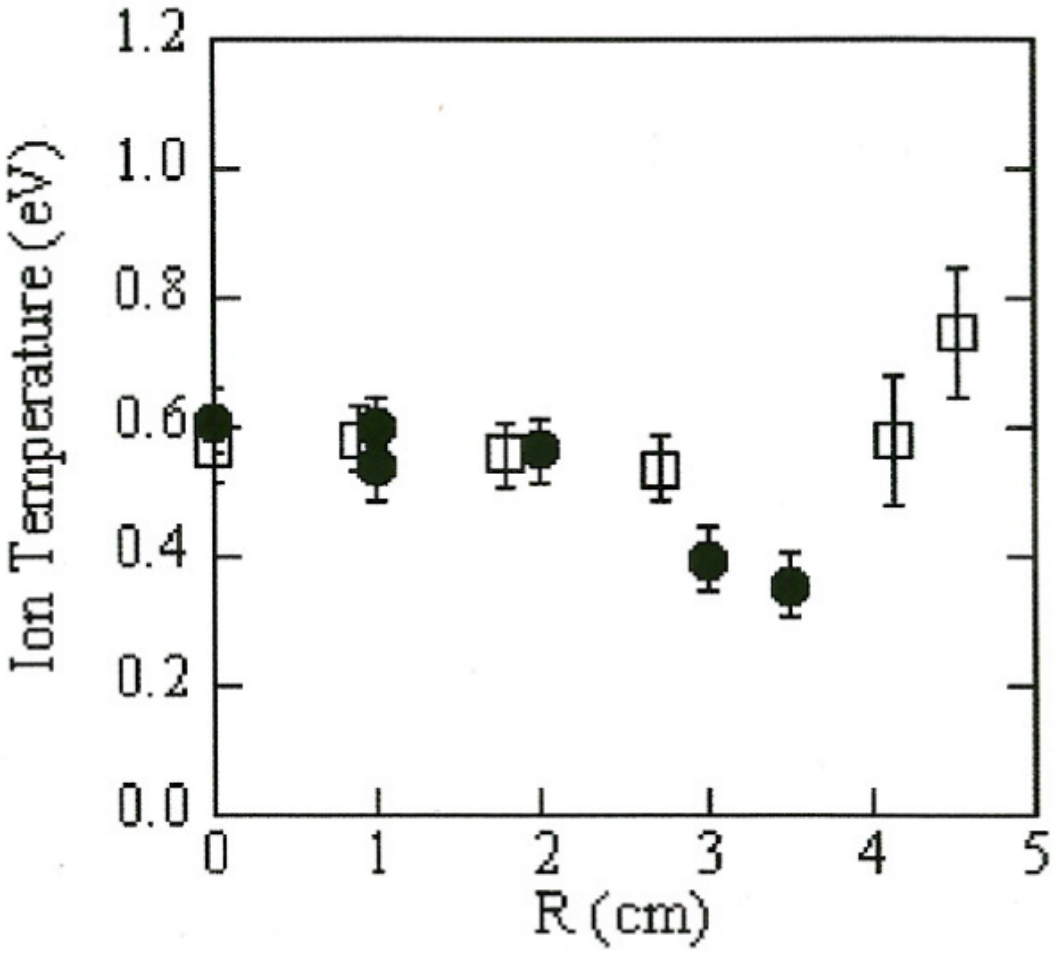

Figure 1.16: Perpendicular (open squares) and parallel (filled circles) ion temperature versus radius for the RF frequency of 9 [MHz] and the magnetic field of 1200 [G] [42].

1.2 Applications

1.2.1 Plasma processing

The interest in helicon sources for etching and deposition of integrated circuits arose because of their high plasma densities and their numerous adjustable parameters, such as device scale, magnetic field strength, and device shape. The standard conventional systems of the semiconductor devices are capacitively coupled plasmas (CCPs) and inductively coupled plasmas (ICPs). The CCP system has parallel plates with silicon wafer mounted on the bottom one as shown in Fig. 1.17 [51]. The RF waves applied on top of the plates generate the plasma, and a bias on the plate accelerates ions onto the wafer. ICPs use antennas on a dome above the wafer chuck to generate a plasma without a B-field as shown in Fig. 1.18 [51]. Helicon sources would generate higher plasma density and decrease the processing time, but they have not yet been accepted by the semiconductor industry [52].

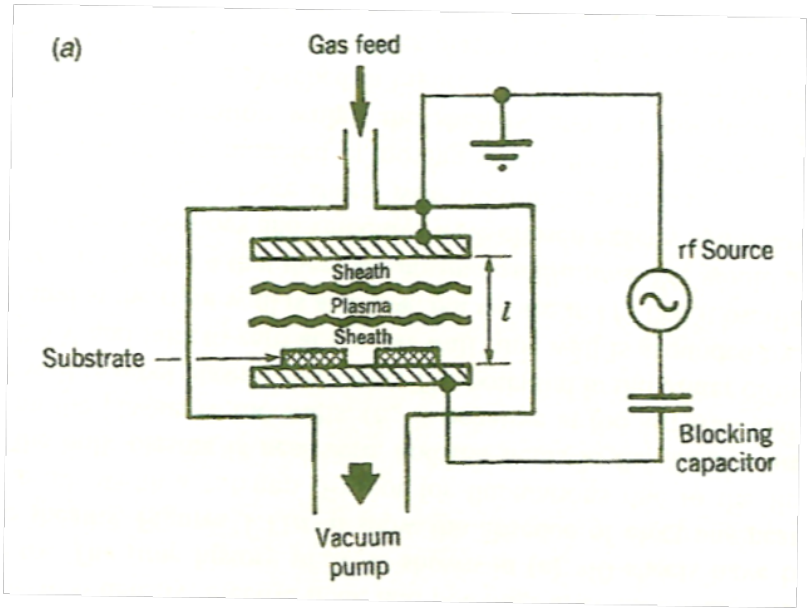

Figure 1.17: Capacitive rf discharges in plane parallel geometry [51].

The first helicon source that can be used for industrial applications was built by Benjamin *et al* [53] in 1991. The comparison of the helicon and electron cyclotron

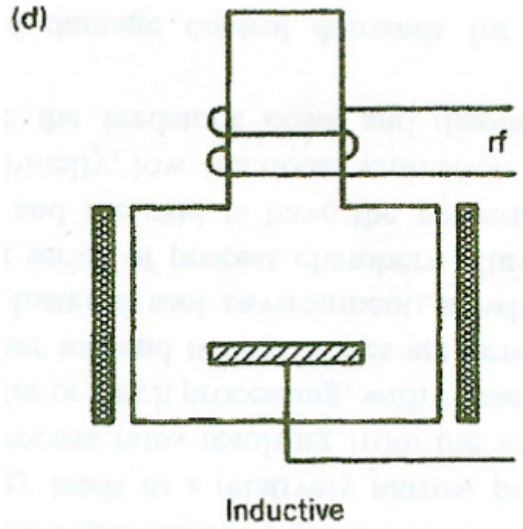

Figure 1.18: Inductively coupled plasma source [51].

resonance (ECR) sources for the etching of the semiconductor was studied by Tepermeister *et al* [54–56], and they found that the helicon source was not better than the ECR source in the etching rate but gave somewhat better uniformity. In 1997, a company called PMT manufactured the MØRI helicon source (Fig. 1.19) [57]. This source has an $m = 0$ antenna comprising of two rings with opposite currents, and two independent magnetic coils. This source has been demonstrated to give good uniformity over the large area, high ion flux, and high selectivity and anisotropy. In a recent study, Chen developed the prototypes of the small helicon source with small permanent magnets (Fig. 1.20) for the future applications [52,58]. This helicon device has seven small helicon tubes, and can produce uniform coverage of the substrate.

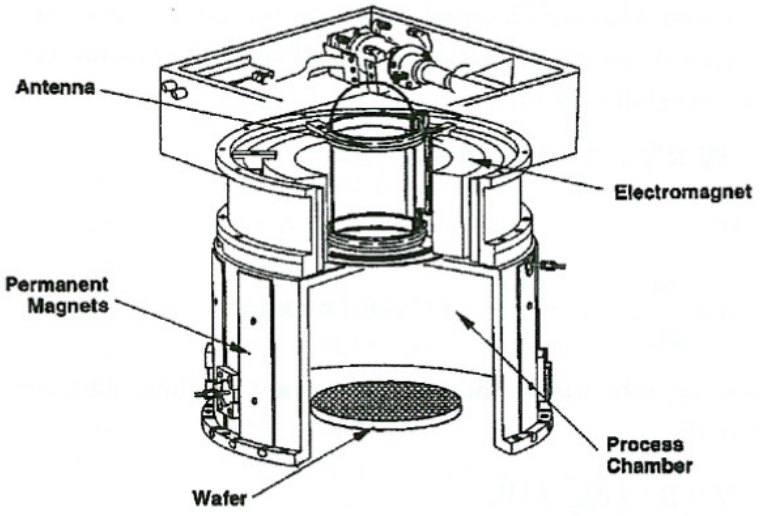

Figure 1.19: A plasma source manufactured by PMT, Inc., based on the $m = 0$ helicon mode [57].

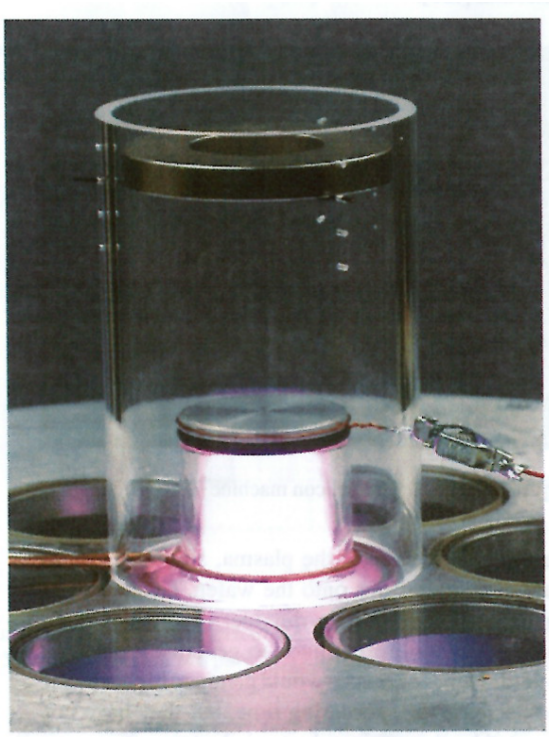

Figure 1.20: Photo of 5 [cm] diameter helicon source using the remote field of a permanent magnet [58].

1.2.2 Spacecraft propulsion

Electric propulsion system for spacecraft has been used for leaving the Earth orbit, attitude control, and traveling into deep space. There are mainly two types of electric propulsion system, that has been used in practical spacecraft missions. Ion thrusters create thrust by accelerating ions electro-statically, using acceleration grids. Electrons are emitted from an external source to neutralize the charges of ejected ions, keeping the spacecraft from charging up. Hall thrusters also accelerate the ions by applying an electric field, but the electrons are held back instead by a dc magnetic field. An external electrons source is still needed to neutralize the ion beam. Helicon thrusters eject a neutral plasma, both ions and electrons, and no neutralizer is necessary. Straightforward application of helicons to Hall thruster would require helicon waves in an annular geometry. This configuration has been studied by Yano and Walker [59].

Now there are some helicon sources in the field of next-generation electric propulsions with electrodeless configuration such as VASIMR (Variable Specific Impulse Magnetoplasma Rocket) (Fig. 1.21) [60], M2P2 (MiniMagnetospheric Plasma Prorpulsion) [61], helicon ion thruster, and other smaller plasma sources [62]. The VASIMR is a high power, radio frequency-driven magnetoplasma rocket, capable of propelling a spaceship to Mars in just 39 days, that is ten times faster than today's chemical rockets while using one-tenth the amount of fuel. The physics and engineering of this device have been under study since 1980. The plasma is produced in an integrated plasma injector by a helicon discharge, and the bulk of the plasma energy is added downstream by ion cyclotron resonance. The system features a magnetic nozzle, which accelerates the plasma particles by converting their azimuthal energy into directed momentum. A conceptual design for a 10 [kW] space demonstrator experiment has been completed [60]. In the recent experiment, a new superconducting device (VX-200) with a total power capability of 200 [kW] is coming into operation [63].

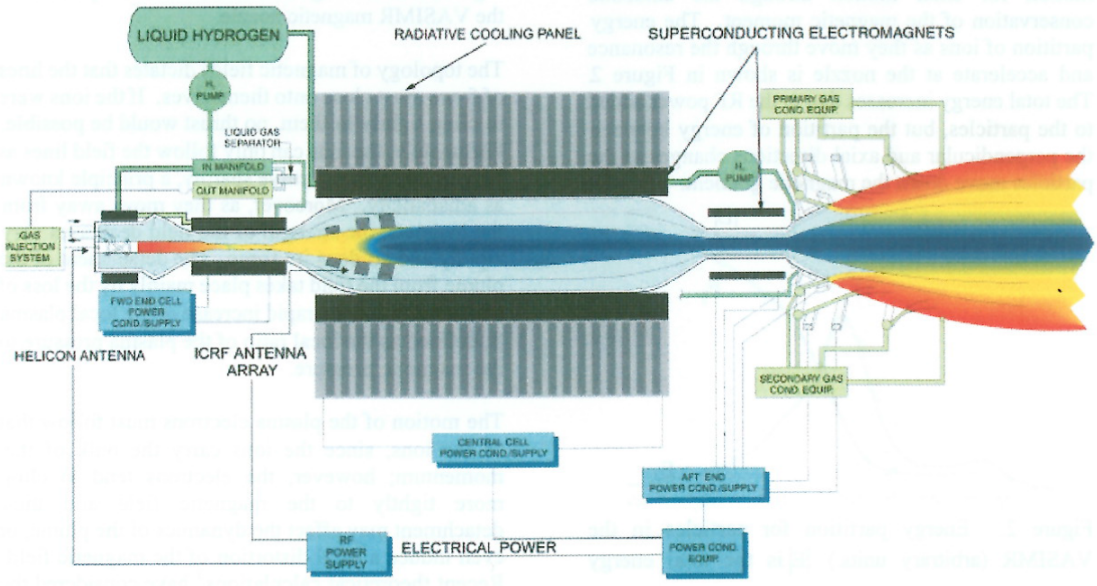

Figure 1.21: The VSIMR concept [60].

A new concept of electrodeless discharge and electromagnetic acceleration for next generation electric propulsion has been developed within the helicon electrodeless advanced thruster (HEAT) project [64–77]. The electrodeless configuration is one of promissing solutions for the problems of erosions and contaminations in conventional electric propulsion systems [64]. Plasma acceleration by the magnetic nozzle has been investigated theoretically by Fruchman [78] in quasi-1D model, and numerically by Ahedo and Merino in 2D computation [79]. Takahashi *et al* also measured the electromagnetic thrust produced by the magnetic nozzle, and confirmed that it can be well explained by a simple model of the magnetic nozzle [65–67]. In addition to the magnetic nozzle acceleration, additional plasma acceleration method has been proposed [64]. The rotating RF electric field (REF) (Fig. 1.22) [68–71] and rotating RF magnetic field (RMF) (Fig. 1.23) [72–75] are based on the concept that the entire acceleration process can be conducted without contacts between electrodes and the plasma by using RF antennas out side of the discharge chamber. In these methods, an azimuthal electric current is induced by the additional REF or RMF, and the

plasma is electromagnetically accelerated in the magnetic nozzle. Ponderomotive acceleration (PA) with the ion cyclotron resonance (ICR) acceleration method (Fig. 1.24) [76] is thought to efficiently heat ions perpendicularly by the ICR, and by applying the RF waves in such a way that the resonance point coincides with the peak of the wave energy density, the ions can gain parallel acceleration because of the EM ponderomotive force [77, 80, 81].

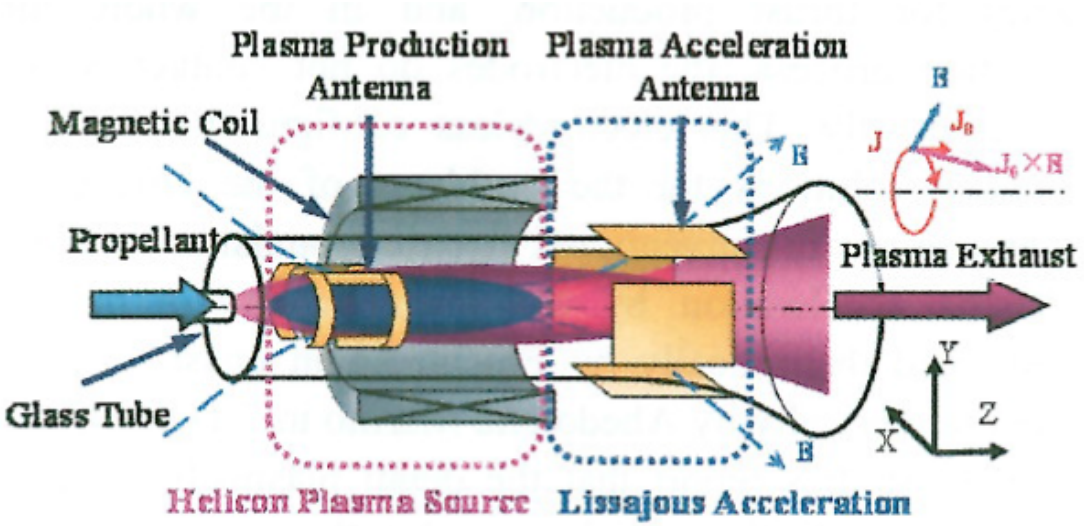

Figure 1.22: Concept of Lissajous (REF) acceleration type plasma thruster [68].

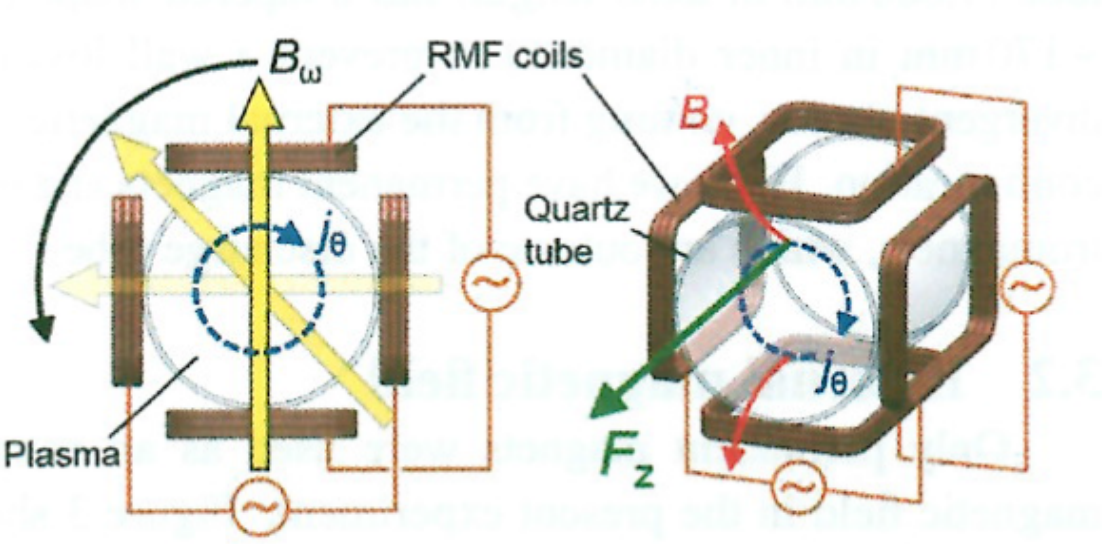

Figure 1.23: Concept of RMF acceleration type plasma thruster [74].

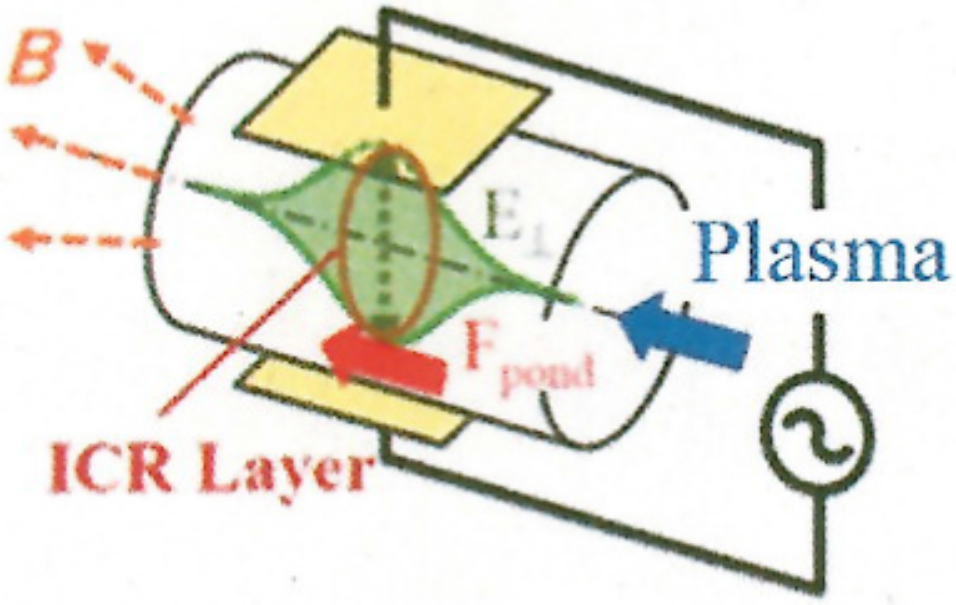

Figure 1.24: Concept of PA with ICR acceleration [76].

1.3 Purpose and outline of this work

Throughout the history of the helicon study, numerous interesting physical problems have been arisen one after another, and a number of authors addressed these problems by experiments and theories, and numerical simulations. Since the helicon study began in 1960, many of the physics issues in helicon discharge have been cleared over the last half century owing to these efforts. However, there still remains the problem about the unified understanding of helicon discharge. Theoretical calculations often assume a steady state such as constant density profile, electron temperature, and other physical parameters. That is not enough to answer the basic question: "Why the helicon plasma is generated ?", it is therefore necessary to investigate the temporal behavior by computing the helicon discharge self-consistently, and bridge the gap between theory and the experiment, in order to develop further beneficial applications.

There are some self-consistent models for the helicon discharge. Kinder *et al* [82] developed the three-dimensional model of the realistic helicon device for the material processing. The time evolutions of the plasma density and the electron temperature are included in this model. They focused on the investigation of the mode transition from the inductively coupled mode (low-density mode) to the helicon discharge mode (high-density mode). However, the density jump in increasing the rf power which is observed in the experiment could no be seen in their result. The disagreement of their result with the experiment may due to the vanishing of the TG waves, which play dominant role on the power absorption into the plasma. Bose *et al* [83] included the TG waves, and they showed that the edge heating due to the TG waves dominate the power absorption under the low external magnetic fields. Cho *et al* [84] studied the effect of the external magnetic field on the radial plasma density profile by the one-dimensional simulation. Unlike above models, they assumed the quasi-neutral plasma without solving the Poisson's equation (thus the diffusion process was treated as the

ambipolar diffusion), and they found the steady states of the electron temperature and the plasma density profiles by the iterating calculations. They found the plasma density changes from relatively flat to steep profile as the external magnetic field increases. Chen *et al* [85] conducted the two-dimensional model of the Boswell's experiment [11]. They found that the classical heat conductivity is too small to sustain a centrally peaked density profile under the experimental conditions, thus the resulting density profile was the hollow density profile. Assuming the enhanced radial heat conductivity and particle transport, they also found the steady state solutions that are in good agreement with the density profile and the density jump observed in the experiment.

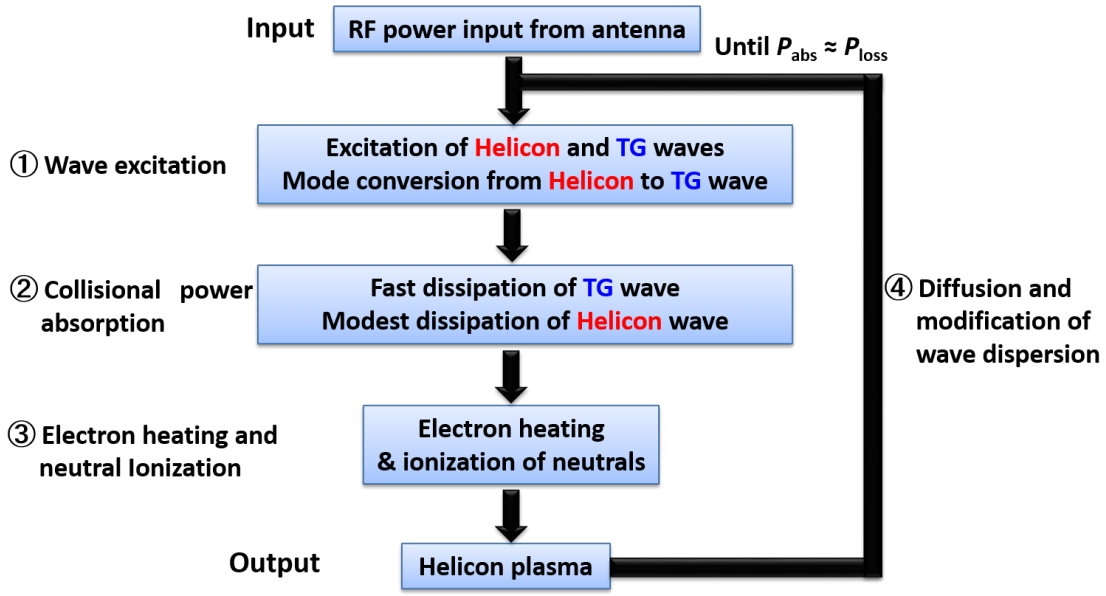

Figure 1.25: The system flow of helicon discharge calculation

In this work, we developed the one- and two-dimensional self-consistent model based on the experiment by Nisoa *et al* [1–3] (the detail about this experiment is introduced in section 2). Figure 1.25 shows the flow chart of the helicon discharge from the antenna current input to the output of helicon plasma production. This system can be divided mainly four parts in time as follows: 1. electromagnetic waves

(the helicon and the TG waves) are excited in a plasma by input antenna current, 2. Waves are dissipated mainly by collisions of electrons, 3. Electrons are heated by Joule heating and the ionization of neutrals is facilitated, and 4. The modification of the electron temperature and density profiles and the diffusion of the back ground plasma, that lead to the time evolution of the dispersion relation. After enough time is passed, the electron temperature and the plasma density relax to the steady state.

The model consists of three parts, electromagnetic wave fields solver, power balance solver, and particle balance solver. The wave fields solver solves Maxwell's equations and linearized electron equation of motion for given plasma parameters by the Finite Difference Time Domain (FDTD) method (Appendix A), and the local collisional power absorption (Joule heating) is calculated from the wave fields. The electron temperature is updated from the energy balance equation, that calculate the electron energy transport with the local power balance between the power absorption and the power losses due to the inelastic collisions (ionization and excitation) and loss energy to the wall. After the electron temperature is updated, the plasma density is updated from the particle balance equation, that includes ionization, recombination, and particle loss to the wall. In our model, two models are used for calculating the motion of bulk (background) plasma. The first model is the ambipolar diffusion model, in which we assume the local charge neutrality $n_e \sim n_i$ and the local flux equality between the electron flux and the ion flux for both of the parallel and the perpendicular directions. The local ambipolarity (charge neutrality) is assumed for simplicity. However, this assumption would not hold when the global ambipolarity is conserved in the way that ions diffuse to the transverse walls while electrons are preferentially lost to the axial walls in the bounded plasma [86]. The second model is the full fluid model, in which the full momentum balance equation is solved for ion but the drift-diffusion approximation (the inertial terms are ignored) is used for the electrons momentum balance equation. The densities of the electron and ion

are solved separately from the independent continuity equations, and the ambipolar electric fields are calculated from the Poisson's equation. Therefore, there is no restrictions such as the charge neutrality and the flux equality in the full fluid model. The details of these two model are described in section 5. Unlike the previous works, in which the steady-state solutions are found by Bose *et al* [83], Cho *et al* [84], and Chen *et al* [85], our results presents the first report on the time evolution of the plasma density and the electron temperature profiles and their maximum values. In this theses, we discuss about the following subjects,

(a) The importance of the bulk mode conversion

This is the classical type of the mode conversion that occurs near the mode conversion surface (MCS) where the dispersion curves of the helicon and TG waves merge, $Re(k_{\perp \mathrm{H}}) = Re(k_{\perp \mathrm{TG}})$ ($k_\perp$ is the radial wave number, and Re stands for the real part). Shamrai [37] argued that the density gradient is a suppressing factor in the efficiency of the bulk mode conversion. Indeed, with flattening of the density profile the width of the synchronism region increases, thus leading to a increasing of the efficiency of the bulk mode conversion. However, some numerical results show that, for some reason, the contribution of the bulk mode conversion to the total power absorption is not high [38].

Aliev and Krämer [87] suggests that the densities at which the bulk mode conversion occurs can be reduced considerably for $m \neq 0$ modes when the density gradient is steep. Kim and Hwang [88] pointed out that collisional dissipation plays an important role near the MCS. The detail about their argument is introduced in section 2.3. We make a quantitative argument on the contribution of the bulk mode conversion and the surface mode conversion on the energy deposition of the helicon wave, by numerically solving a fluid set of Hall MHD equations including the electron mass and the collisional effect. The calculation model and the methodology are described in section 3.1. In this model, all the four wave modes, i.e., the helicon waves (H$\pm$)

and the TG (TG±) waves, with two oppositely propagating directions for both, are included. The energy fluxes associated with these waves are numerically evaluated. We show in section 3.4 that, although the bulk mode conversion takes place anywhere as long as there exists a density gradient in background plasma parameters, the dissipation strongly suppresses the efficiency of the bulk mode conversion due to the separation of the dispersion branches. Our argument is quite different from that of Kims in that the bulk mode conversion occurs even if the helicon and the TG do not merge at the MCS. Note that there is a substantial contribution of the bulk mode conversion for power depositions when the collision frequency is small, if the neutral pressure is low, or a neutral depletion occurs [89]. Therefore, our results presents the first report on the contribution fraction of the bulk mode conversion in contrast to the surface one as a function of the collision frequency. By evaluating power depositions of the helicon and the TG waves, we also confirm the importance of the bulk heating near the MCS by the helicon wave as pointed out by Kim.

(b) The time evolution of the plasma density and the electron temperature profiles and their maximum values.

In section 4.6, using the one-dimensional ambipolar diffusion model, we show the time evolution of the plasma density and the electron temperature profiles, and their maximum vales. The various physical time and space scalings relevant to the helicon discharge are investigated in section 4.5, that well presents the rough characteristics of helicon discharge. Figure. 1.26 shows the radial density profiles measured in the experiment by Nisoa *et al* [2]. Figure 1.26 (a) shows the density profile when $N = 1$ ($k_z = 5$ [1/m]) axial standing wave is excited, and Fig. 1.26 (b) shows the density profiles when $N = 3$ ($k_z = 15$ [1/m]), $N = 3$ ($k_z = 25$ [1/m]) axial standing waves and traveling helicon wave (THW) are excited. The centrally peaked density profiles are observed for $N = 3$, $N = 5$ and THW modes, a hollow profile appears when only $N = 1$ mode is excited. We show that the ambipolar diffusion model can not

explain the centrally peaked density profile as pointed out by Chen [85], and that the density profile becomes highly edge-localized profile (not the hollow profile as shown in Fig. 1.26 (a)) in the ambipolar diffusion model. Some ideas to explain the centrally peaked profile is introduced in section 5.2. The theoretical treatment [37] of the density jumps observed in the experiments is also introduced in section 2.2. Our result show the some threshold vale of the RF input power for the density growth. Under this threshold value, the net total power balance ($P_{\rm abs} - P_{\rm loss}$, these values are integrated over the plasma region) is always minus through the all time evolution, thus the electron temperature decreases and the density can not grow. On the other hand, above the threshold value, the density grows up to $n \sim 10^{20}$ [1/m^3], which is higher value than that observed in the laboratory experiments $n \sim 10^{19}$ [1/m^3] resulting from ignoring the effect of the neutral depletion.

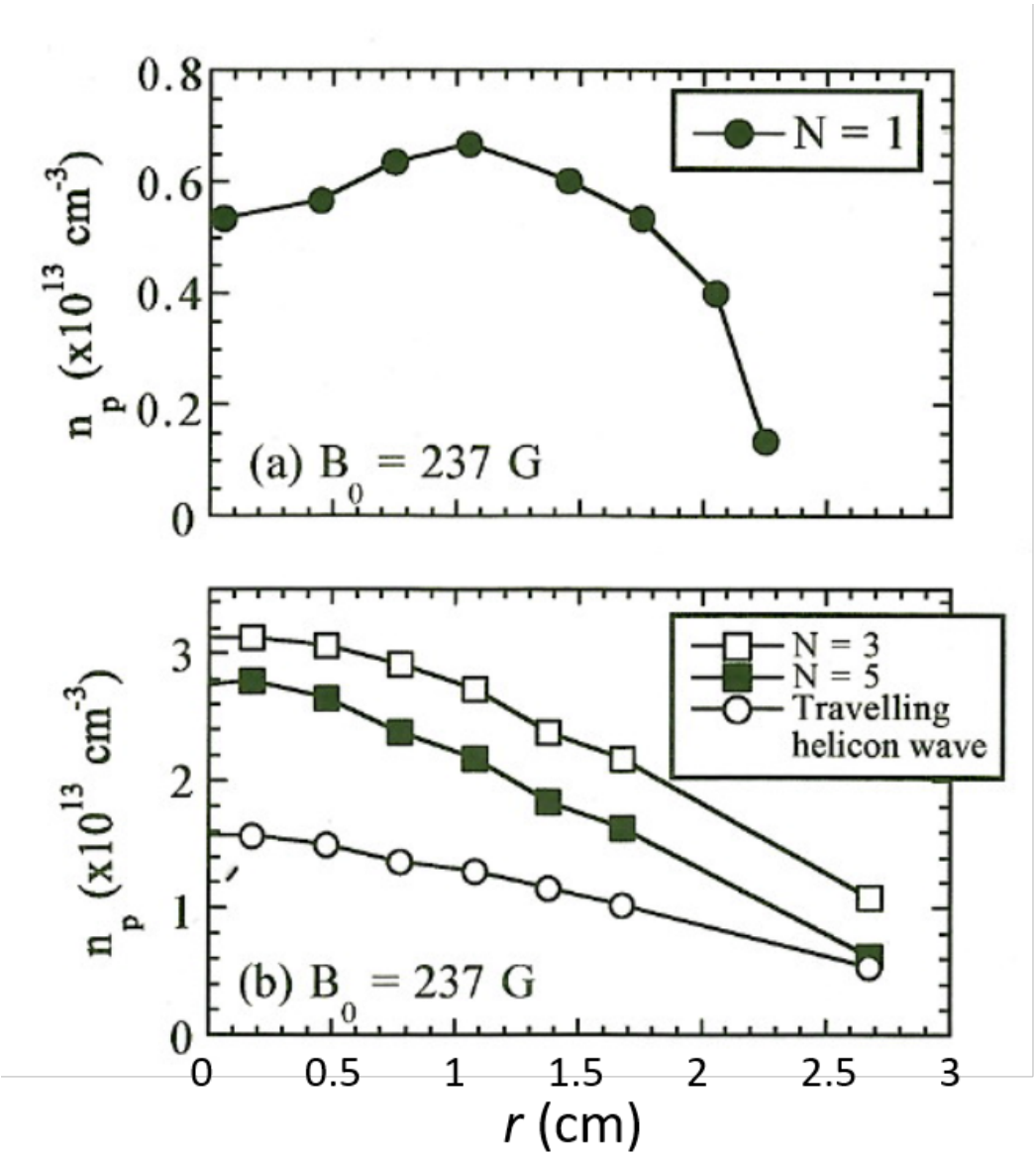

Figure 1.26: Measured plasma density profile in the experiment by Nisoa *et al* [2].

(c) The wave excitation in the two-dimensional cylinder

In section 4.7.1, we show the two-dimensional excited wave profiles at the three uniform plasma density, low density 1.0×10^{16} [1/m^3], intermediate density 5.0×10^{18} [1/m^3], and high density 5.0×10^{19} [1/m^3]. We show that the B_z profile that is measured in the experiment by Nisoa *et al* [1] is not what they call the antenna induction field but the pure imaginary (non-propagating) helicon wave. Furthermore,

the power absorption by the TG wave can play the dominant role on the power absorption even when the low-density mode ($n < 10^{18}$ [1/m^3]). Therefore, as Chen suggested [41], the low-density mode is not the ICP mode, but the low-density helicon mode generated by the TG wave. Actually, in the experiment by Lho *et al* [90], the existence of the TG wave has been shown at the low-density plasma ($n \leq 9.0 \times 10^{16}$[1/m^3]) by fitting the dispersion curve of the TG wave with the observed data.

(d) The comparison between the ambipolar diffusion model and the full fluid model

In section 4.7.2, we show the difference between the ambipolar diffusion model and the full fluid model. In the ambipolar diffusion model, the movement of the thermal electrons is strongly restricted by that of the ions with assuming the charge neutrality. Therefore, the localized power absorption near the antenna by the TG wave leads to the localized profiles of the plasma density and the electron temperature in the very narrow region near the antenna. On the other hand, the thermal electrons can move freely along the magnetic field line in the full fluid model, since there is no assumption of the charge neutrality. The heat transfer is greatly enhanced in the full fluid model, thus the axial broad density profile is obtained in the full fluid model despite the localized power absorption near the antenna by the TG wave. However, the centrally peaked profile can not be seen in both models.

(e) The the fast heat transfer mechanism along the magnetic field

In section 4.7.3, by conducting the simple diffusion test of the magnetized plasma, the difference between the ambipolar diffusion model and the full fluid model is investigated in more detail. In this diffusion test, the hot ($T_e = 9.0$ and $T_i = 0.025$ [eV]) and dense ($n_e = n_i = 6.0 \times 10^{16}$ [1/m^3]) plasma region is located at the center of the back ground cold ($T_e = 4.0$ and $T_i = 0.025$ [eV]) plasma ($n_e = n_i = 1.0 \times 10^{16}$ [1/m^3]) region. Besides the comparison of these two models, this test is conducted by the Prticle In Cell Monte Carlo Collision (PIC-MCC) model [91], which includes the

electron-neutral elastic collision, the ion-neutral-elastic collision, and the ion-neutral charge exchange collision. These results show the fast heat transfer mechanism that is different from the classical ambipolar diffusion.

In the final chapter (chapter 5), the conclusions of the above subjects and some points to be improved in the future works are presented. The most outstanding issues are also introduced in this chapter.

CHAPTER II

Theory of helicon wave

2.1 Dispersion relation

Since the helicon wave is basically a bounded whistler wave propagating in a dc magnetic field, the dispersion relation of the helicon wave is derived from the standard theory of the whistler ones in a cold plasma. It is well known that the simple theory of helicon waves, in which the electron mass m_e is neglected, is valid only if the axial electric field E_z also vanishes [16]. The exact theory with finite m_e and E_z predict the existence of additional highly damped TG modes, which greatly modify the simple theory of helicon waves [16]. In this section, the basic properties of the dispersion relation in a uniform density and a non-uniform density plasma are discussed.

2.1.1 Dispersion relation in a uniform plasma

We consider a linear model [16] composed of the equation of motion of an electron fluid neglecting the advection term (due to weak nonlinearity) and pressure gradient (almost cold plasma) with a back ground axial magnetic field $B_0\hat{\boldsymbol{z}}$. And wave perturbed quantities vary as $\exp[\mathrm{i}(m\theta + k_r\hat{\boldsymbol{r}} + k_z\hat{\boldsymbol{z}} - \omega t)]$ in a cylindrical geometry,

$$m_{\mathrm{e}}\frac{\partial \boldsymbol{u}_{\mathrm{e}}}{\partial t} = -e\left[\boldsymbol{E} + \boldsymbol{u}_{\mathrm{e}} \times \boldsymbol{B}_0\right] - m_{\mathrm{e}}\nu\boldsymbol{u}_{\mathrm{e}}. \tag{2.1}$$

Maxwell's equations,

$$-\frac{\partial \boldsymbol{B}}{\partial t} = \nabla \times \boldsymbol{E}, \tag{2.2}$$

$$\frac{1}{c^2}\frac{\partial \boldsymbol{E}}{\partial t} + \mu_0 \boldsymbol{J} = \nabla \times \boldsymbol{B}, \tag{2.3}$$

$$\nabla \cdot \boldsymbol{B} = 0. \tag{2.4}$$

The angular frequency ω satisfying

$$\omega_{ci} \ll \omega_{LH} < \omega \ll \omega_{ce} \ll \omega_{pe}, \tag{2.5}$$

where ω_{ci}, ω_{ce}, ω_{pe}, and $\omega_{LH} \approx (\omega_{ce}\omega_{ci})^{1/2}$ are the ion cyclotron, electron cyclotron, electron plasma, and the lower hybrid angular frequencies, respectively. Therefore, effects of the ion motion are not considered, and then the plasma current is given by

$$\boldsymbol{J} = -ne\boldsymbol{u}_{\mathrm{e}}, \tag{2.6}$$

and substitute 2.6 to 2.1 to yield [16]

$$\boldsymbol{E} = \frac{1}{ne}\boldsymbol{J} \times \boldsymbol{B}_0 - \eta\left(1 - i\frac{\omega}{\nu}\right)\boldsymbol{J}, \tag{2.7}$$

where $\eta = m_e\nu/ne^2$ is a plasma resistivity. Using 2.3 and 2.7, neglecting the displacement is neglected in 2.3 to eliminate $\boldsymbol{J}$ and $\boldsymbol{E}$, we can write 2.2 as [16]

$$i\frac{\omega{\omega_{pe}}^2}{c^2}\boldsymbol{B} = \frac{e}{m}\left[\nabla \times (\nabla \times \boldsymbol{B} \times \boldsymbol{B}_0)\right] + (\nu - i\omega)\left(\nabla \times \nabla \times \boldsymbol{B}\right). \tag{2.8}$$

Using the following vector identity,

$$\begin{aligned}\nabla \times (\nabla \times \boldsymbol{B} \times \boldsymbol{B}_0) =& B_0(\nabla \times \hat{\boldsymbol{z}})(\nabla \cdot \hat{\boldsymbol{z}}) - \hat{\boldsymbol{z}}(\nabla \cdot \nabla \times \boldsymbol{B}) + (\hat{\boldsymbol{z}} \cdot \nabla)(\nabla \times \boldsymbol{B}) \\ & - [(\nabla \times \boldsymbol{B}) \cdot \nabla]\hat{\boldsymbol{z}} \\ =& B_0(\hat{\boldsymbol{z}} \cdot \nabla)(\nabla \times \boldsymbol{B}) \\ =& ik_z B_0(\nabla \times \boldsymbol{B}) \end{aligned} \tag{2.9}$$

we can simplify the first term of the right side in 2.8, and the vector equation for $\boldsymbol{B}$ is written as [16]

$$(\omega + i\nu)(\nabla \times \nabla \times \boldsymbol{B}) - k_z\omega_{ce}(\nabla \times \boldsymbol{B}) + \frac{\omega{\omega_{pe}}^2}{c^2}\boldsymbol{B} = 0, \tag{2.10}$$

which can be factored as [16]

$$(k_1 - \nabla\times)(k_2 - \nabla\times)\boldsymbol{B} = 0, \tag{2.11}$$

where k_1 and k_2 are the roots of following equation,

$$(\omega + i\nu)k^2 - k_z\omega_{ce}k + \frac{\omega{\omega_{pe}}^2}{c^2} = 0. \tag{2.12}$$

The total wave number k is $({k_z}^2+{k_r}^2)^{1/2}$, where $k_z = k\cos\theta$ is the axial wave number, $k_r = k\sin\theta$ is the radial wave number, and θ is the angle of propagation relative to $B_0\hat{\boldsymbol{z}}$. Substituting $k_z = k\cos\theta$ for 2.12, we then obtain the dispersion relation of the helicon(whistler) wave as [92]

$$\frac{c^2k^2}{\omega^2} = \frac{{\omega_{pe}}^2}{\omega(\omega_{ce}\cos\theta - \omega\gamma)}, \tag{2.13}$$

where

$$\gamma = 1 + i\frac{\nu}{\omega}. \tag{2.14}$$

Assuming the dissipation term is negligible ($\nu/\omega = 0$), a plot of above dispersion relation with constant density and constant magnetic field is shown in upper side of Fig. 2.1. On a plane where the radial wave number is zero, the dispersion branch corresponds to the helicon wave which propagates parallel to the axial magnetic field. Since the angular frequency of the RF input is fixed in laboratory experiments, we consider a plane of the constant angular frequency, then the dispersion relation in a wave number space is shown in bottom side of Fig. 2.1. Furthermore, assuming a standing wave in axial direction, thus k_z is fixed, two roots of k_r are obtained. The smaller one corresponds to the helicon wave and the larger one corresponds to the electrostatic TG wave. The radial component of the group velocity of the TG wave has an opposite sign to its phase velocity.

2.1.2 Dispersion relation in a non-uniform plasma

Solving 2.13 with respect to the radial wave number k_r, the bi-quadratic equation can be obtained and its roots are following form [26],

$${k_{r\pm}}^2 = {k_z}^2 \frac{1}{2\gamma^2\alpha^2\beta^2}(1 - 2\gamma\alpha - 2\gamma^2\alpha^2\beta^2 \pm \sqrt{1 - 4\gamma\alpha}), \tag{2.15}$$

where,

$$\alpha = \frac{{\omega_{pe}}^2}{{\omega_{ce}}^2 N^2} \ , \ \beta = \frac{\omega\omega_{ce}N^2}{{\omega_{pe}}^2} \ , \text{ and } N = \frac{ck_z}{\omega}. \tag{2.16}$$

Two different roots correspond to the helicon wave (subscript +) and the TG wave (subscript −). Figure 2.2 [37] shows the roots in a non-uniform density plasma with omitting the dissipation term. Depending on the propagation/evanescence of the helicon and the TG waves, the plasma can be divided into three distinct regions: low density region ($r > r_{\text{low}}$, $n < n_{\text{low}}$), where only the TG wave can propagates,

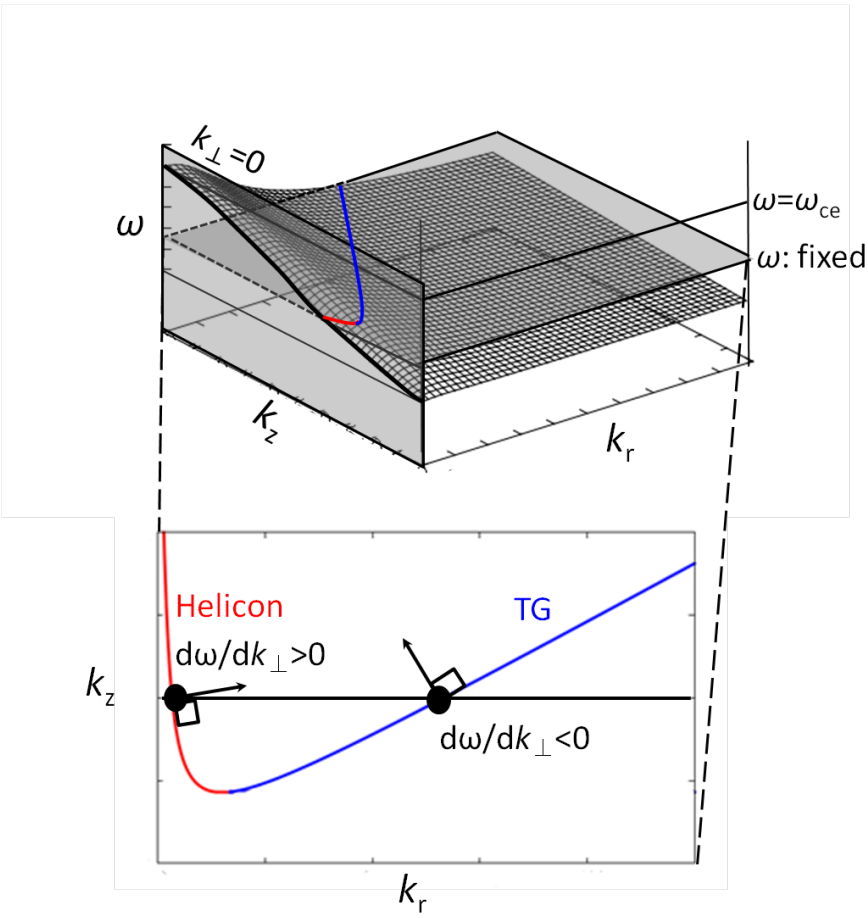

Figure 2.1: Dispersion relation in a uniform density plasma.

intermediate density region ($r_{\rm up} < r < r_{\rm low}$, $n_{\rm low} < n < n_{\rm up}$), where both the helicon and the TG wave can propagate, and high density region ($r < r_{\rm up}$, $n > n_{\rm up}$), where both waves are evanescent.

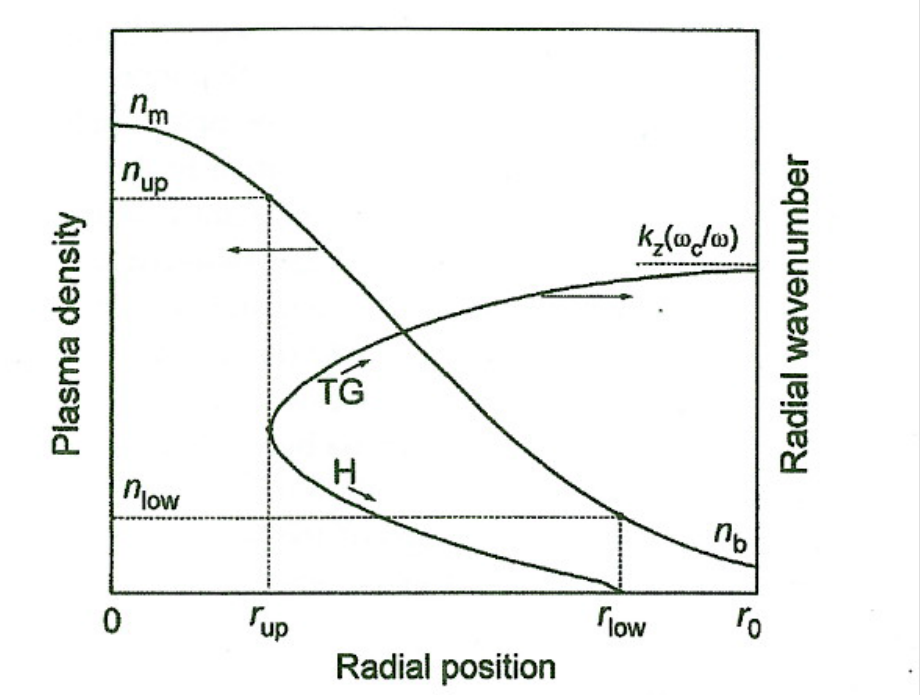

Figure 2.2: Dispersion relation in a non-uniform density plasma [37].

2.1.3 Penetration depth across the magnetic field

In the following analytical treatment, we will suppose $\alpha << 1$ (that is $n << n_{\mathrm{up}}$). Then one can obtain from 2.15 the complex transverse wavenumber of the TG wave [26],

$$k_+ = \frac{k_z}{\gamma\alpha\beta}. \tag{2.17}$$

Since the denominator of 2.17 includes a small parameter α, the TG wave turns out to be short wavelength and strongly damped. The propagating and dissipative parts of 2.17 are found to be independent of the plasma density as follows [26],

$$k_{\mathrm{TG,real}} = \frac{k_z}{|\gamma|^2\alpha\beta} = \frac{k_z\omega_{ce}}{|\gamma|^2\omega}, \tag{2.18}$$

$$k_{\mathrm{TG,imag}} = -\frac{\nu}{\omega}\frac{\omega_{ce}}{|\gamma|^2\omega}. \tag{2.19}$$

If $\alpha << 1$ ($n << n_{\rm up}$), the expression for the transverse wavenumber of helicon wave is obtained [26],

$$k_{\rm H,real} = \frac{k_z}{\beta} = \left[\frac{\{(1-\beta^2)^2 + 4(\nu/\omega_{ce})^2\beta^{-2}\}^{1/2} + (1-\beta^2)}{2}\right]^{1/2}, \tag{2.20}$$

$$k_{\rm H,imag} = \frac{k_z}{\beta} = \left[\frac{\{(1-\beta^2)^2 + 4(\nu/\omega_{ce})^2\beta^{-2}\}^{1/2} - (1-\beta^2)}{2}\right]^{1/2}, \tag{2.21}$$

Both of these quantities depend strongly on the plasma density. If $\beta < 1$, that is the plasma density is above the cut-off density, $n > n_{\rm low}$, from 2.20 and 2.21 one can obtain [26]:

$$k_{\rm H,real} = k_z\frac{1}{\beta}(1-\beta^2)^{1/2} = k_z\left[\left(\frac{n}{n_{\rm low}}\right)^2 - 1\right]^{1/2}, \tag{2.22}$$

$$k_{\rm H,imag} = k_z\frac{\nu}{\omega}\frac{\alpha}{\beta}(1-\beta^2)^{-1/2} = k_z\frac{\nu}{\omega_{ce}}\left(\frac{n}{n_{\rm low}}\right)^3\left[\left(\frac{n}{n_{\rm low}}\right)^2 - 1\right]^{1/2}. \tag{2.23}$$

At $\beta \approx 1$, 2.22 and 2.23 yield

$$k_{\rm H,real} = k_{\rm H,imag} = k_z\left(\frac{\nu}{\omega_{ce}}\right). \tag{2.24}$$

Finally, below the cut-off, i.e. $\beta > 1$, one obtains [26]

$$k_{\rm H,real} = k_z\frac{\nu}{\omega_{ce}}\left(\frac{n}{n_{\rm low}}\right)^3\left[1 - \left(\frac{n}{n_{\rm low}}\right)^2\right]^{-1/2}. \tag{2.25}$$

$$k_{\rm H,imag} = k_z\left[1 - \left(\frac{n}{n_{\rm low}}\right)^2\right]^{1/2}. \tag{2.26}$$

The helicon wave penetrates into a plasma across the magnetic field over a distance $\delta_{\rm H} = k_{\rm H,imag}^{-1}$. This distance is defined by the wave damping in a plasma with density above the cut-off (see 2.23 and 2.24). In the case of the density below the cut-off, the helicon wave turns into an electromagnetic surface wave, that penetrates within

the skin depth defined by 2.26. Figure 2.3 shows the variation of the penetration depth of the helicon and the TG waves penetration into the plasma with density for two different collision frequencies, using the typical experimental parameters. As shown in Fig. 2.3 (a), the penetration depth of the helicon wave is relatively short in the under-cut-off region ($n/n_{\mathrm{low}} < 1$), while it increases sharply near the cut-off density, and then decreases gradually with increasing the density. The penetration depth of the TG wave is always less than 1 cm which is shorter than plasma radius in typical laboratory experiments. The Fig. 2.3 (b) shows the penetration depth versus the density normalized to the upper limit density(n_{up}). One can see the penetration depth of the helicon wave can be quite short ($\delta < 1$ [cm]) near the upper limit density ($n \approx n_{\mathrm{up}}$) when the collision frequency is high ($\nu/\omega = 0.5$). If the density is maximized at the center which is common in laboratory experiments, the helicon and the TG waves are well separated far from the upper limit density, and the TG wave dissipates rapidly near the plasma surface via the collision, while the helicon wave can penetrate into the high density region. The helicon wave can dissipates within the enough short scale with propagating near the upper limit density. However, the exact amount of the damping energy of the helicon wave near the upper limit density should be evaluated carefully because the imaginary part of the wavenumber includes both effects of the energy damping and becoming evanescent above this density $n > n_{\mathrm{up}}$. This argument is discussed in section 2.3.

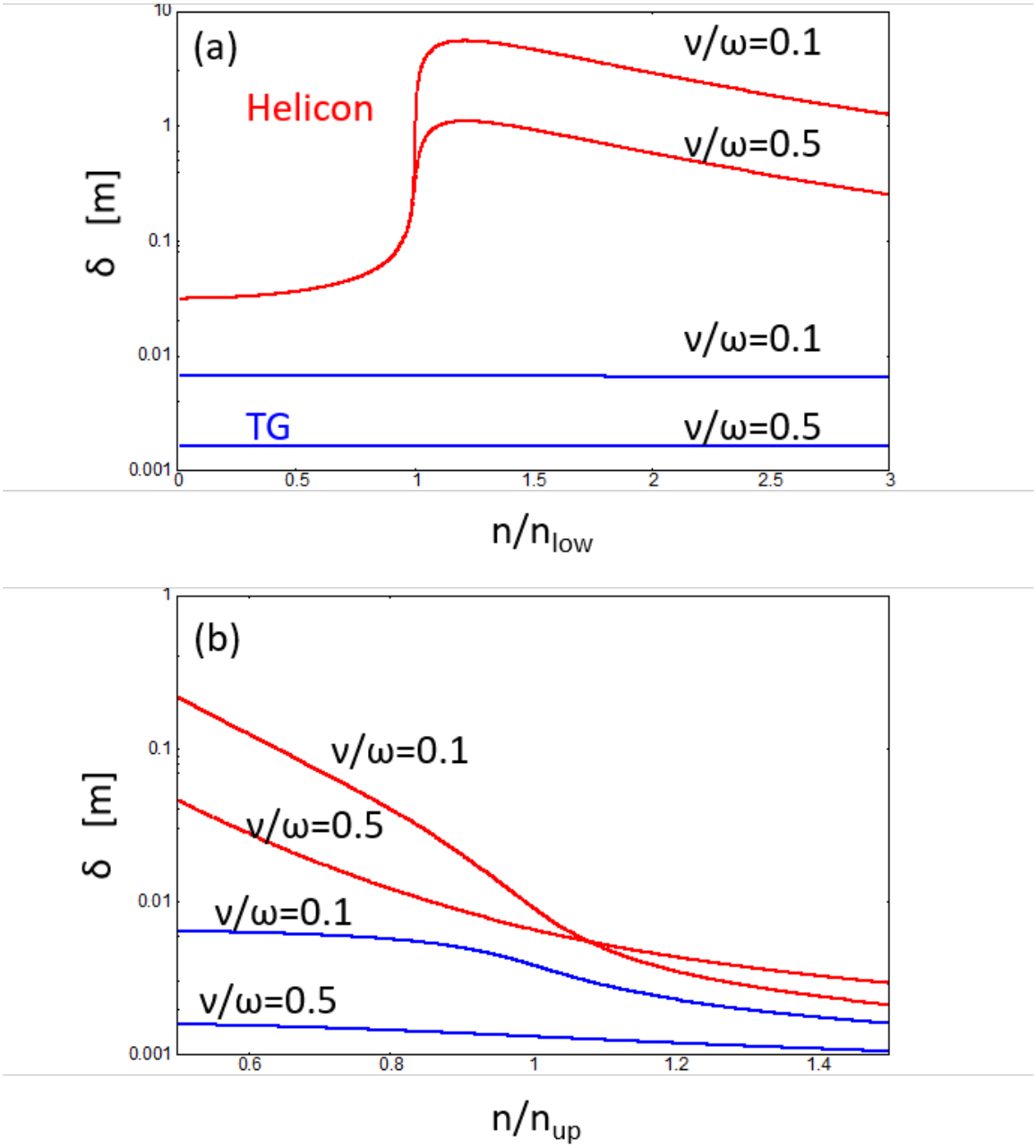

Figure 2.3: The skin depth of the helicon and the TG waves, as a function of normalized plasma density n/n_{low}(a) and n/n_{up}(b), for different values of collision frequency ν/ω, with specific parameters: $\omega/2\pi = 14$ [MHz], $B_0 = 0.024$ [T], $k_z = 0.2/\pi$ [1/m], $n_{\text{low}} \approx 1.3 \times 10^{18}$ [1/m^3], and $n_{\text{up}} \approx 1.6 \times 10^{19}$ [1/m^3]

.

2.2 Non-monotonicity of the power absorption curves

The bounded cavity modes of the helicon and the TG waves are calculated by imposing the boundary conditions of the conductive or insulating walls. The properties of these cavity modes strongly depends on the geometry of the cylinder and wave structures i.e. the dispersion relation. Since the collisional power absorption is dominated mainly by the TG wave, the total absorbed power depends on the amplitude of the cavity mode of the TG wave. When the collision is absent, there exists the TG resonance cavity mode where the amplitude of the TG wave peaks maximum. However, when the relatively weak collision is introduced, the resonance modes is destroyed due to the large imaginary part of the TG wavenumber, but the trace of these resonance modes still remains to some extent even when the collision parameter is increased. These traces of the resonance modes leads to the non-monotonicity functions of the power absorption curves. When the RF frequency and the back ground magnetic field are fixed, the argument of the non-monotonicity function is the plasma density, and this non-monotonicity is strongly related to the theory of the density jump as mentioned in the introduction. In this section, we shall describe the outline of the cavity modes [16, 28, 38], and show some results of the wave excitation tests and power absorption tests by the FDTD simulation and the HELIC code [38].

2.2.1 Wave fields in a uniform-density plasma and in a vacuum

We consider the wave fields in a uniform-density plasma. From 2.11, the most general solution $\boldsymbol{B}$ is the sum of $\boldsymbol{B}_1$ and $\boldsymbol{B}_2$, which satisfy [16]

$$\nabla \times \boldsymbol{B}_1 = k_1 \boldsymbol{B}_1, \;\; \nabla \times \boldsymbol{B}_2 = k_2 \boldsymbol{B}_2. \tag{2.27}$$

Taking the curl of these equations and using 2.4, we obtain a vector Helmholtz equation for each:

$$\nabla^2 \boldsymbol{B}_1 + k_1^2 \boldsymbol{B}_1 = 0, \;\; \nabla^2 \boldsymbol{B}_2 + k_2^2 \boldsymbol{B}_2 = 0. \tag{2.28}$$

Denoting $\partial/\partial r$ by ('), the z component of 2.27 in cylindrical coordinates can be written as follows [16]:

$$B_z'' + \frac{1}{r} B_z' + \left(T^2 - \frac{m^2}{r^2} \right) B_z = 0, \tag{2.29}$$

where the transverse wavenumber T is defined as

$$T_j^2 = k_j^2 - k_z^2, \;\; j = 1 \text{ for the helicon and } j = 2 \text{ for the TG.} \tag{2.30}$$

This is Bessel's equation, and the solution which is finite at $r = 0$ is $J_m(Tr)$:

$$B_z = C J_m(Tr), \tag{2.31}$$

where C is the constant coefficient. The r and θ components of 2.27 are

$$\frac{im}{r} B_z - i k_z B_\theta = k B_r, \tag{2.32}$$

$$i k_z B_r - B_z' = k B_\theta, \tag{2.33}$$

Solving for B_r and B_θ in terms of B_z and B_z', and substituting for B_z from 2.31, we obtain [16]

$$B_r = \frac{iC}{T^2} \left(\frac{m}{r} k J_m - k_z J_m' \right), \tag{2.34}$$

$$B_\theta = \frac{C}{T^2} \left(\frac{m}{r} k_z J_m + k J_m' \right), \tag{2.35}$$

Use of the recursion relations

$$\frac{m}{r}J_m = \frac{T}{2}(J_{m-1} + J_{m+1}), \quad J'_m = \frac{T}{2}(J_{m-1} - J_{m+1}), \tag{2.36}$$

yields

$$B_r = \frac{iC}{2T}\left[(k + k_z)J_{m-1} + (k - k_z)J_{m+1}\right], \tag{2.37}$$

$$B_\theta = -\frac{C}{2T}\left[(k + k_z)J_{m-1} - (k - k_z)J_{m+1}\right], \tag{2.38}$$

Introducing the amplitude

$$A = \frac{iC}{2T}, \tag{2.39}$$

then 2.31, 2.37, and 2.38 are written for the helicon wave (j=1), and the TG wave (j=2) as follows [16]:

$$B_z = -2iA_jT_j\left[(k_j + k_z)J_{m-1}(T_jr) + (k_j - k_z)J_{m+1}(T_jr)\right], \tag{2.40}$$

$$B_r = A_j\left[(k_j + k_z)J_{m-1}(T_jr) + (k_j - k_z)J_{m+1}(T_jr)\right], \tag{2.41}$$

$$B_\theta = -iA_j\left[(k_j + k_z)J_{m-1}(T_jr) - (k_j - k_z)J_{m+1}(T_jr)\right]. \tag{2.42}$$

If we neglect the displacement current in 2.3, that is always almost negligible in usual experiment, and 2.1 can be written as

$$\boldsymbol{E} = -\frac{B_0}{en}(i\delta\boldsymbol{j} + \widehat{\boldsymbol{z}} \times \boldsymbol{j}), \tag{2.43}$$

where $\delta = (\omega + i\nu)/\omega_{ce}$, from 2.27 and 2.3, we see that $\boldsymbol{J}$ is parallel to $\boldsymbol{B}$:

$$\boldsymbol{J} = -\frac{k}{\mu_0}\boldsymbol{B}. \tag{2.44}$$

Using 2.43, 2.44 and 2.40, we find that E_z can be written as

$$E_z = -2\frac{c^2\omega_{ce}}{\omega_{pe}^2}\delta A_j k_j T_j J_m(T_j r). \tag{2.45}$$

The other components of $\boldsymbol{E}$ can be found from 2.2:

$$E_r = \frac{\omega}{k_z}B_\theta - \frac{i}{k_z}E_z', \tag{2.46}$$

$$E_\theta = \frac{m}{k_z r}E_z - \frac{\omega}{k_z}B_r, \tag{2.47}$$

using 2.41-2.43, and 2.35 these can be written as [16]

$$\begin{aligned} E_r = &\frac{iA_j}{k_z}\left[\left(\omega(k_j + k_z) + \frac{c^2\omega_{ce}}{\omega_{pe}^2}\delta k_j T_j^2\right) J_{m-1}(T_j r)\right] \\ &- \frac{iA_j}{k_z}\left[\left(\omega(k_j - k_z) + \frac{c^2\omega_{ce}}{\omega_{pe}^2}\delta k_j T_j^2\right) J_{m+1}(T_j r)\right], \end{aligned} \tag{2.48}$$

$$E_\theta = -2\frac{c^2\omega_{ce}}{\omega_{pe}^2}\delta A_j k_j T_j J_m(T_j r) - \frac{\omega}{k_z}A_j\left[(k_j + k_z)J_{m-1}(T_j r) + (k_j - k_z)J_{m+1}(T_j r)\right], \tag{2.49}$$

In experiment, plasma is usually confined by an insulating tube. For simplicity, the dielectric constant of the insulator is taken to be unity (the small phase shift introduced by a real grass or quartz tube does not change the results), thus there exists vacuum region between the plasma and the wall. For the vacuum region (subscript 3), setting $\boldsymbol{J} = 0$ in 2.3 changes 2.28 to

$$\nabla^2 \boldsymbol{B}_3 + k_0^2 \boldsymbol{B}_3 = 0, \tag{2.50}$$

and 2.29 to

$$T^2 = k_0^2 - k_z^2 = -T_3^2, \tag{2.51}$$

where T_3 is positive. The waves in the vacuum region are highly evanescent (T^2 is negative), since k_z of the helicon wave is larger than $k_0 = \omega/c$ two orders of magnitude. Therefore, the waves in the vacuum region are written by using the modified Bessel functions as shown in Fig. 2.4.

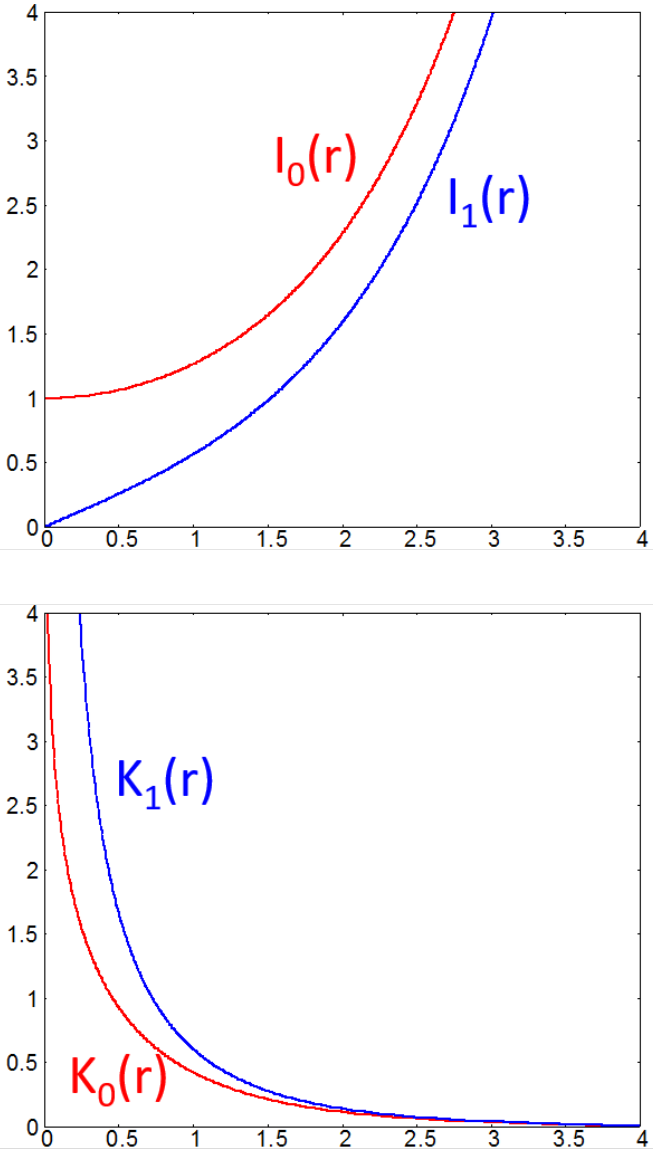

Figure 2.4: Modified Bessel function of 1st kind (top panel) and 2nd kind (bottom panel).

Basically, the $\boldsymbol{B}$ fields of the vacuum region can be written by replacing the functions $J_m(Tr)$ in 2.40-2.42 by $I_m(T_3r)$ and $K_m(T_3r)$ as follows:

$$B^R = \sqrt{2}[C_1 K_{m-1}(T_3 r) + D_1 I_{m-1}(T_3 r)], \tag{2.52}$$

$$B^L = \sqrt{2}[C_2 K_{m-1}(T_3 r) + D_2 I_{m-1}(T_3 r)]. \tag{2.53}$$

The four degree of freedom ($C_{1,2}$ and $D_{1,2}$) corresponds to combination of four waves, two evanescent modes represented by, $K_m(Tr)$, $I_m(Tr)$, and two propagating waves (transverse-electric (TE) mode and transverse-magnetic (TM) mode) in the vacuum region. The $\boldsymbol{B}$ fields can be written as

$$B_r = C_1 K_{m-1}(T_3 r) + C_2 K_{m+1}(T_3 r) + D_1 I_{m-1}(T_3 r) + D_2 I_{m+1}(T_3 r), \tag{2.54}$$

$$B_\theta = i(C_1 K_{m-1}(T_3 r) - C_2 K_{m+1}(T_3 r) + D_1 I_{m-1}(T_3 r) - D_2 I_{m+1}(T_3 r)), \tag{2.55}$$

$$B_z = -i\frac{T_3}{k_z}[(C_1 + C_2) K_m(T_3 r) + (D_1 + D_2) I_m(T_3 r)], \tag{2.56}$$

The $\boldsymbol{E}$ fields can be found from 2.3:

$$-\frac{i\omega}{c^2} E_r = \frac{im}{r} B_z - i k_z B_\theta, \tag{2.57}$$

$$-\frac{i\omega}{c^2} E_\theta = \frac{ik_z}{B}_r - B_z', \tag{2.58}$$

$$-\frac{i\omega}{c^2} E_z = \frac{1}{r} B_\theta + B_\theta' - \frac{im}{r} B_r, \tag{2.59}$$

and using 2.54-2.56 as follows:

$$\begin{aligned} E_r = &-\left(\frac{mc^2}{r\omega} - i\frac{c^2 k_z}{\omega}\right)[C_1 K_{m-1}(T_3 r) + D_1 I_{m-1}(T_3 r)] \\ &-\left(\frac{mc^2}{r\omega} + i\frac{c^2 k_z}{\omega}\right)[C_2 K_{m+1}(T_3 r) + D_2 I_{m+1}(T_3 r)], \end{aligned} \tag{2.60}$$

$$
\begin{aligned}
E_\theta = &-\left(\frac{c^2 k_z}{\omega} - \frac{c^2 T_3^2}{2k_z\omega}\right)[C_1 K_{m-1}(T_3 r) + C_2 K_{m+1}(T_3 r)] \\
&-\left(\frac{c^2 k_z}{\omega} + \frac{c^2 T_3^2}{2k_z\omega}\right)[D_1 I_{m-1}(T_3 r) + D_2 I_{m+1}(T_3 r)],
\end{aligned}
\tag{2.61}
$$

$$
\begin{aligned}
E_z = &\frac{c^2}{\omega}[T_3(C_1 - C_2)K_m(T_3 r) + T_3(D_1 - D_2)I_m(T_3 r)] \\
&-\frac{c^2}{r\omega}(1-m)[C_1 K_{m-1}(T_3 r) + C_2 K_{m+1}(T_3 r) + D_1 I_{m-1}(T_3 r) + D_2 I_{m+1}(T_3 r)],
\end{aligned}
\tag{2.62}
$$

where the following recursion relations are used,

$$
K'_m = -\frac{T}{2}(K_{m-1} + K_{m+1}), \quad I'_m = \frac{T}{2}(I_{m-1} + I_{m+1}). \tag{2.63}
$$

2.2.2 Resonance cavity mode

We consider a cylindrical model that consists of the plasma region ($0 < r < a$), the vacuum region I($a < r < b$), the current sheet ($r = b$), and the vacuum region II ($b < r < c$), surrounded by the conducting wall ($r = c$) where the transverse electric fields (E_θ and E_z) are zero as shown Fig. 2.5 [38]. The cavity modes that

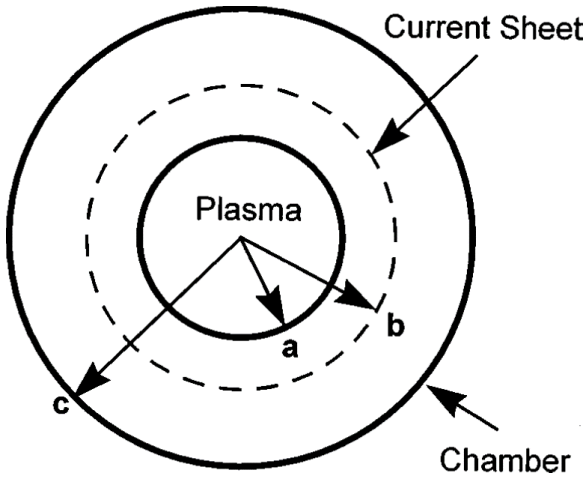

Figure 2.5: The modeled configuration [38].

satisfies the boundary conditions at each boundary can be found from connecting the wave fields in the plasma and the vacuum regions at each boundaries. There are two vacuum regions with two basis functions ($K_m(T_3 r)$ and $I_m(T_3 r)$) and two waves (TE and TM mode) in each region, and inner plasma region with two waves (helicon and TG mode). Therefore there are total ten unknown coefficients to be determined. The boundary conditions are as follows: the tangential electric fields are continuous at the two boundaries ($r = a$ and $r = b$) and the tangential fields are vanished at the conducting wall ($r = c$), the tangential magnetic fields are continuous at the plasma surface ($r = a$) but undergoes a jump across the current sheet ($r = b$). There are therefore ten boundary conditions to determine the ten unknown constants. Chen

and Arnush found the results in conveniently expressed form as follows [38]:

$$V_i = \frac{H_2 v_{1,i}(r) - H_1 v_{2,i}(r)}{D(a, c, k_z)} K_\phi, \tag{2.64}$$

where

$$D(a, c, k_z) = F_1 G_2 - F_2 F_1, \tag{2.65}$$

$$F_n = -i b_{n,r}(a) + \frac{k_z}{T_3} p_m(a) b_{n,z}(a) - i \frac{m}{a T_3^2} \mu_0 [\omega \epsilon_0 e_{n,z}(a)], \tag{2.66}$$

$$G_n = j_{n,r}(a) + i \frac{m}{a} \frac{k_0^2}{T_3^2} \frac{1}{\mu_0} b_{n,z}(a) + \frac{k_z}{T_3} q_m [\omega \epsilon_0 e_{n,z}(a)], \tag{2.67}$$

$$H_n = \frac{k_z b}{T_3 a} p_m(b) \mu_0 G_n - i \frac{m}{a} \frac{k_0^2}{T_3^2} \rho_m F_n, \tag{2.68}$$

and

$$\rho_m(r) = \frac{K_m'(T_3 r) I_m'(T_3 c) - K_m'(T_3 c) I_m'(T_3 r)}{K_m(T_3 a) I_m'(T_3 c) - K_m'(T_3 c) I_m(T_3 a)}, \tag{2.69}$$

$$q_m = \frac{K_m'(T_3 a) I_m(T_3 c) - K_m(T_3 c) I_m'(T_3 a)}{K_m(T_3 a) I_m(T_3 c) - K_m(T_3 c) I_m(T_3 a)}, \tag{2.70}$$

$$\rho_m = \frac{K_m(T_3 b) I_m(T_3 c) - K_m(T_3 c) I_m(T_3 b)}{K_m(T_3 a) I_m(T_3 c) - K_m(T_3 c) I_m(T_3 a)}, \tag{2.71}$$

Here the subscript n is 1 for the helicon wave and 2 for the TG wave, V_i is any wave component $\boldsymbol{E}$, $\boldsymbol{B}$, and $\boldsymbol{J}$, $v_{n,i}(r)$ is the basis function of each wave component written by using Bessel function, m is the azimuthal mode number, $b_{n,i}$, $e_{n,i}$, $j_{n,i}$ are the basis functions for the magnetic and electric fields and the current, K_ϕ is the Fourier transformed form of the antenna current, and the prime (') stands for differentiation with respect to the argument of the Bessel function. For $m = 0$ azimuthal mode, 2.66-2.71 are simplified as follows [38]:

$$F_n = -i b_{n,r}(a) + \frac{k_z}{T_3} p_0(a) b_{n,z}(a), \tag{2.72}$$

$$G_n = j_{n,r}(a) + \frac{k_z}{T_3} q_0[\omega\epsilon_0 e_{n,z}(a)], \tag{2.73}$$

$$H_n = \frac{k_z b}{T_3 a} p_0(b)\mu_0 G_n, \tag{2.74}$$

and

$$\rho_0(r) = \frac{K_0'(T_3 r)I_0'(T_3 c) - K_0'(T_3 c)I_0'(T_3 r)}{K_0(T_3 a)I_0'(T_3 c) - K_0'(T_3 c)I_0(T_3 a)}, \tag{2.75}$$

$$q_0 = \frac{K_0'(T_3 a)I_0(T_3 c) - K_0(T_3 c)I_0'(T_3 a)}{K_0(T_3 a)I_0(T_3 c) - K_0(T_3 c)I_0(T_3 a)}, \tag{2.76}$$

$$\rho_0 = \frac{K_0(T_3 b)I_0(T_3 c) - K_0(T_3 c)I_0(T_3 b)}{K_0(T_3 a)I_0(T_3 c) - K_0(T_3 c)I_0(T_3 a)}, \tag{2.77}$$

and in a uniform-density plasma, the basis functions $b_{n,z}$, $b_{n,r}$, $e_{n,z}$, $j_{n,r}$ can be found from 2.40, 2.41, 2.44, and 2.45 as follows:

$$b_{n,z}(r) = -2iT_n J_0(T_n r), \tag{2.78}$$

$$b_{n,r}(r) = -2k_z J_1(T_n r), \tag{2.79}$$

$$e_{n,z}(r) = -2\frac{c^2\omega_{ce}}{\omega_{pe}^2}\delta k_n T_n J_0(T_n r). \tag{2.80}$$

$$j_{n,r}(r) = -2\frac{k_n k_z}{\mu_0} J_1(T_n r). \tag{2.81}$$

We see from 2.64 that the solution is composed of three parts. First, the fields are proportional to the amplitude of the antenna current ($K_\phi = I_0$ [A] for the $m = 0$ antenna). Second, they are inversely proportional to the dispersion function. When the collision is absent, the equation $D = 0$ gives the resonance cavity mode of the helicon or the TG mode. Third, numerator of 2.64 gives the radial variation of the fields and consists of the basis functions multiplied by the amplitudes H_i, which depend only on the plasma surface and on the geometric functions p, q, and ρ. In most cases in experiment, the displacement current in square brackets in 2.73 can be neglected, therefore we get the more simplified form of 2.64 and 2.65 as [38]

$$V_i(r) = \frac{j_{2,r}(a)v_{1,i}(r) - j_{1,r}(a)v_{2,i}(r)}{D} \frac{bk_z}{a|k_z|p_0(b)\mu_0 K_\phi}, \tag{2.82}$$

$$D = -i[b_{1,r}(a)j_{2,r}(a) - b_{2,r}(a)j_{1,r}(a)] + \frac{k_z}{T_3} p_0(a)[b_{1,z}(a)j_{2,r}(a) - b_{2,z}(a)j_{1,r}(a)]. \tag{2.83}$$

From 2.82 and 2.83, one can see the resonance cavity mode is possible when $j_{2,r}(a)/D$ is maximum for the helicon wave, and when $j_{1,r}(a)/D$ is maximum for the TG wave. Furthermore, the antiresonance (i.e., the production of a pure helicon or pure TG waves) would appear when $j_{2,r}(a) = 0$ for the helicon wave, and when $j_{2,r}(a) = 0$ for the TG wave. This antiresonance condition is same with the result of Shamrai *et al* [36, 92]. They found antiresonance condition as $b_{n,r} = 0$, that corresponds to $j_{n,r} = 0$, since 2.44 is satisfied. Figure 2.6 shows (a) imag(D) and (b) $j_{1,r}(a)/D$ as the function of the plasma density, these are evaluated by using following parameters: $\nu/\omega = 0$, $B_0 = 0.024$ [T], $\omega_{rf}/2\pi = 14$ [MHz], $k_z = 5$ [1/m], $a = 0.0225$ [m], $b = 0.027$ [m], $c = 0.0315$ [m], these are correspond to the experiment of Nisoa *et al* [1], and the antenna current $K_\phi = I_0$ is fixed as 1 [A]. When collision is absent, one can see from Fig. 2.6 that the amplitude of the TG wave $j_{1,r}(a)/D$ peaks sharply at the point where the denominator imag(D) crosses imag(D) = 0, that is the resonance cavity mode of the TG wave.

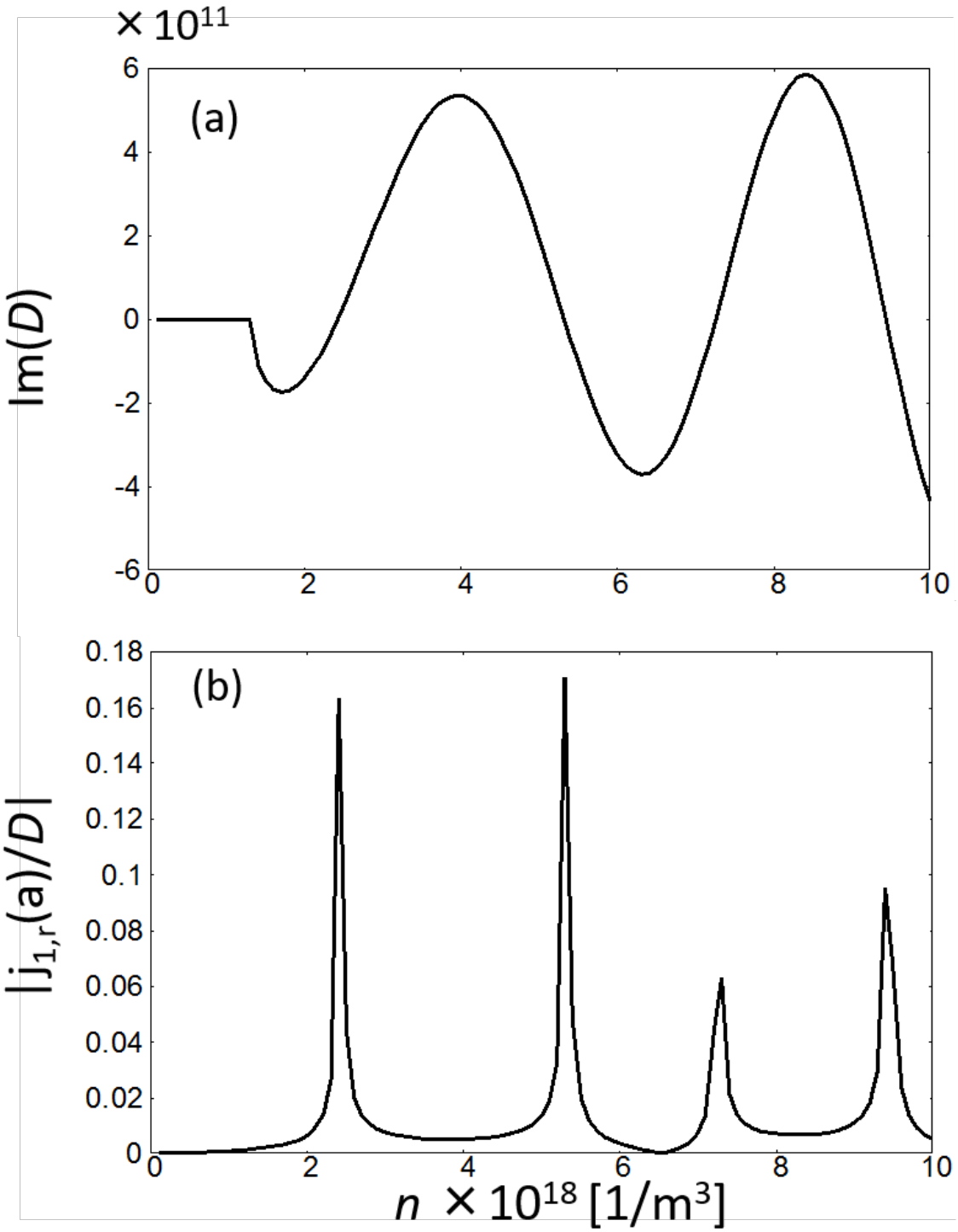

Figure 2.6: The evaluated values of (a) imag(D) and (b) $|j_{1,r}/D|$.

We also conducted the test simulation of the TG resonant excitation by the FDTD simulation in one-dimension with fixed k_z. The same physical parameters with above ones are used except the antenna current, $J = 1.6$ [A/m^2] is used, the plasma density is varied as $1.0 \times 10^{18} \sim 1.0 \times 10^{19}$ [1/m^3] by 0.25×10^{18} [1/m^3] steps, and the computational parameters are as follows, Grid size: $\Delta r = 3.6 \times 10^{-5}$ [m], Time step size: $\Delta t = 9.5 \times 10^{-6} \omega_{RF}$, and Total time: $171 \times \omega_{RF}$. The red line in Fig. 2.7 shows the evaluated poynting flux of the TG wave (when $t = 171 \times \omega_{RF}$), which is defined by $\Gamma_{r,TG} = \mathrm{Re}[\boldsymbol{E}_{TG} \times \boldsymbol{B}_{TG}]$, where the E_{TG} and B_{TG} are the electric field and the (complex conjugate) magnetic field of the TG wave. The black line in Fig. 2.7 shows the analytical solution obtained from $j_{1,r}(a)/D$. Since the antenna current is fixed as $I_0 = 1$ [A] in the analytical solution, that is compared to the simulation result by fitting the first peak amplitude to the simulation. One can see from Fig. 2.7, good agreement of the simulation result with the analytical one. The slight disagreement in the peak amplitudes, the width of the peaks, and the location of the peaks may due to the numerical discretization in the FDTD simulation.

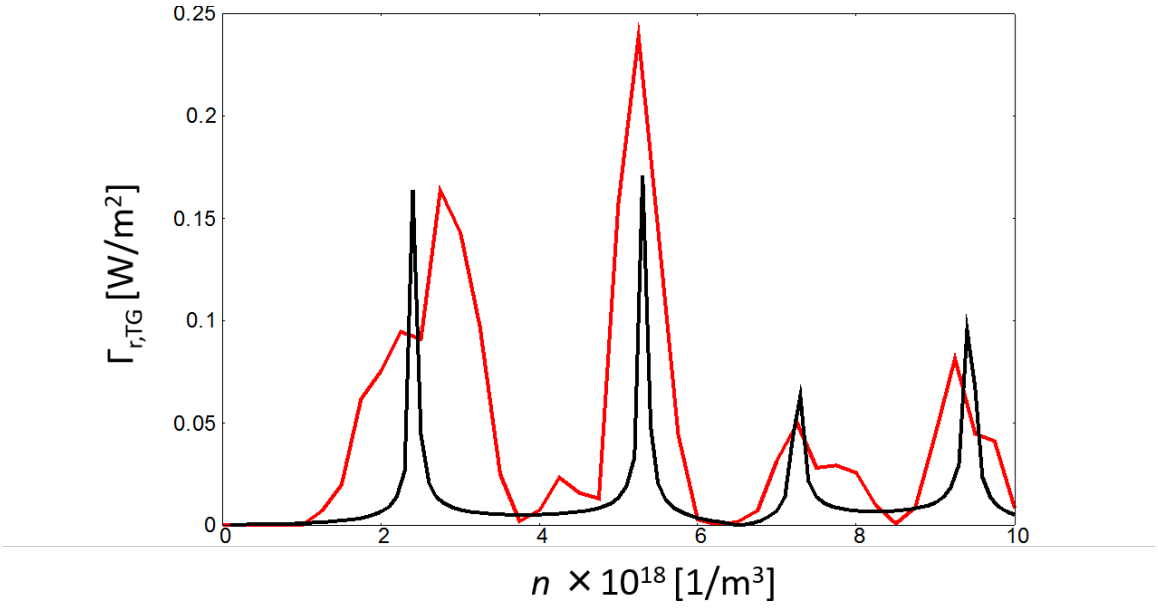

Figure 2.7: The results of the resonant TG wave excitation by FDTD (red line) and analytical solution (black line).

2.2.3 Power absorption curves with a finite collision

When a relatively small collision is introduced, the resonance condition that imag(D) crosses zero collapses due to the large imaginary part of the TG wave (imag(T_2)). Figure 2.8 shows the imag(D) (black line) and real(D) (red line) with $\nu/\omega = 0$ (top panel) and $\nu/\omega = 0.005$ (bottom panel). When the collision is absent, real(D) is basically zero except under the cut-off density ($n = n_{\mathrm{low}}$) where the imaginary part of the helicon wave (imag(T_1)) appears. When a finite collision is introduced ($\nu/\omega = 0.005$), the comparable order of real(D) appears, and $|j_{1,r}/D|$ no longer represents the sharp peak as shown in Fig. 2.9. One can see from Fig. 2.9, the sharpness of the resonance become blunt as increasing the collision frequency. When the collision frequency further increases at $\nu/\omega = 0.05$, there exists only three peaks within the range of $n = 1.0 \times 10^{18} \sim 1.5 \times 10^{19}$ [1/m^3] as shown in Fig. 2.10, and when $\nu/\omega = 0.1$, the third resonance disappears and there exists only two peaks within the same range as shown in Fig. 2.11.

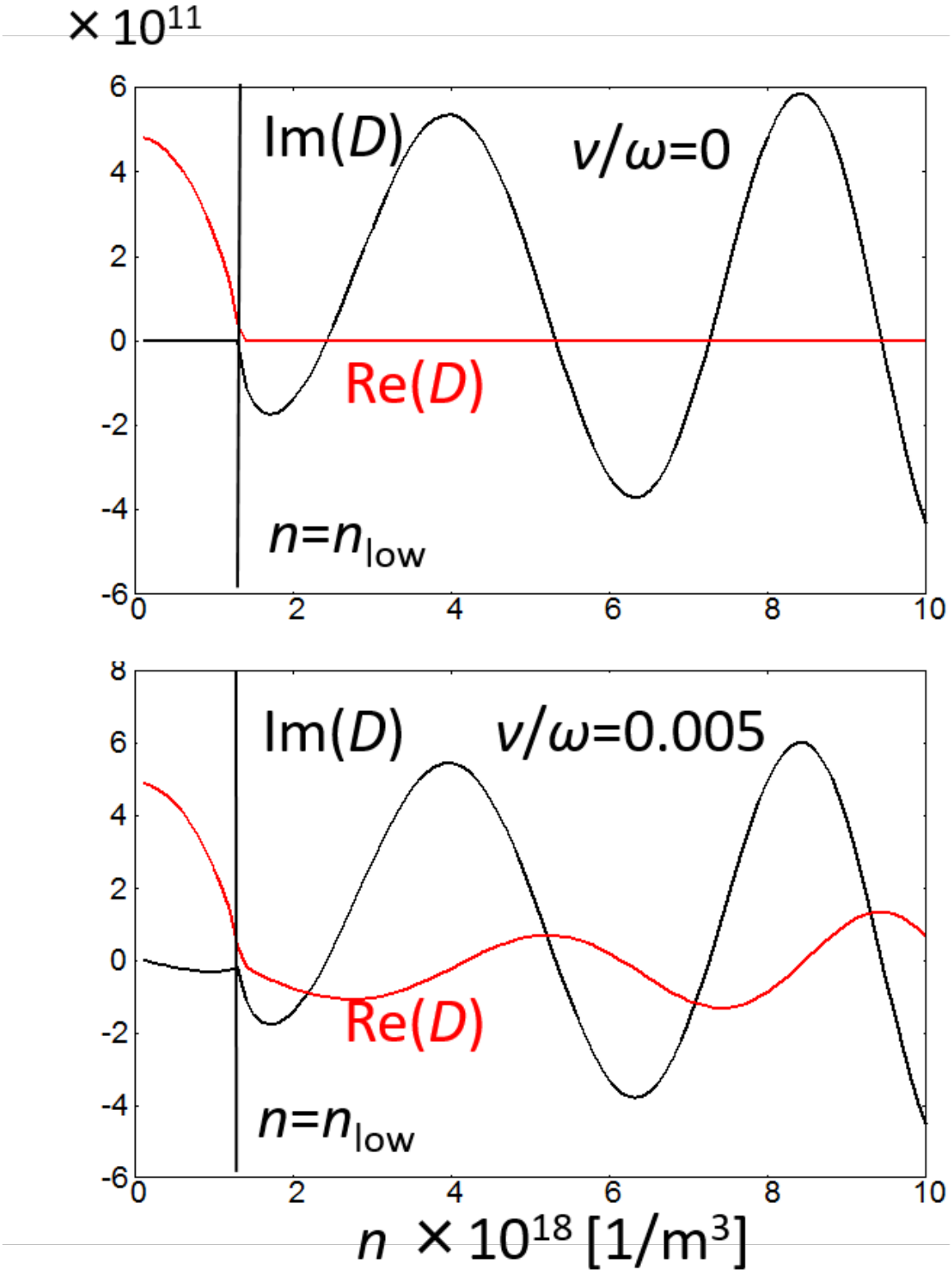

Figure 2.8: The imaginary (red line) and real (black line) parts of D at $\nu/\omega = 0$ (top panel) and $\nu/\omega = 0.005$ (bottom panel).

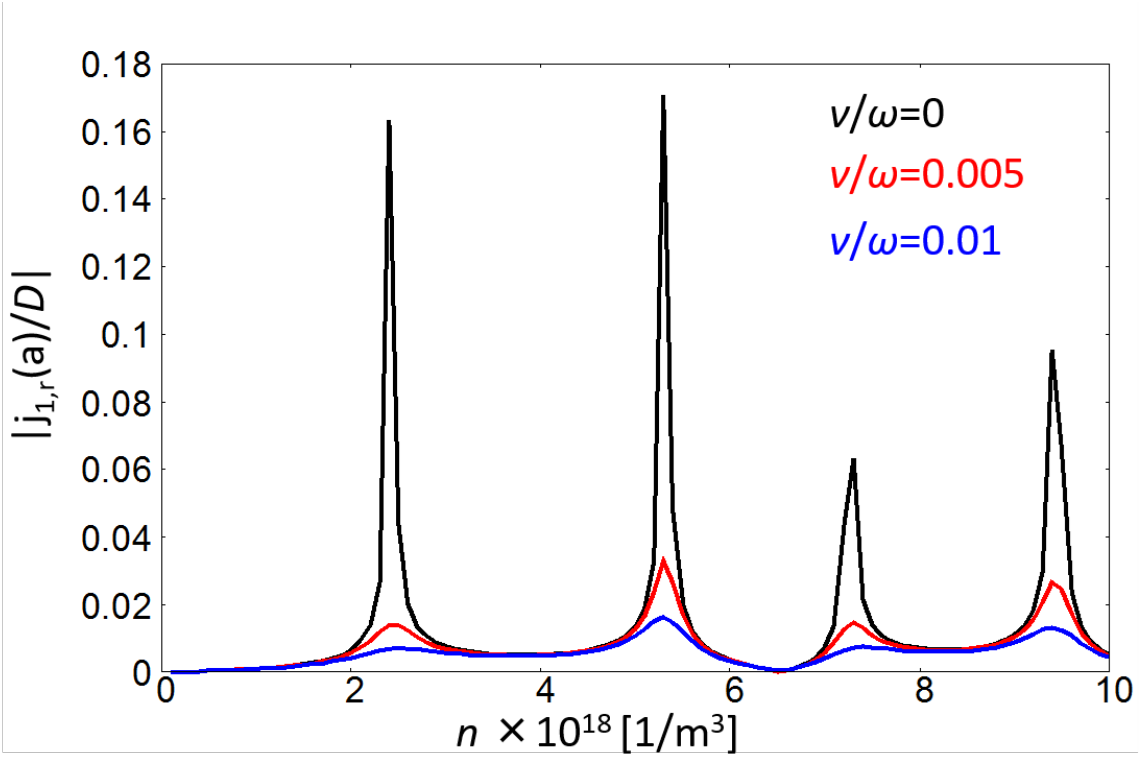

Figure 2.9: The resonant amplitude of the TG wave $|j_{1,r}/D|$ at $\nu/\omega = 0$ (black line), $\nu/\omega = 0.005$ (black line) and $\nu/\omega = 0.01$ (black line).

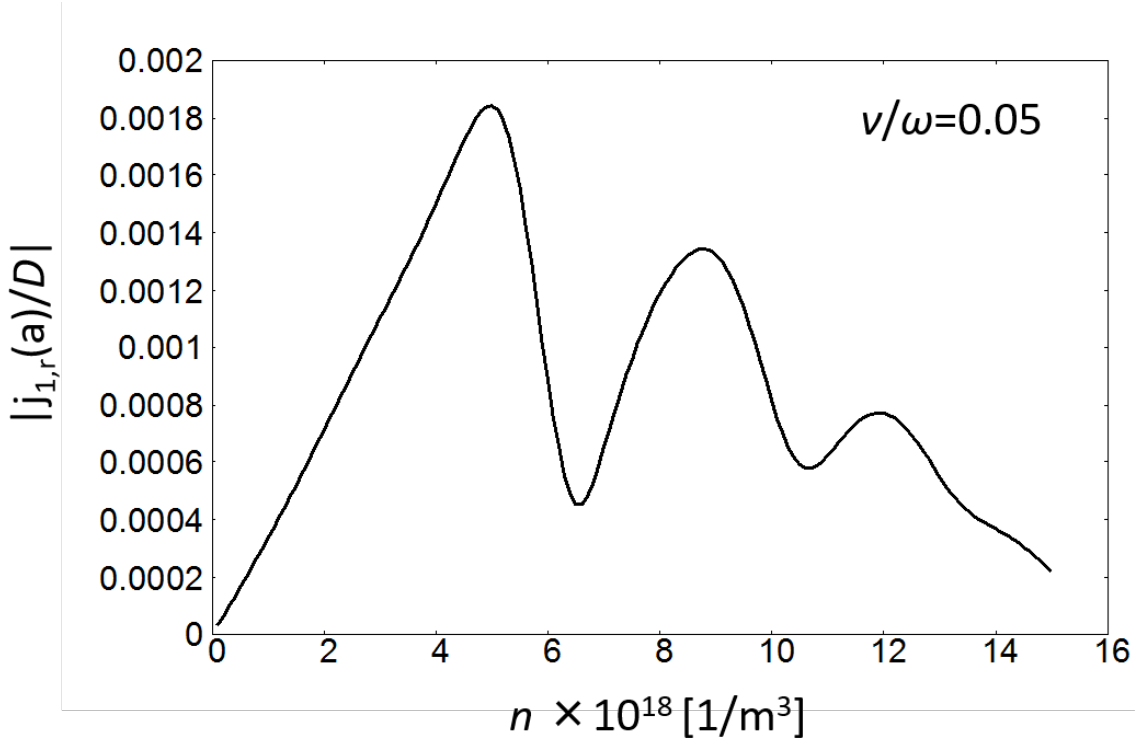

Figure 2.10: The resonant amplitude of the TG wave $|j_{1,r}/D|$ at $\nu/\omega = 0.05$.

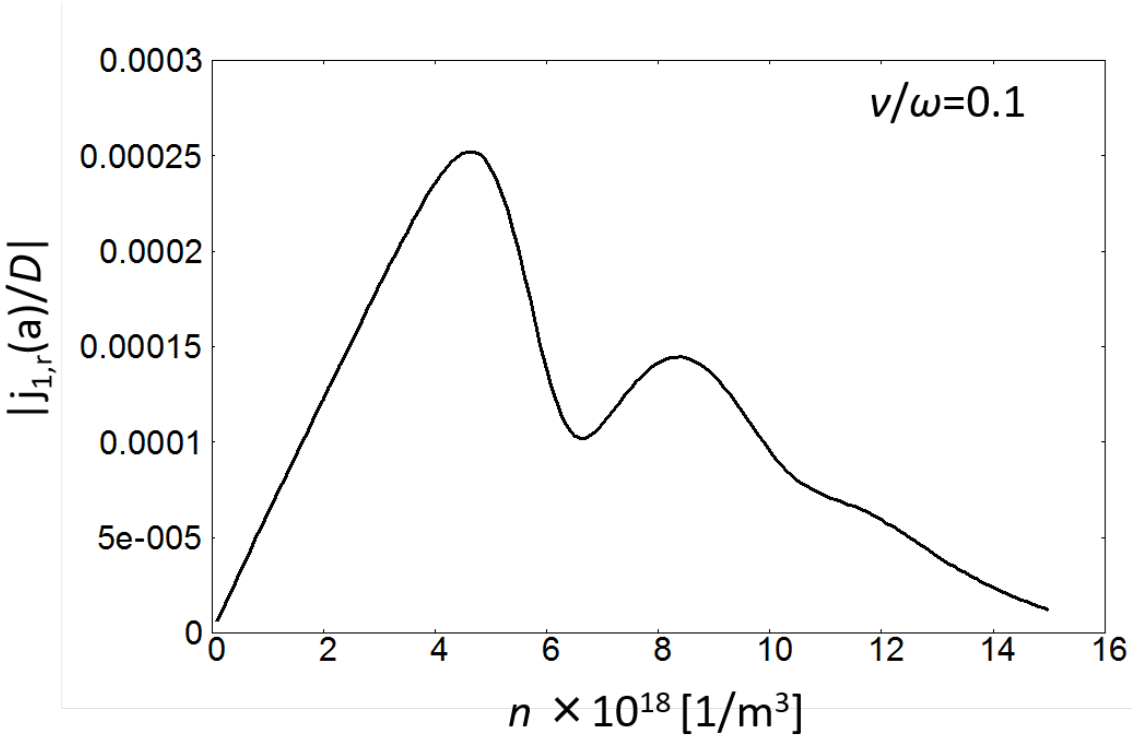

Figure 2.11: The resonant amplitude of the TG wave $|j_{1,r}/D|$ at $\nu/\omega = 0.1$.

Since the collisional power absorption is dominated by the TG wave, the TG resonance curve directly affect the amount of the power absorption. We conducted the power absorption test in a uniform-density plasma by using the HELIC code, which is written by Arnush *et al* [38] and is widely used for the power absorption analysis, and these results are compared with our FDTD results. Figures 2.12 and 2.13 shows the power absorption results of the HELIC code (black line) and the FDTD simulation (red line) at $\nu/\omega = 0.05$ and $\nu/\omega = 0.1$, using the same parameters with ones used in Fig. 2.7. The plasma density is varied as $1.0 \times 10^{18} \sim 1.0 \times 10^{19}$ [1/m^3] by 0.5×10^{18} [1/m^3] steps and $1.0 \times 10^{19} \sim 1.5 \times 10^{19}$ [1/m^3] by 1.0×10^{18} [1/m^3] steps. From Figs. 2.12 and 2.13, the three (when $\nu/\omega = 0.05$) and the two (when $\nu/\omega = 0.1$) power absorption peaks can be shown that corresponds to the resonant TG wave excitation in Figs. 2.10 and 2.11, and shows the good agreement

between the HELIC code and the FDTD simulation results. The power absorption is calculated as the plasma resistance R [Ω] with the fixed antenna current $I_0 = 1$ [A] in the HELIC code, while the total absorbed power $P_{\rm abs}$ [W/m^3] (integrated over the spatial grids) is calculated in the FDTD simulation with the current density $J = 10^6$ [A/m^2], therefore these results are compared by multiplying the plasma resistance by a factor of $\sim 10^9$ and fitting the first peak amplitude of the HELIC code with the FDTD's one.

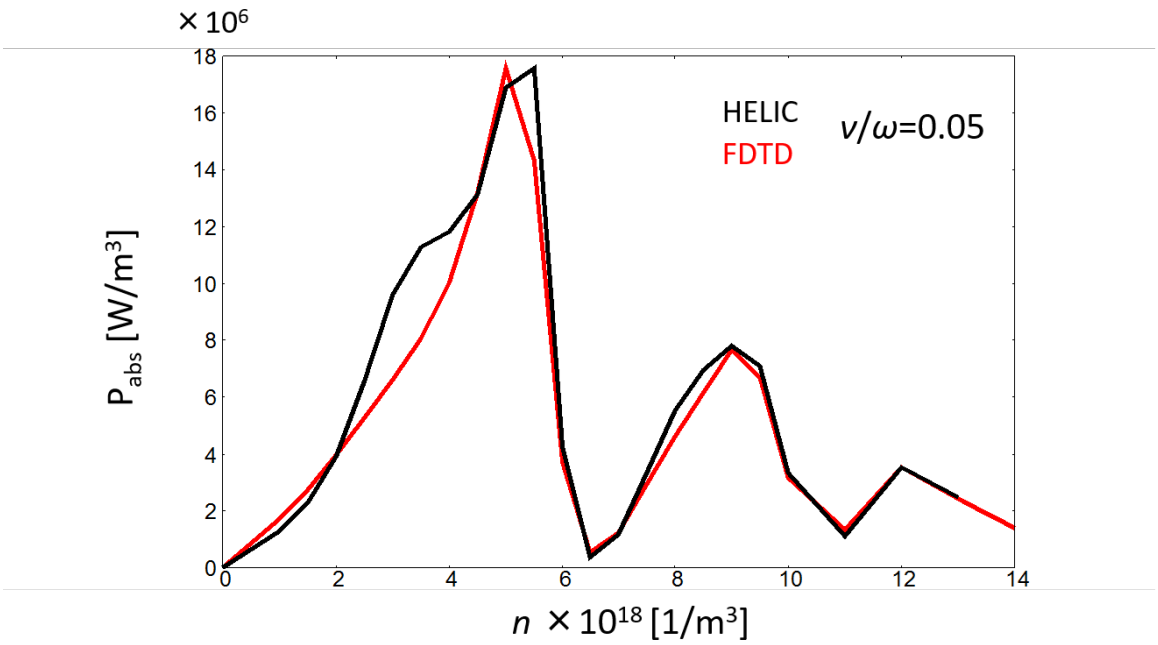

Figure 2.12: The power absorption curves calculated by the HELIC code (black line) and the FDTD simulation (red line) at $\nu/\omega = 0.05$.

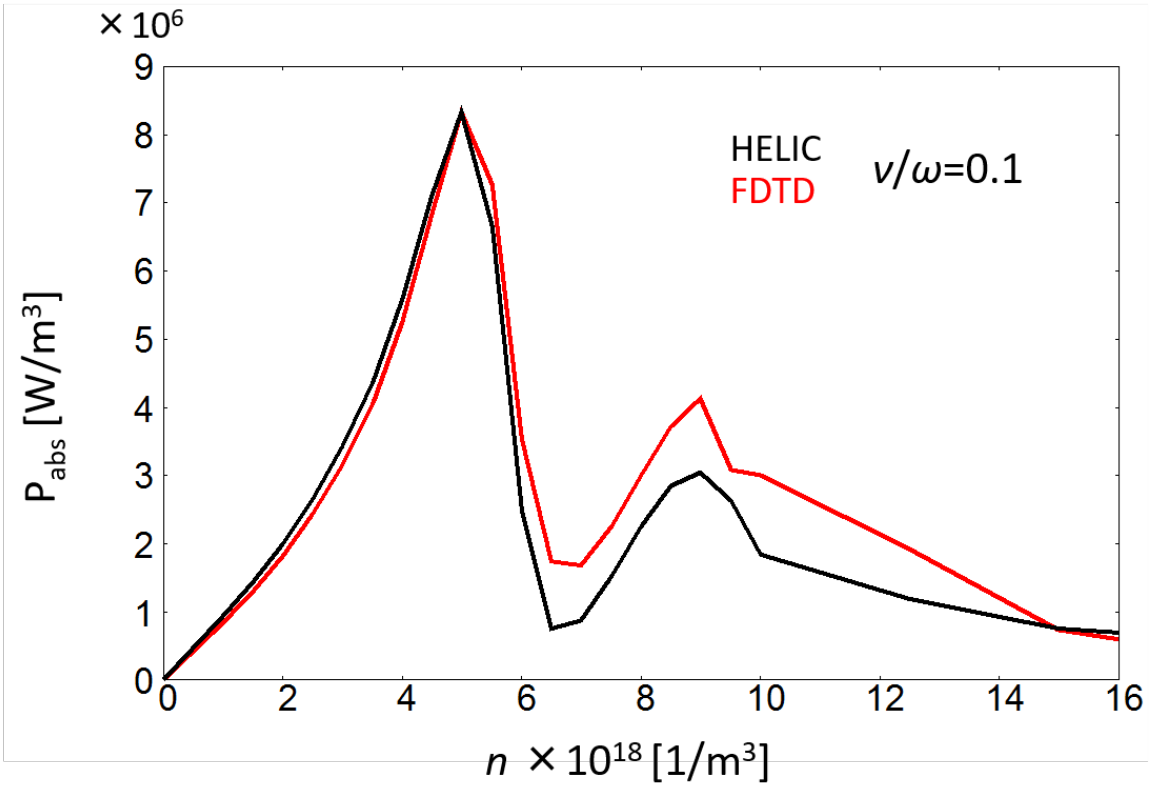

Figure 2.13: The power absorption curves calculated by the HELIC code (black line) and the FDTD simulation (red line) at $\nu/\omega = 0.1$.

2.2.4 Non-monotonicity of the power absorption curves and the density jump

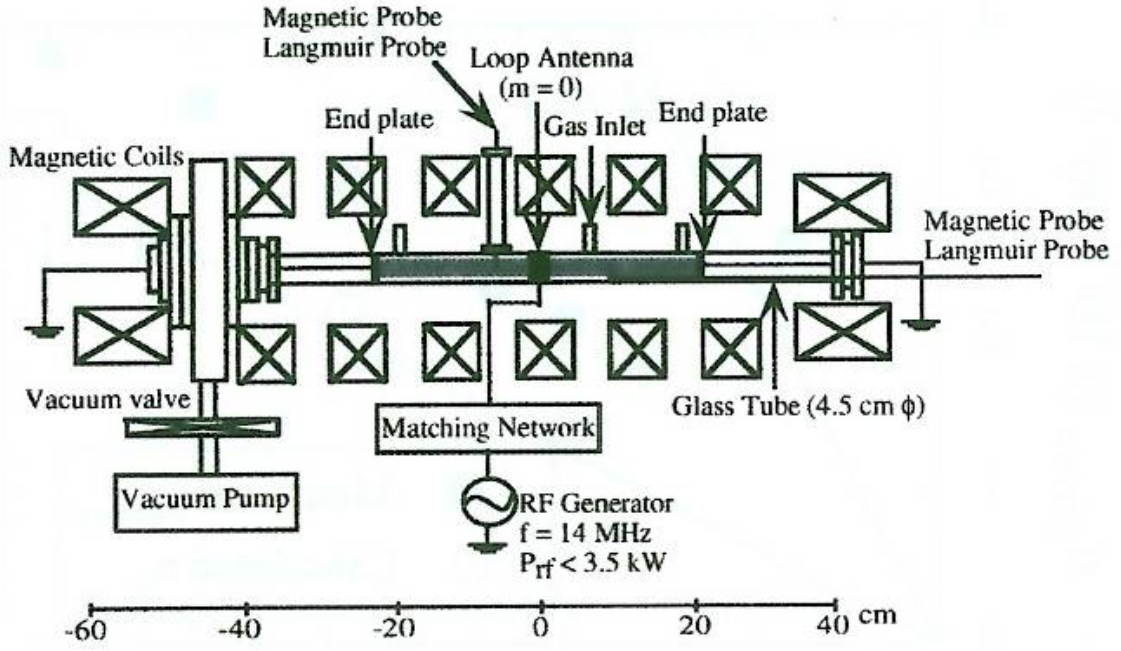

Figure 2.14: Schematic diagram of experimental set up [2].

In this section, we introduce the experiment of Nisoa, Sakawa, and Shoji [1–3]. They investigated the characterization of the excitation of $m = 0$ standing wave (SHWs) and production of high density plasmas of the order of $n_p \approx 10^{19}$ [1/m^3] in a short cylindrical plasma column of 10 [cm] length. Figure 2.14 shows their experimental apparatus. The Pyrex vacuum chamber is 72 [cm] in length and 4.5 [cm] in inner diameter. Two grounded copper end plates (4 [cm] in diameter) limit the length of the plasma column L ($L = 10 - 65$ [cm]). Ar gas is used typically at the pressure 8 [mTorr] and a flow rate of 10 [cc/min] with the base pressure of $P_{\rm Ar} \approx 10^{-5}$ [Torr]. B_0 up to 1 [kG] is generated by eight solenoid coils with a uniformity variation of less than 2% over the plasma length. A single-loop antenna made of a copper strip of 3 [cm] width is wound out side the Pyrex tube at $z = 0$ to excite the $m = 0$ helicon mode. An RF current of $f = 14$ [MHz] and $P_{RF} < 3.5$ [kW] is applied

to the antenna through a matching network.

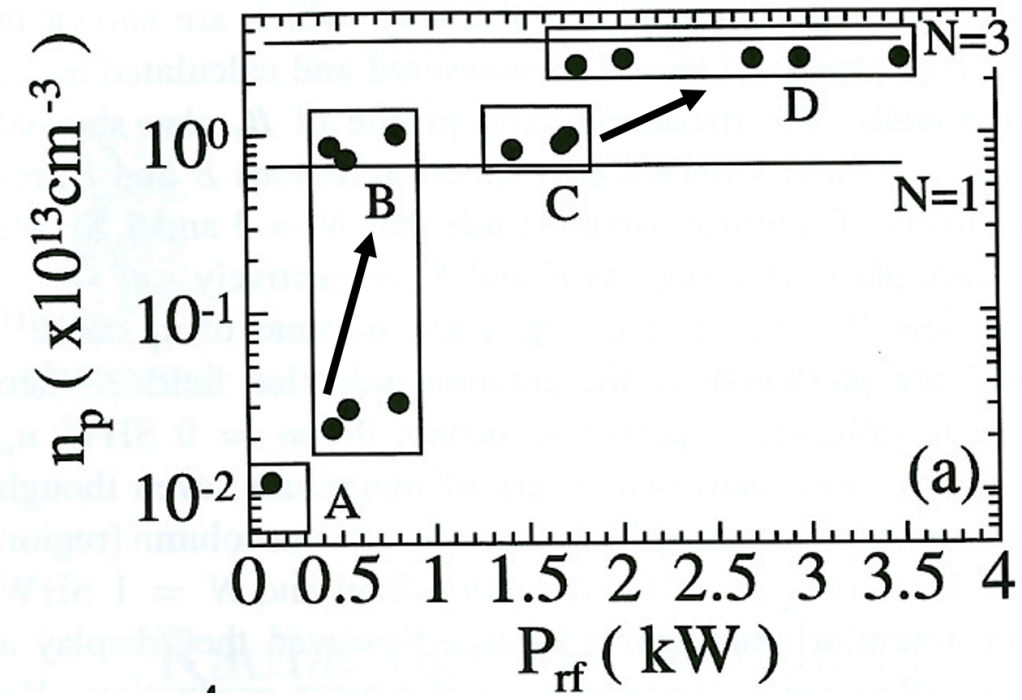

Figure 2.15: Plasma density n_p vs RF input power P_{RF} measured at $B_0 = 237$ [G] [1].

The measured dependence of the plasma density n_p and the RF input power is shown in Fig. 2.15 [1]. One can see that n_p increases stepwise with P_{RF}. They defined the discharge region of $P_{RF} < 0.2$ kW, $P_{RF} = 0.2 - 0.8$ [kW], $P_{RF} = 1.4 - 1.7$ [kW], and $P_{RF} > 1.8$ [kW] as regions A, B, C and D, respectively. From Fig. 2.15, the density jump by nearly two orders off magnitude from region A to C. n_p in region B is unstable and fluctuates between the density level of regions A and C within the pulse width of 0.4 [ms]. When P_{RF} is increased to 1.4 [kW], stable plasmas are created in region C. n_p jumps from region C to D as P_{RF} reaches about 1.8 [kW] and slightly increases with P_{RF} up to the maximum power of 3.5 [kW].

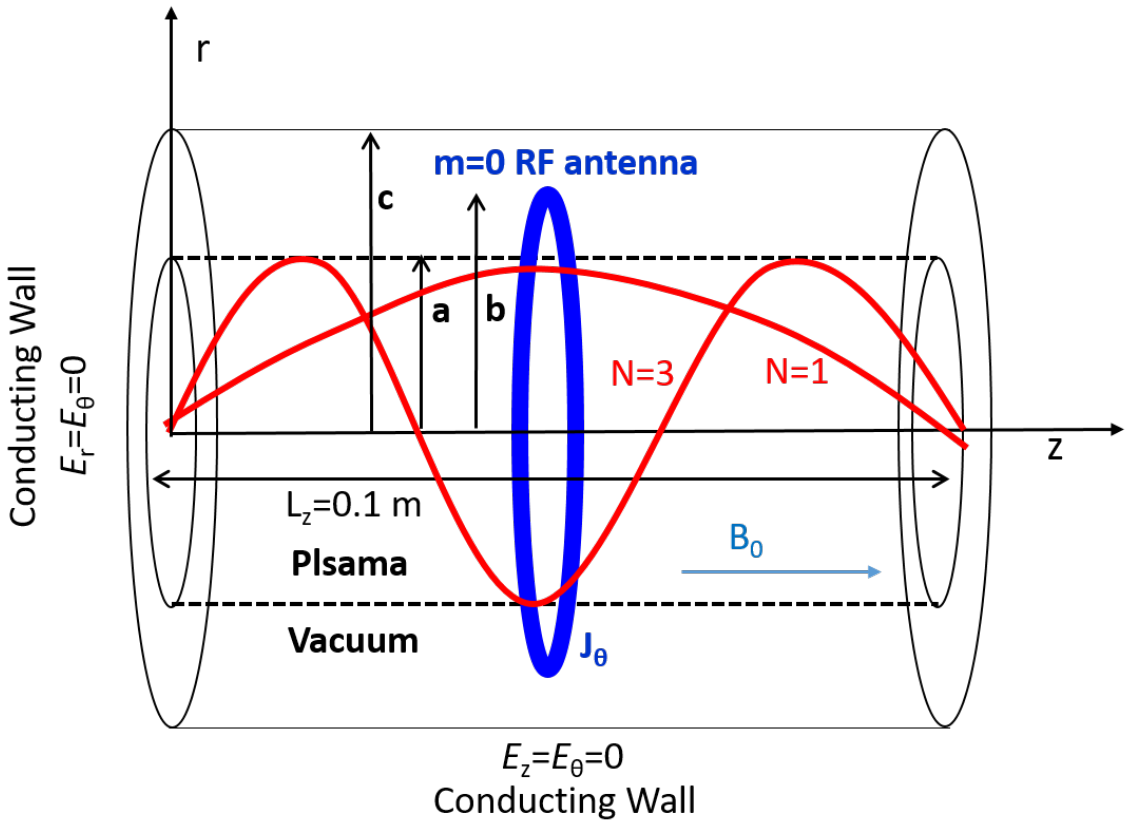

Figure 2.16: Schematic diagram of the experiment and the $N = 1$ and $N = 3$ SHWs modes.

The RF antenna is located at the plasma center $z = 0$ [cm], and confined by the conducting walls (the grounded copper end plates) $z = 5$ [cm] and $z = -5$ [cm] where the tangential field of the electric field vanishes. Therefore the standing waves that have the half wavelength $N = 1$ ($\lambda_z = 0.2$ [m], $k_z = 5$ [1/m]) or the one-half wavelength $N = 3$ ($\lambda_z = 0.2/3$ [m], $k_z = 15$ [1/m]) are basically excited as shown in Fig. 2.16. When the magnetic field is fixed, which is dominantly excited depends on the plasma density, and the geometries such as the location of the antenna and boundaries ($r = a, b$ and c), as discussed in previous section.

Figure 2.17 shows the power absorption curves of the $N = 1$ mode and the $N = 3$ mode, calculated by FDTD (red line) and HELIC (black line) in one-dimension with

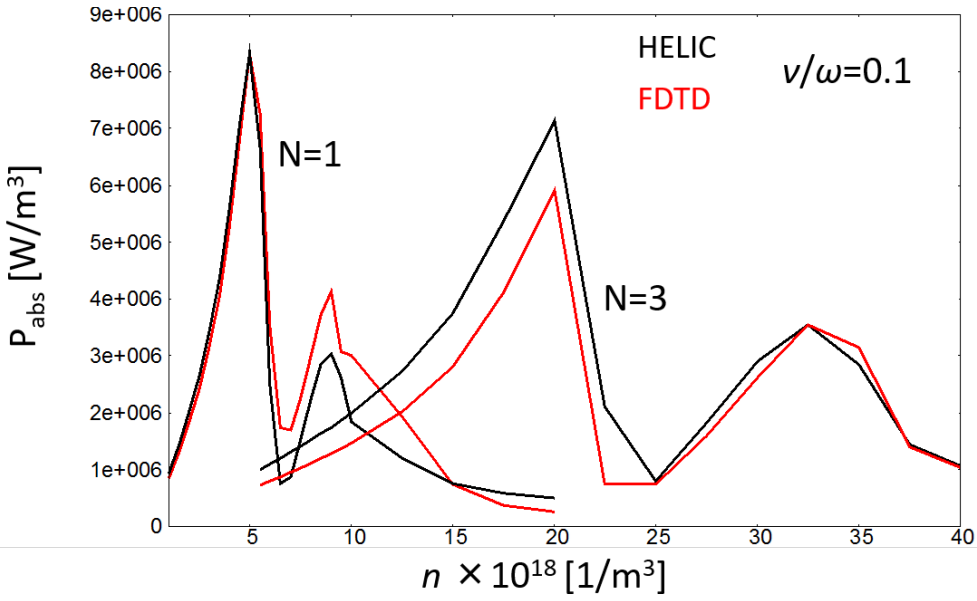

Figure 2.17: The power absorption curves of the $N = 1$ and the $N = 3$ modes, calculated by the HELIC code (black line) and the FDTD simulation (red line) at $\nu/\omega = 0.1$.

the fixed axial modes ($N = 1$ and $N = 3$), using the same parameters with previous ones. As shown Fig. 2.17, in the low density region $n_p < 1.0 \times 10^{19}$ [1/m^3], the power absorption by the $N = 1$ mode is dominant i.e. the $N = 1$ mode is excited dominantly, and at the high density region $n_p > 1.0 \times 10^{19}$ [1/m^3], the power absorption by the $N = 3$ mode is dominant i.e. the $N = 3$ mode is excited dominantly. Actually, in their experiment, the $N = 1$ mode and the $N = 3$ mode are observed in the low density region B and C and in the high density region A respectively ($N = 1$ and $N = 3$ in Fig. 2.15 mean the observed mode at each density region).

The power balance equation for the whole plasma is expressed as

$$\frac{d}{dt} n_p (W_e + W_i) V = P_{\text{net}} - P_{\text{loss}} = \eta P_{RF} - P_{\text{loss}}, \tag{2.84}$$

where W_e and W_i are the averaged electron and ion energies, respectively, V is the plasma volume, P_{net} is the net rf power absorbed by the plasma, $\eta = R/(R + R_c)$ is

the coupling coefficient of the antenna where R is the plasma resistance, R_c is the equivalent antenna resistance, and $P_{\rm loss}$ is the power absorbed by the plasma. The absorbed power is used to ionize the background gas by inelastic collisions and is carried away by direct particle loss from the plasma to the axial walls [51]. $P_{\rm loss}$ is given by

$$P_{\rm loss} = 2\pi a^2 E_T C_s n_p, \tag{2.85}$$

where C_s is the ion sound speed and E_T is the total energy loss for a single electron-ion pair lost at the wall. For Ar plasma of $T_e = 4$ [eV], $E_T = 69$ [eV] is obtained [51]. At the steady state, $d/dt = 0$ and 2.84 yields

$$\eta(n_p) = \frac{P_{\rm loss}(n_p)}{P_{RF}} = 0.28 \times \frac{n_p[10^{19}1/\mathrm{m}^3]}{P_{RF}[\mathrm{kW}]}. \tag{2.86}$$

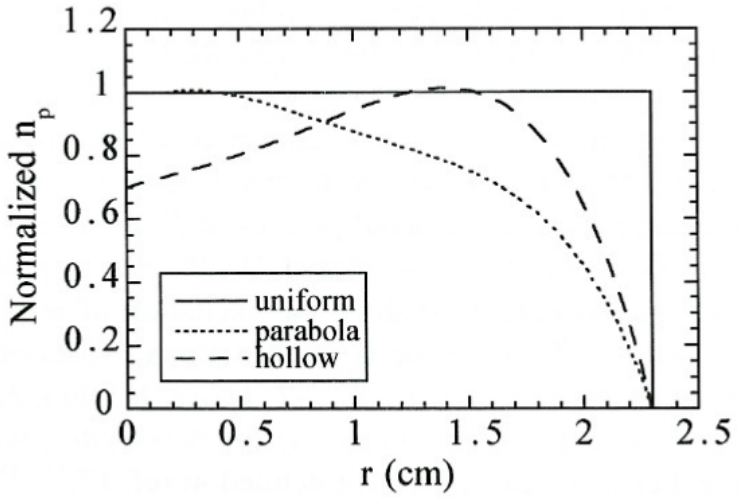

Figure 2.18: Three radial n_p profiles, uniform (solid line), hollow (dashed line) and parabolic (dotted line) profiles, used in 2D wave code calculation [2].

Nisoa *et al* calculated the power absorption curves by using a 2D wave code (TASK/WF) [93]. They used the observed n_p profiles as shown in Fig. 2.18, parabolic and hollow n_p profiles are used in the calculations for $B_0 = 237$ and 637 [G], respectively. Figure 2.19 shows the power absorption curves in terms of the plasma re-

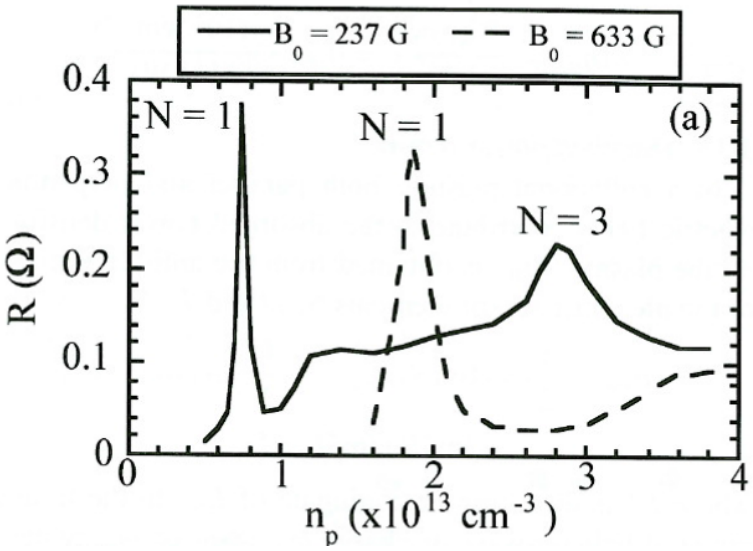

Figure 2.19: The plasma resistance R vs n_p for $B_0 = 237$ [G] (solid line) and $B_0 = 633$ [G] (dashed line) [2].

sistance R obtained from the wave calculations for $B_0 = 237$ and 637 [G]. Since this power absorption curve is plotted by using the total plasma resistance (power absorption), the first and second peaks for $B_0 = 237$ [G] in Fig. 2.19 corresponds to the first peak of the $N = 1$ mode and the first peak of the $N = 3$ mode in Fig. 2.17 respectively (almost the same parameters with in Fig. 2.17 are used except for the collision parameter and the plasma density profile). The steady state of the power balance 2.86 is solved graphically by plotting $\eta(n_p)$ for $R_c = 0.25$ [Ω] and $P_{\rm loss}(n_p)/P_{RF}$ versus n_p as shown in Fig. 2.20. In Fig. 2.20, $P_{\rm loss}(n_p)/P_{RF}$ for $P_{RF} = 0.4, 1.4, 1.8$, and 3.0 [kW] are also shown. The solutions of 2.86 are the plasma density (n_p) at which the curves of η and $P_{\rm loss}/P_{RF}$ intersect. However, these solutions consist of both stable and unstable solutions.

Shamrai [37] suggested the stable conditions of the steady state solutions of discharge equilibrium. He investigated the stability at some equilibrium density $n_p = n_{eq}$

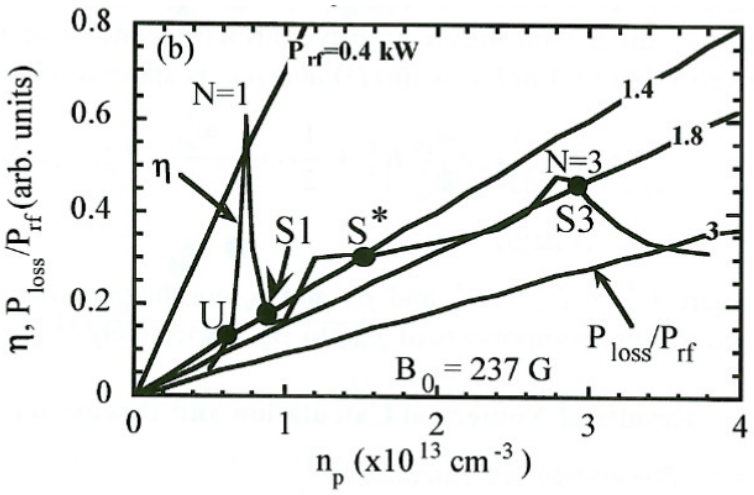

Figure 2.20: The coupling coefficient η (thick line) for $B_0 = 237$ [G] and P_{loss}/P_{RF} (thin lines) for $P_{RF} = 0.4, 1.4, 1.8$, and 3 [kW] vs n_p [2].

by expanding RHS of 2.84 in a small vicinity of the equilibrium point as follows

$$\begin{aligned}\frac{d}{dt}(n_p - n_{eq}) = \alpha \left[\frac{\partial P_{\text{net}}}{\partial n} - \frac{\partial P_{\text{loss}}}{\partial n}\right]_{n_p = n_{eq}} (n_p - n_{eq}) \\ + \frac{\alpha}{2}\left[\frac{\partial^2 P_{\text{net}}}{\partial n^2} - \frac{\partial^2 P_{\text{loss}}}{\partial n^2}\right]_{n_p = n_{eq}} (n_p - n_{eq})^2,\end{aligned} \tag{2.87}$$

where $\alpha = 1/(W_e + W_i)V$. One can see that the equilibrium is stable provided that

$$\frac{\partial P_{\text{net}}}{\partial n_p} < \frac{\partial P_{\text{loss}}}{\partial n_p}, \quad \text{at } n_p = n_{eq}. \tag{2.88}$$

If this inequality holds, any fluctuational deviation of the discharge from the equilibrium (either increasing or decreasing the density) is followed by a return to n_{eq} with the exponential rate. Indeed, the first term in the RHS of 2.87 is dominating at small deviations, and thus $\partial(n_p - n_{eq})/\partial t \propto -(n_p - n_{eq})$. Stability condition 2.88 fails at a critical equilibrium point of a saddle type with equal rates of variation with the density of absorption and losses

$$\frac{\partial P_{\text{net}}}{\partial n_p} = \frac{\partial P_{\text{loss}}}{\partial n_p}, \quad \text{at } n_p = n_{eq}. \tag{2.89}$$

Near such a point the stability is determined by the second term in the RHS of 2.87 which is proportional to the squared density variation. Its capacity to restore the equilibrium depends not only on the sign of the difference of the second derivatives in 2.87, but on the sign of the density variation, too. If the difference is positive,

$$\frac{\partial^2 P_{\text{net}}}{\partial n_p^2} - \frac{\partial^2 P_{\text{loss}}}{\partial n_p^2} > 0, \tag{2.90}$$

the density increases after a fluctuation of any sign is given. Indeed, $\partial(n_p - n_{eq})/\partial t \propto (n_p - n_{eq})^2$, so that the fluctuational decrease of the density will be followed by a return to the equilibrium, and *vice versa*, so the increase of the density progresses. The inverse is true if the difference of the second derivative is negative at the equilibrium point

$$\frac{\partial^2 P_{\text{net}}}{\partial n_p^2} - \frac{\partial^2 P_{\text{loss}}}{\partial n_p^2} < 0. \tag{2.91}$$

In this case, the restoration of equilibrium occurs at a fluctuational increase of density whereas it does not at a decrease. Note that $\partial^2 P_{\text{loss}}/\partial n^2$ is actually close to zero because losses normally linearly depend on density. In Fig. 2.20, the stability condition 2.88 and the saddle type condition 2.90 can be discussed by following equations:

$$\frac{\partial \eta}{\partial n_p} - \frac{\partial (P_{\text{loss}}/P_{RF})}{\partial n_p} < 0, \quad \text{at } n_p = n_{eq}, \tag{2.92}$$

and

$$\frac{\partial^2 \eta}{\partial n_p^2} > \frac{\partial^2 (P_{\text{loss}}/P_{RF})}{\partial n_p^2}, \quad \text{at } \left[\frac{\partial \eta}{\partial n_p} = \frac{\partial (P_{\text{loss}}/P_{RF})}{\partial n_p}\right]_{n_p = n_{eq}}. \tag{2.93}$$

Therefore, the solution U is unstable, while S is stable in Fig. 2.20.

The calculated stable n_p versus P_{RF} for B_0 is plotted in Fig. 2.21. The stable solutions of n_p exist for $P_{RF} = 1.2 - 1.6$ [kW]. The higher n_p values that appear between the lines of $N = 1$ and $N = 3$ modes are caused by the small peak in η (peaks at $n_p \approx 1.2 \times 10^{19}$ [1/m^3]), which corresponds to the second peak of the $N = 1$

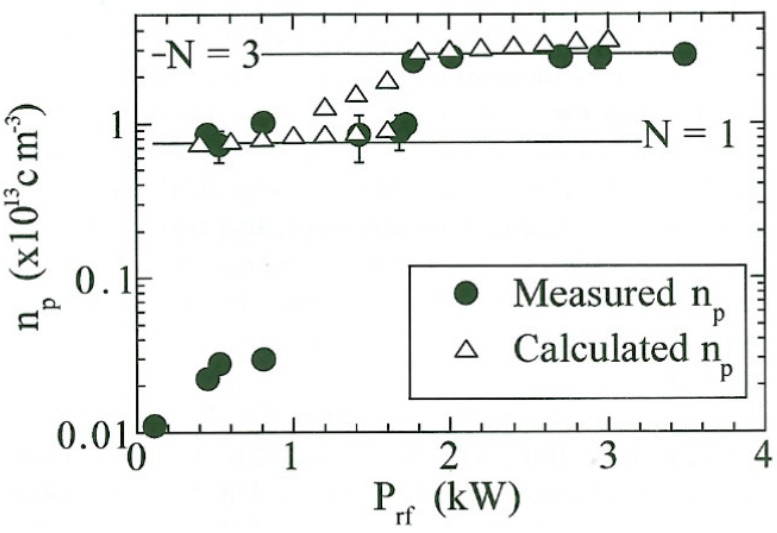

Figure 2.21: Measured n_p at $B_0 = 237$ [G] and the calculated stable n_p vs P_{RF}. Lines represent n_p at the peaks in η for $N = 1$ and $N = 3$ modes shown in Fig. 2.20 [2].

in Fig. 2.17. These n_p values are not observed in the experiment. They mentioned that when there are two stable solutions, n_p can not exceed that of the lower stable solution. Therefore for $P_{RF} = 1.4$ [kW] in Fig. 2.20, the lower stable $n_p(S_1)$ is attained instead of the higher stable $n_p(S^*)$. However, the detail reason is not mentioned in their argument. If there exists the saddle type point where 2.93 is satisfied, the density would jumps from S_1 to S_3, but there seems to be no such a point at below $P_{RF} < 1.8$ [kW]. Therefore, although they concluded that the calculation predicted the density jump from the intermediate density region B, C to the high density region D in Fig. 2.15 , the reason why the stable solutions of n_p at $P_{RF} = 1.2 - 1.6$ [kW] are not observed in experiment is not certain. Furthermore, they did not explain the density jump from the low density region A to the intermediate density region B and C in Fig. 2.15. Although they mentioned that the density jump from the low density region ($n_p \approx 10^{17}$ [1/m^3]) to the intermediate density region ($n_p \approx 10^{19}$ [1/m^3]) may be explained by the mode transition form the ICP mode to the helicon mode, there still remains the question in this argument. As Chen [41] pointed out, the finite

magnetic field precludes the ICP mode in the helicon discharge system. In conclusion, their calculation well predicts the equilibrium discharge state at the density region B, C and D in Fig. 2.15 qualitatively, but there still remain the problems about the discharge equilibrium state between the intermediate density region (B and C) and the high density region (D) (this may due to the parameters used in the calculation, since the small peaks at $n_p \approx 1.2 \times 10^{19}$ [1/m^3] are very sensitive to the variations of parameter such as the collision frequency), and the density jump from the low density mode (A) to the intermediate mode (B and C).

2.3 Bulk mode conversion

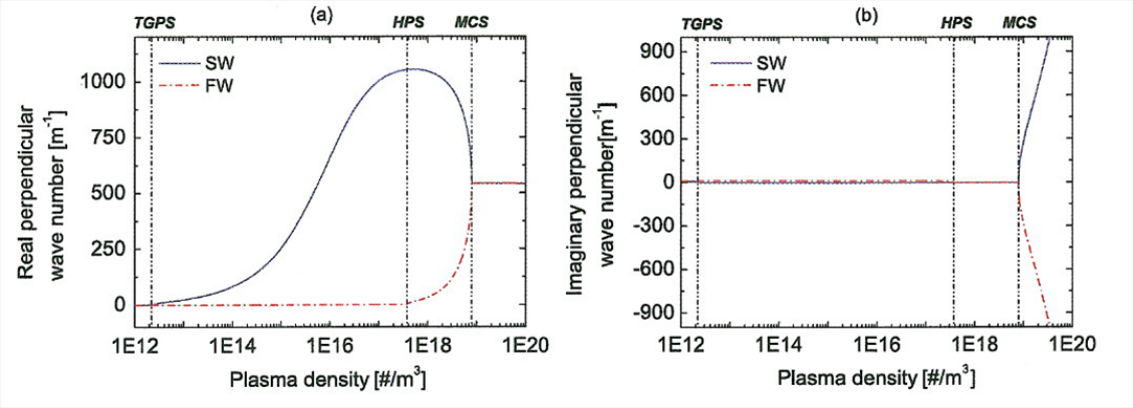

Figure 2.22: Perpendicular wave numbers without collision: (a) real perpendicular wave number, (b) imaginary perpendicular wave number [88].

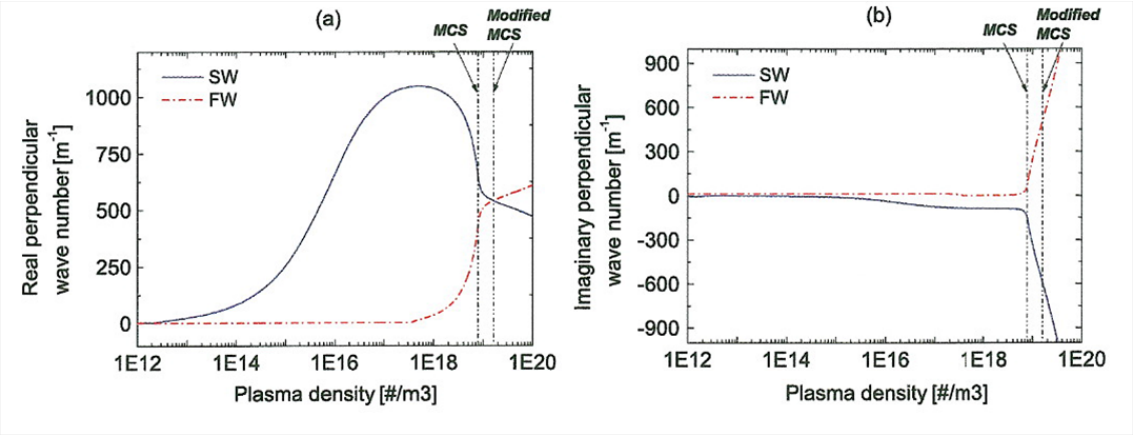

Figure 2.23: Perpendicular wave numbers with collision at 2 [mTorr]: (a) real perpendicular wave number, (b) imaginary perpendicular wave number [88].

The bulk mode conversion is the classical type of the mode conversion that occurs near the mode conversion surface (MCS). Based on a fluid model, Kim [88] pointed out that in the bulk mode conversion, collisional dissipation plays an important role near the MCS. Figures 2.22 and 2.23 show the dispersion branches of the Fast wave (FW) and the Slow wave (SW) without collisional dissipation and with finite collisional dissipation, respectively. The fast wave and the slow wave correspond to the helicon wave and the TG wave respectively. When the collision is absent, dispersion curves

of the helicon and the TG merge at the MCS. Finite dissipation makes the dispersion curves split and the MCS moves slightly toward a higher density region as seen in Fig. 2.23. Kim argued that the helicon wave is dissipated strongly before it can reach the MCS, making the mode conversion at the MCS practically absent. Kim further argued that the collisional damping rate of the helicon wave near the MCS is large enough to explain the central core heating (i.e., density profile peaked at the center), a typical property of the helicon plasma in laboratories. Kim estimated the damping length of the helicon wave near the MCS using $k_{\perp \mathrm{imag}}$. However, this is misleading since the imaginary part of $k_\perp$ arises both due to the damping and the evanescence.

2.4 Surface mode conversion

The surface mode conversion is a universal excitation mechanism of the TG wave, which occurs in the region of the plasma column with density $n_0 < n_{\mathrm{up}}$ [37]. The TG component is well electrostatic in this region. To excite it efficiently, there should be a mechanism producing a space charge. Indeed, the rate of work, which the electron current related to the helicon wave, $\boldsymbol{j}^{(\mathrm{H})}$, does to excite the TG wave, takes the form [37]

$$\begin{aligned} P_{\mathrm{conv}} &= \int \boldsymbol{E}^{(\mathrm{T})} \cdot \boldsymbol{j}^{(\mathrm{H})} dV \approx \int \phi^{(\mathrm{T})} \nabla \cdot \boldsymbol{j}^{(\mathrm{H})} dV \\ &= i\omega \int \phi^{(\mathrm{T})} \rho^{(\mathrm{H})} dV, \end{aligned} \tag{2.94}$$

where $\boldsymbol{E}^{(\mathrm{T})} \approx -\nabla \phi^{(\mathrm{T})}$ is the electrostatic component of the TG wave, and we integrated by parts and used the following continuity equation

$$\rho^{(\mathrm{H})} = -(i/\omega) \nabla \cdot \boldsymbol{j}^{\mathrm{H}} = i(e/\omega) \left[n_0 \nabla \cdot \boldsymbol{v}^{(\mathrm{H})} + \boldsymbol{v}^{(\mathrm{H})} \cdot \nabla n_0 \right]. \tag{2.95}$$

Since the velocity of the electron fluid in helicon fields, $\boldsymbol{v}^{(\mathrm{H})}$, obeys the relation $\nabla \cdot \boldsymbol{v}^{(\mathrm{H})} \approx 0$ [94], one obtains $\nabla \cdot \boldsymbol{j}^{\mathrm{H}} \approx -\boldsymbol{v}^{\mathrm{H}} \cdot \nabla n_0$. Then 2.94 yields [37]

$$P_{\mathrm{conv}} - e \int \phi^{\mathrm{T}} \boldsymbol{v}^{\mathrm{H}} \nabla n_0 dV. \tag{2.96}$$

As seen, the surface mode conversion arises due to a redundant polarization induced by helicon fields in the non-uniform plasma.

An essential contribution in integral 2.96 is due to a steep density gradient naturally arising at the boundary of the plasma column with the chamber wall. If n_b is the boundary value of the plasma density, the gradient at the boundary reads $\nabla n_0 = -\boldsymbol{e}_r n_b \delta(r_0 - r)$, with δ being the Dirac delta-function, and $\boldsymbol{e}_r$ the radial unit vector. The gain of integral 2.96 due to this source of polarization is [37]

$$P_{\text{surf. conv}} \approx \pi r_0 Lec n_b B_0^{-1} \left| \phi^{(\mathrm{T})} E_\theta^{(\mathrm{H})} \right|_{r=r_0}. \tag{2.97}$$

One can see from 2.97 that the surface mode conversion occurs at an insulating wall only, because $\phi^{\mathrm{T}} = 0$ on a conducting wall.

CHAPTER III

Spatial behavior in non-uniform plasma

3.1 Spatial behavior (mode conversion) in a non-uniform helicon plasma

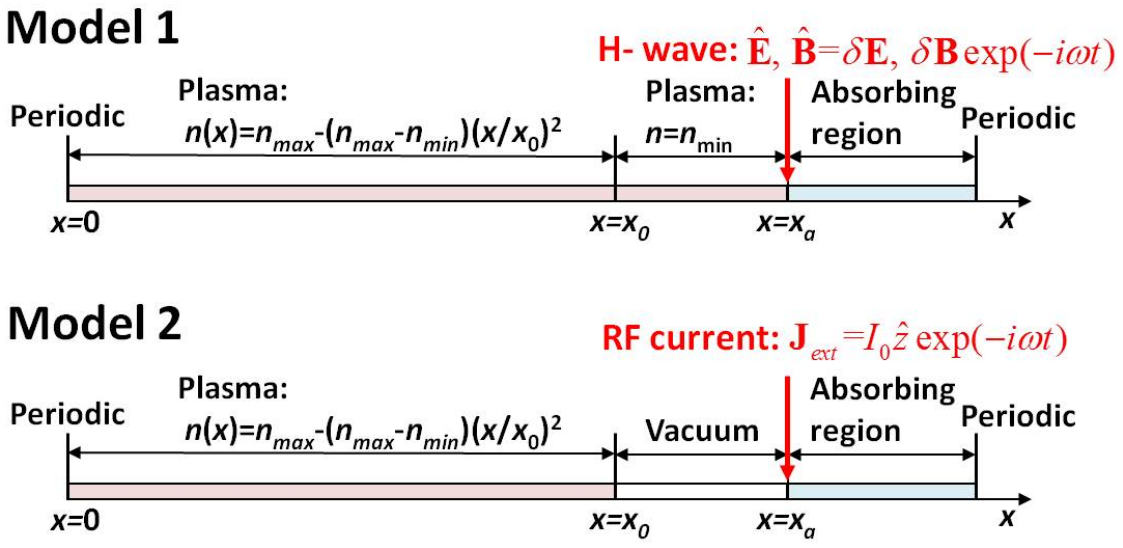

Figure 3.1: Computational models used in FDTD simulation. The helicon wave propagating toward the plasma is directly excited in model 1, and the RF wave is excited by the given current in model 2.

Two models are considered as shown in Fig. 3.1. In the model 1, only the helicon wave that propagates toward the plasma is directly excited so that any other wave components are excluded, and we focus the bulk mode conversion process. The

model 2 is used for investigating the power absorption profiles of all wave fields (including the surface mode conversion process), and the relative importance of the bulk mode conversion process for the total power absorption is discussed. We consider the electron fluid equation of motion 2.1 and Maxwell's equations 2.2-2.4 with $\nabla = (\partial/\partial x, ik_y, 0)$, $\boldsymbol{J} = -en_0(x)\boldsymbol{u}_\mathrm{e} + \boldsymbol{J}_\mathrm{ext}$, and the external RF current density $\boldsymbol{J}_\mathrm{ext} = I_0\hat{z}\exp(-i\omega t)\delta(x - x_\mathrm{a})$. All other notations are standard. Cartesian coordinates are used instead of cylindrical coordinates, assuming that essential physics involved remains the same (the values of energy flux and power deposition are slightly centrally high in cylindrical coordinates compared to Cartesian coordinates in our calculation). The main axis is the x-axis (corresponding to the radial direction in the cylindrical helicon device), along which the zero-th order density is varied. Since there are no background variations in the y direction (corresponding to the axial direction in the cylindrical helicon device), all the variables are already Fourier transformed in this direction. Furthermore, the absence of nonlinear terms that may cause wave-wave interactions allows us to treat the initial k_y (the y component of the wave number) as a constant. Thus, we choose the axial mode $l_y = k_y L/\pi = 10$ excited in typical experiment (the axial length of the plasma column $L = 1.6$ [m] is assumed).

In both models, the region $0 < x < x_0$ is filled with a plasma having the background density

$$n(x) = n_\mathrm{max} - (n_\mathrm{max} - n_\mathrm{min})(x/x_0)^2. \tag{3.1}$$

Figure 3.2 shows dispersion relations of the H- (red lines) and TG+ waves (blue lines) in this region, where the minus sign represents the sign of the wave phase velocity (note that the perpendicular component of the TG wave group velocity has an opposite sign to that of the phase velocity). Dispersion curves with $\nu/\omega = 0$ (solid lines), 0.01 (dashed), and 0.08 (dotted) are superposed. Figure 3.2 (a) shows the real wave number. When the collision is absent, dispersion curves of H- and TG+ merge at $x = x_\mathrm{up}$, corresponding to the MCS where the discriminant in 2.15 is zero, and

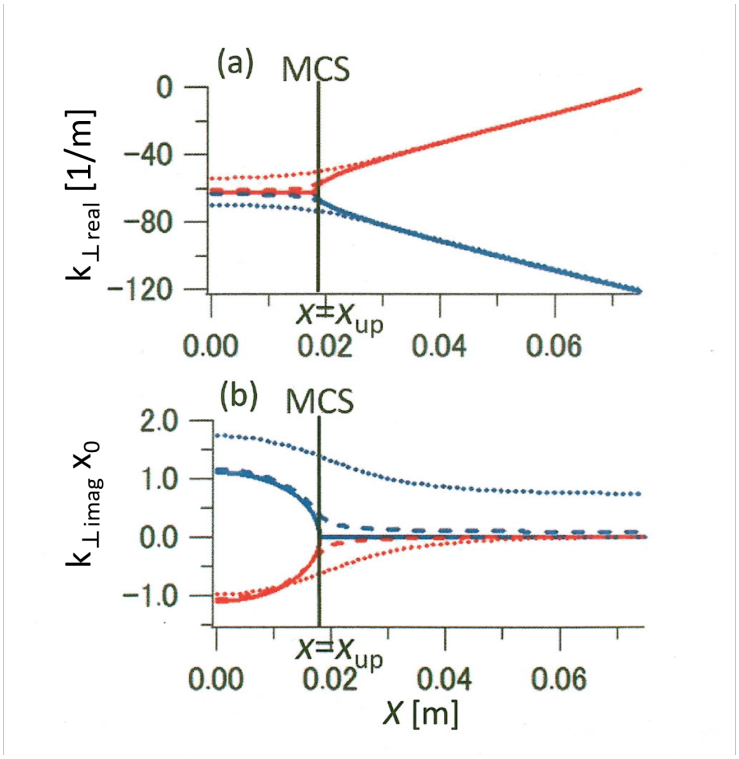

Figure 3.2: Dispersion relation of the H- wave (red) and the TG+ wave (blue), with $\nu/\omega = 0$ (solid), 0.01 (dashed), and 0.08 (dotted).

the H- mode converts to the TG+ as the reflected wave. When a finite collision is added, the dispersion curves are separated because the discriminant in 2.15 includes the imaginary part and cannot be zero (the same discussion holds for the case with including the effect of strong density gradient [87] in 2.15). The separation is increased as ν/ω is increased, reducing efficiency of the mode conversion between the H- and TG+ waves. Figure 3.2 (b) shows the normalized imaginary wave number, $k_{\perp \mathrm{imag}} x_0$, showing the reciprocal of damping scale normalized to the size of the plasma column. When $\nu/\omega \neq 0$, $k_{\perp \mathrm{imag}} x_0 \ll 1$ in the low density region. As the H- wave propagates toward the center where the density is increased, $k_{\perp \mathrm{imag}} x_0$ becomes larger, and the wave penetrates into the evanescent region ($x > x_{\mathrm{up}}$).

The adjacent region $x_0 < x < x_{\mathrm{a}}$ is either a plasma with a constant density (model 1) or vacuum (model 2). At $x = x_{\mathrm{a}}$, either the helicon wave (model 1) or the external RF current (model 2) is given, with the angular frequency ω satisfying

2.5. The region $x > x_{\rm a}$ is the wave absorber. Reflected waves are fully damped in this region as shown in Fig. 3.1. The model 1 is employed in order to study the bulk mode conversion process. In this model, the plasma is uniform ($n = n_{\rm min}$) and non-dissipative ($\nu/\omega = 0$) in the region $x_0 < x < x_{\rm a}$, and only the helicon wave propagating toward the plasma (H-) is directly excited at $x = x_{\rm a}$. In the model 2, the RF wave excited by the given current at $x = x_{\rm a}$ propagates through a vacuum area and reaches the plasma. In both models, the background magnetic field B_0 is along the longitudinal (y) axis.

Numerical calculations are conducted using the following typical experimental parameters: $x_0 = 7.5$ [cm], $x_{\rm a} = 8.5$ [cm], $\omega/2\pi = 7.0$ [MHz], $B_0 = 0.01$ [T], electron temperature $T_{\rm e} = 3.0$ [eV], Ar neutral pressure $P_{\rm Ar} = 0.75 \sim 10$ [mTorr], $n_{\rm max}(0) = 4.6 \times 10^{18}$ [1/m^3], $n_{\rm min}(x_0) = 4.6 \times 10^{17}$ [1/m^3], and $I_0 = 1.0 \times 10^6$ [A/m^2]. Under these parameters the MCS is located near the plasma center, and this is convenient for investigating the bulk conversion process. We note that details of the used parameters such as those specifying the boundary or the absorbing regions do not significantly alter the main conclusion of the present study.

We assume that the electron-neutral collision is dominant, and this allows us to replace the collision frequency in 2.1 by the electron-neutral collision frequency, $\nu = \nu_{\rm en}$, which is given approximately by [95]

$$\nu_{\rm en}[{\rm sec}^{-1}] \approx 1.3 \times 10^6 \; P_{\rm Ar}[{\rm mTorr}] \; T_{\rm e}[{\rm eV}], \tag{3.2}$$

and thus the electron-neutral collision frequency is within the range $\nu/\omega \approx 0.067 \sim 0.89$.

3.2 Parameters used in the FDTD simulation

In the FDTD simulation (Appendix A), numerical iterations are conducted using the following parameters: step size in space $dx = 6.0 \times 10^{-5}$ [m] ($\approx 0.02 \times \lambda_{TG}$: the wave length of the TG wave at $n = 10^{18}$ [1/m^3]), step size in time $dt = 0.9dx/c$ [s] (which satisfies the Courant-Friedrichs-Lewy condition), number of grid in plasma region($0 < x < x_0$): 1250, number of grid in vacuum region($x_0 < x < x_{\rm a}$): 166, number of grid in absorbing region($x_{\rm a} < x$): 500, and typical execution time step: 3.0×10^7 ($\approx 38 \times 2\pi/\omega$). Here, the following boundary conditions are automatically satisfied at $x = x_0$: the tangential components of all fields and the normal component of **B** field are continuous.

3.3 Analytic solution

After a transient time period, the magnetic field perturbations satisfy a set of equations derived by Fourier transforming 2.1-2.3 in t,

$$B_x^{'} = -ik_y B_y, \tag{3.3}$$

$$B_y^{''} = -ik_y \left(\frac{n^{'}}{n} B_x - B_x^{'} \right) + \frac{\omega_{pe}^2}{c^2 \gamma} B_y + \frac{n^{'}}{n} B_y^{'} - \frac{\omega_{ce} k_y}{\omega \gamma} \left(\frac{n^{'}}{n} B_z - B_z^{'} \right), \tag{3.4}$$

$$B_z^{''} = i \frac{\omega_{ce}}{\omega \gamma} k_y^2 B_x - \frac{\omega_{ce}}{\omega \gamma} k_y B_y^{'} + \left(\frac{\omega_{pe}^2}{c^2 \gamma} + k_y^2 \right) B_z + \frac{n^{'}}{n} B_z^{'}, \tag{3.5}$$

where $\gamma = 1 + i(\nu/\omega)$ and $'$ denotes d/dx. The boundary value problem at the plasma region ($0 < x < x_0$) defined by 3.3-3.5 is solved using the fourth-order Runge Kutta method. The values at the boundaries are given at the plasma center ($x = 0$) as

follows,

$$\left(\begin{array}{ccccc} B_x & B_y & B_z & B_y^{'} & B_z^{'} \end{array} \right)_{x=0} = \left(\begin{array}{ccccc} B_{x,H-} & B_{y,H-} & B_{z,H-} & B_{y,H-}^{'} & B_{z,H-}^{'} \end{array} \right)_{x=0}, \tag{3.6}$$

where the subscript H- denotes the H- mode. The relative values of each component are determined by the dispersion relation with the density at the plasma center $n(0)$. Variables at the plasma edge ($x = x_0$) are to be determined after integration of 3.3-3.5.

3.4 Mode decomposition

Since the boundary value problem above and also the FDTD simulation system are both linear, waves included in these systems can be decomposed into the combination of the four modes (H+, TG+, H-, TG-), i.e., the helicon (H) and the TG waves propagating both in the positive (+) and the negative (-) directions with respect to the x-axis. The decomposition can be carried out by solving the dispersion relation at each location assuming validity of the WKB approximation. The zeroth-order condition to apply the WKB method is given by the factor [88],

$$f_{\mathrm{WKB}} = \left| \frac{1}{k_x^2} \frac{dk_x}{dx} \right|. \tag{3.7}$$

Figure 3.3 shows f_{WKB} for the helicon and the TG waves for $\nu/\omega =$ (a) 0.003, (b) 0.005, (c) 0.01, and (d) 0.05. We see that $f_{\mathrm{WKB}} < 1$ for the entire space for the TG wave, and near the center of the plasma including the MCS for the helicon wave. We should also note that f_{WKB} is not much less than unity near the MCS, and it exceeds unity for the helicon wave for $x > 0.04$ [m]. Therefore, the WKB decomposition is approximately valid (but not exact) near the center of the plasma including the MCS, since the gradient scale of the background is less than the helicon wavelength near the

plasma edge. Here we wish to stress that our solutions of the boundary value problem and the FDTD simulations are correct, within the accuracy of numerical errors and using discrete grids with a finite width.

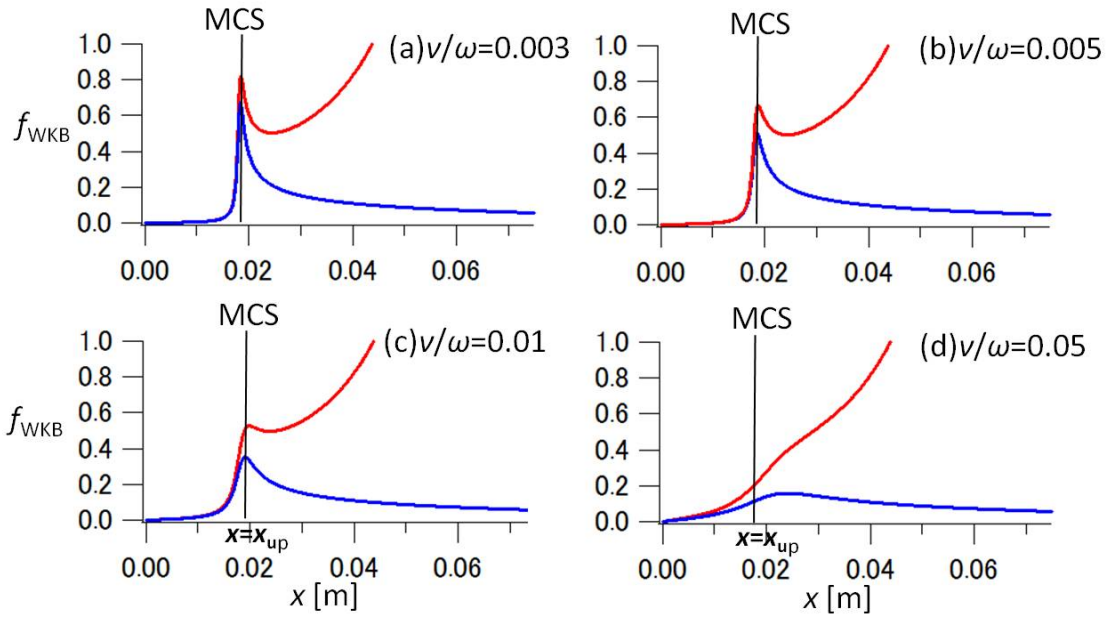

Figure 3.3: $f_{\rm WKB}$ profiles of the helicon (red) and the TG (blue) waves for ν/ω =(a) 0.003, (b) 0.005, (c) 0.01, and (d) 0.05.

3.5 Wave energy flux profiles

Now we discuss the bulk mode conversion by using model 1. Figure 3.4 shows a typical result of numerical time integration of 2.1-2.3 by solid lines. Initially, there is no perturbation field in the system, and the H- wave is introduced at $x = x_a = 8.5$ [cm]. Plotted in (a) and (c) are the real part of wave magnetic field, Re$[B_y]$, of H- (red lines) and TG+ (blue lines) waves at $t = 3.4 \times 2\pi/\omega_{RF}$, with $\nu/\omega = 0$ in (a) and $\nu/\omega = 0.02$ in (c). Numerical solutions of 3.3-3.5 are also shown as dotted lines. In model 1, almost no H+ and TG- waves are excited because only the H- wave is excited in this model. Sharp peaks of the magnetic perturbations around $x = x_{\rm up}$ in

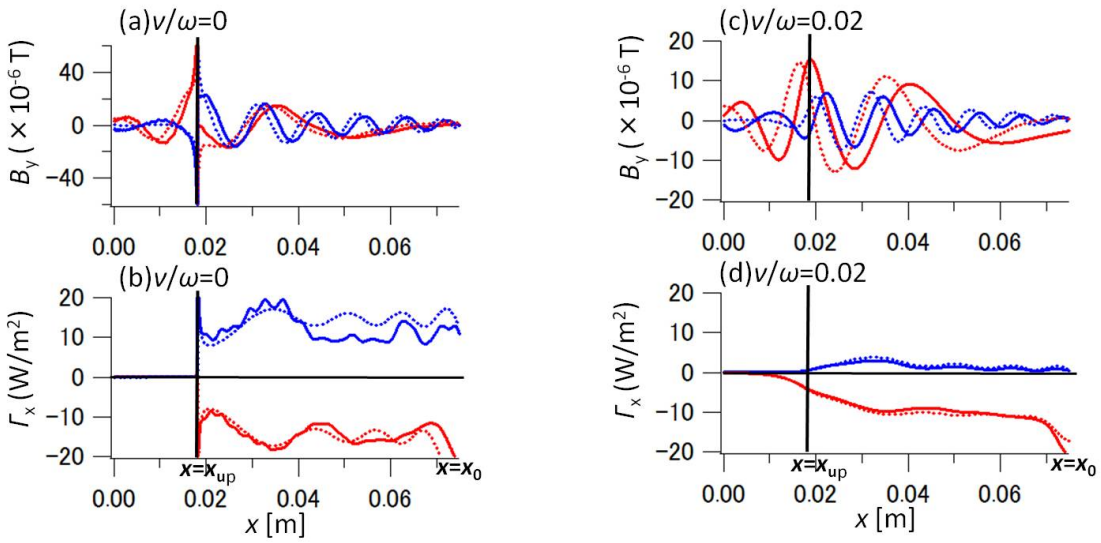

Figure 3.4: Wave fields: Re$[B_y]$ (top), and x components of energy flux: Γ_x (bottom) at $t = 38 \times 2\pi/\omega$, with the H- wave (red line) and the TG+ wave (blue line), FDTD simulation (solid line) and numerical analytical solutions (dotted line) of 3.3-3.5.

(a) are due to the degeneracy of H- and TG+ waves: the perturbation field cannot be decomposed into the four wave modes when the waves are degenerated. The total field perturbation has no singular behavior. Figures 3.4 (b) and (d) show the computed x-component of the energy flux in the boundary value problem (Eqs. 3.3-3.5) and the FDTD simulation, $\Gamma_{x,\text{H-}} = \text{Re}[\boldsymbol{E}_{\text{H-}} \times \boldsymbol{B}^*_{\text{H-}}]_x/\mu_0$, for the H- ($\Gamma_{x,\text{H-}} < 0$) waves, and $\Gamma_{x,\text{TG+}} = \text{Re}[\boldsymbol{E}_{\text{TG+}} \times \boldsymbol{B}^*_{\text{TG+}}]_x/\mu_0$, for the TG+ ($\Gamma_{x,\text{TG+}} > 0$) waves (The Poynting flux also involves such terms as $\text{Re}[\boldsymbol{E}_{\text{H-}} \times \boldsymbol{B}^*_{\text{TG+}}]_x/\mu_0$, but due to the difference in the wavenumbers for different wave modes, the direction of the cross product oscillates in space and they do not contribute much in conveying the energy flux over the entire plasma region). When $\nu/\omega = 0$, waves become evanescent at $x = x_{\text{up}}$, and total Γ_x vanishes because the energy flux carried into the plasma are all reflected. In particular, we see in (b) that the energy flux conveyed by H- is all converted to that of TG+. The electromagnetic field perturbations penetrates into the evanescent region ($x > x_{\text{up}}$), but there is no energy flux associated with the perturbations. When $\nu/\omega = 0.2$, the balance of energy flux does not hold due to the wave dissipation, and the total

Γ_x does not vanish. The wave amplitude of TG+ in this case is considerably smaller than the collision-less case. The decrease of the transformed energy by the bulk mode conversion is due to the separation of the helicon and the TG wave branches in the dispersion relation. The energy flux of helicon wave flows into bulk area ($x > x_{\rm up}$) and the helicon wave directly decays near the MCS ($x \approx x_{\rm up}$) because $k_{\perp {\rm imag}} x_0$ becomes larger (Fig. 3.2). However, the bulk mode conversion is still visible in this case $\nu/\omega = 0.02$.

3.6 Bulk mode conversion efficiency

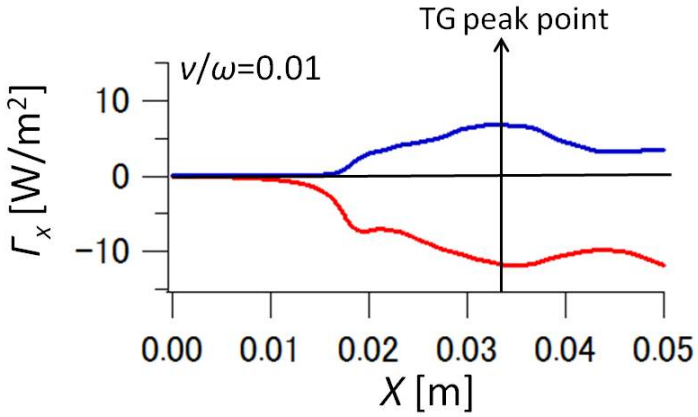

Figure 3.5: The energy flux profiles of the helicon (red) and the TG waves (blue). Λ is evaluated at the point where the TG energy flux is maximum.

The efficiency of TG wave excited by the bulk mode conversion strongly depends on the dissipation as stated above. Here, we evaluate the efficiency as a function of the dissipation parameter. We define the mode conversion efficiency as $\Lambda = \Gamma_{x,\mathrm{TG+}}/\Gamma_{x,\mathrm{H\text{-}}}$. Figure 3.5 compares the energy flux carried by the H- and TG+ waves for $\nu/\omega = 0.01$. The MCS is located near $x = 0.02$. Due to the uncertainty of the location of the mode conversion, it is difficult to evaluate Λ exactly. Here, we identify the point where the TG energy flux is maximum, and compute Λ at this point. Table 3.1 and Figure 3.6 show the dependence of Λ on ν/ω. $\Gamma_{x,\mathrm{H\text{-}}}$, $\Gamma_{x,\mathrm{TG+}}$ and Λ are evaluated by both FDTD simulation and numerical solutions of 3.3-3.5 as shown in Table 3.1 (numerical results of $\Gamma_{x,\mathrm{H\text{-}}}$ and $\Gamma_{x,\mathrm{TG+}}$ are not listed).

As ν/ω is increased, $\Gamma_{x,\mathrm{H\text{-}}}$ and Λ decrease monotonically. The decrease in $\Gamma_{x,\mathrm{H\text{-}}}$ is due to the collisional dissipation of the helicon wave. In particular, Λ is almost 100% when $\nu/\omega = 0$, Λ remains above 50% when $\nu/\omega < 0.01$, and $\Lambda < 10\%$ when $\nu/\omega > 0.04$, corresponding to usual laboratory experiments (assuming no neutral depletion). The bulk mode conversion is important only when the dissipation is small.

Table 3.1: The evaluated energy fluxes of the helicon and the TG waves, and the computed mode conversion efficiency

ν/ω	$\Gamma_{x,\text{H-}}$ [W/m^2]	$\Gamma_{x,\text{TG+}}$ [W/m^2]	Λ [%]	
	Simulation	Simulation	Simulation	Analysis
0	-29.81	29.12	98	100
0.003	-29.17	29.73	95	81
0.005	-27.79	23.71	85	71
0.008	-26.51	16.67	63	60
0.01	-25.55	13.34	52	52
0.02	-21.24	4.82	23	28
0.03	-18.20	1.98	11	16
0.04	-16.12	0.90	6	9
0.05	-14.71	0.45	3	6
0.06	-13.80	0.24	2	4

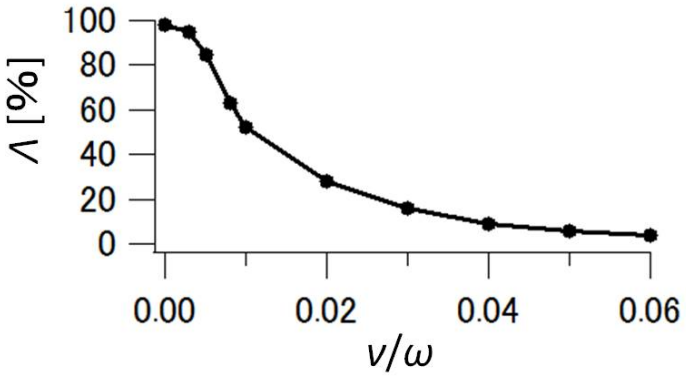

Figure 3.6: The dependence of computed mode conversion efficiency (from the H-wave to the TG+ wave) Λ in the FDTD simulation, on the normalized collision frequency, ν/ω.

3.7 Power deposition

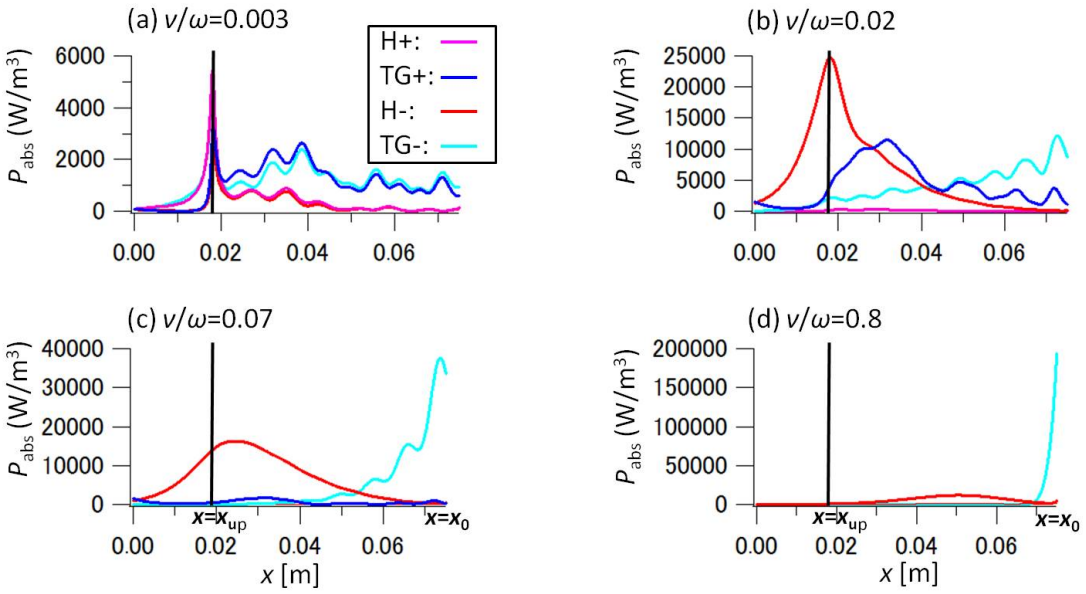

Figure 3.7: Power deposition profiles of the four modes (H+, TG+, H-, TG-) for ν/ω =(a)0.003, (b)0.02, (c)0.07 and (d)0.8.

By using the model 2, we discuss the power deposition (local joule heating) profiles of the four modes, in order to investigate the relative importance of the heating by each mode wave. The power absorption $P_{\rm abs}$ is calculated as

$$\begin{aligned} P_{\rm abs}(x) &= {\rm Re}[\boldsymbol{E}\cdot\boldsymbol{J}] \\ &= \frac{\omega\varepsilon_0}{2}{\rm Im}\left\{S\left(|E_x|^2+|E_z|^2\right)+P|E_y|^2\right\}, \end{aligned} \tag{3.8}$$

where S and P are the notations used in Stix [96]. Figure 3.7 compares $P_{\rm abs}$ of the four wave modes for various values of ν/ω. When (a) $\nu/\omega = 0.003$, the power deposition profiles exhibit sharp peaks near the MCS, indicating an abrupt change of the damping scale length near the MCS (see Fig. 3.2 (b)). The power deposition of the TG+ wave excited by the bulk mode conversion is comparable to that of the TG- wave excited by the surface mode conversion. The power absorption by the H+ wave is very small. This is due to the reverse bulk mode conversion, i.e., the energy

transfer occurs from TG- to H+. When (b) $\nu/\omega = 0.02$, the power deposition by the bulk mode conversion decreases, but still is comparable to that of the surface mode conversion, and the power deposition of the H- wave becomes dominant. The H- wave mainly heats the bulk region while the TG+ and TG- waves heat the plasma over an extended region. Under typical experimental conditions ((c) $\nu/\omega = 0.07$ and (d) 0.8), the bulk mode conversion cannot be seen and the H- wave is directly damped over the extended region. The power deposition is comparable to that of the TG+ wave. Our results here are quite different from conventional analysis of the collisional power absorption where the analysis was made only at locations far from the MCS. The power deposition of the TG+ wave becomes more dominant and localized at the edge ($x \approx x_0$) as ν/ω is increased. Actually, the energy of the TG- wave, excited by the surface mode conversion, depends on the edge density (increases as the edge density increases, and vise versa). Therefore, the relative importance of the heating by each wave also depends on the edge density.

3.8 Conclusion

We clarified the contribution of the bulk mode conversion and the helicon wave for the power deposition under typical experimental conditions: the efficiency of the bulk mode conversion strongly depends on the collision frequency. We also investigated the power deposition profiles due to the four modes (H+, TG+, H-, TG-) varying the collision frequency. In conclusion, the structure of the power deposition can be roughly classified into the following cases:

Case 1: Small collision frequency ($\nu/\omega < 0.01$): Highly efficient bulk mode conversion occurs. The TG waves are excited by the bulk mode conversion and the surface mode conversion plays crucial roles in the plasma heating. Power deposition is maximized near the MCS for all the wave modes.

Case 2: Moderate collision frequency ($0.01 < \nu/\omega < 0.06$): The bulk mode conversion is not as evident as in case 1, but is still important for the power deposition as the surface mode conversion. The central heating by the helicon wave is most dominant.

Case 3: Large collision frequency ($0.06 < \nu/\omega$): This is the case for typical laboratory experiments. The bulk mode conversion is not dominant. The input helicon wave energy directly dissipates and heats the plasma. The power deposition of the TG wave excited by the surface mode conversion becomes more dominant at the plasma edge as the collision frequency increases.

The bulk mode conversion and the bulk helicon heating are important only when the collision frequency is small (case 1 and 2). However, when the plasma density is high, significant plasma heating may trigger development of a neutral depletion in an actual helicon discharge, and the bulk mode conversion and the bulk helicon heating may become important. Therefore, further arguments of the helicon power deposition should include a non-uniform distribution of the collision frequency due to the neutral depletion and the plasma heating.

CHAPTER IV

Temporal behavior of helicon discharge

In this chapter, we describe the self-consistent discharge model of helicon plasma to simulate the first step of time evolution of the plasma density, electron temperature, and their profiles. The simulation model is based on the experiment of Nisoa *et al.* as shown in Figs. 2.14 and 2.16. The model consists of three parts, a electromagnetic wave fields solver, a power balance solver, and a particle balance solver. The wave fields solver solves Maxwell's equations and linearized electron equation of motion for given plasma parameters by FDTD simulation (Appendix A), and the local collisional power absorption (Joule heating) is calculated from the wave fields. The electron temperature is updated from the energy balance equation, that calculate the electron energy transport with the local power balance between the power absorption and the power losses due to the inelastic collisions (ionization and excitation) and loss energy to the wall. After the electron temperature is updated, the plasma density is updated from the particle balance equation, that includes ionization, recombination, and particle loss to the wall.

4.1 Governing equations

The behavior of the plasma particles in the helicon discharge is complicated in that the charged particles are both affected by external electric field and magnetic

fields and contribute to them. Furthermore, the inter-particle collisions (between the electrons, the ions, and the neutrals) occur in space and time scales that are usually much shorter than those of the applied fields or the fields due to the average motion of the particles. To make progress with such a complicated system, various simplifying approximations are needed [51]. The inter-particle collisions are considered to be independently of the larger scale fields to determine an equilibrium distribution of the charged particle velocities. The velocity distribution is averaged over velocities to obtain the macroscopic motion [51]. The macroscopic motion takes place in external applied fields and in the macroscopic fields generated by the average particle motion. Actually these self-consistent fields are non-linear, but we linearize the motion of charged particle in calculating the wave fields (FDTD calculation). The collisions such as the ionization, recombination, and elastic scattering, are treated as an average friction force between different particles species and energy exchanges among species. In this chapter, we consider the basic equations [97] that govern the plasma medium, concentrating attention on the macroscopic system.

The continuity, momentum, and energy conservation equation for a fluid plasma are obtained from the Boltzmann equation

$$\frac{\partial f}{\partial t} + \boldsymbol{v} \cdot \nabla f + \frac{\boldsymbol{F}}{m} \cdot \nabla_{\boldsymbol{v}} f = \frac{\delta_c f}{\delta t}, \tag{4.1}$$

where f is the distribution function in a phase space and time ($\boldsymbol{r}$, $\boldsymbol{v}$, t) ($\boldsymbol{r}$ is the position coordinates, and $\boldsymbol{v}$ is the velocity coordinates), $\boldsymbol{F}$ is the force which can be written by the Lorentz force $\boldsymbol{F} = q[\boldsymbol{E} + \boldsymbol{v} \times \boldsymbol{B}]$, and $\delta_c f/\delta t$ is a collision operator. Here we shall show the derivation of moment equations of the Boltzmann equation [97]

4.1.1 Zeroth moment

The zeroth moment of the Boltzmann equation 4.1 is obtained by multiplying $v^0 = 1$ and integrate over all of velocity space, V, which gives [97]

$$\int_V \frac{\partial f_s}{\partial t} d^3v + \int_V \boldsymbol{v} \cdot \nabla f_s d^3v + \frac{1}{m_s} \int_V \boldsymbol{F} \cdot \nabla_{\boldsymbol{v}} f_s d^3v = \int_V \frac{\delta_c f_s}{\delta t} d^3v, \tag{4.2}$$

where s is the particle species. The first integral on the left of this equation can be written

$$\int_V \frac{\partial f_s}{\partial t} d^3v = \frac{\partial \int}{\partial t}_V f_s d^3v = \frac{\partial n_s}{\partial t}, \tag{4.3}$$

where n_s is the average number density. Similarly, the second integral on the left can be written

$$\int_V \boldsymbol{v} \cdot \nabla f_s d^3v = \nabla \cdot \int_V \boldsymbol{v} f_s d^3v = \nabla \cdot (n_s \boldsymbol{U}_s), \tag{4.4}$$

where $\boldsymbol{U}_s$ is the average velocity. Noting that $\nabla_{\boldsymbol{v}} \cdot (\boldsymbol{v} \times \boldsymbol{B}) f_s = (\boldsymbol{v} \times \boldsymbol{B}) \cdot \nabla_{biv} f_s$, the third integral on the left can be rewritten

$$\int_V \boldsymbol{F} \cdot \nabla_{\boldsymbol{v}} f_s d^3v = \int_V \nabla_{\boldsymbol{v}} \cdot (\boldsymbol{F} f_s) d^3v = \int_V (\boldsymbol{F} f_s) d\boldsymbol{s}_v = 0, \tag{4.5}$$

where Gauss' theorem is used to convert the volume integral to a surface integral at infinity. The surface integral is assumed to vanish if $f(\boldsymbol{v})$ decays sufficiently rapidly at infinite velocity. The integral on the right side of 4.2 involving the collision term is zero,

$$\int_V \frac{\delta_c f_s}{\delta t} d^3v = \frac{\delta_c n_s}{\delta t} = 0, \tag{4.6}$$

since collisions do not change the density. Combining 4.3-4.6 and adding the particle generation term $P_{\text{generation}}$ (due to the ionization) and the particle loss term P_{loss} (due to the recombination and the wall loss) on the right side, the zeroth moment of the

Boltzmann equation 4.2 yields [97]

$$\frac{\partial n_s}{\partial t} + \nabla \cdot (n_s \boldsymbol{U}_s) = P_{\text{generation}} - P_{\text{loss}}. \tag{4.7}$$

This equation is simply the continuity equation for the sth species.

4.1.2 First moment

The first moment is obtained by multiplying the Boltzmann equation 4.1 by $\boldsymbol{v}$ and integrating over all of velocity space. It is more convenient to multiply by the momentum $m_s\boldsymbol{v}$, which gives [97]

$$m_s \int_V \boldsymbol{v} \frac{\partial f_s}{\partial t} d^3v + m_s \int_V \boldsymbol{v}(\boldsymbol{v} \cdot \nabla f_s) d^3v + \int_V \boldsymbol{v}(\boldsymbol{F} \cdot \nabla_{\boldsymbol{v}} f_s) d^3v = m_s \int_V \boldsymbol{v} \frac{\delta_c f_s}{\delta t} d^3v. \tag{4.8}$$

The first integral on the left of the above equation can be written

$$m_s \int_V \boldsymbol{v} \frac{\partial f_s}{\partial t} d^3v = \frac{\partial}{\partial t} \left[m_s \int_V \boldsymbol{v} \frac{\partial f_s}{\partial t} d^3v \right] = \frac{\partial(}{\partial t} m_s n_s \boldsymbol{U}_s). \tag{4.9}$$

The second integral can be written

$$m_s \int_V \boldsymbol{v}(\boldsymbol{v} \cdot \nabla f_s) d^3v = \nabla \cdot \left[m_s \int_V \boldsymbol{v}\boldsymbol{v} f_s d^3v \right]. \tag{4.10}$$

It is convenient to rewrite the $\boldsymbol{v}\boldsymbol{v}$ tensor by making use of the following identity,

$$\boldsymbol{v}\boldsymbol{v} = (\boldsymbol{v} - \boldsymbol{U}_s)(\boldsymbol{v} - \boldsymbol{U}_s) + \boldsymbol{U}_s\boldsymbol{v} + \boldsymbol{v}\boldsymbol{U}_s - \boldsymbol{U}_s\boldsymbol{U}_s. \tag{4.11}$$

The integral in 4.10 then simplifies to

$$\left[m_s \int_V \boldsymbol{v}\boldsymbol{v} f_s d^3v \right] = m_s \int_V (\boldsymbol{v} - \boldsymbol{U}_s)(\boldsymbol{v} - \boldsymbol{U}_s) f_s d^3v + m_s n_s \boldsymbol{U}_s \boldsymbol{U}_s. \tag{4.12}$$

The first term on the right in the above equation is just the pressure tensor, defined by

$$\boldsymbol{P}_s = \int_V m_s (\boldsymbol{v} - \boldsymbol{U}_s)(\boldsymbol{v} - \boldsymbol{U}_s) f_s d^3v. \tag{4.13}$$

Equation 4.10 then can be rewritten

$$m_s \int_V \boldsymbol{v}(\boldsymbol{v} \cdot \nabla f_s) d^3v = \nabla \cdot \boldsymbol{P}_s + \nabla \cdot (m_s n_s \boldsymbol{U}_s \boldsymbol{U}_s). \tag{4.14}$$

The third integral on the left of 4.8 is of the form

$$\int_V \boldsymbol{v}(\boldsymbol{F} \cdot \nabla_{\boldsymbol{v}} f_s) d^3v = \int_V (v_x \hat{\boldsymbol{x}} + v_y \hat{\boldsymbol{y}} + v_z \hat{\boldsymbol{z}}) \left[\frac{\partial}{\partial v_x}(F_x f_s) + \frac{\partial}{\partial v_z}(F_z f_s) + \frac{\partial}{\partial v_z}(F_z f_s) \right] d^3v, \tag{4.15}$$

where the below fact for the Lorentz force is used,

$$\boldsymbol{F} \cdot \nabla_{\boldsymbol{v}} f_s = \nabla_{\boldsymbol{v}} \cdot (\boldsymbol{F} f_s). \tag{4.16}$$

Of the nine integrals that must be computed, six are of the type

$$\int_V v_y \frac{\partial}{\partial v_z}(F_z f_s) d^3v = \int_{-\infty}^{\infty} \int_{-\infty}^{\infty} dv_x dv_y dv_z \int_{-\infty}^{\infty} \frac{\partial}{\partial v_z}(F_z f_s) dv_z, \tag{4.17}$$

which can be integrated directly to give

$$\int_{-\infty}^{\infty} \frac{\partial}{\partial v_z}(F_z f_s) dv_z = [F_z f_s]_{-\infty}^{\infty}. \tag{4.18}$$

If we assume that f_s goes to zero sufficiently rapidly at infinite velocity, these integrals are all zero. The remaining three integrals are of the type

$$\int_{-\infty}^{\infty}\int_{-\infty}^{\infty} dv_x dv_y \int_{-\infty}^{\infty} dv_z v_z \frac{\partial}{\partial v_z}(F_z f_s), \tag{4.19}$$

which, after integrating by parts once, gives

$$\int_{-\infty}^{\infty} dv_z v_z \frac{\partial}{\partial v_z}(F_z f_s) = [v_z F_z f_s]_{-\infty}^{\infty} - \int_{-\infty}^{\infty} F_z f_s dv_z. \tag{4.20}$$

If we again assume that f_s goes to zero sufficiently rapidly at infinite velocity, the first term on the right is zero. Combining all of these integrals, 4.15 can be written

$$\int_V \boldsymbol{v}(\boldsymbol{F}\cdot\nabla_{\boldsymbol{v}} f_s)d^3v = -\int_V \boldsymbol{F} f_s d^3v. \tag{4.21}$$

After substituting the Lorentz force for $\boldsymbol{F}$ and integrating, the above equation yields the simple result

$$\int_V \boldsymbol{v}(\boldsymbol{F}\cdot\nabla_{\boldsymbol{v}} f_s)d^3v = -e_s n_s(\boldsymbol{E} + \boldsymbol{U}_s \times \boldsymbol{B}). \tag{4.22}$$

Finally, the first moment of the collision term on the right of 4.8 can be written

$$m_s \int_V \boldsymbol{v}\frac{\delta_c f_s}{\delta t} d^3v = \frac{\delta_c \boldsymbol{p}_s}{\delta t}, \tag{4.23}$$

where $\delta_c \boldsymbol{p}_s/\delta t$ is the average rate of change of the momentum per unit volume due to collisions. Using 4.9, 4.14, 4.22, and 4.23, 4.8 becomes

$$\frac{\partial}{\partial t}(m_s n_s \boldsymbol{U}_s) + \nabla\cdot(m_s n_s \boldsymbol{U}_s \boldsymbol{U}_s) = n_s e_s(\boldsymbol{E} + \boldsymbol{U}_s \times \boldsymbol{B}) - \nabla\cdot\boldsymbol{P}_s + \frac{\delta_c \boldsymbol{p}_s}{\delta t}. \tag{4.24}$$

The two terms on the left of this equation can be written in a more useful form by expanding the time derivative and using the identity $\nabla\cdot(\boldsymbol{AB}) = (\nabla\cdot\boldsymbol{A})\boldsymbol{B}+(\boldsymbol{A}\cdot\nabla)\boldsymbol{B}$, which gives

$$\frac{\partial}{\partial t}(m_s n_s \boldsymbol{U}_s) + \nabla\cdot(m_s n_s \boldsymbol{U}_s \boldsymbol{U}_s) = m_s n_s \frac{\partial \boldsymbol{U}_s}{\partial t} + m_s \boldsymbol{U}_s \left[\frac{\partial n_s}{\partial t} + \nabla\cdot(n_s \boldsymbol{U}_s)\right] + m_s n_s (\boldsymbol{U}_s\cdot\nabla)\boldsymbol{U}_s. \tag{4.25}$$

From the continuity equation 4.7, the term in the brackets on the right side of the above equation is seen to be zero. The first moment of the Boltzmann equation then becomes [97]

$$m_s n_s \left[\frac{\partial \boldsymbol{U}_s}{\partial t} + (\boldsymbol{U}_s\cdot\nabla)\boldsymbol{U}_s\right] = n_s e_s(\boldsymbol{E} + \boldsymbol{U}_s\times\boldsymbol{B}) - \nabla\cdot\boldsymbol{P}_s + \frac{\delta_c \boldsymbol{p}_s}{\delta t}. \tag{4.26}$$

Using the ideal gas law, the pressure term in above equation can be written as

$$\boldsymbol{P}_s = P_s = n_s k_B T_s, \tag{4.27}$$

where k_B is the Boltzmann constant. In the Lorentz gas model it is assumed that the plasma particles are scattered by fixed immobile scattering centers. If, in addition, we assume that the scattering is isotropic, the average momentum change per collision is simply $-m_s\boldsymbol{v}$, since the averaged momentum after a collision is zero [97] when the Maxwellian distribution function is assumed. The average drag force per unit volume for a particle is then given by

$$\frac{\delta_c \boldsymbol{p}_s}{\delta t} = -\nu_s m_s n_s \boldsymbol{U}_s. \tag{4.28}$$

Using 4.27 and 4.28, 4.26 can be written as [97]

$$m_s n_s \left[\frac{\partial \boldsymbol{U}_s}{\partial t} + (\boldsymbol{U}_s\cdot\nabla)\boldsymbol{U}_s\right] = n_s e_s(\boldsymbol{E} + \boldsymbol{U}_s\times\boldsymbol{B}) - \nabla P_s - \nu_s m_s n_s \boldsymbol{U}_s. \tag{4.29}$$

4.1.3 Second moment

The second moment is obtained by multiplying the Boltzmann equation by the tensor $\boldsymbol{v}\boldsymbol{v}$ and integrating over all of velocity space. This procedure leads to a symmetric matrix with nine elements only six of which are independent, since the off-diagonal elements of a symmetric matrix are equal to each other. Here we will restrict our discussion to the trace of this matrix, which is obtained by multiplying the Boltzmann equation by the kinetic energy $(1/2)m_s v^2$ and integrating over the velocity space, which gives [97]

$$\frac{m_s}{2}\int_V v^2\frac{\partial f_s}{\partial t}d^3v + \frac{m_s}{2}\int_V v^2(\boldsymbol{v}\cdot\nabla f_s)d^3v + \frac{1}{2}\int_V v^2(\boldsymbol{F}\cdot\nabla_{\boldsymbol{v}} f_s)d^3v = \frac{m_s}{2}\int_V v^2\frac{\delta_c f_s}{\delta t}d^3v. \tag{4.30}$$

The first integral on the left of the above equation can be written

$$\frac{m_s}{2}\int_V v^2\frac{\partial f_s}{\partial t}d^3v = \frac{\partial}{\partial t}\left[\int_V \frac{1}{2}m_s v^2 f_s d^3v\right] = \frac{\partial W_s}{\partial t}, \tag{4.31}$$

where W_s is the kinetic energy density. We assume the Maxwell distribution function

$$f_s = A\exp\left[-\frac{m_s v^2}{2k_B T_s}\right], \tag{4.32}$$

where A is defined as

$$A = n_s\left(\frac{m_s}{2\pi k_B T_s}\right)^{3/2}, \tag{4.33}$$

By replacing $\boldsymbol{v}$ with the combination $\boldsymbol{v} = \boldsymbol{v}_r + \boldsymbol{u}$, where $\boldsymbol{v}_r$ is the random thermal velocity and $\boldsymbol{U}$ is the drift velocity, the total kinetic energy density W_s can be calculated as

$$W_s = \frac{m_s}{2}\int_V |\boldsymbol{v}_r + \boldsymbol{U}|^2\frac{\delta_c f_s}{\delta t}d^3v_r. \tag{4.34}$$

The integration in above equation can be calculated as

$$W_s = \frac{1}{2} n_s m_s U^2 + \frac{3}{2} n_s k_B T_s, \tag{4.35}$$

where we use Gaussian integrals

$$\int_{-\infty}^{\infty} e^{-ax^2} dx = \sqrt{\frac{\pi}{a}}, \quad \int_{-\infty}^{\infty} x e^{-ax^2} dx = 0, \quad and \int_{-\infty}^{\infty} x^2 e^{-ax^2} dx = \sqrt{\frac{\pi}{4a^3}}. \tag{4.36}$$

The second integral in 4.30 can be written

$$\frac{m_s}{2} \int_V v^2 (\boldsymbol{v} \cdot \nabla f_s) d^3 v = \nabla \cdot \left[\int_V \frac{1}{2} m_s \boldsymbol{v} v^2 f_s d^3 v \right] = \nabla \cdot \boldsymbol{Q}_s, \tag{4.37}$$

where

$$\boldsymbol{Q}_s = \int_V \frac{1}{2} m_s \boldsymbol{v} v^2 f_s d^3 v \tag{4.38}$$

is the kinetic energy flux, which can be rewritten by using $\boldsymbol{v}_r$ and $\boldsymbol{U}$ as follows

$$\boldsymbol{Q}_s = \int_V \frac{1}{2} m_s (\boldsymbol{v} + \boldsymbol{U}) |\boldsymbol{v}_r + \boldsymbol{U}|^2 f_s d^3 v_r. \tag{4.39}$$

The integration of this equation can be calculated by using 4.37 as

$$\boldsymbol{Q}_s = \left(\frac{1}{2} n_s m_s \boldsymbol{U}^2 + \frac{5}{2} n_s k_B T_s \right) \boldsymbol{U} + \boldsymbol{q}, \tag{4.40}$$

where $\boldsymbol{q}$ is the heat flux density defined as

$$\boldsymbol{q} = \frac{m_s}{2} \int_{\infty}^{\infty} v_r^2 \boldsymbol{v}_r d^3 v_r. \tag{4.41}$$

This flux is carried by particles of a given species and represents the transport energy associated with the random thermal motion. The third integral in 4.30 can be simplified by integrating by parts which, after discarding the contribution at infinite velocity, gives

$$\frac{1}{2}\int_V v^2(\boldsymbol{F}\cdot\nabla_{\boldsymbol{v}} f_s)d^3v = -\frac{1}{2}\int_V f_s(\boldsymbol{F}\cdot\nabla_{\boldsymbol{v}} v^2)d^3v. \tag{4.42}$$

Introducing the Lorentz force and noting that $\nabla_{\boldsymbol{v}} v^2 = 2\boldsymbol{v}$, and that $\boldsymbol{v}\cdot(\boldsymbol{v}\times\boldsymbol{B}) = 0$, the integral on the right side of the above equation can be written

$$\frac{1}{2}\int_V v^2(\boldsymbol{F}\cdot\nabla_{\boldsymbol{v}} f_s)d^3v = -e_s\boldsymbol{E}\cdot\int_V \boldsymbol{v} f_s = -\boldsymbol{E}\cdot(n_s e_s \boldsymbol{U}_s) = -\boldsymbol{E}\cdot\boldsymbol{J}_s, \tag{4.43}$$

where $\boldsymbol{J}_s$ is the current contributed by the species s. Using 4.31, 4.35, 4.37, 4.40, and 4.43, the second moment of the Boltzmann equation becomes

$$\begin{aligned}\frac{\partial}{\partial t}\left(\frac{3}{2}n_s k_B T_s + \frac{1}{2}n_s m_s U_s^2\right) + \nabla\cdot\left[\left(\frac{1}{2}n_s m_s \boldsymbol{U}_s^2 + \frac{5}{2}n_s k_B T_s\right)\boldsymbol{U}_s + \boldsymbol{q}\right] \\ - \boldsymbol{E}\cdot\boldsymbol{J}_s = \frac{m_s}{2}\int_V v^2\frac{\delta_c f_s}{\delta t}d^3v.\end{aligned} \tag{4.44}$$

It is convenient to eliminate the kinetic energy from above equation by means of the continuity 4.7 and the equation of motion 4.29, finally we obtain an equation for the transport of internal energy, or the heat balance equation [97]:

$$\frac{\partial}{\partial t}\left(\frac{3}{2}P_s\right) + \nabla\cdot\frac{3}{2}(P_s\boldsymbol{U}_s) + P_s\nabla\cdot\boldsymbol{U}_s + \nabla\cdot\boldsymbol{q} = \frac{m_s}{2}\int_V v^2\frac{\delta_c f_s}{\delta t}d^3v. \tag{4.45}$$

Here $\frac{3}{2}P_s = \frac{3}{2}n_s k_B T_s$ is the thermal energy density, $\frac{3}{2}P_s\boldsymbol{U}_s$ is the macroscopic thermal energy flux, representing the flow of the thermal energy density at the fluid velocity $\boldsymbol{U}_s$, $P_s\nabla\cdot\boldsymbol{U}_s$ gives the heating or cooling of the fluid due to the compression or expansion of its volume, and collisional term includes all collisional process that change the thermal energy density. These include ionization, excitation, elastic scattering,

and frictional (ohmic) heating. The equation is usually closed by letting $\boldsymbol{q} = -\kappa\nabla T$, where κ is the thermal conductivity.

4.2 Modeling particle and energy balances

The excited wave fields are dissipated by the collisions of electrons, and the power absorption by the helicon wave and the TG wave (mainly by the TG wave) are calculated from these wave fields profiles as the local ohmic heating as shown in the previous chapter (Fig. 3.7). This calculated power absorption is substituted in the energy balance equation 4.45, which also includes the power loss due to the elastic and inelastic (ionization and excitation) collisions, and particle loss toward the wall. Since the energy exchange between electrons and ions are small because of the small mass ratio, and electron-electron collisions are enough frequent that its distribution function relaxes to local Maxwellian in high-density helicon plasma, it is reasonable to describe the energy balance of helicon discharge by the energy equation of electrons with a single electron temperature if the external field effect is small. In the energy balance equation, the local electron temperature is calculated in each time.

The motions of the background charged particles are solved by the momentum equation 4.26 separately from those of the wave fields (the coherent motions of charged particles with applied external electromagnetic fields). In our calculation, two types of model are used for this calculation. As the first approach, we assume that the charge neutrality is always conserved and the electron and ion fluxes are equal at any plasma region. This assumption can be made in the highly collisional regime, in which we neglect the acceleration (the first term on the left) and inertial force (the second term on the left) on the momentum equation 4.26 both of electron and ion (this assumption is called the drift-diffusion approximation). In this regime, electrons motion, which is much faster than that of ions due to the small mass, is restricted by an electric field that spring up to maintain the local flux balances. Therefore, we

can treat the motion of the charged particle as an ambipolar diffusion by combining the momentum equation and the continuity equation in this regime [51]. Since the background magnetic field is applied along the axial direction in the helicon discharge system, the charge particles are highly magnetized, and thus charged particles can not diffuse easily across the magnetic field (in the radial direction). As a second approach, we evaluate the validity of above assumptions (drift-diffusion approximation), and consider the more realistic model. Actually, in the helicon discharge system and in many situations of another discharge system, we can not ignore the acceleration and inertial terms with respect to the ions momentum equation, but we can ignore the electrons ones. Therefore, we solve the drift-diffusion approximated momentum equation for electron and full momentum equation for ion. The continuity equations for electron and ion are solved and the densities of the ion and electron are updated separately.

4.2.1 Ambipolar diffusion model

The ambipolar diffusion model discussed in this section uses the simplifying assumption that the local charge neutrality holds anywhere in the plasma region, thus we can describe the bulk plasma motion by using the simple diffusion equation with the sheath boundary conditions. In more realistic model, the sheath formation should be included self-consistently. Especially in the bounded magnetized plasma, the wall losses of the electrons and ions should be treated separately with no local ambipolarity assumptions, since the ions diffuse to the transverse walls (due to their large Larmor radii) while electrons are preferentially lost to the axial walls (due to their large thermal speed) [86]. The motions of charged particles are described by using the momentum equation 4.26 as follows,

$$m_s n_s \left[\frac{\partial \boldsymbol{u}_s}{\partial t} + (\boldsymbol{u}_s \cdot \nabla) \boldsymbol{u}_s \right] = n_s e_s (\boldsymbol{E} + \boldsymbol{u}_s \times \boldsymbol{B}_0) - \nabla p - m_s n_s \nu_s \boldsymbol{u}_s, \qquad (4.46)$$

where $s = e$ and i for electrons and ions, respectively, ν_s is the momentum transfer collision frequency of sth species, the second term of the right hand side is originated from the divergence of the pressure tensor, that is used by an isotropic version when collisions maintain an isotropic velocity distribution. In a following highly collisional regime,

$$\frac{\partial}{\partial t} << \nu_j, \quad \text{and} \quad \nabla u_j << \nu_j, \tag{4.47}$$

are assumed to be satisfied. In this regime, the momentum equation can be written as the drift-diffusion, and then the acceleration (the first term) and the inertial force (the second term) terms on the left in 4.46 are neglected, and 4.46 is written for ion and electron as

$$n_i e\left(\boldsymbol{E} + \boldsymbol{u}_i \times \boldsymbol{B}_0\right) - \nabla p - m_i n_i \nu_i \boldsymbol{u}_i = 0, \quad \text{for ion} \tag{4.48}$$

and

$$-n_e e\left(\boldsymbol{E} + \boldsymbol{u}_e \times \boldsymbol{B}_0\right) - \nabla p - m_e n_e \nu_e \boldsymbol{u}_e = 0, \quad \text{for electron} \tag{4.49}$$

respectively, where B_0 is the back ground magnetic field applied along the axial direction, and the zeroth-order terms of electromagnetic fields and fluid velocity are assumed to be dominant, thus the higher order terms are ignored. Using 4.27, and solving 4.48 and 4.49 with respect to $\boldsymbol{u}_\perp$ (the index $\perp$ means the perpendicular direction with respect to the back ground magnetic field), we obtain

$$\boldsymbol{u}_{i,\perp} = \mu_{i,\perp}\boldsymbol{E} - D_{i,\perp}\frac{\nabla n_i}{n_i} + \frac{\boldsymbol{u}_{i,E} + \boldsymbol{u}_{i,D}}{1 + (\nu_i/\omega_{ci})^2}, \quad \text{for ion} \tag{4.50}$$

and

$$\boldsymbol{u}_{e,\perp} = -\mu_{e,\perp}\boldsymbol{E} - D_{e,\perp}\frac{\nabla n_e}{n_e} + \frac{\boldsymbol{u}_{e,E} + \boldsymbol{u}_{e,D}}{1 + (\nu_e/\omega_{ce})^2}, \quad \text{for electron} \tag{4.51}$$

where the perpendicular mobility $\mu_{s,\perp}$ and the perpendicular diffusion coefficient $D_{s,\perp}$ are defied as,

$$\mu_{s,\perp} = \frac{\mu_s}{1+(\omega_{cs}/\nu_s)^2}, \quad D_{s,\perp} = \frac{D_s}{1+(\omega_{cs}/\nu_s)^2}, \tag{4.52}$$

$$\mu = \frac{|e_s|}{m_s}\nu_s, \quad \text{and} \quad D = k_B T_s/m_s\nu_s. \tag{4.53}$$

Here $\boldsymbol{u}_{j,E}$, and $\boldsymbol{u}_{j,D}$ are the $E \times B$ drift and the diamagnetic drift velocities that are perpendicular to the field and the gradients:

$$\boldsymbol{u}_{j,E} = \frac{\boldsymbol{E}\times\boldsymbol{B}}{B_0^2}, \quad \boldsymbol{u}_{j,D} = -\frac{kT_j}{q{B_0}^2}\frac{\nabla n_j \times \boldsymbol{B}_0}{n_j}. \tag{4.54}$$

As shown in 4.51, the $E \times B$ drift and the diamagnetic drift are slowed by collisions. In some plasma discharges, these drift terms can be important because they can lead to instabilities with a resulting anomalous transport and they can also lead to large current flows. In our model, for simplicity, we omit the nonlinear $E \times B$ drift term and the diamagnetic drift term from 4.54. However, since there is a possibility that these drift terms would improve the perpendicular diffusion so as to transport the density more rapidly than the usual diffusion [98], and the centrally peaked density profile could be explained, our model should be improved to include these drift terms in a future work. Using the assumption of the charge neutrality ($n_e = n_i = n$) and the flux equality ($\Gamma_{e,\perp} = \Gamma_{i,\perp}$) among electrons ($\Gamma_{e,\perp} = n_e \boldsymbol{u}_{e,\perp}$) and ions ($\Gamma_{i,\perp} = n_i \boldsymbol{u}_{i,\perp}$), we obtain

$$\mu_{i,\perp} n\boldsymbol{E} - D_{i,\perp}\nabla n = \mu_{e,\perp} n\boldsymbol{E} - D_{e,\perp}\nabla n, \tag{4.55}$$

and this equation can be solved for $\boldsymbol{E}$ in terms of ∇n, we obtain the cross-field ambipolar electric field $\boldsymbol{E}_{a,\perp}$ as

$$\boldsymbol{E}_{a,\perp} = \frac{D_{i,\perp} - D_{e,\perp}}{\mu_{i,\perp} - \mu_{e,\perp}}\frac{\nabla n}{n}. \tag{4.56}$$

Substituting this equation into following the common flux equation,

$$\mu_{s,\perp} n \boldsymbol{E}_{a,\perp} - D_{s,\perp} \nabla n, \quad \text{for electron and ion} \tag{4.57}$$

we obtain

$$\Gamma_\perp = -\frac{\mu_{i,\perp} D_{e,\perp} + \mu_{e,\perp} D_{i,\perp}}{\mu_{i,\perp} + \mu_{e,\perp}} \nabla n. \tag{4.58}$$

The coefficient of the cross-field ambipolar diffusion is introduced as

$$D_{a,\perp} = \frac{\mu_{i,\perp} D_{e,\perp} + \mu_{e,\perp} D_{i,\perp}}{\mu_{i,\perp} + \mu_{e,\perp}}. \tag{4.59}$$

where we assume that plasma can be lost only across the magnetic field. However the assumption that the diffusion takes place only across the magnetic field is generally not satisfied. Even for a finite length system in which l (along B_0) $>> d$ (across B_0), the more rapid diffusion along B_0 is usually important. When we consider the two-dimensional model on $(x-z)$ plane, the following equations should be combined,

$$\frac{\partial n}{\partial t} = D_e \frac{\partial^2 n}{\partial z^2} + \mu_e \frac{\partial}{\partial z}(nE_z) + D_{\perp e} \frac{\partial^2}{\partial x^2} + \mu_{\perp e} \frac{\partial}{\partial x}(nE_x), \tag{4.60}$$

and

$$\frac{\partial n}{\partial t} = D_i \frac{\partial^2 n}{\partial z^2} - \mu_i \frac{\partial}{\partial z}(nE_z) + D_{\perp i} \frac{\partial^2}{\partial x^2} - \mu_{\perp i} \frac{\partial}{\partial x}(nE_x), \tag{4.61}$$

these equation are obtained from the continuity equation for electrons and ions. Exact two-dimensional solutions to these two coupled nonlinear diffusion equations have not been obtained. If we consider the limiting case $E_x d < T_i$ and T_e, where E_x is the electrostatic field generated in the bulk plasma region (except the sheath region), we can drop the perpendicular mobility terms in 4.60 and 4.61 [51]. Multiplying 4.60 by

μ_i and 4.61 by μ_e and adding the two equations, we obtain

$$\frac{\partial n}{\partial t} = \frac{\mu_i D_e + \mu_e D_i}{\mu_i + \mu_e}\frac{\partial^2 n}{\partial z^2} + \frac{\mu_i D_{\perp e} + \mu_e D_{\perp i}}{\mu_i + \mu_e}\frac{\partial^2 n}{\partial x^2}. \tag{4.62}$$

Thus, the ambipolar coefficients are

$$D_{\parallel a} = \frac{\mu_i D_e + \mu_e D_i}{\mu_i + \mu_e}, \tag{4.63}$$

parallel to the field, and

$$D_{\perp a} = \frac{\mu_i D_{\perp e} + \mu_e D_{\perp i}}{\mu_i + \mu_e}, \tag{4.64}$$

perpendicular field. Using these coefficients, finally we obtain the particle balance equation as follows

$$\frac{\partial n}{\partial t} = D_{\parallel a}\nabla_{\parallel}^2 n + D_{\perp a}\nabla_{\perp}^2 n + G - L. \tag{4.65}$$

In the right side of above equation, G and L represent the volume source and sink respectively, that are given by ionization rate ($\alpha_{\rm iz}$) and recombination rate ($\alpha_{\rm rec}$) as follows,

$$G = \alpha_{\rm iz} n_g n, \quad \text{and} \quad L = \alpha_{\rm rec} n_g n. \tag{4.66}$$

where n_g is the back ground neutral density. Since the particle loss due to the recombination is usually much smaller than that due to the particle loss to the wall, the following loss term at the boundary affects on the above particle balance equation dominantly,

$$L\,|_{r=a} = L_{r,\rm wall}, \quad at\ \ r = a\ (\text{:Insulating wall}) \tag{4.67}$$

and

$$L\,|_{z=\pm\frac{L_z}{2}} = L_{z,\rm wall}, \quad at\ \ z = \pm\frac{L_z}{2}\ (\text{:Conducting wall}) \tag{4.68}$$

where $L_{r,\rm wall}$ and $L_{z,\rm wall}$ are given by the average particle flux toward the sheath boundary as shown in the next section.

4.2.2 Full fluid model

The validity of the drift-diffusion approximation is reconsidered in this section. Crude estimations of the ion inertial term to the drift and diffusion terms are

$$\frac{m_i n_i \boldsymbol{u}_i \cdot \nabla \boldsymbol{u}_i}{e n_i \boldsymbol{E}} \sim \frac{m_i u_B^2}{e V_s} \sim O(0.1), \tag{4.69}$$

$$\frac{m_i n_i \boldsymbol{u}_i \cdot \nabla \boldsymbol{u}_i}{T_i \nabla n_i} \sim \frac{m_i u_B^2}{T_i} >> 1, \tag{4.70}$$

where V_s is the pre-sheath voltage drop and $u_B = (k_B T_e/m_i)^{1/2}$ is the Bohm velocity (ions are accelerated up to this velocity in the pre-sheath region). For example, a rough estimation for $T_e = 3.0$ [eV] and $T_i = 0.026$ [eV] Ar discharge gives $u_B \sim 1.5 \times 10^3$ [m/s], $eV_s = 14$ [eV] which results in $m_i u_B^2/(eV_s) \sim 0.2 \sim O(0.1)$ and $m_i u_B^2/T_i \sim 38 >> 1$. These results show that the ion inertial term can be comparable to the drift term and is larger than diffusion term. Similarly, rough estimations for electrons are

$$\frac{m_e n_e \boldsymbol{u}_e \cdot \nabla \boldsymbol{u}_e}{e n_e \boldsymbol{E}} \sim \frac{m_e u_B^2}{e V_s} << 1, \tag{4.71}$$

$$\frac{m_e n_e \boldsymbol{u}_e \cdot \nabla \boldsymbol{u}_e}{T_e \nabla n_e} \sim \frac{m_e u_B^2}{T_e} << 1. \tag{4.72}$$

We can easily check that the inertial term in the electron momentum equation can always be neglected in the usual discharge conditions, for example, using the same parameters with the discussion for ions, $m_e u_B^2/(eV_s) \sim 2.9 \times 10^{-6} << 1$ and $m_i u_B^2/T_i \sim 1.4 \times 10^{-5} << 1$. Therefore, we can apply the drift-diffusion approximation for electrons momentum equation, while the full momentum equation is solved for ions as follows

$$m_i n_i \left[\frac{\partial \boldsymbol{u}_i}{\partial t} + (\boldsymbol{u}_i \cdot \nabla)\, \boldsymbol{u}_i \right] = e\,(\boldsymbol{E} + \boldsymbol{u}_i \times \boldsymbol{B}_0) - \nabla p - m_i n_i \nu_i \boldsymbol{u}_i, \quad \text{for ion} \tag{4.73}$$

and

$$n_e \boldsymbol{u}_e = \boldsymbol{\Gamma}_e = -\frac{n_e e}{m_e}\boldsymbol{E} - \frac{e}{m_e}\boldsymbol{\Gamma}_{\perp,e} \times B_0 - \nabla(\frac{n_e k_B T_e}{m_e}). \text{ for electron} \tag{4.74}$$

4.2.3 Energy balance equation

From 4.45 the energy balance equation for electron is written as follows

$$\frac{\partial}{\partial t}\left(\frac{3}{2}p_e\right) + \nabla \cdot \mathbf{q}_e = -\boldsymbol{\Gamma}_e \cdot \boldsymbol{E} - \frac{3m_e}{m_i}\nu_{en} n_e k_B (T_e - T_n) + P_{\text{abs}} - P_{\text{loss}}, \tag{4.75}$$

where P_{abs} is the power absorption, calculated by the Ohmic heating of wave fields:

$$\begin{aligned} P_{\text{abs}} &= \text{Re}[\boldsymbol{E} \cdot \boldsymbol{J}] \\ &= \frac{\omega\varepsilon_0}{2}\text{Im}\left\{S\left(|\delta E_r|^2 + |\delta E_\theta|^2\right) + P|\delta E_z|^2\right\}, \end{aligned} \tag{4.76}$$

where δ represents the perturbation of electromagnetic wave fields. The first term of 4.75 is the Joule heating due to the ambipolar electric field, and the second term is the energy loss due to the elastic collision between electron and neutral (ν_{en} is the elastic collision frequency and T_n is the temperature of neutral particles). P_{loss} is the power loss mainly by inelastic collisions between electrons and neutrals, which is given by

$$P_{\text{loss}} = n_{\text{g}} n_{\text{e}} \left(\alpha_{\text{iz}}\epsilon_{\text{iz}} + \alpha_{\text{ex}}\epsilon_{\text{ex}}\right), \tag{4.77}$$

where ϵ_{iz} and ϵ_{ex} are the corresponding energy losses per one electron-ion pair is created and excitation of one neutral occurs respectively. For Ar, these values are $\epsilon_{\text{iz}} = 15.76$ [eV] and $\epsilon_{\text{ex}} = 12.14$ [eV]. One can notice that the second and third terms in 4.45 are included in $\boldsymbol{q}$ as

$$\boldsymbol{q}_e = \frac{5}{2}\boldsymbol{\Gamma}_e k_B T_e - \kappa \nabla T_e, \tag{4.78}$$

where the thermal conductivity κ is given by

$$\kappa_{\parallel} = \frac{5}{2} n_e k_B D_e = \frac{5}{2} \frac{p_e}{m_e \nu_e}, \quad \text{for parallel direction} \tag{4.79}$$

and

$$\kappa_{\perp} = \frac{\kappa_{\parallel}}{1 + (\omega_{ce}/\nu_e)^2}, \quad \text{for perpendicular direction} \tag{4.80}$$

in the full fluid model, and

$$\kappa_{a,\parallel} = \frac{5}{2} n_e k_B D_{a,\parallel}, \quad \text{for parallel direction} \tag{4.81}$$

and

$$\kappa_{a,\perp} = \frac{\kappa_{a,\parallel}}{1 + (\omega_{ce}/\nu_e)^2}, \quad \text{for perpendicular direction} \tag{4.82}$$

in the ambipolar diffusion model. Since $\omega_{ce}/\nu_e >> 1$ for a typical helicon discharge, the thermal energy flux also can not be transported in the perpendicular direction i.e. $\kappa_{\parallel} >> \kappa_{\perp}$. The electron fluid velocity is typically much smaller than the electron thermal velocity $v_{th,e}$, thus the first term on the right side of 4.78 can be negligible compared to the second term. This first term is included in the full fluid model, while not included in the ambipolar diffusion model.

4.2.4 Spatial discretization of full fluid model

The development of numerical methods to simulate processing plasmas has been ongoing for over three decades. Prior to 1990, simulations were typically one dimensional [99,100], either with a fluid model or a particle model of the plasma since then, two-dimensional and three-dimensional simulations with detailed chemistry have been developed [101]. Nitschke and Graves developed a one-dimensional fluid model for a helium discharge growth [102]. They compared results from particle and fluid simulations for the same mode based on helium. They found that the two methods agree

well for pressures greater than or equal to 100 [mTorr]. The discrete equations are derived using the finite volume method, and the up-winding method is commonly used for spatial discretization of the electron flux [103]. These equations are written by using the grid number j for the r direction and k for the z direction, and spatial grid size Δr and Δz, as follows:

Ion continuity

$$\begin{aligned}\frac{dn_{i(j,k)}}{dt} =& -\frac{1}{\Delta r}\left[\left(\frac{n_{i(j,k)}+n_{i(j+1,k)}}{2}\right)u_{ir(j+1/2,k)} - \left(\frac{n_{i(j-1,k)}+n_{i(j,k)}}{2}\right)u_{ir(j-1/2,k)}\right] \\ & -\frac{1}{2r}\left[\left(\frac{n_{i(j,k)}+n_{i(j+1,k)}}{2}\right)u_{ir(j+1/2,k)} + \left(\frac{n_{i(j-1,k)}+n_{i(j,k)}}{2}\right)u_{ir(j-1/2,k)}\right] \\ & -\frac{1}{\Delta z}\left[\left(\frac{n_{i(j,k)}+n_{i(j,k+1)}}{2}\right)u_{iz(j,k+1/2)} - \left(\frac{n_{i(j,k-1)}+n_{i(j,k)}}{2}\right)u_{iz(j,k-1/2)}\right] \\ & +\alpha_{iz}n_g n_e - \alpha_{rec}n_g n_e.\end{aligned} \tag{4.83}$$

Ion momentum

$$\begin{aligned}\frac{du_{ir(j+1/2,k+1/2)}}{dt} =& -\frac{u_{ir(j+1/2,k+1/2)}}{2\Delta r}\left(u_{ir(j+3/2,k+1/2)} - u_{ir(j-1/2,k+1/2)}\right) \\ & -\frac{u_{iz(j+1/2,k+1/2)}}{2\Delta z}\left(u_{ir(j+1/2,k+3/2)} - u_{ir(j+1/2,k-1/2)}\right) + \frac{u^2_{i\theta(j+1/2,k+1/2)}}{r} \\ & +\frac{e}{m_i}E_{r(j+1/2,k+1/2)} + \omega_{ci}u^2_{i\theta(j+1/2,k+1/2)} - \nu_i u_{ir(j+1/2,k+1/2)},\end{aligned} \tag{4.84}$$

$$\begin{aligned}\frac{du_{i\theta(j+1/2,k+1/2)}}{dt} =& -\frac{u_{ir(j+1/2,k+1/2)}}{2\Delta r}\left(u_{i\theta(j+3/2,k+1/2)} - u_{i\theta(j-1/2,k+1/2)}\right) \\ & -\frac{u_{iz(j+1/2,k+1/2)}}{2\Delta z}\left(u_{i\theta(j+1/2,k+3/2)} - u_{i\theta(j+1/2,k-1/2)}\right) \\ & +\frac{u_{i\theta(j+1/2,k+1/2)}u_{ir(j+1/2,k+1/2)}}{r} \\ & -\omega_{ci}u_{ir(j+1/2,k+1/2)} - \nu_i u_{i\theta(j+1/2,k+1/2)},\end{aligned} \tag{4.85}$$

and

$$\begin{aligned}\frac{du_{iz(j+1/2,k+1/2)}}{dt} =& -\frac{u_{ir(j+1/2,k+1/2)}}{2\Delta r}\left(u_{iz(j+3/2,k+1/2)} - u_{iz(j-1/2,k+1/2)}\right) \\ &-\frac{u_{iz(j+1/2,k+1/2)}}{2\Delta z}\left(u_{iz(j+1/2,k+3/2)} - u_{iz(j+1/2,k-1/2)}\right) \\ &+\frac{e}{m_i}E_{z(j+1/2,k+1/2)} - \nu_i u_{iz(j+1/2,k+1/2)}.\end{aligned} \tag{4.86}$$

Electron continuity

$$\begin{aligned}\frac{dn_{e(j,k)}}{dt} =& -\frac{1}{\Delta r}\left(\Gamma_{r(j+1/2,k+1/2)} - \Gamma_{r(j-1/2,k+1/2)}\right) \\ &-\frac{1}{2r}\left(\Gamma_{r(j+1/2,k+1/2)} + \Gamma_{r(j-1/2,k+1/2)}\right) \\ &-\frac{1}{\Delta z}\left(\Gamma_{z(j+1/2,k+1/2)} - \Gamma_{z(j+1/2,k-1/2)}\right) \\ &+\alpha_{iz} n_g n_e - \alpha_{rec} n_g n_e.\end{aligned} \tag{4.87}$$

Electron energy

$$\begin{aligned}\frac{3}{2}\frac{d(n_e T_e)_{(j,k)}}{dt} =& -\frac{1}{\Delta r}\left(q_{er(j+1/2,k+1/2)} - q_{er(j-1/2,k+1/2)}\right) \\ &-\frac{1}{2r}\left(q_{er(j+1/2,k+1/2)} + q_{er(j-1/2,k+1/2)}\right) \\ &-\frac{1}{\Delta z}\left(q_{ez(j+1/2,k+1/2)} - q_{ez(j+1/2,k-1/2)}\right) \\ &-\frac{e}{2}\left(\Gamma_{er(j-1/2,k+1/2)}E_{r(j-1/2,k+1/2)} + \Gamma_{er(j+1/2,k+1/2)}E_{r(j+1/2,k+1/2)}\right) \\ &-\frac{e}{2}\left(\Gamma_{ez(j+1/2,k-1/2)}E_{z(j+1/2,k-1/2)} + \Gamma_{ez(j+1/2,k+1/2)}E_{z(j+1/2,k+1/2)}\right) \\ &-\frac{3m_e}{m_i}n_{e(j,k)}\nu_{en}k_B\left(T_{e(i,j)} - T_n\right) \\ &+P_{abs(j,k)} - P_{loss(j,k)}.\end{aligned} \tag{4.88}$$

The electron fluxes are discretized by using up-winding scheme as follows when

$E_r < 0$,

$$\Gamma_{er(j+1/2,k+1/2)} = -\frac{1}{m_e\nu_e[1+(\omega_{ce}/\nu_e)^2]}\left[n_{e(j,k)}eE_{r(j+1/2,k+1/2)} + \frac{k_B}{\Delta r}\left(n_eT_{e(j+1,k)} - n_eT_{e(j,k)}\right)\right], \tag{4.89}$$

when $E_r > 0$,

$$\Gamma_{er(j+1/2,k+1/2)} = -\frac{1}{m_e\nu_e[1+(\omega_{ce}/\nu_e)^2]}\left[n_{e(j+1,k)}eE_{r(j+1/2,k+1/2)} + \frac{k_B}{\Delta r}\left(n_eT_{e(j+1,k)} - n_eT_{e(j,k)}\right)\right] \tag{4.90}$$

when $E_z < 0$,

$$\Gamma_{ez(j+1/2,k+1/2)} = -\frac{1}{m_e\nu_e[1+(\omega_{ce}/\nu_e)^2]}\left[n_{e(j,k)}eE_{z(j+1/2,k+1/2)} + \frac{k_B}{\Delta z}\left(n_eT_{e(j,k+1)} - n_eT_{e(j,k)}\right)\right], \tag{4.91}$$

and when $E_z > 0$,

$$\Gamma_{ez(j+1/2,k+1/2)} = -\frac{1}{m_e\nu_e[1+(\omega_{ce}/\nu_e)^2]}\left[n_{e(j,k+1)}eE_{z(j+1/2,k+1/2)} + \frac{k_B}{\Delta z}\left(n_eT_{e(j,k+1)} - n_eT_{e(j,k)}\right)\right] \tag{4.92}$$

The heat fluxes are given as follows

$$\begin{aligned} q_{er(j+1/2,k+1/2)} =& \frac{5}{2}\Gamma_{er(j+1/2,k+1/2)}\left(\frac{T_{e(j,k)}+T_{e(j+1,k)}}{2}\right) \\ &- \frac{5k_B^2}{2m_e\nu_e}\left(\frac{n_eT_{e(j,k)}+n_eT_{e(j+1,k)}}{2}\right)\left(\frac{n_eT_{e(j+1,k)}-n_eT_{e(j,k)}}{\Delta r}\right), \end{aligned} \tag{4.93}$$

and

$$\begin{aligned} q_{ez(j+1/2,k+1/2)} =& \frac{5}{2}\Gamma_{ez(j+1/2,k+1/2)}\left(\frac{T_{e(j,k)}+T_{e(j,k+1)}}{2}\right) \\ &- \frac{5k_B^2}{2m_e\nu_e}\left(\frac{n_eT_{e(j,k)}+n_eT_{e(j,k+1)}}{2}\right)\left(\frac{n_eT_{e(j,k+1)}-n_eT_{e(j,k)}}{\Delta z}\right). \end{aligned} \tag{4.94}$$

Poisson equation

The Poisson equation is discretized by using the central difference calculus as follows

$$\begin{aligned} &\frac{\Phi_{(j-1,k)} - 2\Phi_{(j,k)} + \Phi_{(j+1,k)}}{\Delta r^2} + \frac{\Phi_{(j+1,k)} - \Phi_{(j-1,k)}}{r2\Delta r} \\ &\frac{\Phi_{(j,k-1)} - 2\Phi_{(j,k)} + \Phi_{(j,k+1)}}{\Delta z^2} = -\frac{\rho_{(j,k)}}{\epsilon_0}, \end{aligned} \tag{4.95}$$

this equation is calculated by using the SOR (Successive Over-Relaxation) method, and the ambipolar electric fields are obtained as

$$E_{r(j+1/2,k+1/2)} = -\frac{\Phi_{(j+1,k)} - \Phi_{(j,k)}}{\Delta r},\ E_{z(j+1/2,k+1/2)} = -\frac{\Phi_{(j,k+1)} - \Phi_{(j,k)}}{2\Delta z}. \tag{4.96}$$

The strong coupling which exists between the calculation of the potential and the electron density in the fluid simulation can lead to numerical instabilities when 4.87, 4.89-4.92, and 4.95 are solved independently (i.e., explicitly) using a numerical time step greater then relaxation time τ_d [102]:

$$\tau_d = \frac{\nu_e}{\omega_{pe}^2}. \tag{4.97}$$

Since this time step limitation is much smaller than other general Courant conditions $(\Delta r/v)$, above equations should be solved implicitly in time by using some implicit methods such as Euler method, the second-order Runge-Kutta method [104], or other methods. However, since we have not yet introduced such a implicit method in our simulation model, we proceeded the time integration of above equations by taking the tiny time step which satisfies 4.97 to avoid numerical instabilities.

4.3 Boundary condition

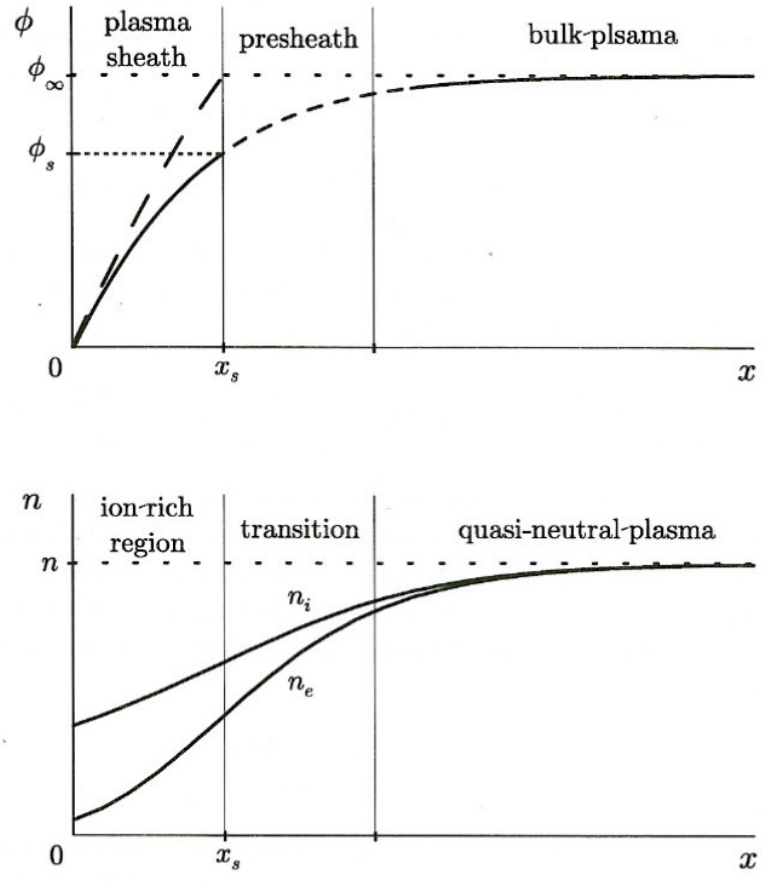

Figure 4.1: Behavior of the electrostatic potential and electron and ion densities in the sheath, presheath (or transition) and bulk plasma regions of a plasma in contact with a grounded wall [105].

When a grounded object $V = 0$ [V] is inserted in an electro-positive plasma, consisting of equal numbers of positive ions and electrons, the electrons that are far more mobile than ions are lost faster than ions toward the wall. The plasma will therefore charge positively with respect to a grounded wall. The non-neutral potential region between the plasma and the wall is called a sheath. In a weakly ionized plasma, the energy to sustain the plasma is dominantly heating of the electrons by the RF source, while the ions are at rest near equilibrium with back ground gas. The electron temperature is then typically of few volts, while ions are cold. In this situation we

may think of mono-energetic ions being accelerated through the sheath potential, while the electron density decreases according to the Boltzmann factor. The electron density would then decay on the order of a Debye length λ_{De}, to shield the electrons from the wall. In a steady state, the loss rate of the electrons and ions must be equal so that the plasma can be quasi-neutral. Therefore, a plasma in contact with a grounded wall will charge up positively, and be quasi-neutral throughout most of the plasma, but have a positively charged plasma sheath region near the wall. Figure 4.1 shows the conceptual geometry of a one-dimensional sheath [105]. The potential drop Φ_∞ $(= V_s)$ between the bulk plasma and the grounded wall in Fig. 4.1 can be obtained from the flux balance condition between the electrons and ions. The flux of ions to the wall is given by

$$\Gamma_i = n_i u_B \tag{4.98}$$

where u_B is well known as the Bohm velocity, that is the minimum velocity, satisfying the Bohm criterion:

$$u_i \geq u_B. \tag{4.99}$$

The Bohm sheath criterion implies that ions must enter the sheath region sufficiently rapidly to compensate for the electron charge leakage through the sheath to the wall. Therefore, to give the ions the directed velocity u_B, there must be a finite electric field in the plasma over some region, typically much wider than the sheath, called the presheath. At the sheath-presheath interface there is a transition from subsonic $(u_i < u_B)$ to supersonic $(u_i > u_B)$ ion flow, where the condition of charge neutrality must break down. The electrons flux, which flows toward the wall is given by

$$\Gamma_e = \frac{1}{4} n_e \bar{u_e} \exp\left(-\frac{\Phi_\infty}{T_e}\right), \tag{4.100}$$

where $\bar{u_e} = (8k_B T_e/\pi m_e)^{1/2}$ is a averaged velocity over the Maxwellian. The rough estimation of the potential drop Φ_∞ is obtained by equating 4.99 and 4.100 with

common density ($n_i = n_e = n_\infty$) at the presheath edge as follows

$$\left(\frac{k_B T_e}{m_i}\right)^{1/2} = \frac{1}{4}\bar{u_e}\exp\left(-\frac{\Phi_\infty}{T_e}\right). \tag{4.101}$$

From above equation, Φ_∞ is obtained as

$$\Phi_\infty = -T_e \ln\left(\frac{m_i}{2\pi m_e}\right)^{1/2}, \tag{4.102}$$

or $\Phi_\infty = 4.7\, T_e$ for Argon. In this estimation, we assume that there are no significant voltages applied across the sheath, then for an insulating wall. At an undriven conducting wall, the fluxes need not balance, although the integrated fluxes (particle currents) must be balance. However, if the fluxes are not too dissimilar, then 4.102 remains a good estimate due to the logarithmic dependence of Φ_∞ on the ratio of fluxes [51]. Although lots additional physics such as the effect of magnetization and collision needs to be included to precisely determine the potential drop between the plasma and the wall, these effects may not change the entire features of the helicon discharge dramatically, thus $\Phi_\infty = V_s = 4.7\, T_e$ is used as the boundary condition at the wall (either at the conducting and the insulating boundaries) in the ambipolar diffusion model. The averaged electron energy flux, that is lost to the wall is calculated as

$$W_{e,\text{wall}} = 2k_B T_e \Gamma_e, \tag{4.103}$$

where Γ_e is given by 4.100. In the full fluid model, the wall potential is calculated self-consistently by solving the Poisson equation, and thus the boundary conditions used in this model are determined as

$$\Gamma_{er} = \frac{1}{4} n_e \bar{u_e} \exp\left(\frac{\Phi_{r=a} - \Phi_{r=a-dr}}{T_e}\right), \quad \text{at } r = a \tag{4.104}$$

$$\Gamma_{ez} = \pm\frac{1}{4} n_e \bar{u_e} \exp\left(\frac{\Phi_{z=\pm\frac{L_z}{2}} - \Phi_{z=\pm\frac{L_z}{2}\mp dz}}{T_e}\right), \quad \text{at } z = \pm\frac{L_z}{2} \tag{4.105}$$

for the electrons continuity equation,

$$q_{er} = 2\Gamma_{er}|_{r=a} k_B T_e, \quad \text{at} r = a \tag{4.106}$$

$$q_{ez} = \pm 2\Gamma_{ez}|_{z=\pm\frac{L_z}{2}} k_B T_e, \quad \text{at } z = \pm\frac{L_z}{2} \tag{4.107}$$

for the electrons energy balance equation, and

$$\Phi_{r=a, z=\pm\frac{L_z}{2}} = 0, \tag{4.108}$$

for the Poisson equation.

4.4 Collisions in plasma

4.4.1 Collisions between electrons, ions and neutrals

The electron-neutral cross sections used in our model are shown in Fig. 4.2 [106]. In our model, the rate constants α [m^3/s] are obtained by averaging the above cross sections over the distribution function. The rate constants for elastic collision, excitation, and ionization averaged over an isotropic Maxwellian are shown in Fig. 4.3. In Fig. 4.3, we use the numerically fitting curves as a function of the electron temperature [51] as follows

$$\alpha_{el} = 2.336 \times 10^{-14} T_e^{1.609} \exp[0.0618(\ln T_e)^2 - 0.1171(\ln T_e)^3], \tag{4.109}$$

$$\alpha_{ex} = 2.48 \times 10^{-14} T_e^{0.33} \exp\left(\frac{-12.78}{T_e}\right), \tag{4.110}$$

and

$$\alpha_{iz} = 2.34 \times 10^{-14} T_e^{0.59} \exp\left(\frac{-17.44}{T_e}\right). \tag{4.111}$$

The recombination rate constants are given by theoretical model [107]. Assuming the heating of ions is trivial in the helicon discharge, the ion temperature is fixed as $T_i = 0.026$ [eV] in our model, and the rate constants for charge exchange ($\alpha_{\rm cx}$) and the elastic scattering ($\alpha_{\rm el}$) are calculated by averaging the cross section data obtained from Fig. 4.4 [108] over an isotropic Maxwellian. Since the ion temperature is smaller than the typical experimental conditions ($T_i > 0.1$ [eV], ions are heated by some mechanisms as introduced in 1.1.6 [42]), the more realistic value of the ion temperature should be set in the future model. The collision frequencies per one particle for each collision are obtained by multiplying the target density i.e. the neutral density n_g.

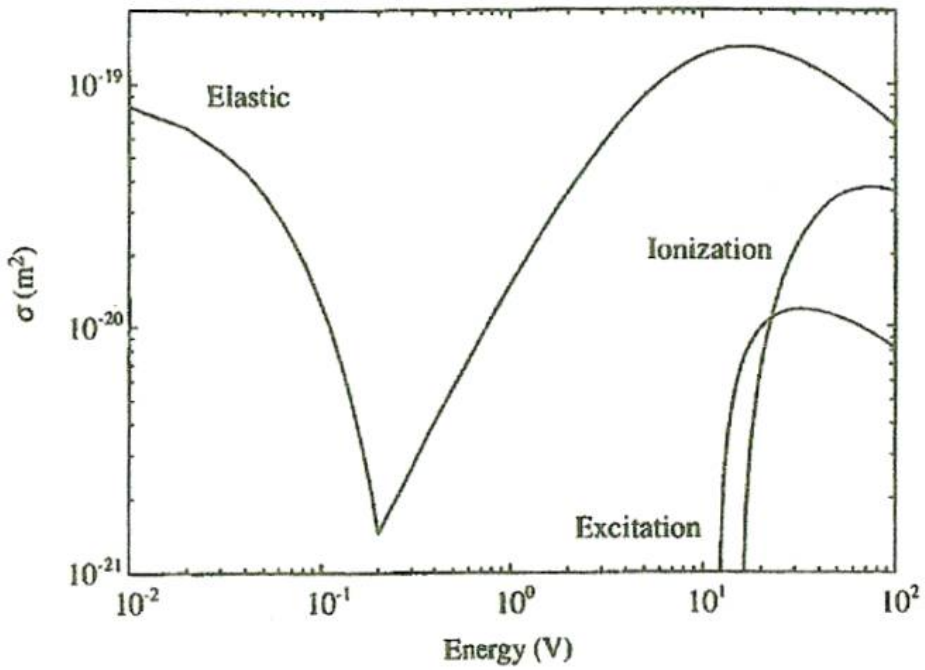

Figure 4.2: Ionization, excitation and elastic scattering cross sections for electrons in argon gas [106].

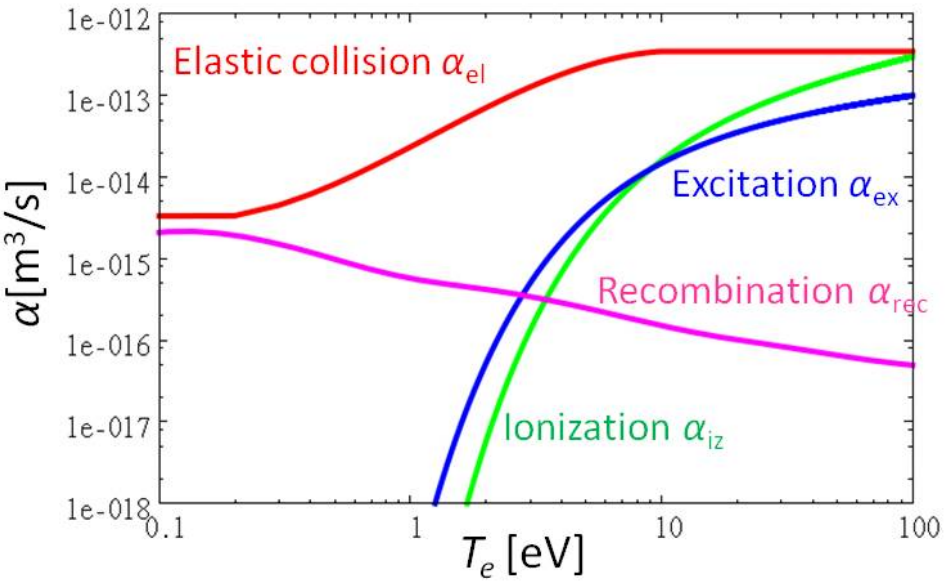

Figure 4.3: Electron collision rate constants for ionization (α_{iz}), excitation (α_{ex}), elastic (α_{el}), and recombination (α_{rec}) versus T_e in argon gas [51].

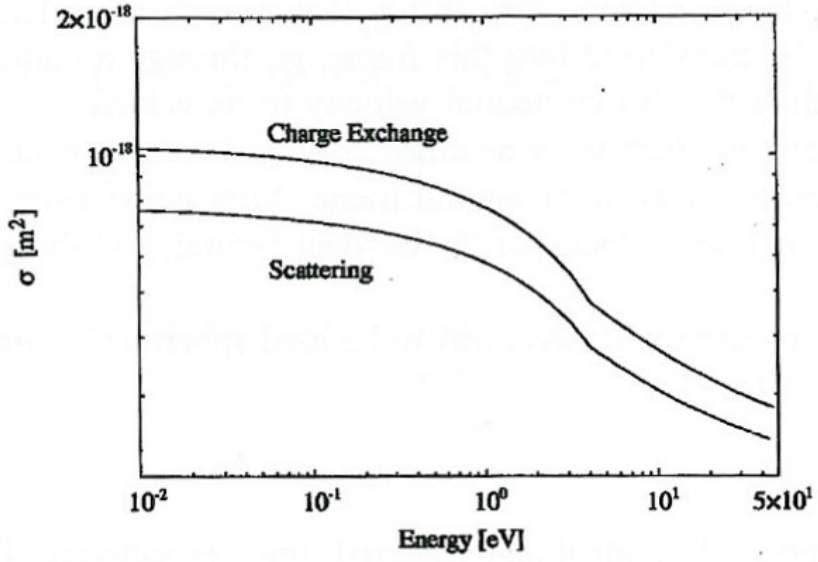

Figure 4.4: Charge exchange, and elastic scattering cross sections for ions in argon gas [108].

4.4.2 Coulomb collisions

The Maxwellian distribution collision frequencies for the coulomb collisions of charged particles are obtained by theoretical formula [105, 109] as follows,

$$\nu_{e-i} = \frac{\sqrt{2}}{3\sqrt{\pi}} n \left(\frac{e^2}{4\pi\epsilon_0} \right)^2 \frac{4\pi}{{m_e}^{1/2} {T_e}^{3/2}} \ln\Lambda_e, \tag{4.112}$$

$$\nu_{e-e} = \frac{1}{\sqrt{2}} \nu_{e-i}, \tag{4.113}$$

$$\nu_{i-e} = \frac{m_e}{m_i} \nu_{e-i}, \tag{4.114}$$

$$\nu_{i-i} = \frac{\sqrt{2}}{3\sqrt{\pi}} n \left(\frac{q^2}{4\pi\epsilon_0} \right)^2 \frac{4\pi}{\sqrt{2}{m_i}^{1/2} {T_i}^{3/2}} \ln\Lambda_i, \tag{4.115}$$

where $\ln\Lambda_e$ and $\ln\Lambda_i$ are the Coulomb Logarithm defined as

$$\Lambda_s = \frac{\lambda_{Ds}}{b_{\min}}, \tag{4.116}$$

where λ_{Ds} is the Debye length for sth species, and $b_{\min}$ is the minimum impact parameter.

4.5 Time and space scalings and the features of helicon discharge

Since there are various physical time and space scalings relevant to the helicon discharge, it is necessary to estimate these scales, in order to capture a characteristic of the helicon discharge. A crude estimation of physical time scalings are shown in Fig. 4.5 and space scalings are shown in Fig. 4.6. These estimations were made by using the specific parameters in the experiment of Nisoa *et al.*

Figure 4.5 shows evaluated time scales by using typical plasma parameters. Since the RF drive frequency ω_{RF} satisfies $\omega_{ci} \ll \omega_{LH} < \omega \ll \omega_{ce} \ll \omega_{pe}$, the effect of ions motions on the wave fields can be ignored. The transit time scales of the helicon and

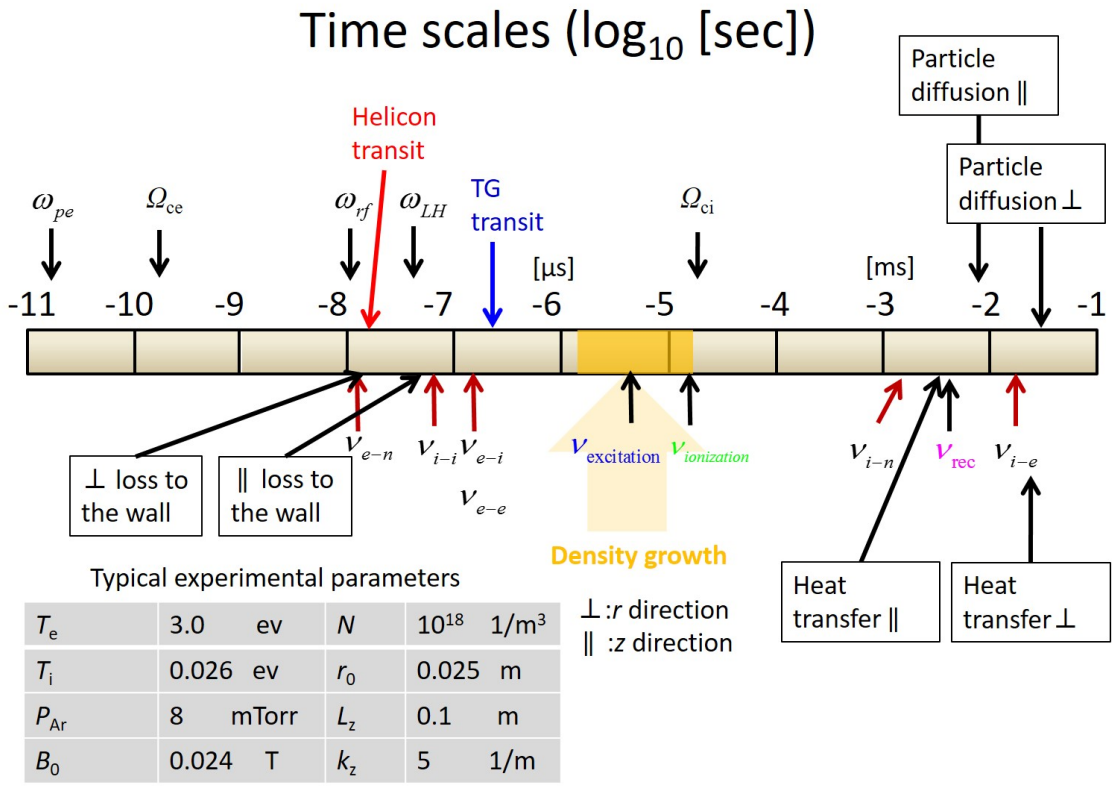

T_e	3.0 ev	N	10^{18} 1/m^3
T_i	0.026 ev	r_0	0.025 m
P_{Ar}	8 mTorr	L_z	0.1 m
B_0	0.024 T	k_z	5 1/m

Figure 4.5: Time scales of the physics of a helicon discharge

the TG waves in a plasma (plasma radius $a = 0.0225$ [m]) are evaluated by using their phase velocities v_ϕ as

$$\tau_{\text{wave transit}} = a/v_{\phi,\text{TG,Helicon}}. \tag{4.117}$$

The transit time scale of the helicon wave is much faster than that of the TG wave, since the perpendicular wave number of the helicon and the TG wave is well separated (the wavenumber of the TG wave is much larger than that of the helicon wave). The diffusion time scales of particle and heat flux are evaluated as

$$\tau_{\text{particle diffusion},\perp} = \frac{a^2}{D_{a,\perp}}, \tag{4.118}$$

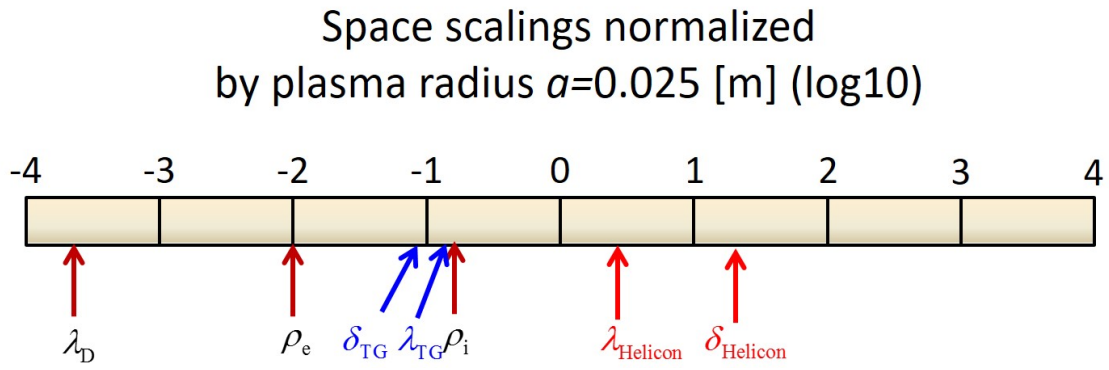

Figure 4.6: Length scales normalized by the plasma radius, where the same parameters are used with in Fig. 4.5.

$$\tau_{\text{particle diffusion},\parallel} = \frac{L_z^2}{D_{a,\parallel}}, \tag{4.119}$$

$$\tau_{\text{heat transfer},\perp} = \frac{3na^2}{2\kappa_{a,\perp}} = \frac{3}{5}\frac{a^2}{D_{a,\perp}}, \tag{4.120}$$

$$\tau_{\text{heat transfer},\parallel} = \frac{3nL_z^2}{2\kappa_{a,\parallel}} = \frac{3}{5}\frac{L_z^2}{D_{a,\parallel}}. \tag{4.121}$$

Since the diffusion coefficient is basically proportional to $v_{th,e}^2/\nu_e$, above diffusion time scales are proportional to the collision frequency ν_e, square of the plasma size a^2 and L_z^2, and square inverse of the thermal velocity $1/v_{th,e}^2$. Since the electron diffusion is strongly restricted by the assumptions of the ambipolar diffusion (the charge neutrality and the flux equality), the diffusion time scales are dominated by the ions diffusion, and thus it takes much long time (over [ms]) for the above diffusions. As shown in Fig. 4.6, since the charged particle is strongly magnetized (ions Larmor radius: $\rho_i/a \sim 0.2$, and electrons Larmor radius: $\rho_e/a \sim 0.01$), the perpendicular diffusion time scales are longer than that of the parallel diffusion. The time scales of the loss to the wall are evaluated by using the electron mean velocity $\bar{u_e} = (8k_BT_e/\pi m_e)^{1/2}$. The space scalings of the wavelength λ and the penetration depth δ in Fig. 4.6 are evaluated from the perpendicular wavenumbers of the helicon and the TG waves. As shown in Fig. 4.6, the penetration depth of the TG wave is much shorter than the plasma size,

while the helicon one is much larger than the plasma size.

Summarizing the above scalings, the general description of the helicon discharge can be captured as follows: Once the RF current is applied from the antenna, the helicon and the TG waves are excited and they travel in the plasma within $t \sim 0.1$ [μs], however the TG wave strongly decay at the plasma edge $r \sim a$, while the helicon wave penetrates into the center of the plasma $r = 0$. As a result, the electrons around the plasma edge are heated by the TG wave, and ionization of neutrals are accelerated, and the plasma density grows within several μs or tens of μs (since the electron temperature would increase several eV due to the Joule heating, and thus the ionization time scale is evaluated within the range of $3 < T_e < 5$ [eV]) near the plasma edge. The plasma density and the electron temperature are determined by the balance of the gain (ionization and power absorption) and the loss (due to the inelastic collisions and the wall loss). Since the diffusion time scales are much longer than these physical time scales, the plasma density and the electron temperature can not diffuse within the growth time scale, thus the density and the electron temperature growths are localized near the plasma edge as shown in Fig. 4.7. Finally, in a steady state, these growths will be balanced with the losses of the energy flux and particles toward the wall.

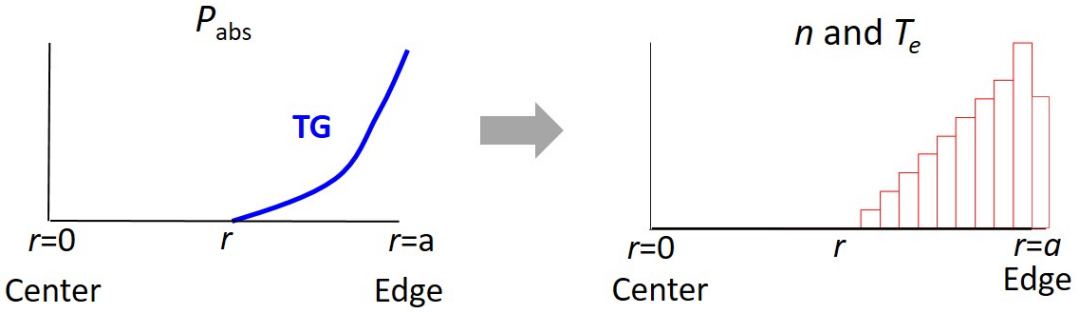

Figure 4.7: The expected profiles of the power absorption, the plasma density, and the electron temperature. The edge-localized power absorption profile by the TG wave would lead to the edge-localized profiles of the electron temperature and the plasma density.

4.6 One-dimensional cylindrical ambipolar diffusion model

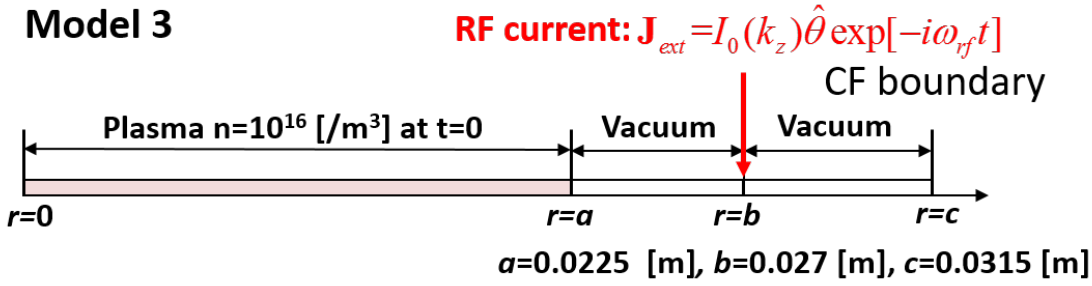

Initial conditions and Experimental parameters

T_e (t=0)	3.0 ev	$T_{i,N}$ (fixed)	0.026 ev
n (t=0)	10^{16} /m^3	k_z (fixed)	π/0.1 /m
P_{Ar} (t=0)	8 mTorr	B_0 (fixed)	0.024 T

Figure 4.8: The one-dimensional cylindrical helicon discharge model. The plasma density is updated by the ambipolar diffusion equation

In this section, we show the results by using the one-dimensional cylindrical helicon discharge model as shown in Fig. 4.8. In this model, electromagnetic wave fields are solved by using the FDTD method with the fixed axial wave number $k_z = 5$ [1/m] (axial uniformity of all parameters are assumed), where we assume that $N = 1$ the axial standing wave is excited in the short cylindrical plasma column with $L_z = 0.1$ [m] length as shown in Fig. 2.16. The model includes the plasma region ($0 < r < a$) and the vacuum region ($a < r < b$ and $b < r < c$).

In this simulation, numerical iterations are conducted using the following parameters: step size in space $dr = 1.5 \times 10^{-4}$ [m] ($\approx 0.03 \times \lambda_{TG}$: the wave length of the TG wave at $n = 10^{18}$ [1/m^3]), step size in time $dt = 0.9dx/c$ [s], number of grid in plasma region($0 < r < r_0$): 150, and number of grid in vacuum region($a < r < b$ and $b < r < c$): 30.

The $m = 0$ antenna current $J_\theta = 2.8 \sim 3.0 \times 10^6$ [A/m^2] (that corresponds to

the roughly estimated antenna power of $P_{\mathrm{RF}} \sim 0.4$ [kW] when the P_{abs} is integrated over the plasma volume (plasma radius $a = 0.0225$ [m] and length $L_z = 0.1$ [m]) with the uniform plasma density $n = 5.0 \times 10^{18}$ [1/m^3]) is applied at $r = b$. The azimuthal spatial variation of all parameters are also not included. The conducting boundary is introduced at $r = c$ where the tangential electric wave fields (δE_θ and δE_z) are vanished. The initial conditions at $t = 0$ [s] are set to be uniform over the plasma region as follows: electron temperature $T_e = 3.0$ [eV], plasma density $n = 10^{16}$ [1/m^3], Ar neutral pressure $P_{Ar} = 8$ [mTorr] $\sim n_N = 2.6 \times 10^{20}$ [1/m^3], and ion and neutral temperatures are fixed as the room temperature $T_e = 0.026$ [eV]. The electron temperature is time integrated by using the energy balance equation 4.75, and the plasma density is time integrated by using the ambipolar diffusion equation 4.65. In this model, the mode transition of the axial standing wave from the $N = 1$ ($k_z = 5$ [1/m]) mode to the $N = 3$ ($k_z = 15$ [1/m]) mode in not included. That mode transition will be discussed by using the two-dimensional cylindrical model in the next section. The another effects such as the ion heating and the neutral dynamics are not included, and thus these effects should be included in the future model. In this section, we focus the basic understanding of the helicon discharge.

4.6.1 The time evolution of the plasma density and the electron temperature profiles

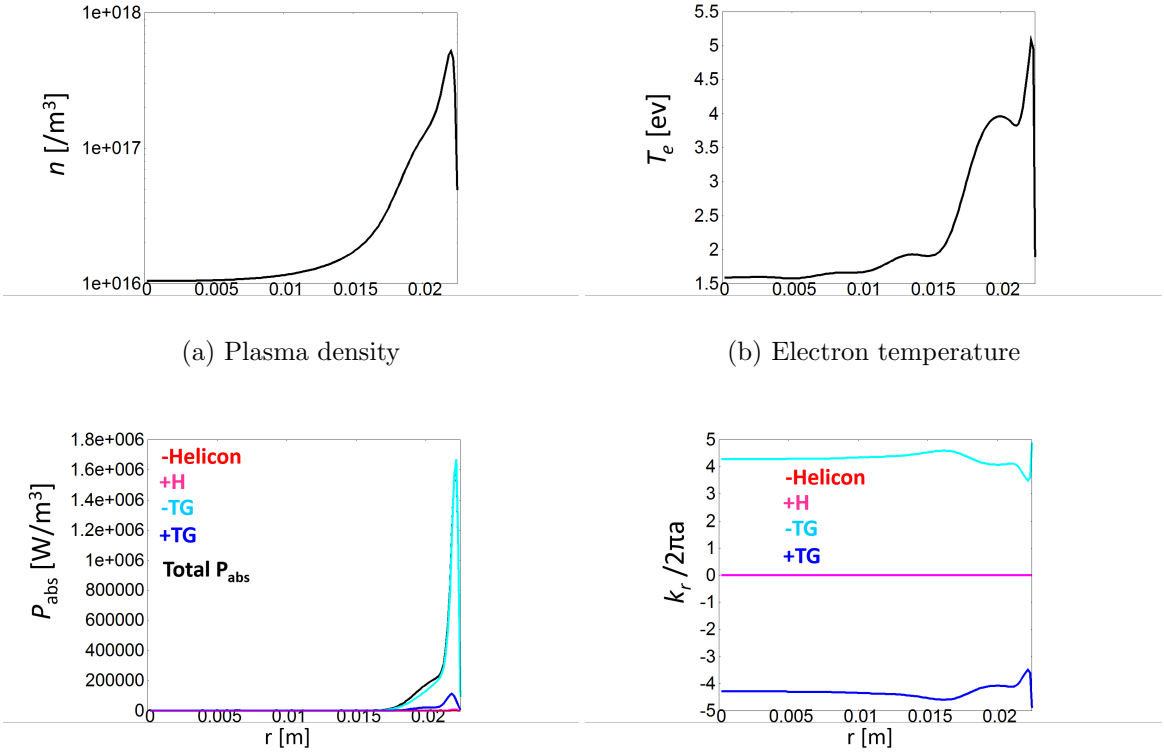

(a) Plasma density

(b) Electron temperature

(c) Power absorption

(d) Radial wave number normalized by the plasma radius

Figure 4.9: (a) Plasma density profile, (b) electron temperature profile, (c) power absorption profiles by H+, H-, TG+, TG- waves, and total power absorption profile, and (d) radial wave numbers (real part) of each wave normalized by the plasma radius at $t = 60$ [μs] with $J_{\text{ext}} = 3.0 \times 10^6$ [A/m^2].

Figure 4.9 shows the spatial profiles of (a) plasma density, (b) electron temperature, (c) power absorption by H+, H-, TG+, TG-, where the minus and plus sign represent the sign of the wave phase velocity (note that the perpendicular component of the TG wave group velocity has an opposite sign to that of the phase velocity), and total power absorption (black line), and (d) radial wave numbers of each wave at $t = 60$ [μs], when the azimuthal current $J_{\text{ext}} = 3.0 \times 10^6$ [A/m^2] is applied. From Fig.

4.9, one can see the edge-localized electron temperature (the maximum temperature is $T_e \sim 5.0$ [eV]) resulting from the power absorption by TG- wave, that leads to the edge-localized density growth (the maximum density is $n \sim 4.0 \times 10^{17}$ [1/m^3]). Since the power absorption by the TG- wave is localized at the plasma edge due to its small penetration depth, the electron temperature and the plasma density profiles are also localized around the plasma edge. The centrally peaked profile or the hollow profile observed in the experiment (Fig. 1.27) can not be seen in this result because of the long time delay of the ambipolar diffusion ($\sim$[ms]). From Fig. 4.9 (d), one can see the real part of the helicon wave number is zero, and thus the helicon wave number is pure imaginary at the under-cut-off density region $n < n_{\mathrm{low}}$, where the cut-off density is $n_{\mathrm{low}} \sim 1.3 \times 10^{18}$ [1/m^3] in this case.

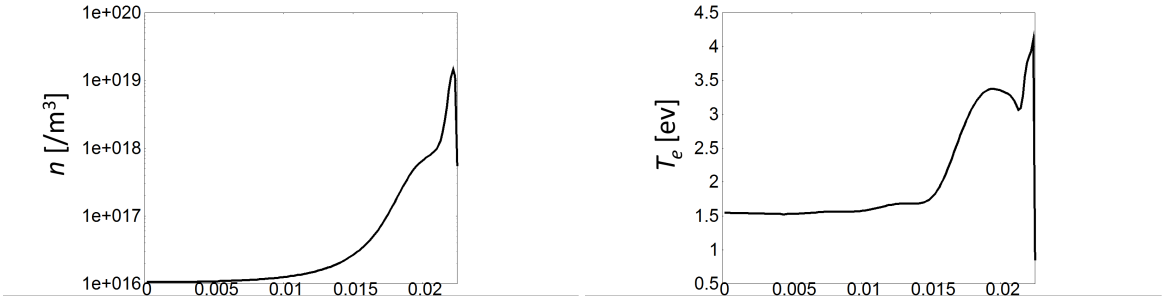

(a) Plasma density

(b) Electron temperature

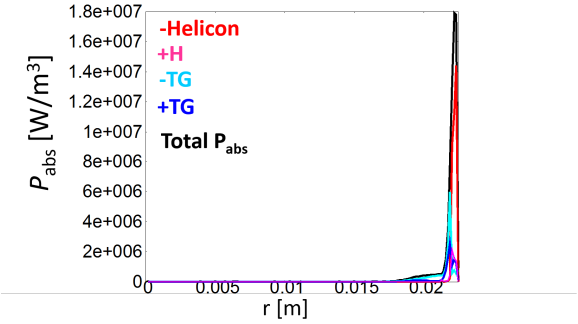

(c) Power absorption

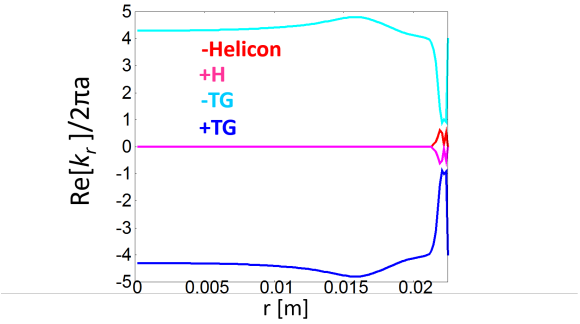

(d) Radial wave number normalized by the plasma radius

Figure 4.10: (a) Plasma density profile, (b) electron temperature profile, (c) power absorption profiles by H+, H-, TG+, TG- waves, and total power absorption profile, and (d) radial wave numbers (real part) of each wave normalized by the plasma radius at $t = 73$ [μs] with $J_{\text{ext}} = 3.0 \times 10^6$ [A/m^2].

Figure 4.10 shows the same profiles with Fig. 4.9 at $t = 72$ [μs]. As shown in Fig. 4.10, the maximum plasma density reaches at $n \sim 10^{19}$ [1/m^3] and the maximum electron temperature decreases to $T_e \sim 4.0$ [eV] due to the energy loss by the ionization. In Fig. 4.10 (c), it is interesting to notice that the power absorption by H- wave become dominant near the plasma edge, that is due to the nearly merging of the helicon and the TG branches as shown in Fig. 4.10 (d).

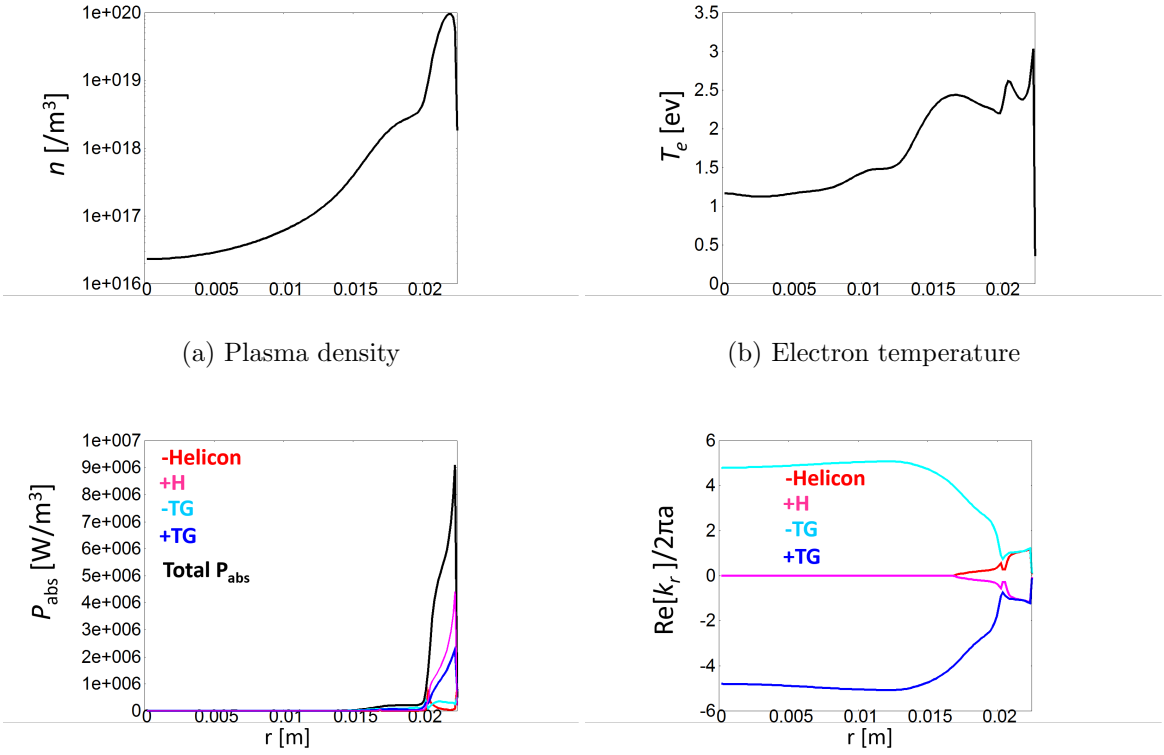

(a) Plasma density

(b) Electron temperature

(c) Power absorption

(d) Radial wave number normalized by the plasma radius

Figure 4.11: (a) Plasma density profile, (b) electron temperature profile, (c) power absorption profiles by H+, H-, TG+, TG- waves, and total power absorption profile, and (d) radial wave numbers (real part) of each wave normalized by the plasma radius at $t = 200$ [μs] with $J_{\text{ext}} = 3.0 \times 10^6$ [A/m^2]

After enough time is passed, the helicon discharge reaches almost steady state at $t = 200$ [μs] as shown in Fig. 4.11. The maximum density relaxes at $n \sim 10^{20}$ [1/m^3], and the maximum electron temperature relaxes at $T_e \sim 3.0$ [eV]. At above the upper limit density n_{up}, where $n_{\text{up}} \sim 1.6 \times 10^{19}$ [1/m^3] in this case, the helicon and the TG branches completely merging as shown in Fig. 4.11 (d), and both waves become evanescent in this region. Therefore, we can not decompose the wave fields into the helicon and the TG waves precisely, that leads to the difference between the total power absorption profile and the summation of four power absorption profiles

in the density region $n > 1.6 \times 10^{19}$ [1/m^3] as shown in Fig. 4.11 (c). Although the both waves become evanescent in the density region $n > 1.6 \times 10^{19}$ [1/m^3], Fig. 4.11 (c) shows the considerable amount of power absorption in this region. The power absorption in this region is due to the penetration of the surface waves that are excited at the plasma edge, where the plasma density is much smaller than the upper limit density $n_{\rm edge} \sim 1.8 \times 10^{18}$ [1/m^3] $<< n_{\rm up}$. Even at the nearly steady state, the centrally peaked profile can not be seen, since the time scale of the ambipolar diffusion of $t > 1$ [ms] is much longer than $t = 200$ [μs].

4.6.2 The time evolution of the maximum plasma density and the electron temperature

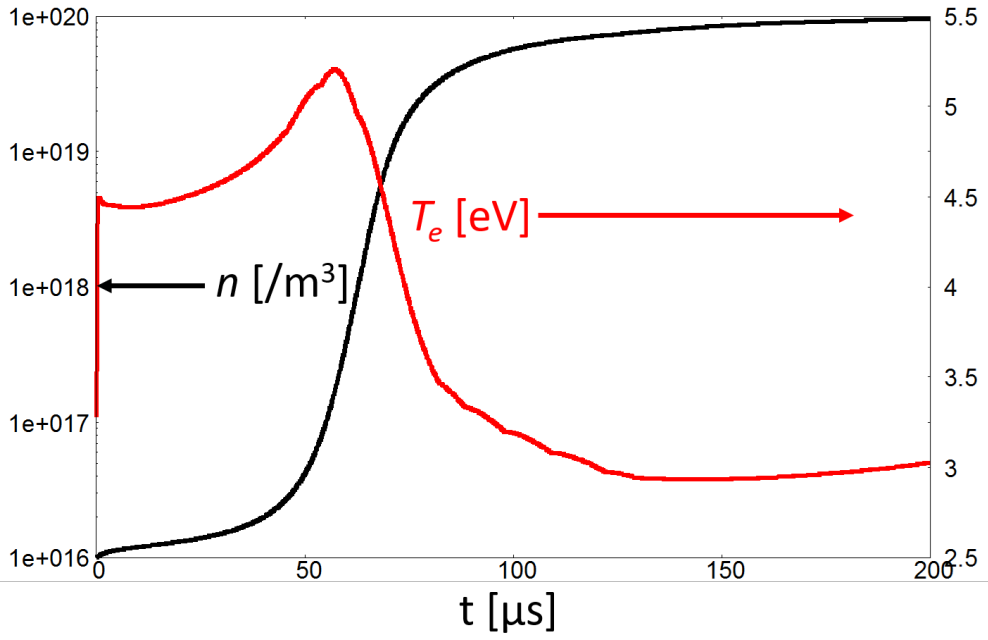

Figure 4.12: The time evolution of the maximum plasma density (black line) and the maximum electron temperature (red line) with $J_{\rm ext} = 3.0 \times 10^6$ [A/m^2].

Figure 4.12 shows the time evolution of the maximum density and the maximum electron temperature at the applied rf current $J_{\rm ext} = 3.0 \times 10^6$ [A/m^2]. When the rf

current is applied, the electron temperature increases immediately within $t < 1$ [μs] and the plasma density. The density and the electron temperature increases gradually until $t \sim 60$ [μs], and abrupt density growth can bee seen from $n \sim 2.0 \times 10^{16}$ [1/m^3] at the time $60 < t < 80$ [μs], while the electron temperature abruptly decreases at that time.

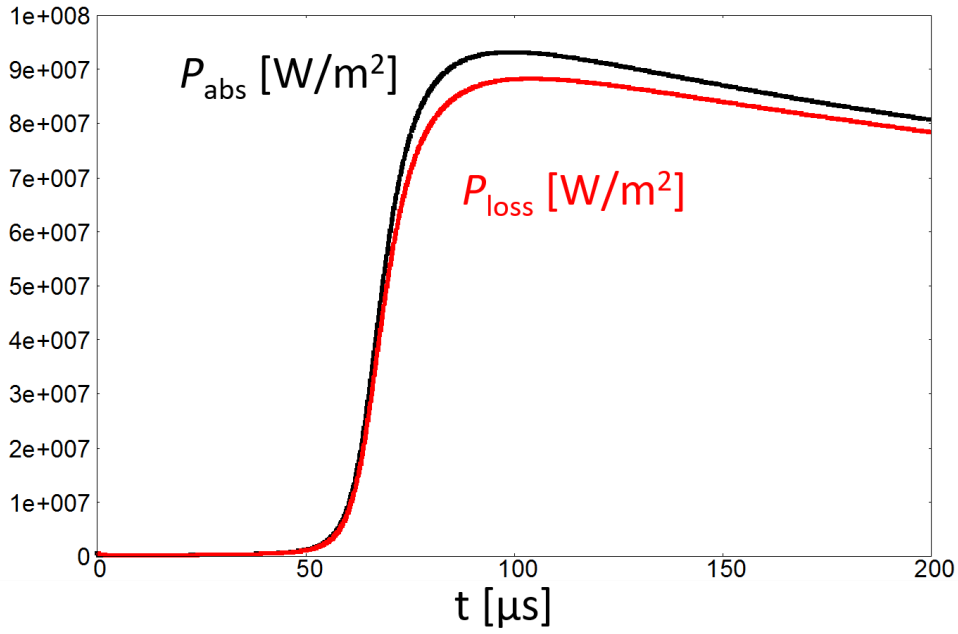

Figure 4.13: The time evolution of the total amount of the power absorption (black line) and power loss (red line) with $J_{ext} = 3.0 \times 10^6$ [A/m^2].

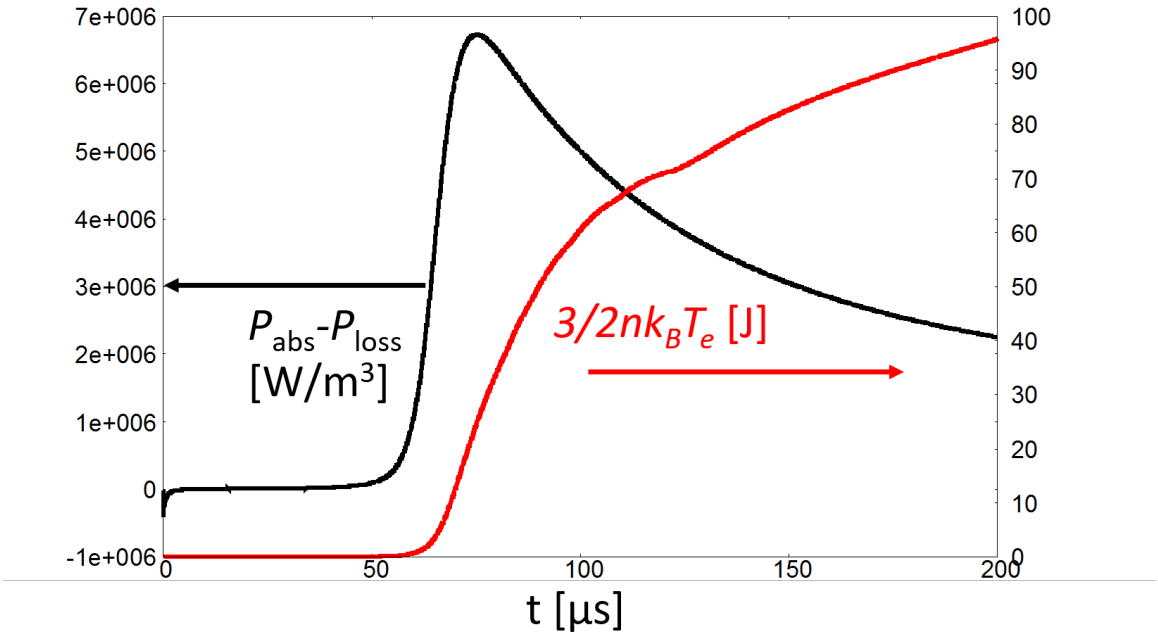

Figure 4.14: The time evolution of the power balance $P_{\rm abs} - P_{\rm loss}$ (black line) and the internal energy $3/2nk_BT_e$ (red line) with $J_{\rm ext} = 3.0 \times 10^6$ [A/m^2].

Figure 4.13 shows the time evolution of the total power absorption which is integrated over the plasma volume, and the total power loss due to the inelastic collisions and the wall loss, that are integrated over the plasma volume. As shown in Figs. 4.12 and 4.13, when the density reaches some critical value ($n \sim 2.0 \times 10^{16}$ [1/m^3]), the total power absorption and the total power loss also increase abruptly from that density point. This abrupt increasing of the power absorption may be associated with the resonant excitation of the TG wave as was discussed in chapter 2, but the detailed analysis of the TG wave excitation with such a edge localized density profile as shown in Figs. 6.9-6.11 should be made for the further discussion. The abrupt increasing of the density also result in the abrupt increasing of the total power loss, since the increasing of the density directly reflected in the power loss. Figure 4.14 shows the time evolution of the power balance ($P_{\rm abs} - P_{\rm loss}$) and the internal energy ($3/2nk_BT_e$). As seen from Figs. 4.12 and 4.14, the net power gain increases with

increasing the density, that leads to the increasing of the internal energy. When the density increases abruptly, since the absorbed power is distributed to the newly generated electrons, the electron temperature decreases despite the increasing of the net power gain. As seen from Fig. 4.12, after the abrupt increasing of the plasma density and decreasing of the electron temperature $t > 80$ [μs], the plasma density relaxes to $n \sim 10^{20}$ [1/m^3] and the electron temperature relaxes to $T_e \sim 3.0$ [eV]. From Fig. 4.14, one can see that the power balance approaches zero in that time, that leads to the relaxation of the internal energy, and that result in the density and the electron temperature. At the nearly steady state, although the electron temperature 3 [eV] is a reasonable value observed in the experiment (the electron temperature is not measured in this experiment but several eV of the electron temperature is measured in the another experiments [14, 110]), the plasma density above the 3.0×10^{19} [1/m^3] is not observed in the experiment. Since that density limit in the experiment may due to the neutral depletion, the neutral dynamics should be included in a more realistic discharge model. Furthermore, fixing of the parallel wave number as the $N = 1$ ($k_z = 5$ [1/m]) mode in this one-dimensional model is not valid above the upper limit density $n_{up} \sim 1.6 \times 10^{19}$ [1/m^3], since the mode transition from the $N = 1$ ($k_z = 5$ [1/m]) mode to the $N = 3$ ($k_z = 15$ [1/m]) mode would occurs in the actual situation. This mode transition of the axial standing wave will be discussed in the next section (the wave excitation test).

4.6.3 The time evolution of the maximum plasma density at various input power

Figure 4.15 shows the time evolution of the maximum plasma density at $J_{\rm ext} = 3.0, 2.88, 2.86, 2.84 \times 10^6$ [A/m^2] up to $\sim t = 400$ [μs], which is the measurement time in the experiment [2]. From Fig. 4.15, when $J_{\rm ext} \geq 2.88 \times 10^6$ [A/m^2], the maximum density reaches $n \sim 10^{20}$ [1/m^3] at $t = 400$ [μs], but when $J_{\rm ext} \leq 2.86 \times 10^6$ [A/m^2], the maximum density reduces through all the time. Therefore, there is some threshold value between $J_{\rm ext} = 2.88 \times 10^6$ and 2.86×10^6 [A/m^2] for the density growth. In both cases of $J_{\rm ext} = 3.0 \times 10^6$ and 2.88×10^6 [A/m^2], the maximum density abruptly increases from the critical value $n \sim 2.0 \times 10^{16}$ [1/m^3].

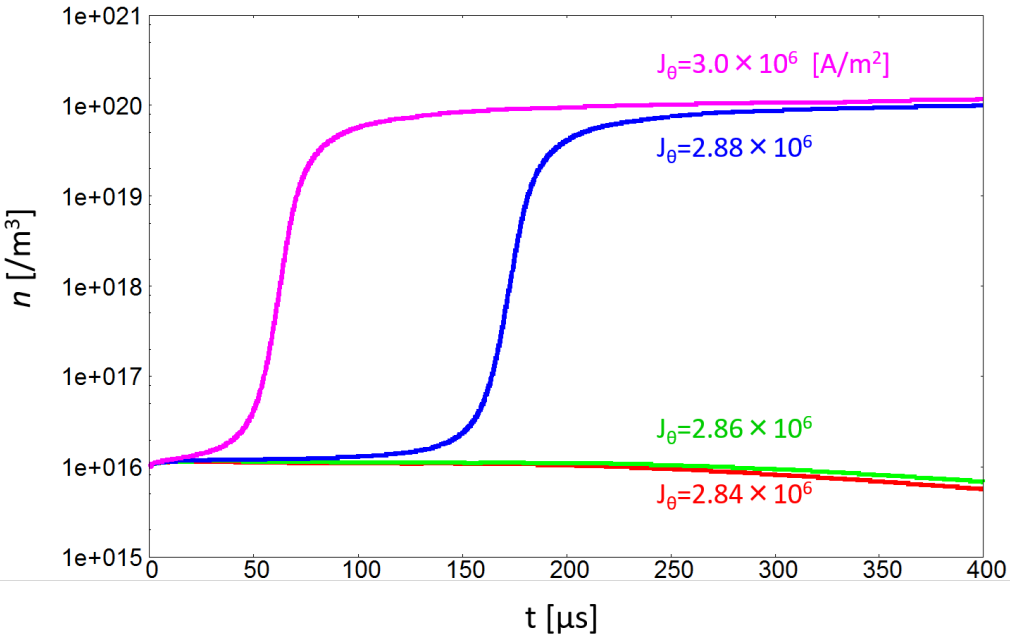

Figure 4.15: The time evolution ($\sim t = 400$ [μs]) of the maximum plasma density at $J_{\rm ext} = 3.0, 2.88, 2.86$, and 2.84×10^6 [A/m^2].

Figure 4.16 shows the time evolution of the maximum electron temperature at each current density, and Figs. 4.17 and 4.18 show the total net power gain ($P_{\rm abs} - P_{\rm loss}$) at $J_{\rm ext} = 3.0, 2.88 \times 10^6$ [A/m^2] and $J_{\rm ext} = 2.86, 2.84 \times 10^6$ [A/m^2] respectively. From

Fig. 4.16, one can see that the maximum electron temperature also decreases under the threshold value of the current density, that is due to the net minus power gain as seen from Fig. 4.18. Tease results indicate that the density can not grow when the power balance ($P_{\rm abs} - P_{\rm loss}$) on the initial stage of the discharge is negative, and once the density reaches the critical value ($n \sim 2.0 \times 10^{16}$ [1/m^3]), the density grows immediately within a few tens of μs. Therefore, the separation of the steady state density results in the power balance not in the steady state but on the initial stage (before the density growth) of the discharge. That argument is different from the usual one, that the density jump is discussed from the power balance on the steady state as mentioned in chapter 2. However, the low density and the intermediate density mode ($n < 10^{19}$ [1/m^3]) observed in the experiment can not be seen in our results.

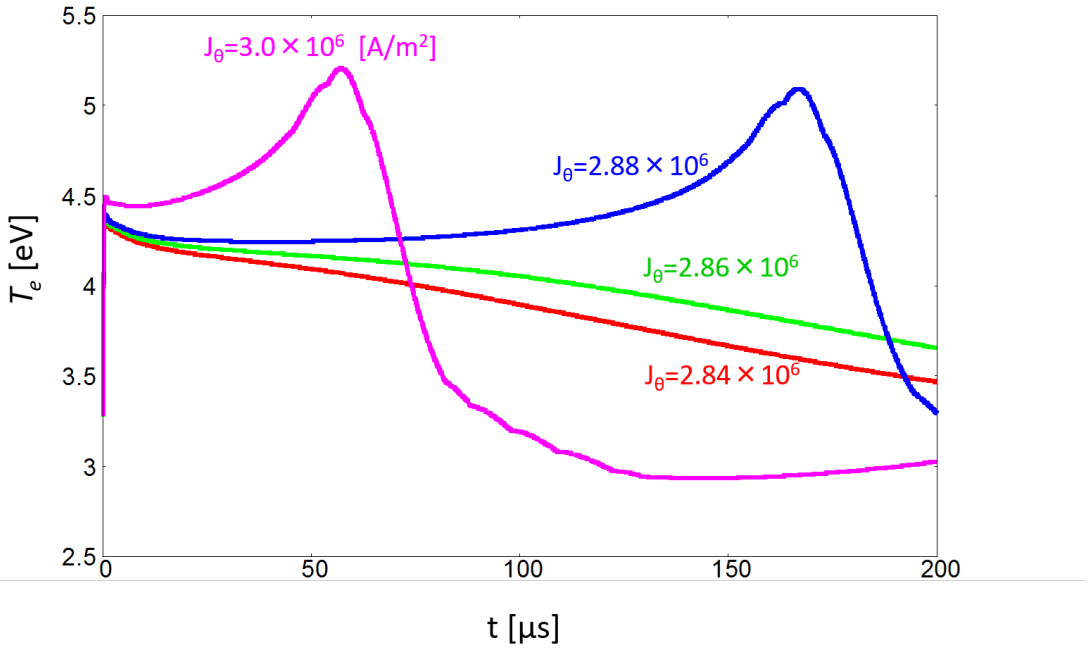

Figure 4.16: The time evolution ($\sim t = 400$ [μs]) of the maximum electron temperature at $J_{\rm ext} = 3.0, 2.88, 2.86$, and 2.84×10^6 [A/m^2].

The threshold value of the current density and the critical value of the plasma

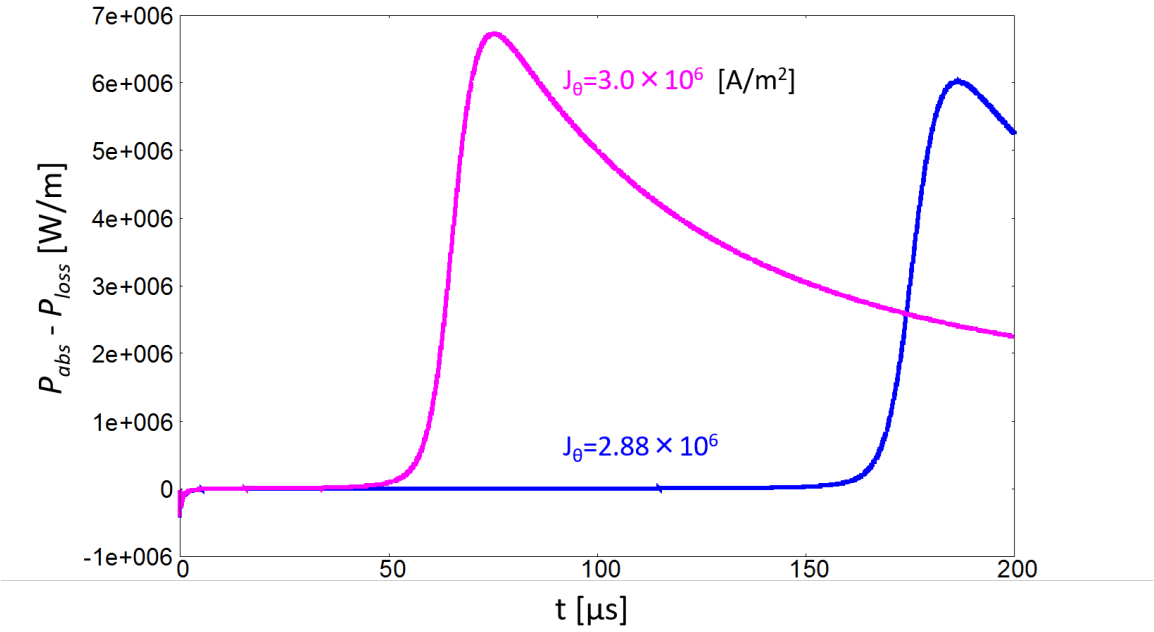

Figure 4.17: The time evolution ($\sim t = 400$ [μs]) of the integrated net power gain ($P_{\rm abs} - P_{\rm loss}$) over the plasma region at $J_{\rm ext} = 3.0$, and 2.88×10^6 [A/m^2].

density for the density growth depends on the initial plasma density as shown in Fig. 4.19 (the initial density is $n = 1.0 \times 10^{15}$ [1/m^3]). As seen from Fig. 4.19, when the current density is above $J_{\rm ext} \geq 3.8$ [A/m^2], the plasma density grows but there is long time delay in the density growth at $J_{\rm ext} = 3.8 \times 10^6$ [A/m^2], while the density decreases from $t \sim 200$ [μs] at $J_{\rm ext} = 3.0 \times 10^6$ [A/m^2]. Once the plasma density reaches $n \sim 7.0 \times 10^{15}$ [1/m^3], the density grows immediately. Since the axial loss of the particles is not included in this one-dimensional model, the further discussions about the steady state and the density jump should be made in the two-dimensional model.

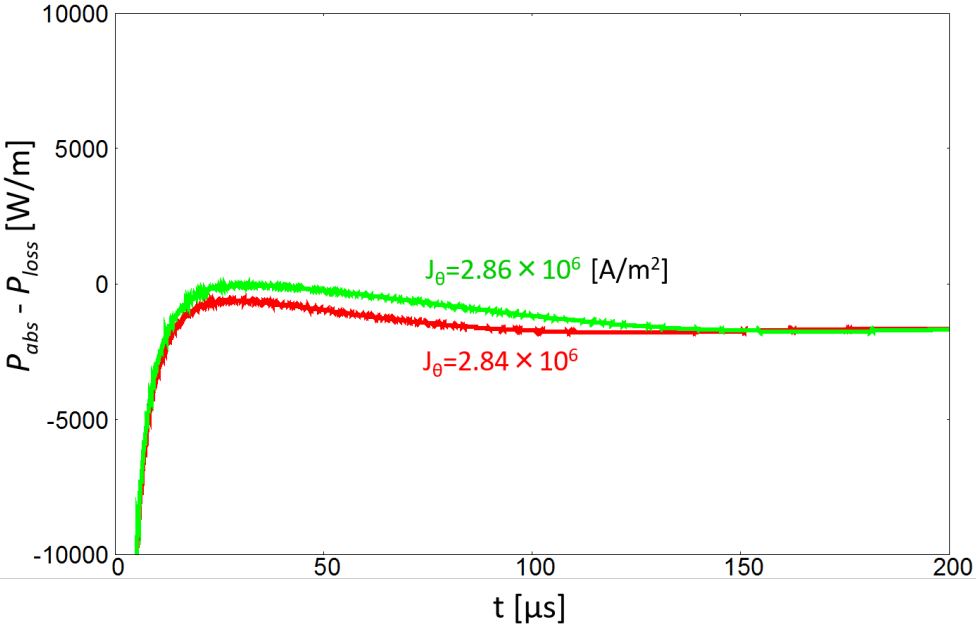

Figure 4.18: The time evolution ($\sim t = 400$ [μs]) of the integrated net power gain ($P_{\rm abs} - P_{\rm loss}$) over the plasma region at $J_{\rm ext} = 2.86$, and 2.84×10^6 [A/m^2].

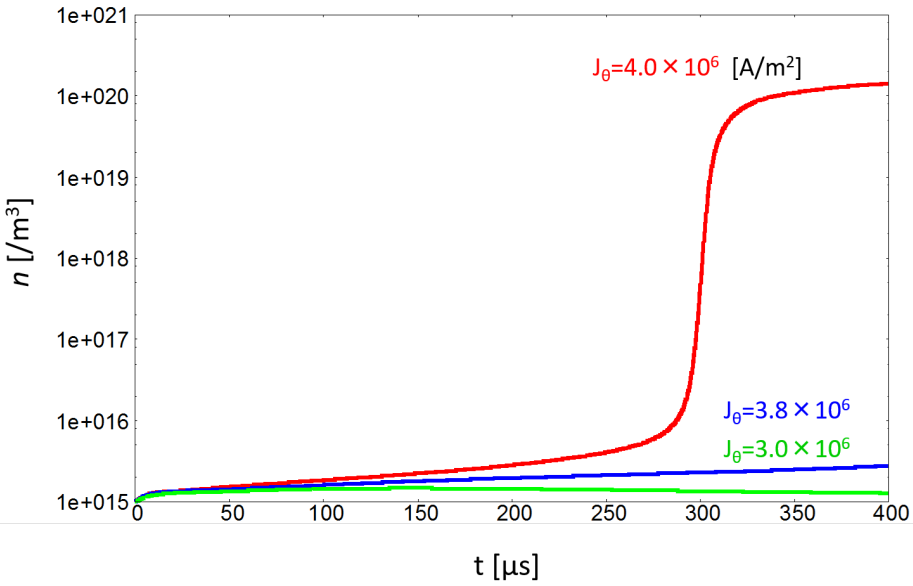

Figure 4.19: The time evolution ($\sim t = 400$ [μs]) of the maximum plasma density at $J_{\rm ext} = 4.0$, and 3.8×10^6 [A/m^2], with the initial plasma density $n = 10^{15}$ [1/m^3].

4.7 Two-dimensional cylindarical model

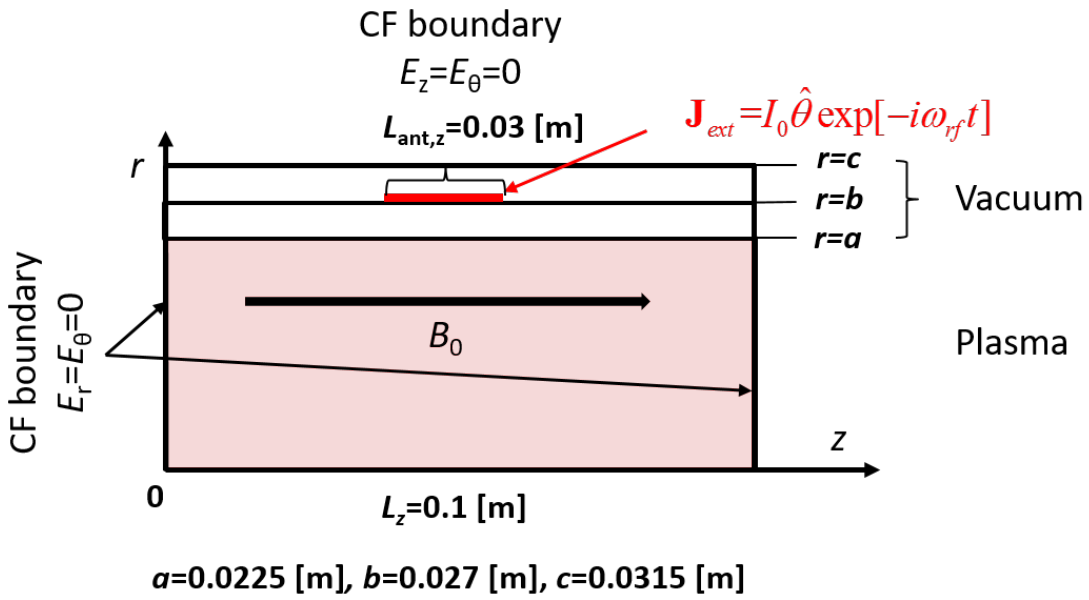

Figure 4.20: The two-dimensional cylindrical helicon discharge model.

In this section, we show the results of the two-dimensional cylindrical model as shown in Fig. 4.20. In this model, the conducting boundaries are introduced at $r = c$ and $z = 0, L_z$, where the tangential electric wave fields δE_θ, δE_z are vanished at $r = c$ and δE_r, δE_θ are vanished at $z = 0, L_z$. The azimuthal current $J_\theta = 2 \times 10^7$ [A/m^2] which has a finite width ($L_{\mathrm{ant},z} = 0.03$ [m] and $L_{\mathrm{ant},r} = 0.15$ [mm], thus the antenna current can be calculated as $I_0 = J_\theta L_{\mathrm{ant},r} L_{\mathrm{ant},z} \sim 90$ [A]) is applied at $r = b$ and $z = L_z/2$. The antenna current density $J_\theta = 2 \times 10^7$ [A/m^2] corresponds to the roughly estimated antenna power of 11.0 [kW] when the P_{abs} is integrated over the plasma volume (plasma radius $a = 0.0225$ [m] and length $L_z = 0.1$ [m]) with the uniform plasma density $n = 5.0 \times 10^{18}$ [1/m^3] . The antenna power of 11.0 [kW] is several times larger than that applied in the Nisoa's experiment ($0.1 \sim 3.5$ [kW]). This large antenna current is applied in order to accelerate the time evolution of the discharge and decrease the computational load, where the time step is severely limited

by 4.97 ($\Delta t \sim 1.0 \times 10^{-15}$ [s]), Actually, more realistic value of the antenna current should be used in the future model by using the implicit method to calculate the time integration of the balk motion of the plasma. Therefore, we focus on the basic characteristics of the time evolution of the helicon discharge, and make comparison between the ambipolar diffusion model and the full fluid model. The axial wavelength of the excited standing wave is determined from the above geometries (locations of the boundary and the antenna), and thus the mode numbers of half wave length $N = 1$ ($k_z = 5$ [1/m]) or $N = 3$ ($k_z = 15$ [1/m]) are excited in the axial direction. All another initial conditions and experimental parameters are same with ones used in Fig. 4.8. In the first subsection, we show the results of the simple wave excitation test by fixing the uniform plasma density at $n = 10^{16}, 5 \times 10^{18}$ and 5×10^{19} [1/m^3] with a finite collision frequency ($\nu_e/\omega = 0.1$), in order to investigate the basic structures of the excited waves. In the next subsection, we show the results including the time evolution of the helicon discharge, and compare the results of the ambipolar diffusion model and the full fluid model.

4.7.1 The wave excitation test

◯ **Low density**

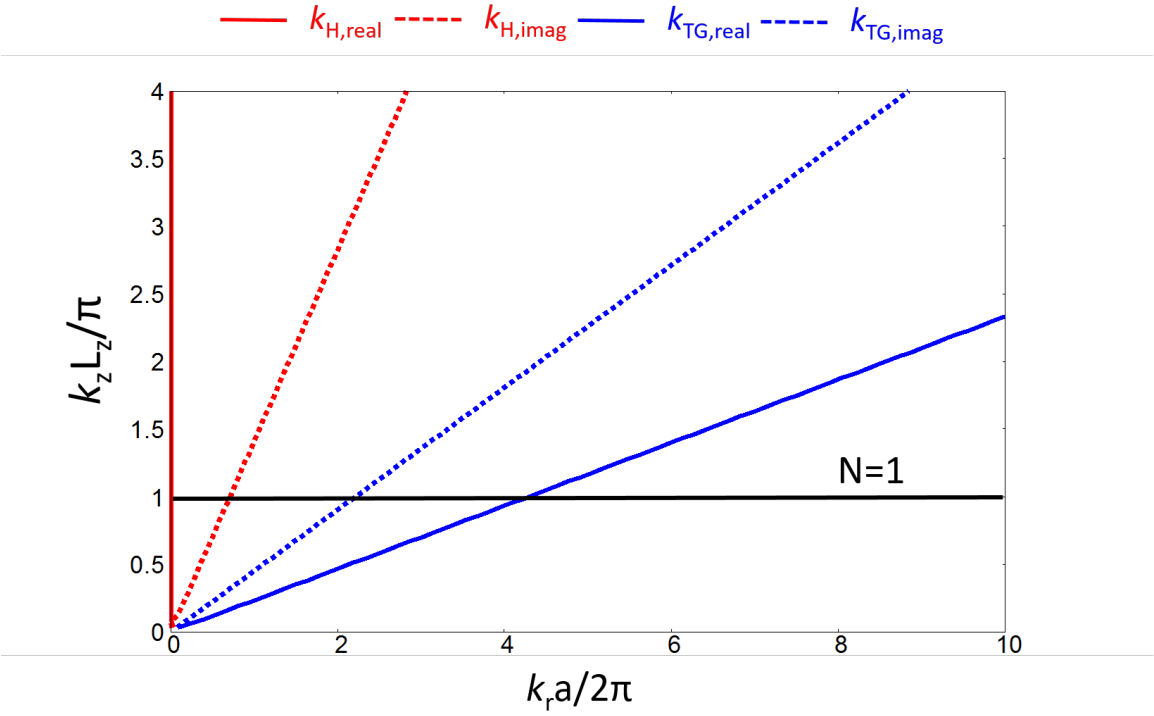

Figure 4.21: Dispersion relation of the helicon (red line) and the TG (blue line) waves at $n = 10^{16}$ [1/m^3], where the perpendicular wave number is normalized by the plasma radius a, and the axial wave number is normalized by the twice plasma length $2L_z$, the black line represent the $N = 1$ ($k_z = 5$ [1/m]) mode of the axial standing wave. The solid lines and dotted lines represent the real part and the imaginary part of the perpendicular wave number respectively.

Figure 4.21 shows the dispersion relation 2.15 of the helicon wave (red line) and the TG wave (blue line) at $n = 10^{16}$ [1/m^3] in the wave number space, where the perpendicular wave number is normalized by the plasma radius a, and the axial wave number is normalized by the twice plasma length $2L_z$. The solid lines and dotted lines represent the real part and the imaginary part of the perpendicular wave number respectively. Figures 4.22-4.25 show the E_r, E_θ, E_z, and B_z spatial profiles of the excited wave respectively, where the boundary of the vacuum region and the plasma

region is at $r/\delta r = 64$. When the plasma density is low $n = 10^{16}$ [1/m^3], which is much smaller than the cut-off density $n_{\rm low} \sim 1.3 \times 10^{18}$ [1/m^3] for the $N = 1$ mode, the helicon wave can not propagate, and as shown in Fig. 4.21, the perpendicular wave number of the helicon wave is almost pure imaginary (the small finite real part of the helicon wave number is due to the finite collision frequency $\nu/\omega = 0.1$). In Figs 4.23 and 4.25, the skin depth of this pure imaginary helicon wave can be calculated as $\delta_H/\delta r = 1/k_{h,\rm imag}\delta r \sim 90$, where δr is the spatial grid size.

The ratio of the wave components for each wave can be calculated from the dispersion relation, and their amplitudes can be obtained by fixing the value of one component. The amplitudes of the wave components for the helicon wave are $E_r \sim 56$ [V/m], $E_\theta \sim 4200$ [V/m], $E_z \sim 88$ [V/m], and $B_z \sim 0.0015$ [T], where B_z is fixed. The amplitudes of the wave components for the TG wave are $E_r \sim 80000$ [V/m], $E_\theta \sim 0.4$ [V/m], $E_z \sim 2097$ [V/m], and $B_z \sim 5.0 \times 10^{-6}$ [T], where E_r is fixed. From the amplitudes of these wave components and Fig. 4.21, we can identify whose (the helicon wave or the TG wave) structure can be seen dominantly in each component profile. From Figs. 4.22 and 4.24, one can see that the $N = 1$ mode of the TG wave which has $k_r a/2\pi \sim 4$ perpendicular wave number is excited in the plasma region. From Figs. 4.23 and 4.25, one can see that the $N = 1$ mode of the pure imaginary helicon wave which penetrates within the $\delta_{\rm H}/\delta r \sim 90$ skin depth is excited in the plasma region. This non-propagating helicon wave is essentially different from the antenna induction field (when $B_0 = 0$), since its skin depth slightly increases as the density increases ($\delta_{\rm H} = 0.03125, 0.03127$, and 0.0313 [m] at $n = 1.0 \times 10^{15}, 5.0 \times 10^{16}$, and 1.0×10^{17} [1/m^3], respectively), while that of the antenna induction field decreases ($\delta_0 = 0.031, 0.019$, and 0.014 [m] at $n = 1.0 \times 10^{15}, 5.0 \times 10^{16}$, and 1.0×10^{17} [1/m^3], respectively), where the skin depth of the antenna induction field is calculated from 2.1-2.3 without the background magnetic field ($B_0 = 0$). Using 2.1-2.3, the vector equation for $\boldsymbol{E}$ is written as

$$\nabla \times (\nabla \times \boldsymbol{E}) - \frac{\omega^2}{c^2}\boldsymbol{E} - \frac{\omega_{pe}^2}{c^2}\frac{i\omega}{\nu - i\omega}\boldsymbol{E}. \tag{4.122}$$

From 4.122, the dispersion relation for E_θ component is obtained as follows,

$$k_r^2 + k_z^2 = \frac{1}{c^2}\left(\omega^2 - \frac{\omega\omega_{pe}^2}{\omega + i\nu}\right). \tag{4.123}$$

In general experimental condition, k_z^2 is much larger than the right of 4.123, hence the k_r becomes pure imaginary and the skin depth of the antenna induction field is obtained as

$$\delta_0 = 1/k_{r,\text{imag}}, \quad \text{where } k_{r,\text{imag}} = \sqrt{\frac{1}{c^2}\left(\omega^2 - \frac{\omega\omega_{pe}^2}{\omega + i\nu}\right) - k_z^2}. \tag{4.124}$$

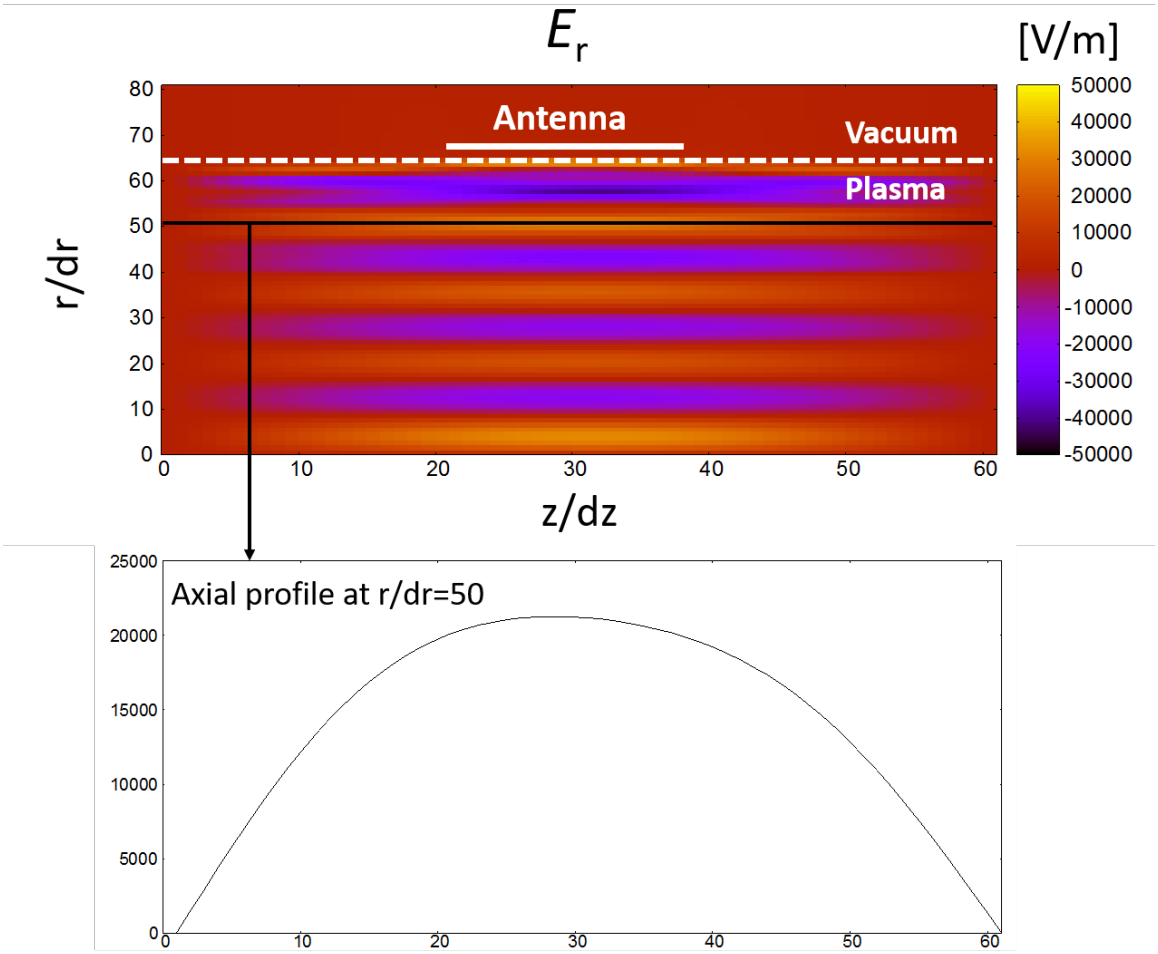

Figure 4.22: The wave profile of the E_r component at $n = 10^{16}$ [1/m^3].

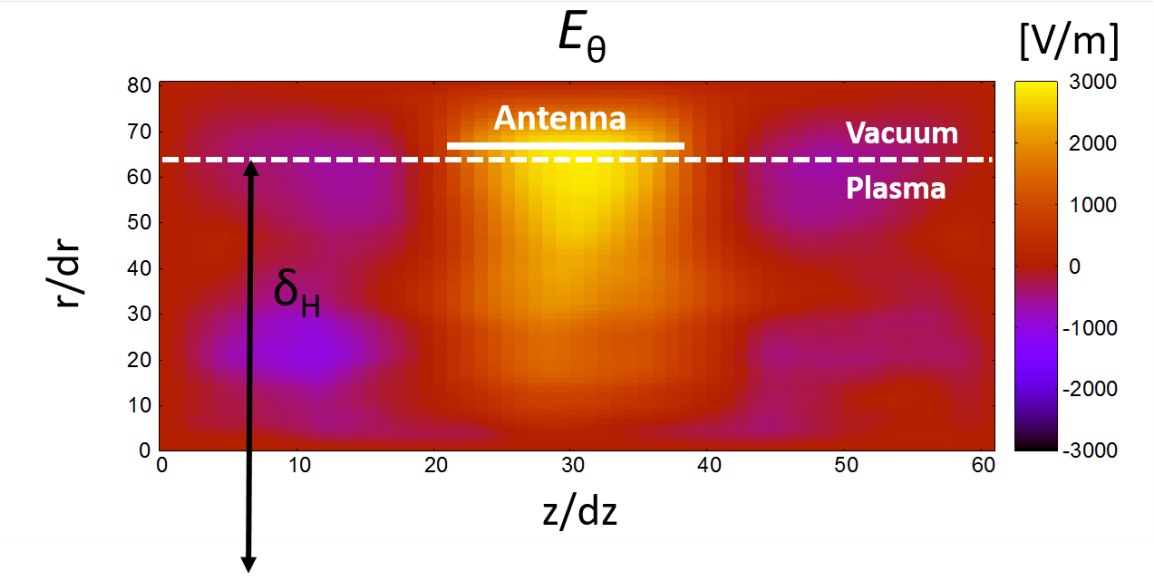

Figure 4.23: The wave profile of the E_θ component at $n = 10^{16}$ [1/m^3], where $\delta_{\mathrm{H}} = 1/k_{\mathrm{H,imag}}$ represents the skin depth of the helicon wave.

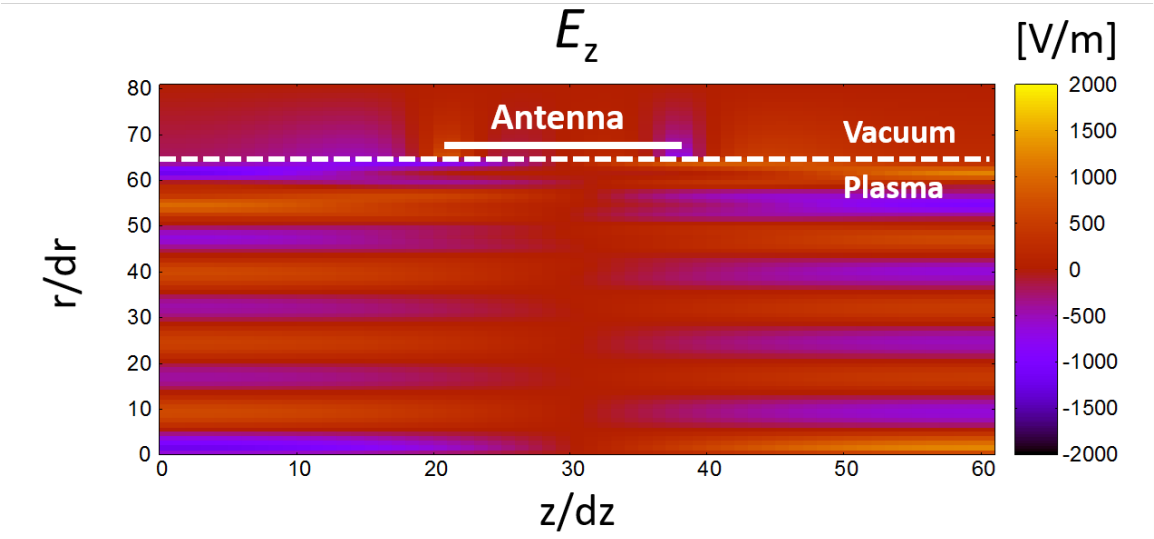

Figure 4.24: The wave profile of the E_z component at $n = 10^{16}$ [1/m^3].

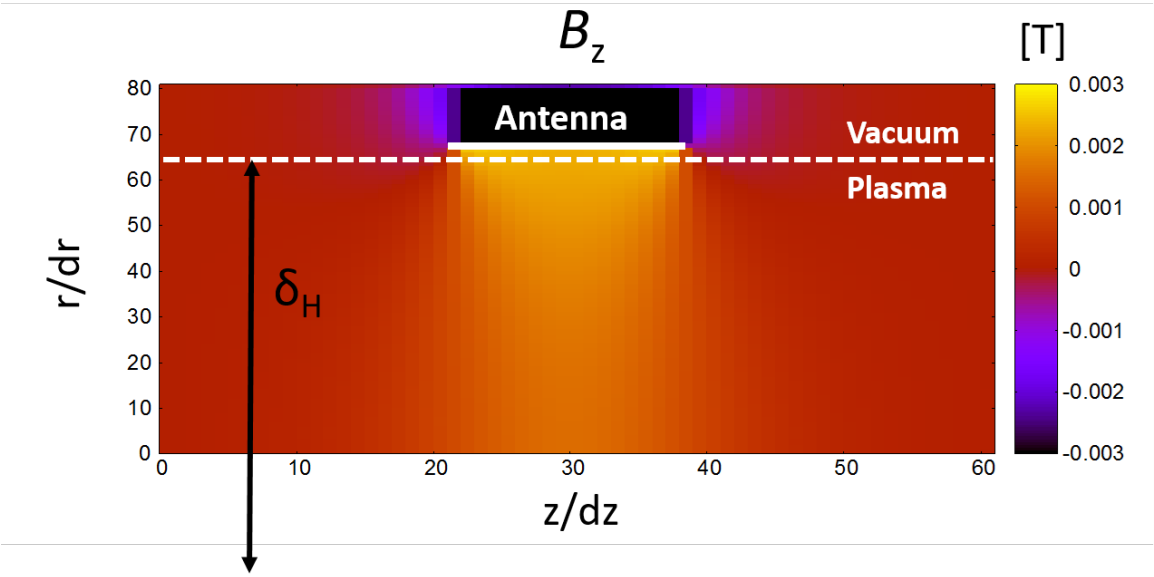

Figure 4.25: The wave profile of the B_z component at $n = 10^{16}$ $[1/\mathrm{m}^3]$, where δ_H represents the skin depth of the helicon wave.

◯ **Intermediate density**

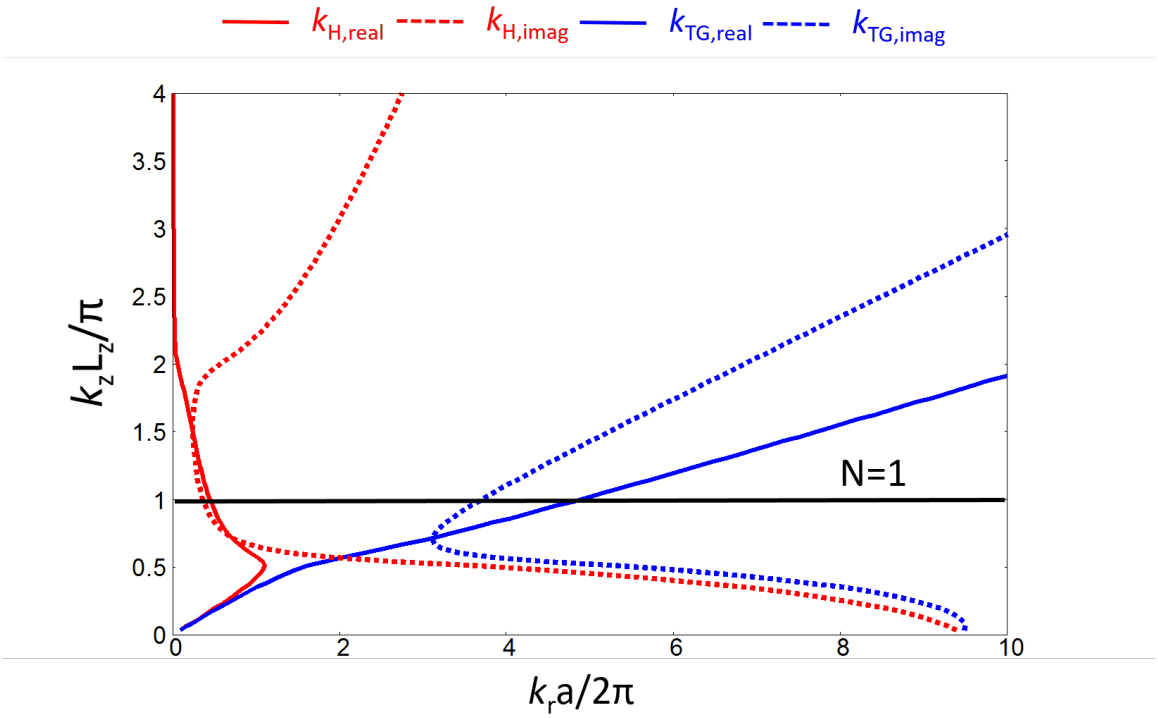

Figure 4.26: Dispersion relation of the helicon (red line) and the TG (blue line) waves at $n = 5 \times 10^{18}$ [1/m^3], where the perpendicular wave number is normalized by the plasma radius a, and the axial wave number is normalized by the twice plasma length $2L_z$, the black line represent the $N = 1$ ($k_z = 5$ [1/m]) mode of the axial standing wave. The solid lines and dotted lines represent the real part and the imaginary part of the perpendicular wave number respectively.

Figures 4.26-4.30 represent the same plots with previous ones when $n = 5 \times 10^{18}$ [1/m^3]. When the plasma density increases up to the intermediate density $n = 5 \times 10^{18}$ [1/m^3], since that density is above the cut-off density $n_{\text{low}} \sim 1.3 \times 10^{18}$ [1/m^3] for the $N = 1$ mode, the helicon wave gets to be able to propagate, but its wave length is smaller than the plasma radius as shown in Fig. 4.26. The wave number of the TG wave becomes a little larger $k_r a/2\pi \sim 5$ than previous one.

The amplitudes of the wave components for the helicon wave are $E_r \sim 13308$ [V/m], $E_\theta \sim 4200$ [V/m], $E_z \sim 270$ [V/m], and $B_z \sim 0.004$ [T], where E_θ is fixed.

The amplitudes of the wave components for the TG wave are $E_r \sim 80000$ [V/m], $E_\theta \sim 156$ [V/m], $E_z \sim 1687$ [V/m], and $B_z \sim 0.002$ [T], where E_r is fixed. From Figs. 4.27 and 4.29, one can see the wave structure of the $N = 1$ mode of the TG wave which has the perpendicular wave number $k_r a/2\pi \sim 5$. Form Figs. 4.28 and 4.30, one can see the wave structure of the $N = 1$ mode of the helicon wave which has the perpendicular wave number $k_r a/2\pi \sim 0.6$. Since the B_z component of the TG is comparable order to that of the helicon wave, one can see the superposition structure of the helicon and the TG waves from Fig. 4.27.

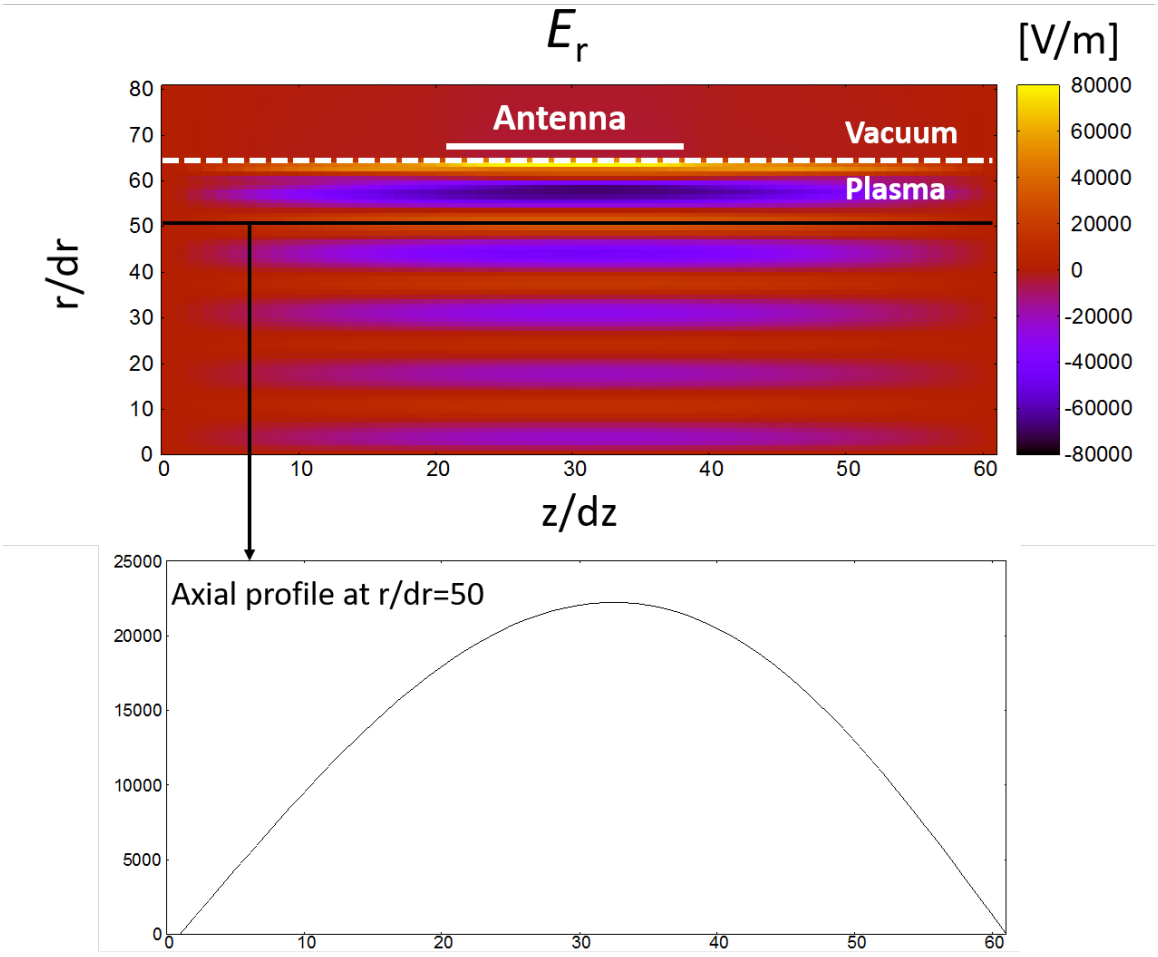

Figure 4.27: The wave profile of the E_r component at $n = 5 \times 10^{18}$ [1/m^3].

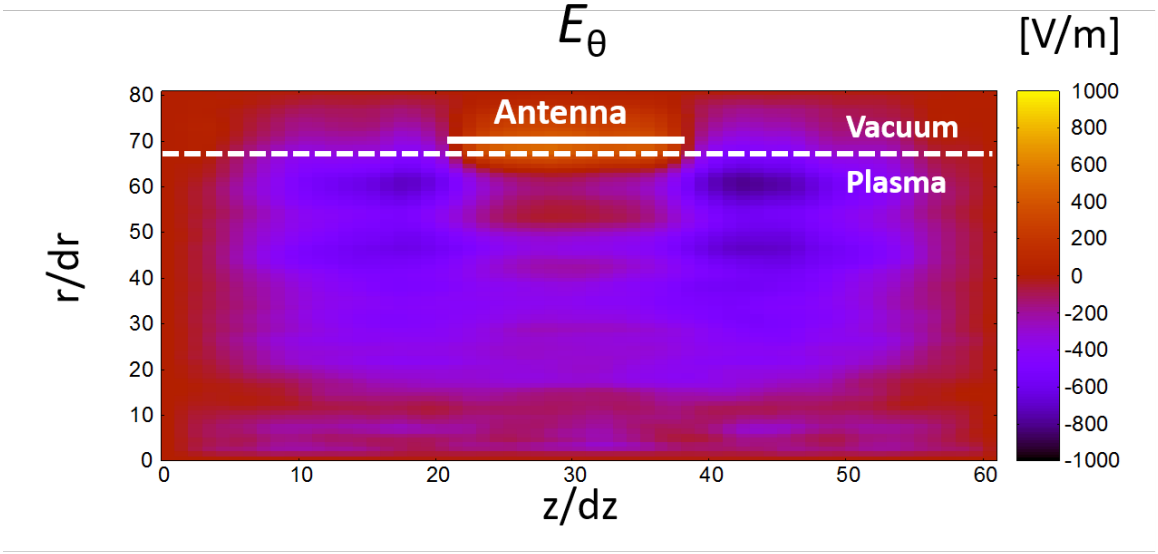

Figure 4.28: The wave profile of the E_θ component at $n = 5 \times 10^{18}$ [1/m^3].

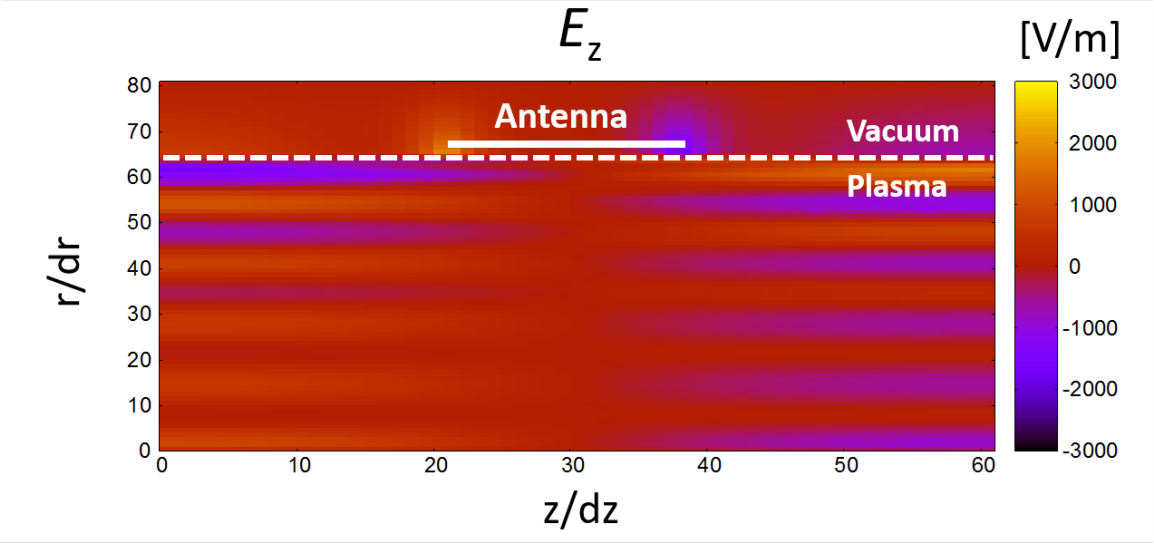

Figure 4.29: The wave profile of the E_z component at $n = 5 \times 10^{18}$ [1/m^3].

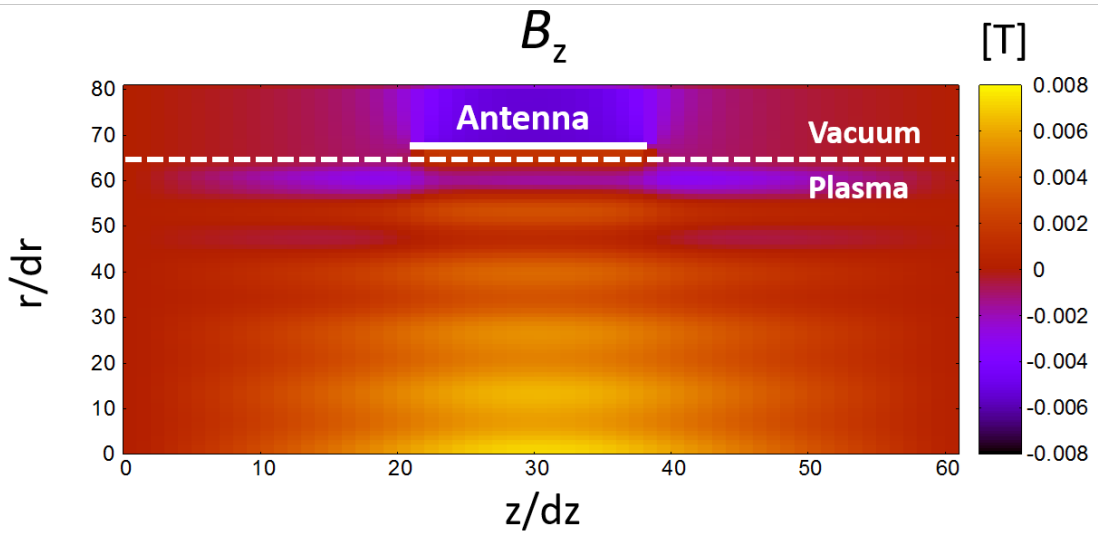

Figure 4.30: The wave profile of the B_z component at $n = 5 \times 10^{18}$ [1/m^3].

◯ **High density**

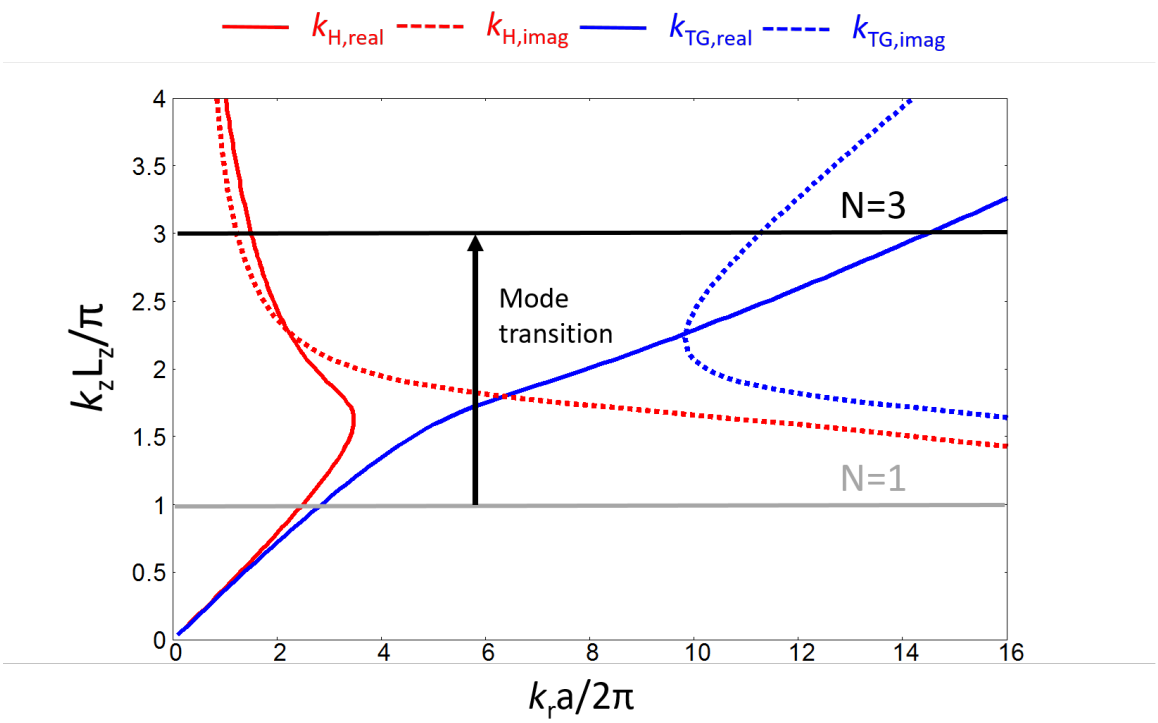

Figure 4.31: Dispersion relation of the helicon (red line) and the TG (blue line) waves at $n = 5 \times 10^{19}$ [1/m^3], where the perpendicular wave number is normalized by the plasma radius a, and the axial wave number is normalized by the twice plasma length $2L_z$, the gray and black line represent the $N = 1$ ($k_z = 5$ [1/m]) and $N = 3$ ($k_z = 15$ [1/m]) modes of the axial standing wave respectively. The solid lines and dotted lines represent the real part and the imaginary part of the perpendicular wave number respectively.

Figures 4.31-4.35 also represent the same plots with previous ones when $n = 5 \times 10^{19}$ [1/m^3]. When the plasma density increases up to the high density, that is above the upper limit density $n_{\rm up} \sim 1.6 \times 10^{19}$ [1/m^3] for the $N = 1$ mode, as seen form Fig. 4.31, $N = 1$ mode of both waves can no longer propagate and become evanescent, and then the mode transition form the $N = 1$ mode to the $N = 3$ mode occurs.

The amplitudes of the wave components for the helicon wave are $E_r \sim 7065$

[V/m], $E_\theta \sim 1400$ [V/m], $E_z \sim 144$ [V/m], and $B_z \sim 0.006$ [T], where E_θ is fixed. The amplitudes of the wave components for the TG wave are $E_r \sim 20000$ [V/m], $E_\theta \sim 44$ [V/m], $E_z \sim 421$ [V/m], and $B_z \sim 0.002$ [T], where E_r is fixed. Since the wave components of the helicon and the TG wave are all comparable order except for the E_θ component, the superposition of the $N = 3$ mode of the helicon and the TG waves, which has the perpendicular wave number $k_r a/2\pi \sim 2$ and $k_r a/2\pi \sim 14$ respectively, can be seen from Figs. 4.32, 4.34, and 4.35.

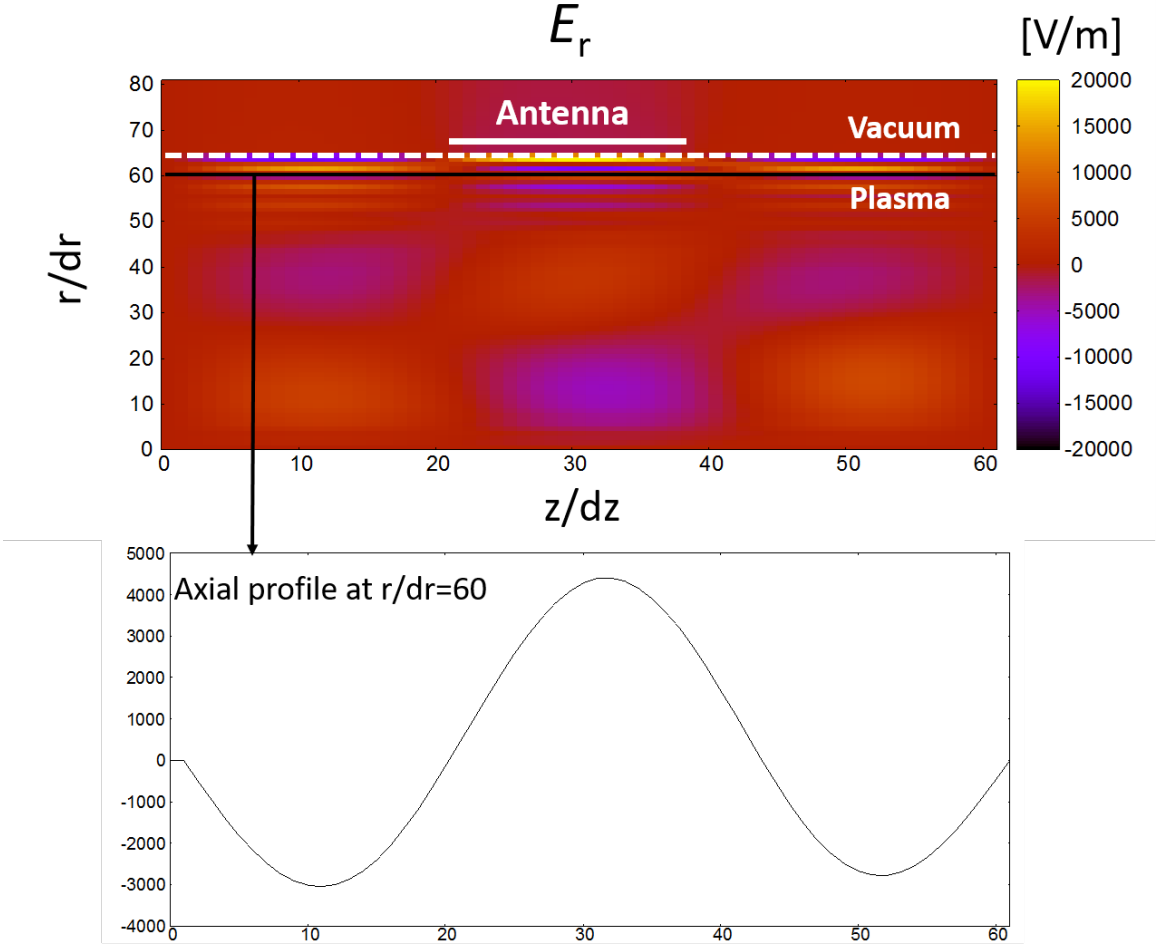

Figure 4.32: The wave profile of the E_r component at $n = 5 \times 10^{19}$ [1/m^3].

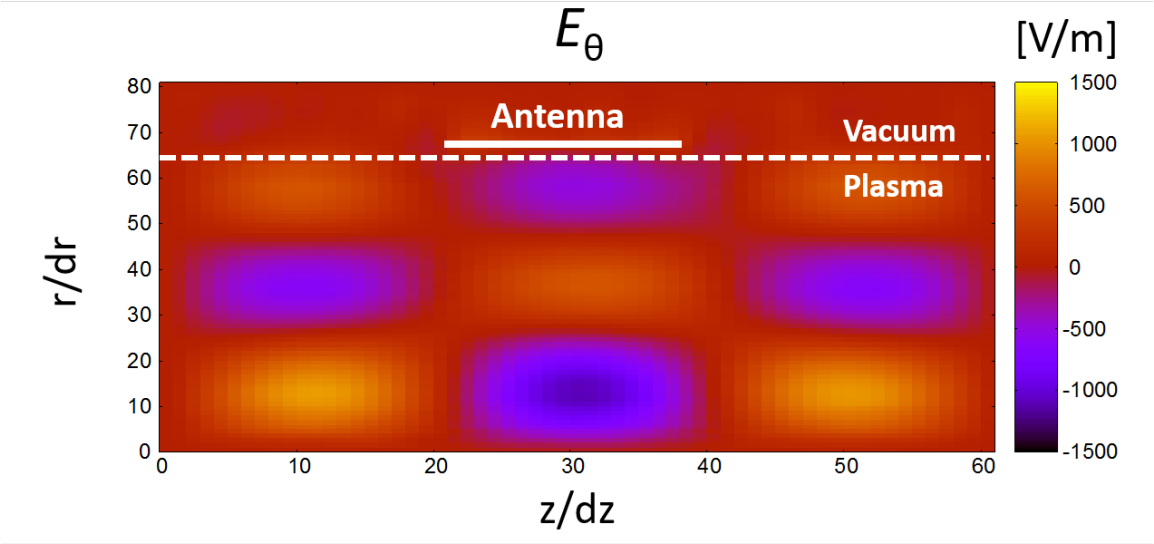

Figure 4.33: The wave profile of the E_θ component at $n = 5 \times 10^{19}$ [1/m^3].

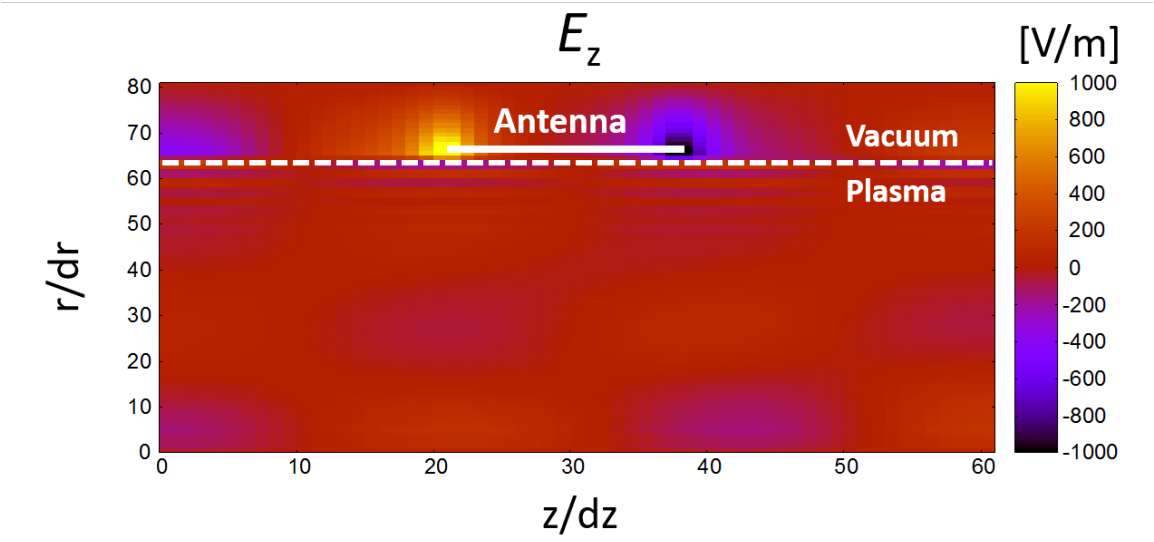

Figure 4.34: The wave profile of the E_z component at $n = 5 \times 10^{19}$ [1/m^3].

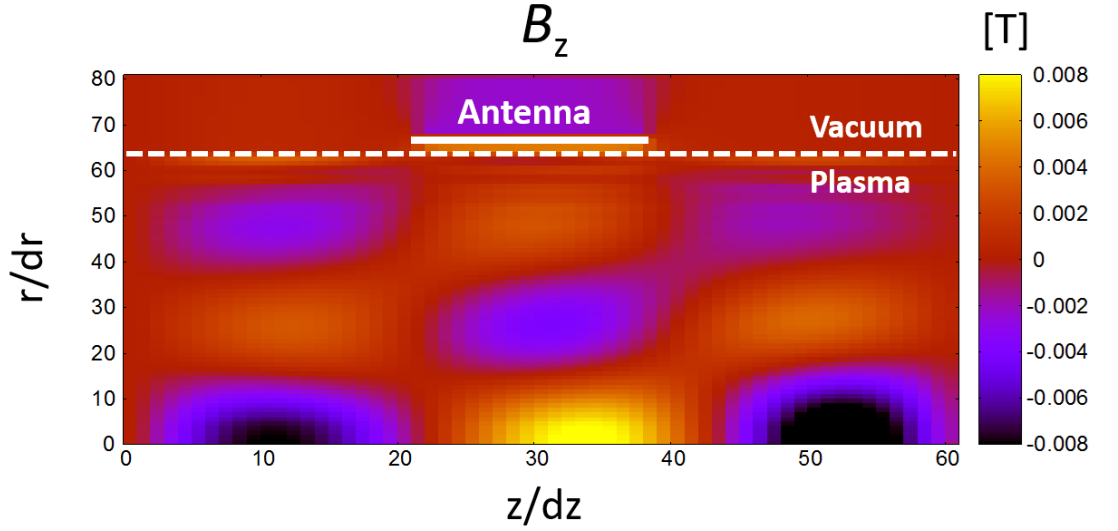

Figure 4.35: The wave profile of the B_z component at $n = 5 \times 10^{19}$ [1/m^3].

In the frequency range of $\omega_{ci} << \omega << \omega_{ce}$, the power absorption 4.76 can be approximated as [2]

$$P_{\text{abs}} = \frac{\nu\varepsilon_0}{2}\left\{A\left(|\delta E_r|^2 + |\delta E_\theta|^2\right) + B|\delta E_z|^2\right\}, \tag{4.125}$$

where the ratio of the notations $A = \omega_{pe}^2/\omega_{ce}^2$ and $B = \omega_{pe}^2/(\omega^2 + \nu^2)$ is typically $A << B$, when $\omega << \omega_{ce}$ is satisfied. From the above relation and Figs. 4.22-4.24, one notice that the TG wave is excited dominantly, even when the density is low (under the cut-off density), and the its wave components E_r and E_z can play the dominant role for the power absorption. That is a remarkable fact, since the Nisoa *et al* [2] and many other authors have been believed that the low-density mode in the helicon discharge is generated by the antenna induction field. The structure of B_z profile is not the antenna induction field, but the pure imaginary (non-propagating) helicon wave, these fields are very similar as shown in Figs 4.25 and 4.36. As Chen pointed out [41], when the finite magnetic field is applied, there can no longer exists the antenna induction field, then the density jump from the low-density mode to the

intermediate density mode is not the mode transition from the ICP mode, but the low-density helicon mode which is generated by the TG wave. One can confirm this fact if we could observe the wave profiles of E_r or E_z components of the TG wave in the experiment.

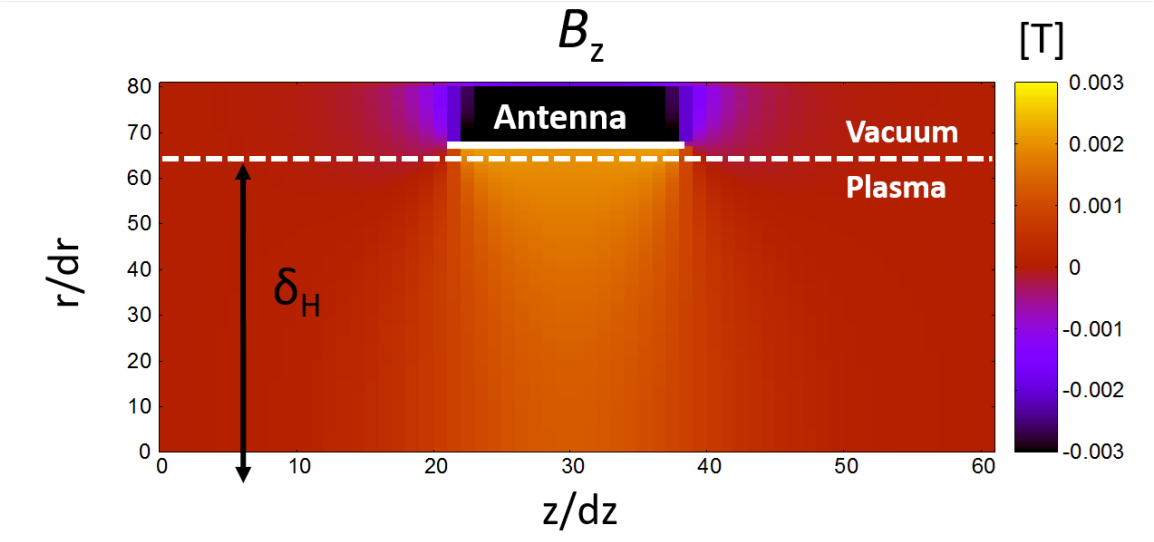

Figure 4.36: Antenna induction field $B_0 = 0$, where $\delta_{\text{skin}}/\delta r \sim 70$ represents the skin depth of the induction field.

4.7.2 Two-dimensional self-consistent discharge simulation

In this subsection, we show the results of the self-consistent simulation, and compare the results of the ambipolar diffusion model and the full fluid model. In both models, the time scale of the density growth is faster (several [μs]) than that of the experiment (several tens of [μs]), since the antenna current is larger than that applied in the experiment as mentioned above. When the discharge simulation starts from $n = 10^{16}$ [1/m^3], the pure imaginary helicon wave and the TG wave are excited, and the power absorption by the TG wave contributes to the electron heating and density growth, and thus the density profile becomes edge localized profile due to the long time scale of the perpendicular diffusion (which is due to the highly magnetization

of the charged particles) as seen in the one-dimensional results. Therefore, there still remain the question about the particle and the heat flux diffusions in the perpendicular direction. However, we found the clear difference between the ambipolar diffusion model and the full fluid model with respect to the axial heat transfer.

In the ambipolar diffusion model, the axial diffusion of the electron heat flux is strongly restricted by that of the massive ions due to the assumption of the charge neutrality $n_e = n_i$ and the flux equality $\Gamma_e = n_e u_e = \Gamma_i = n_i u_i$, and thus its time scale is much longer than that of the ionization, that leads to the axial localized density profile near the antenna. In the full fluid model, since there is no restrictions due to the above assumptions, the thermal electron can move freely along the magnetic field, that leads to considerable improvement of the axial heat transfer. We will discuss the detail of above difference in the next section. In order to make the further investigation about the axial diffusion mechanism, we conducted the simple diffusion test by the ambipolar diffusion model, the full fluid model, and the PIC-MCC model [91].

◯ **Results of the ambipolar diffusion model**

Figures 4.37-4.39 show the spatial profiles of the plasma density, the electron temperature, and the power absorption at $t \sim 0.27$ [μs] respectively. From above figures, one can see that the localized power absorption by the TG wave near the antenna result in the localized electron temperature and the density profiles. That localized density and the electron temperature profiles are resulting from the long time delay of the particle and heat flux diffusions, that time scales are strongly restricted by the assumptions of the ambipolar diffusion approximation. In this simulation, since the amount of the applied RF current density is about ten times larger than that applied in the experiment as mentioned above, the electron temperature reaches to the value over $T_e = 30$ [eV] near the antenna as seen from Fig. 4.38, which is much higher than that observed in the experiment (usually just over ten or several eV). Since such a localized density and the electron temperature in the narrow antenna region have not been observed in the experiment, these results are clearly incorrect, and thus the assumption of the ambipolar diffusion approximation is not valid as discussed above.

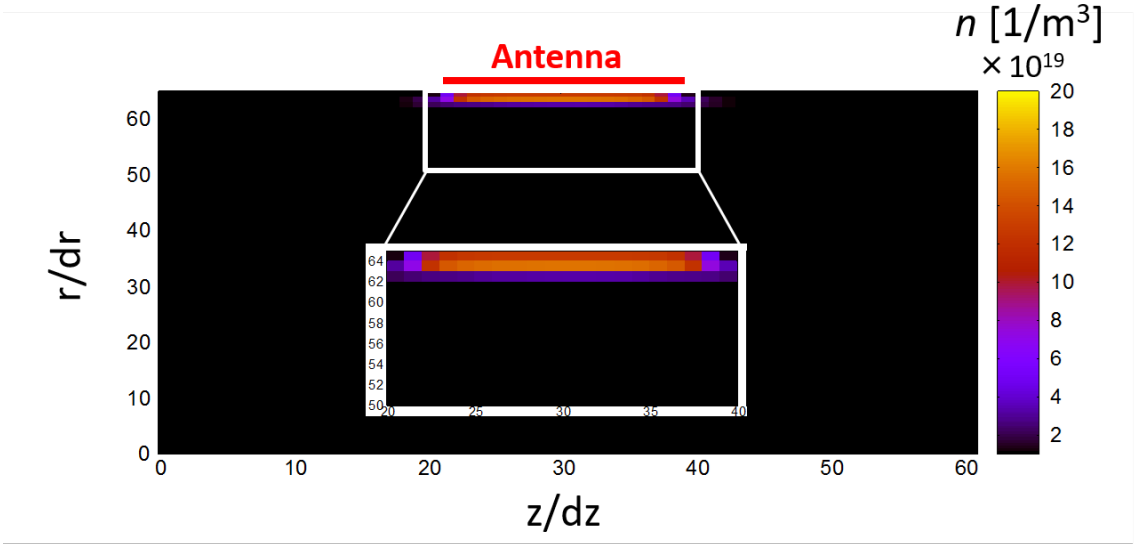

Figure 4.37: The density profile in the plasma region at $t \sim 0.27$ [μs] with applied current density $J_\theta = 3.0 \times 10^7$ [A/m^2].

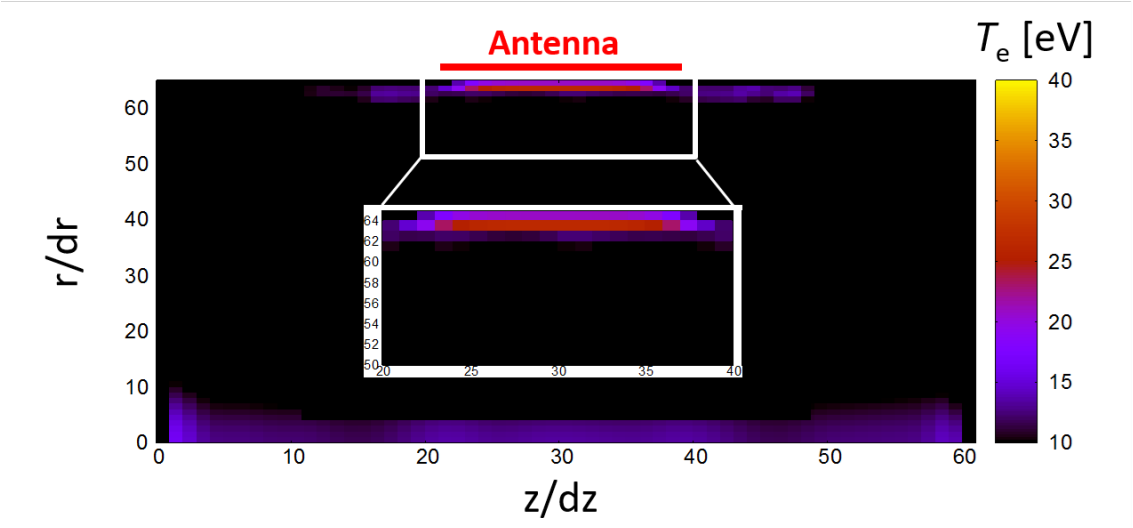

Figure 4.38: The electron temperature profile in the plasma region at $t \sim 0.27$ [μs] with applied current density $J_\theta = 3.0 \times 10^7$ [A/m^2].

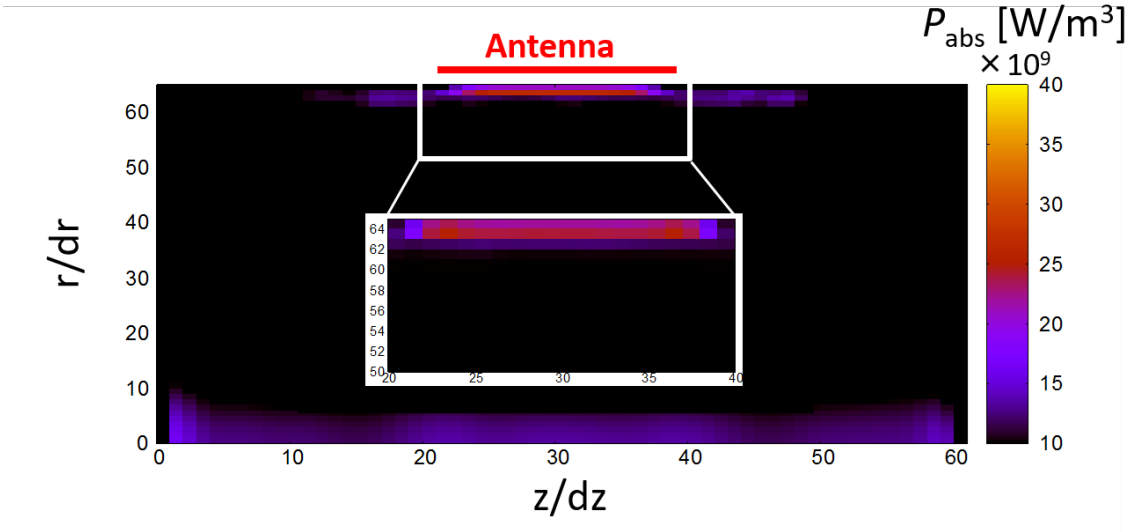

Figure 4.39: The power absorption profile in the plasma region at $t \sim 0.27$ [μs] with applied current density $J_\theta = 3.0 \times 10^7$ [A/m^2].

◯ Results of the full fluid model

Figures 4.40-4.43 show the spatial profiles of the plasma density, the electron temperature, the power absorption, and the wave field of the E_r component respectively $t \sim 0.24$ [μs] with applied current density $J_\theta = 3.0 \times 10^7$ [A/m^2]. As one can see from Figs. 4.40-4.42 and Figs. 4.44-4.46, axial profile of the electron temperature (the value over 50 [eV] is much higher than that observed in the experiment, and thus the time scale of the density growth within 1 [μs] is also faster than that within several tens of μs in the experiment) is almost uniform, and that leads to the axially broad density profile despite the localized power absorption profile near the antenna. The axial heat flux diffusion is greatly enhanced in the full fluid model. Since there is no restriction of the flux equality between the electrons and ions in the full fluid model, energetic electrons can move freely at its thermal speed, and that leads to much faster heat flux diffusion than that in the ambipolar diffusion. The difference of the axial heat transfer between the two models will be discussed in the next subsection.

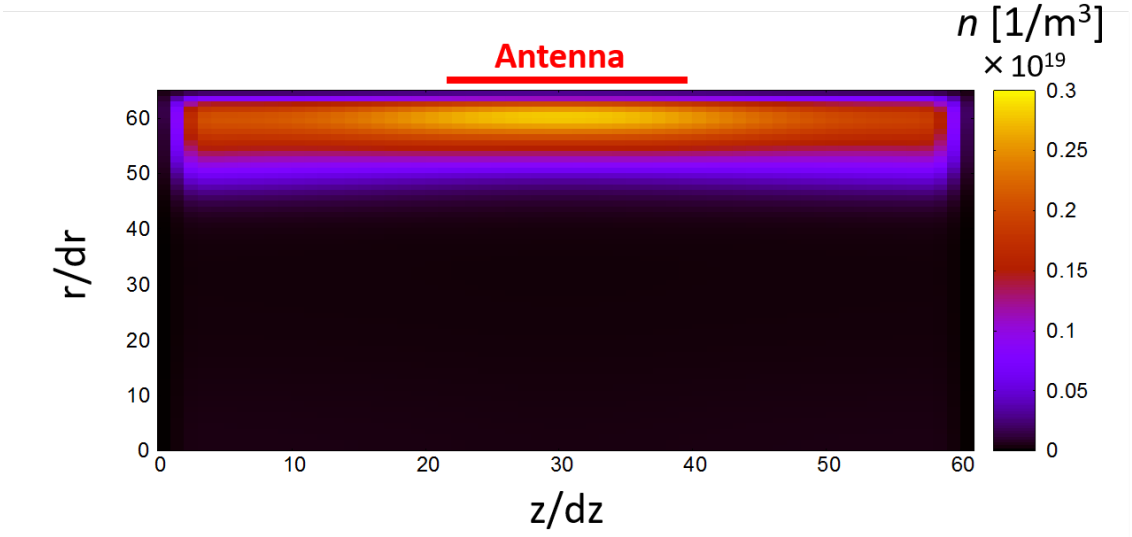

Figure 4.40: The density profile in the plasma region at $t \sim 0.24$ [μs] with applied current density $J_\theta = 3.0 \times 10^7$ [A/m^2].

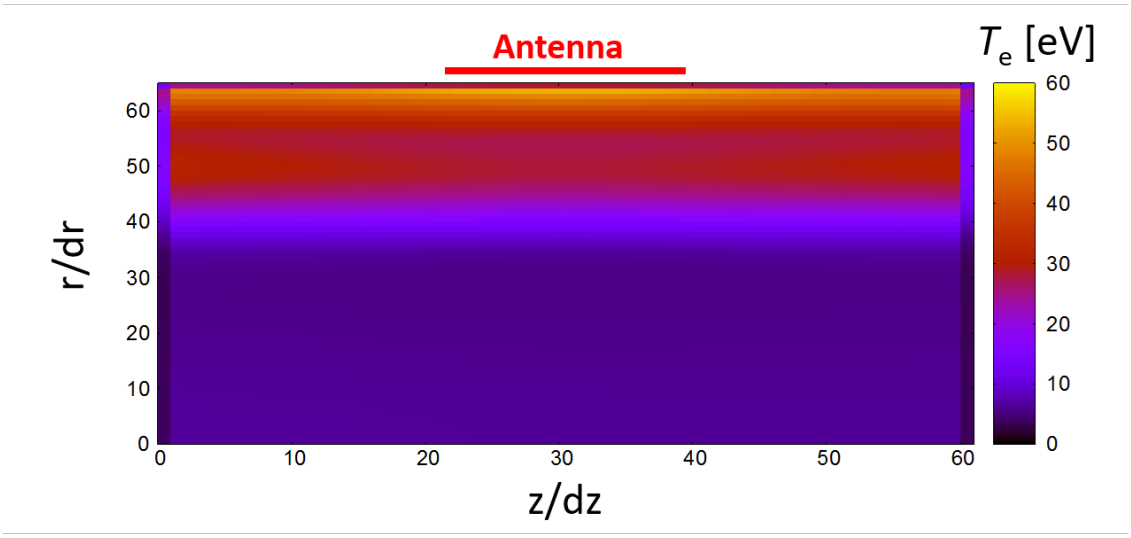

Figure 4.41: The electron temperature profile in the plasma region at $t \sim 0.24$ [μs] with applied current density $J_\theta = 3.0 \times 10^7$ [A/m^2].

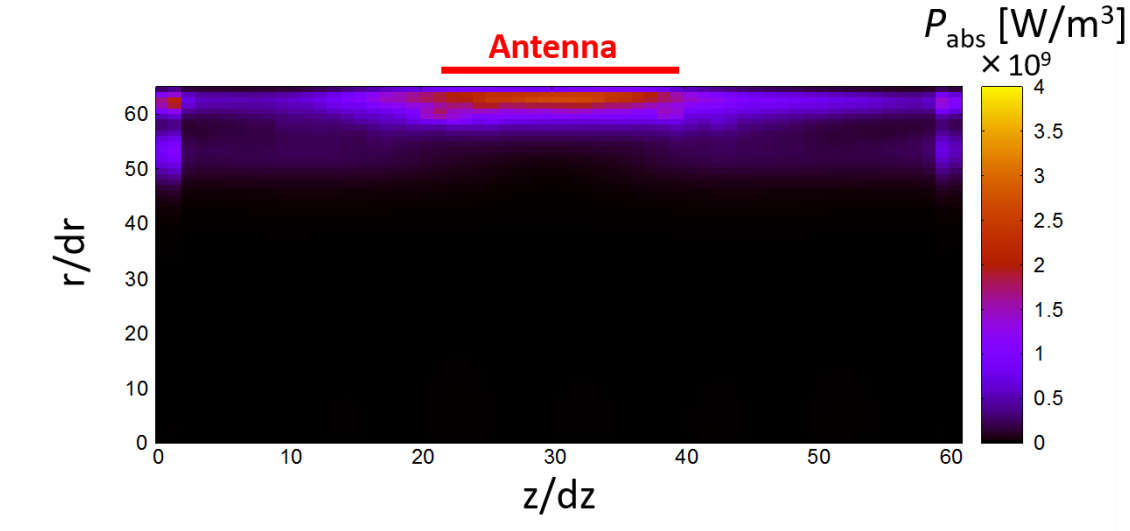

Figure 4.42: The power absorption profile in the plasma region at $t \sim 0.24$ [μs] with applied current density $J_\theta = 3.0 \times 10^7$ [A/m^2].

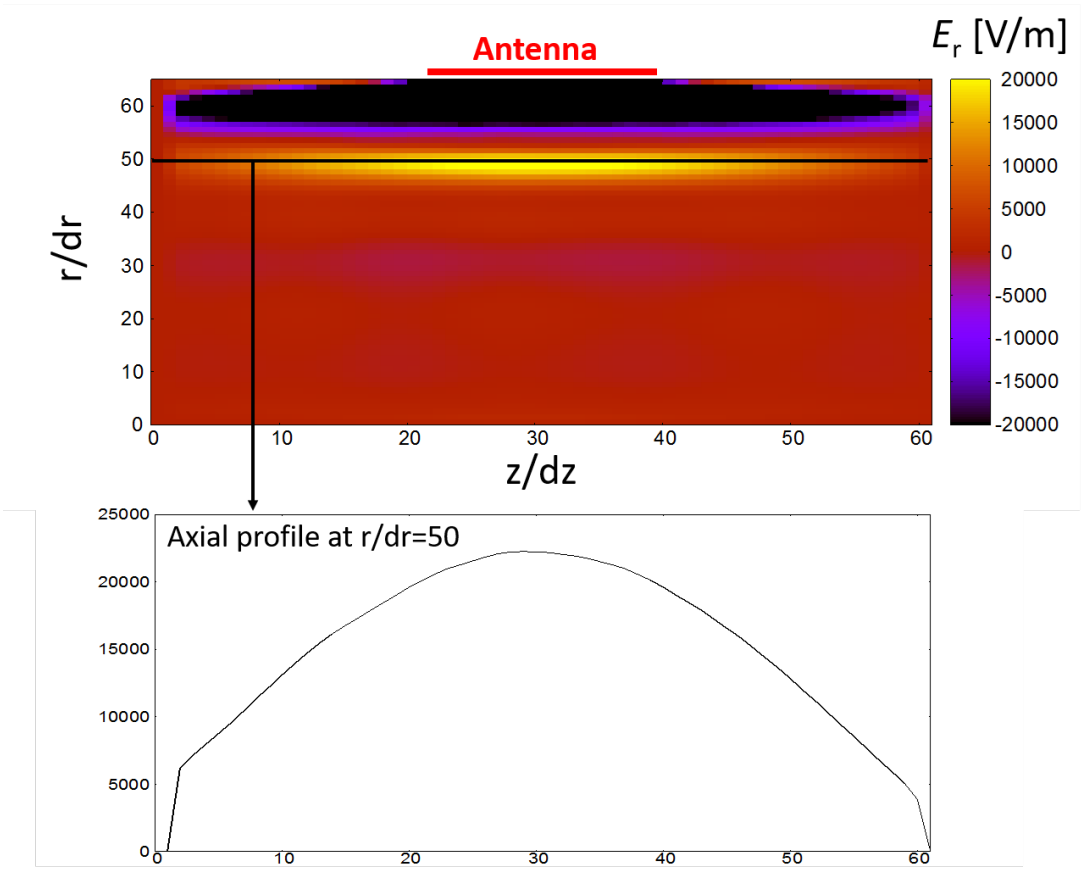

Figure 4.43: The wave field E_r profile in the plasma region at $t \sim 0.24$ [μs] with applied current density $J_\theta = 3.0 \times 10^7$ [A/m^2].

Figures 4.44-4.47 show the same results with Figs. 4.40-4.43 but at $t \sim 0.45$ [μs] instead of $t \sim 0.24$ [μs]. At that time ($t \sim 0.45$ [μs]), the $N = 1$ mode TG wave is excited in the plasma region as shown in Fig. 4.43. At $t \sim 0.45$ [μs], the plasma density increases up to $n \sim 7.0 \times 10^{19}$ [1/m^3], and the electron temperature relaxes to the value just over a dozen. Since the $N = 1$ mode become evanescent in the high density (above the upper limit density $n_{up} \sim 1.6 \times 10^{19}$ [1/m^3]) region, one can see the $N = 3$ mode is excited in the high density region near the antenna as shown in Fig. 4.47. Since $t \sim 0.45$ [μs] is not enough time to discuss the steady state and the input power is about ten times higher than that in the experiment, the discussions about the steady state and the density jump should be made by the future improved model using the implicit method for time integration.

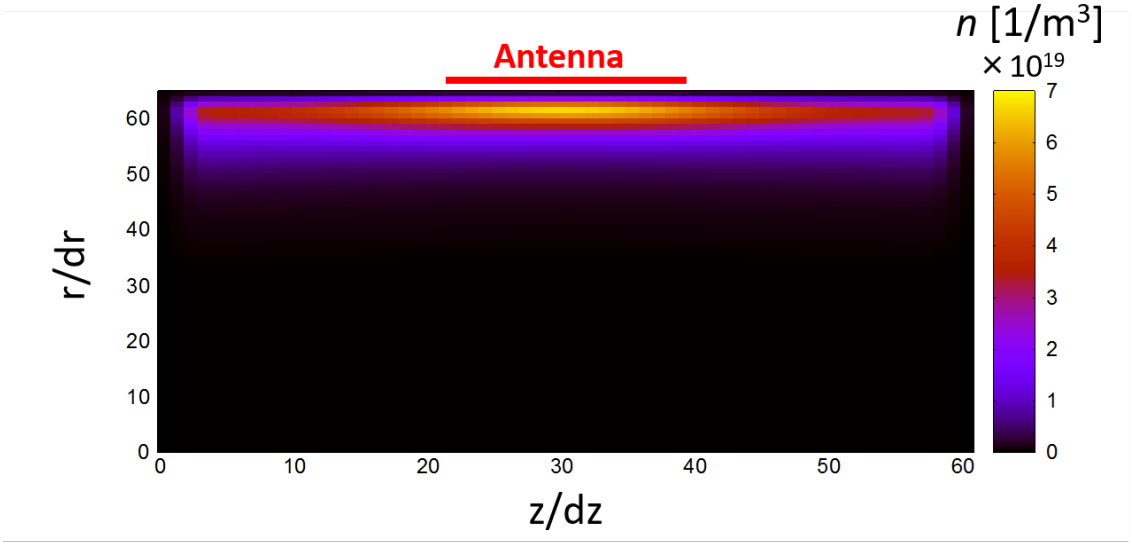

Figure 4.44: The density profile in the plasma region at $t \sim 0.45$ [μs] with applied current density $J_\theta = 3.0 \times 10^7$ [A/m^2].

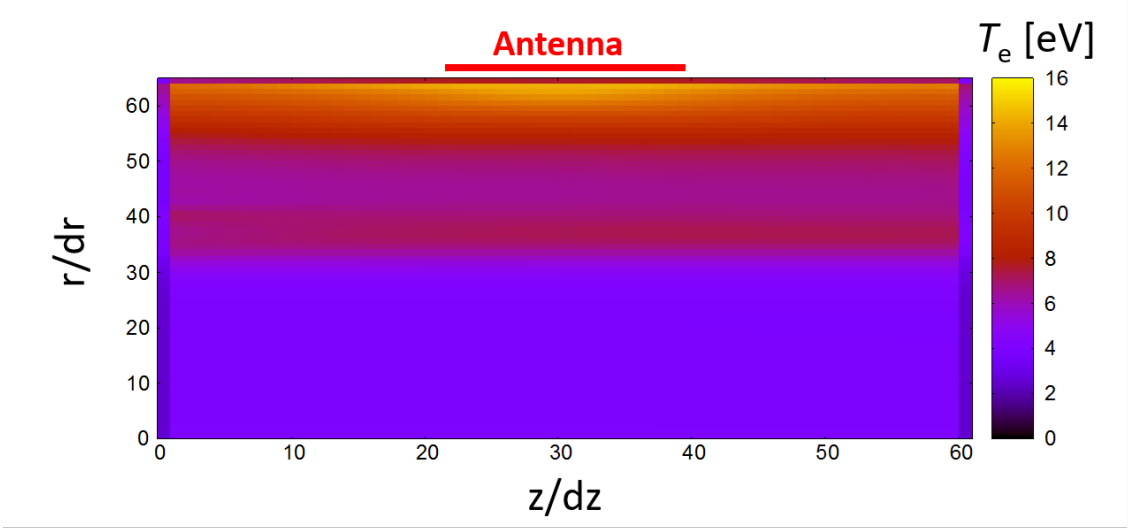

Figure 4.45: The electron temperature profile in the plasma region at $t \sim 0.45$ [μs] with applied current density $J_\theta = 3.0 \times 10^7$ [A/m^2].

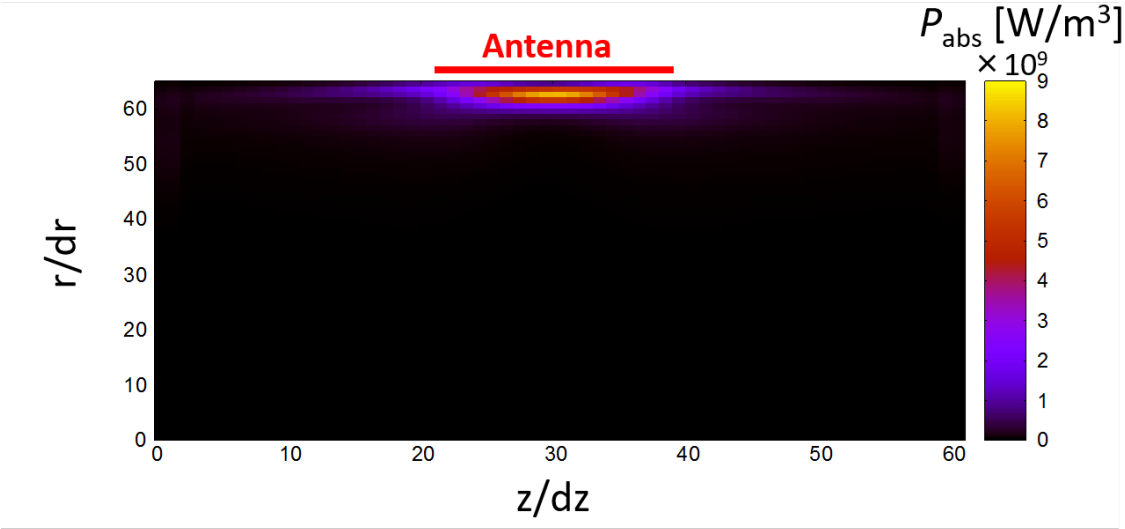

Figure 4.46: The power absorption profile in the plasma region at $t \sim 0.45$ [μs] with applied current density $J_\theta = 3.0 \times 10^7$ [A/m^2].

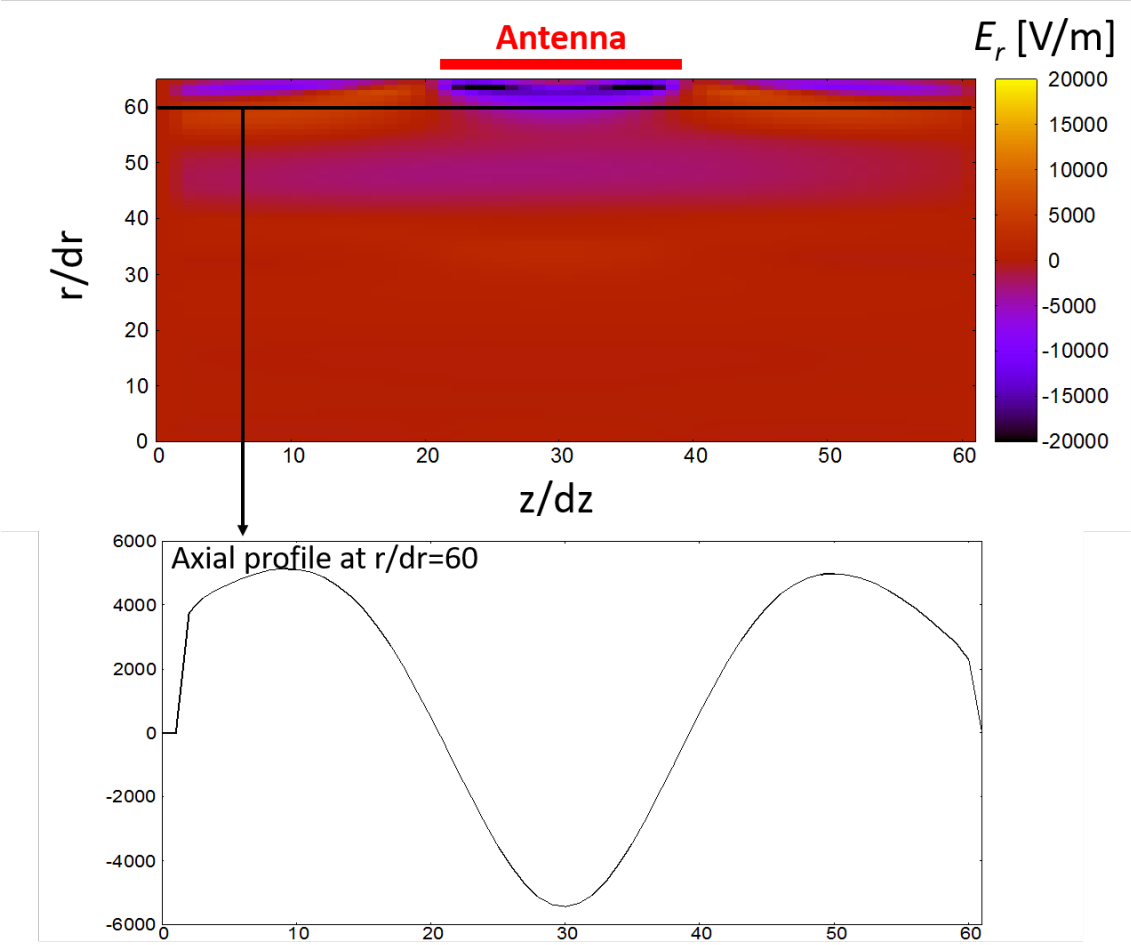

Figure 4.47: The wave field E_r profile in the plasma region at $t \sim 0.45$ [μs] with applied current density $J_\theta = 3.0 \times 10^7$ [A/m^2].

4.7.3 The diffusion test

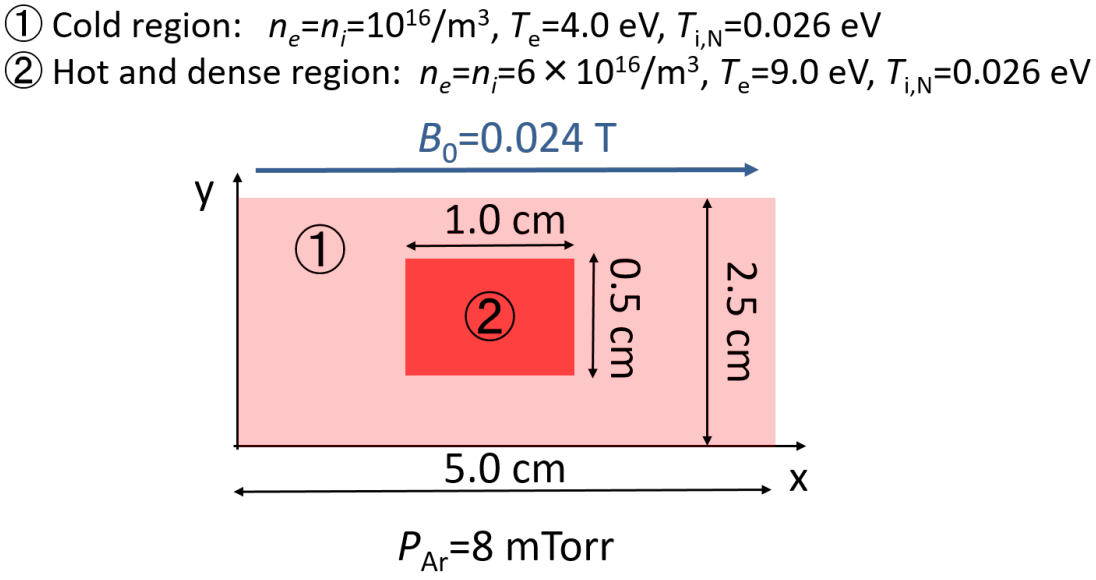

Figure 4.48: The model used in the diffusion test. There consist of the region 1. The cold electron region, where $T_e = 4.0$ [eV], $T_i = 0.026$ [eV], and $n_e = n_i = 10^{16}$ [1/m^3], and the region 2. The hot-dense region, where $T_e = 10.0$ [eV], $T_i = 0.026$ [eV], and $n_e = n_i = 6.0 \times 10^{16}$ [1/m^3].

The model used for the diffusion test is shown in Fig. 4.48 that consists of the cold electron region (region 1), where $T_e = 4.0$ [eV], $T_i = 0.026$ [eV], and $n_e = n_i = 10^{16}$ [1/m^3], and the hot-dense region (region 2), where $T_e = 10.0$ [eV], $T_i = 0.026$ [eV], and $n_e = n_i = 6.0 \times 10^{16}$ [1/m^3]. In this section, we show the results of the diffusion test, in order to investigate the axial heat transfer mechanism and clear the difference between the ambipolar diffusion and the full fluid model by comparing their results. Besides these two models, we conducted this diffusion test by the PIC-MCC model [91].

◯ Comparison between the ambipolar diffusion model and the full fluid model

Figures 4.49 and 4.50 show the results of the plasma density profile $n_e = n_i$ and the electron temperature profile in the ambipolar diffusion model respectively, and Figs. 4.51 and 4.52 show the same results in the full fluid diffusion model. These results are obtained at $t \sim 0.033$ [μs] which is much faster than the ionization time scale $t \sim 0.1$ [μs] in the both models. One can see the clear difference in the electron temperature profile between the result of the ambipolar diffusion model and the full fluid model as shown in Figs. 4.50 and 4.52. Since the axial heat flux diffusion is much faster than that in the ambipolar diffusion model, the electron temperature profile is relatively uniform over the axial direction in the full fluid model, while that is still localized in the hot-dense region in the ambipolar diffusion model. In both models, the perpendicular diffusion of the heat flux can not be seen due to the strong magnetization of the charge particles, and there still remains the dense region of the plasma density.

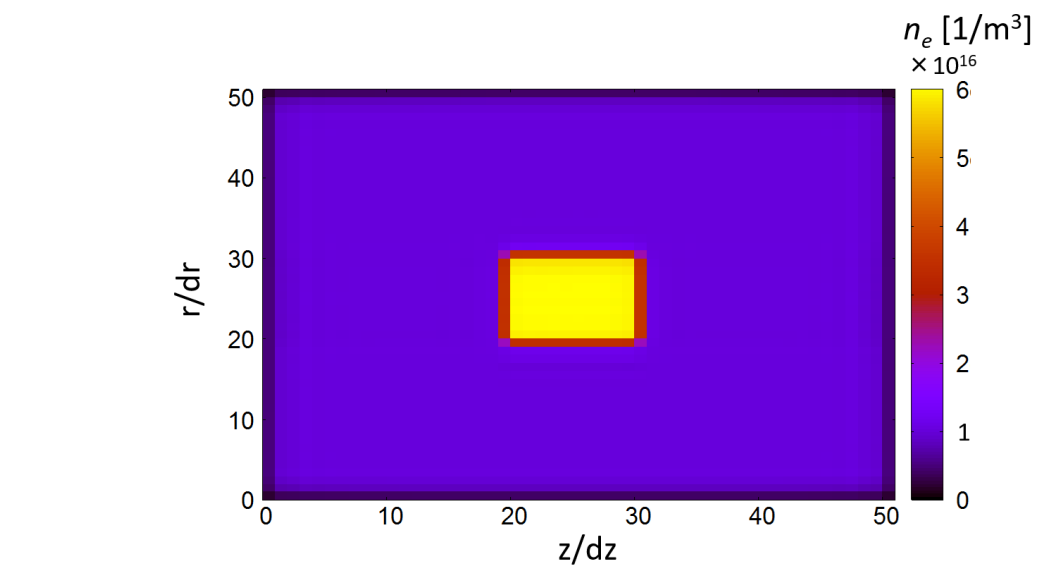

Figure 4.49: The plasma density $n_e = n_i$ profile in the ambipolar diffusion model at $t \sim 0.033$ [μs].

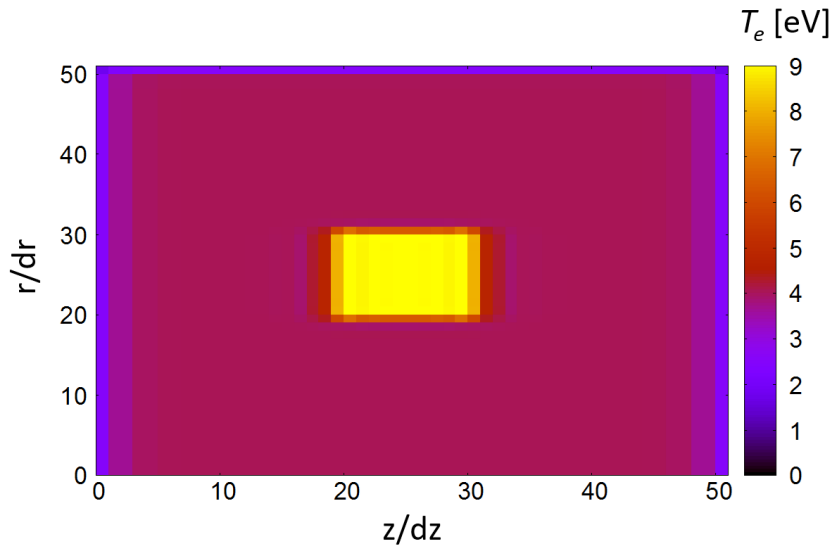

Figure 4.50: The electron temperature T_e profile in the ambipolar diffusion model at $t \sim 0.033$ [μs].

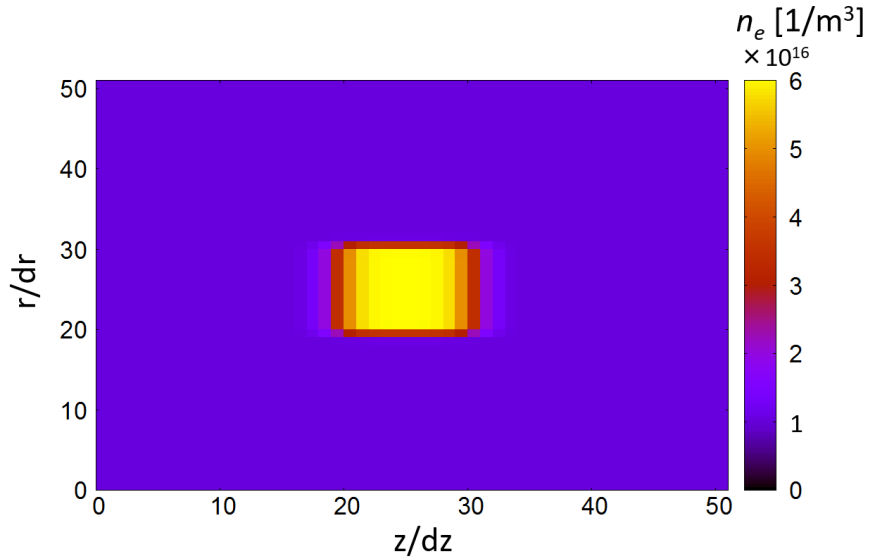

Figure 4.51: The plasma density $n_e \sim n_i$ profile in the full fluid model at $t \sim 0.033$ [μs].

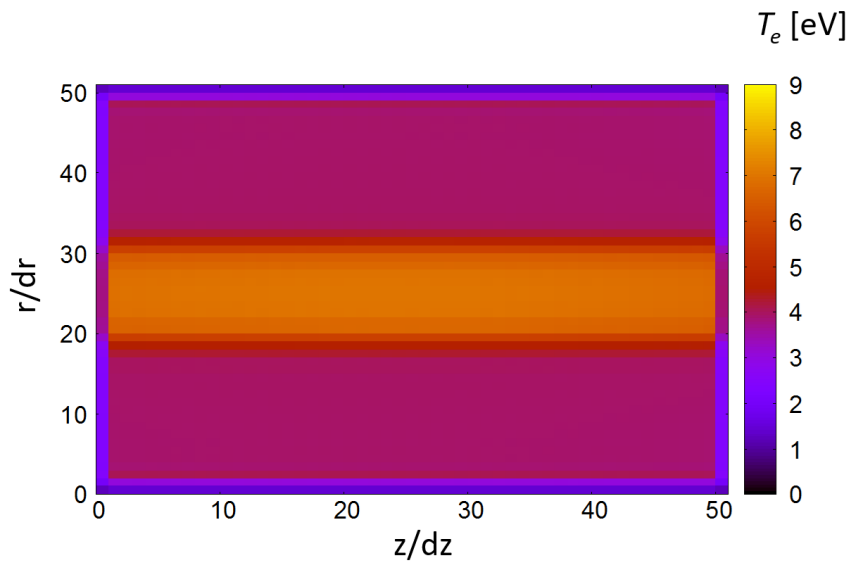

Figure 4.52: The electron temperature T_e profile in the full fluid model at $t \sim 0.033$ [μs].

The difference between these two models is associated with the term of heat flux in the energy balance equation 4.45. Here, we rewrite the electron heat flux in each model: For the ambipolar diffusion model,

$$\boldsymbol{q}_e = -\kappa_\perp \nabla_\perp T_e - \kappa_\parallel \nabla_\parallel T_e \quad [J/m^2 s], \tag{4.126}$$

where the thermal conductivity κ is given by

$$\kappa_{a,\parallel} = \frac{5}{2} n_e k_B D_{a,\parallel}, \quad \text{for parallel direction} \tag{4.127}$$

and

$$\kappa_{a,\perp} = \frac{\kappa_{a,\parallel}}{1 + (\omega_{ce}/\nu_e)^2}. \quad \text{for perpendicular direction} \tag{4.128}$$

The flow of the thermal energy density at the fluid velocity u_e is neglected in the ambipolar diffusion model, and thus the heat flux consists of only the energy transport associated with the random thermal motion. However, since the electrons can not diffuse independently due to the ambipolar electric field that attracts electrons to ions to keep the charge neutrality, the heat conductivity is given by using the ambipolar diffusion coefficient. The denomination on the right in 4.128 represents the effect of the magnetization, which is usually much larger than unity since the electron cyclotron frequency is much larger than the electron collision frequency $\omega_{ce} >> \nu_e$. For the full fluid model,

$$\boldsymbol{q}_e = \frac{5}{2} \boldsymbol{\Gamma}_e k_B T_e - \kappa_\perp \nabla_\perp T_e - \kappa_\parallel \nabla_\parallel T_e \quad [J/m^2 s], \tag{4.129}$$

where the thermal conductivity κ is given by

$$\kappa_\parallel = \frac{5}{2} n_e k_B D_e = \frac{5}{2} \frac{p_e}{m_e \nu_e}, \quad \text{for parallel direction} \tag{4.130}$$

and

$$\kappa_{\perp} = \frac{\kappa_{\parallel}}{1 + (\omega_{ce}/\nu_e)^2}. \quad \text{for perpendicular direction} \tag{4.131}$$

In the full fluid model, the heat flux consists of the energy transport associated with the drift motion (the first term on the right in 4.129, and the random thermal motion (the second term on the right in 4.129. Since there is no restrictions of the flux equality between the electrons and ions, the heat conductivity is given by the electron diffusion coefficient.

Figure 4.53 shows the heat flux 4.126 profile evaluated in the ambipolar diffusion model at $t \sim 0.0033$ [μs], and Figs. 4.54 and 4.55 show the profiles of the heat flux associated with the drift motion (the first term on the right in 4.129 and the random thermal motion (the second term on the right in 4.129 respectively. As seen form above figures, it is clear that the energy transport by the electron random thermal motion in the full fluid model (the heat flux over the axial direction is due to the gradient of the electron temperature) is much larger than that in the ambipolar diffusion model and that by the drift motion in the full fluid model. Therefore, the random thermal motion of the electrons plays important role on the axial energy transport, and that leads to the axial uniform electron temperature profile and the axial broaden plasma density profile in the helicon discharge despite the localized power absorption profile near the antenna. However, there still remain the questions about why the plasma density does not change in the dense region as shown in Fig. 4.51 and how the charge neutrality is conserved when the thermal electrons diffuse freely in the axial direction. Actually, the answers to these questions are associated with the particle transport mechanism from the background plasma (cold region) to the hot-dense region. This particle transport mechanism can be understood clearly by the results of the PIC-MCC model.

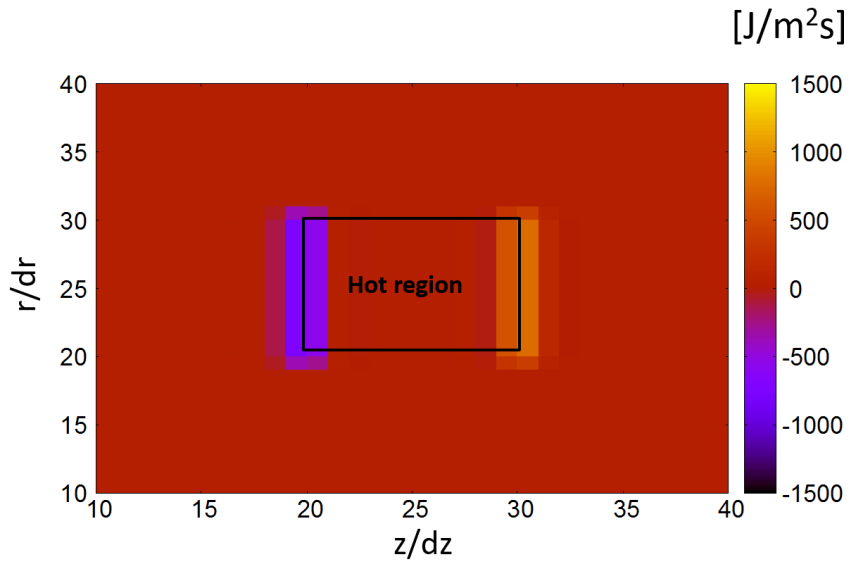

Figure 4.53: The profile of the axial heat flux 4.126 [J/m^{2}s] in the ambipolar diffusion model at $t \sim 0.0033$ [μs].

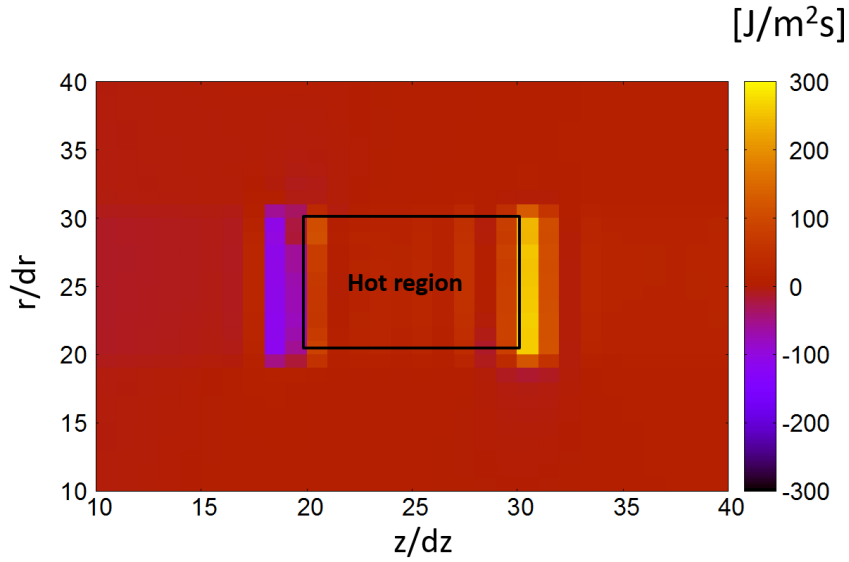

Figure 4.54: The profile of the axial heat flux [J/m^{2}s] associated with the drift motion (the first term on the right in 4.129 in the full fluid model at $t \sim 0.0033$ [μs].

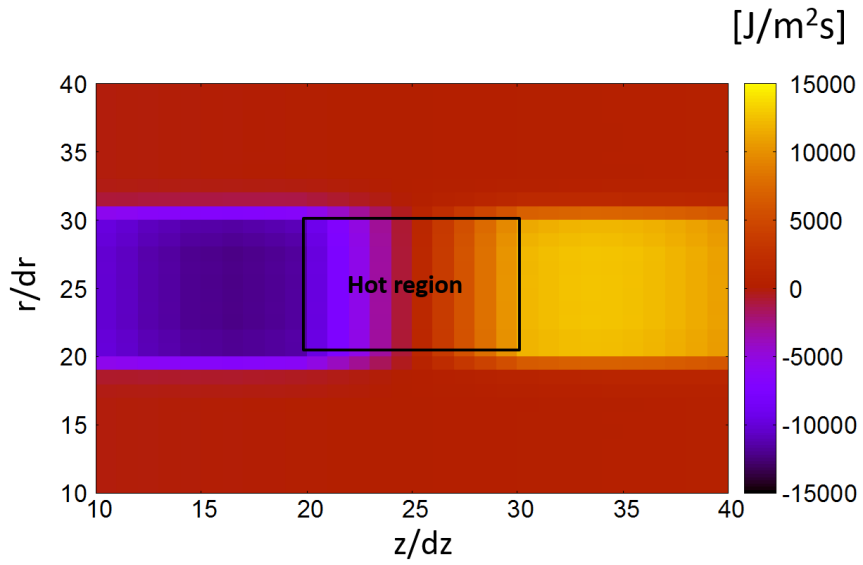

Figure 4.55: The profile of the axial heat flux [J/m^{2}s] associated with the random thermal motion (the second term on the right in 4.129) in the full fluid model at $t \sim 0.0033$ [μs].

◯ **The results of the PIC-MCC model**

In the PIC-MCC simulation, the following parameters are used, the density of the super particle: $n_{\text{super}} = 1.0 \times 10^{14}$ [1/m^3], the number of super particle per cell: $n_{\text{pcel}} = 100$ in the background (region 1) and $n_{\text{pcel}} = 600$ in the dense region (region 2), the velocities of the electrons and ions are given by the Maxwellian at $T_e = 4.0$, $T_i = 0.026$ [eV] in the cold region (region 1) and at $T_e = 9.0$, $T_i = 0.026$ [eV] in the hot region (region 2), the grid size: $\Delta x = 0.19 \times \lambda_e$(the Debye length at $T_e = 4.0$ [eV]), and $\Delta x = 0.39 \times \lambda_e$, the time step size: $\Delta t = 1.3 \times 10^{-12}$ [s], the number of the spatial grid: $n_{ng,x} = n_{ng,z} = 50$, and the number of time step: $nt = 24000$. The collisions of the electron-neutral (only the elastic collision, excitation and ionization are omitted) and ion-neutral (the elastic collision and the charge exchange) are included with the Ar neutral pressure $P_{\text{Ar}} = 8$ [mTorr] in the PIC-MCC model.

Figures 4.56 and 4.57 show the electron temperature profile and the density profile, and Figs 4.58 and 4.59 show the profiles of the cold electron density and the hot electron density respectively, Fig. 4.60 shows the electric field E_x profile, which is generated by the potential difference between the hot-dense region and the background cold region, and Figs 4.61 and 4.62 show the spatial distributions of ions and electrons respectively, where the particles in the hot-dense region and in the background cold region are plotted separately. From Figs 4.56 and 4.57, one can see that the electron temperature diffuses in the axial direction, while the electron density in the hot region remains constant.

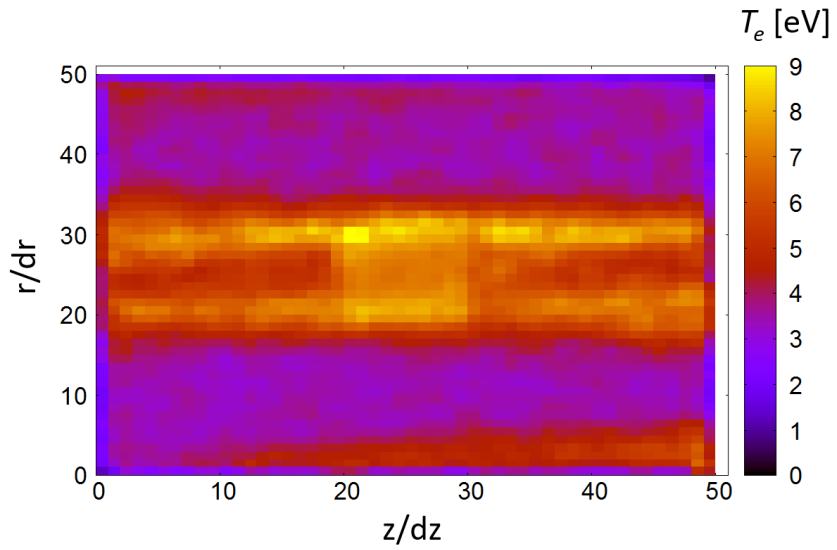

Figure 4.56: The electron temperature T_e profile at $t \sim 0.032$ [μs].

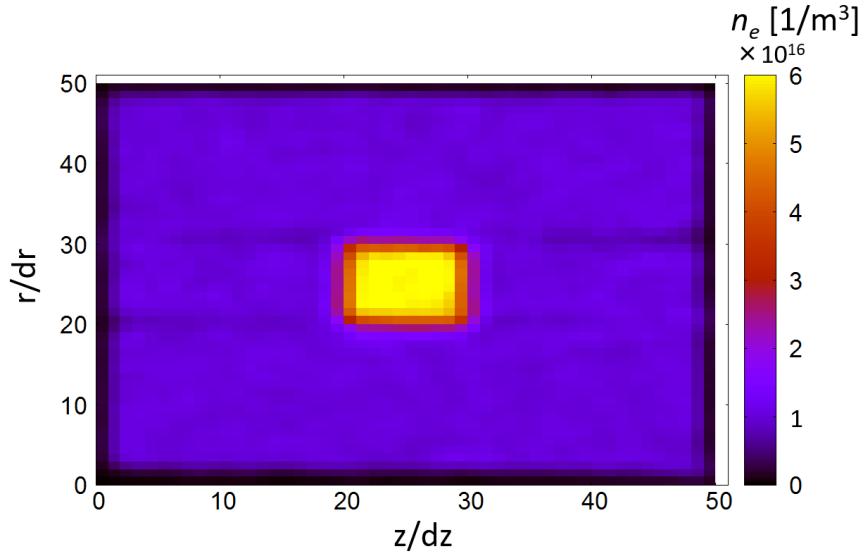

Figure 4.57: The plasma density $n_e \approx n_i$ profile at $t \sim 0.032$ [μs].

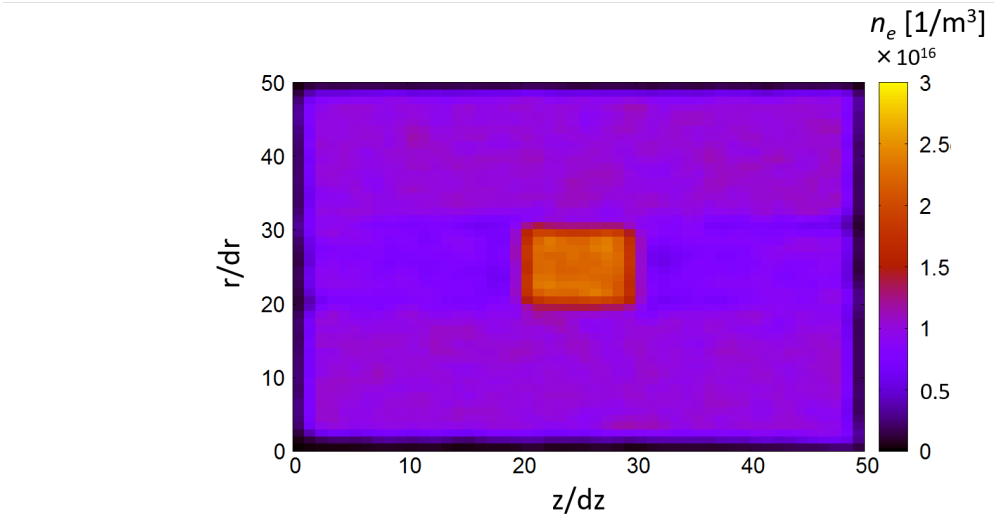

Figure 4.58: The cold electron density profile at $t \sim 0.032$ [μs].

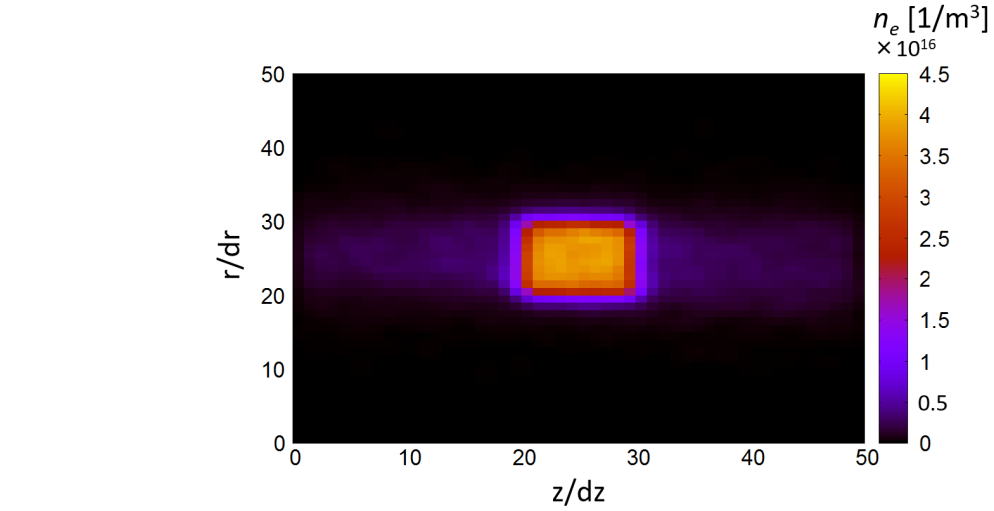

Figure 4.59: The hot electron density profile at $t \sim 0.032$ [μs].

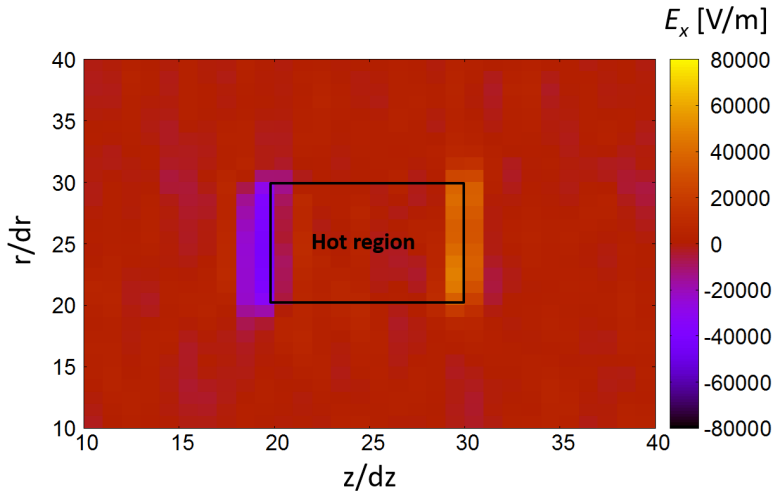

Figure 4.60: The electric field E_x profile at $t \sim 0.032$ [μs], which is generated by the potential difference between the hot-dense region and the background cold region.

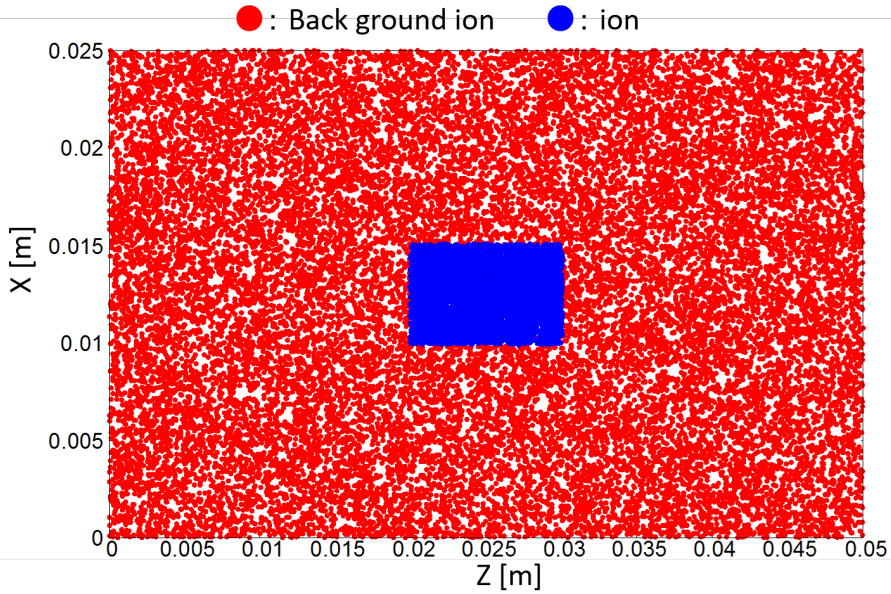

Figure 4.61: The spatial distributions of the ions in the hot-dense region (blue) and in the background cold region (red) at $t \sim 0.032$ [μs].

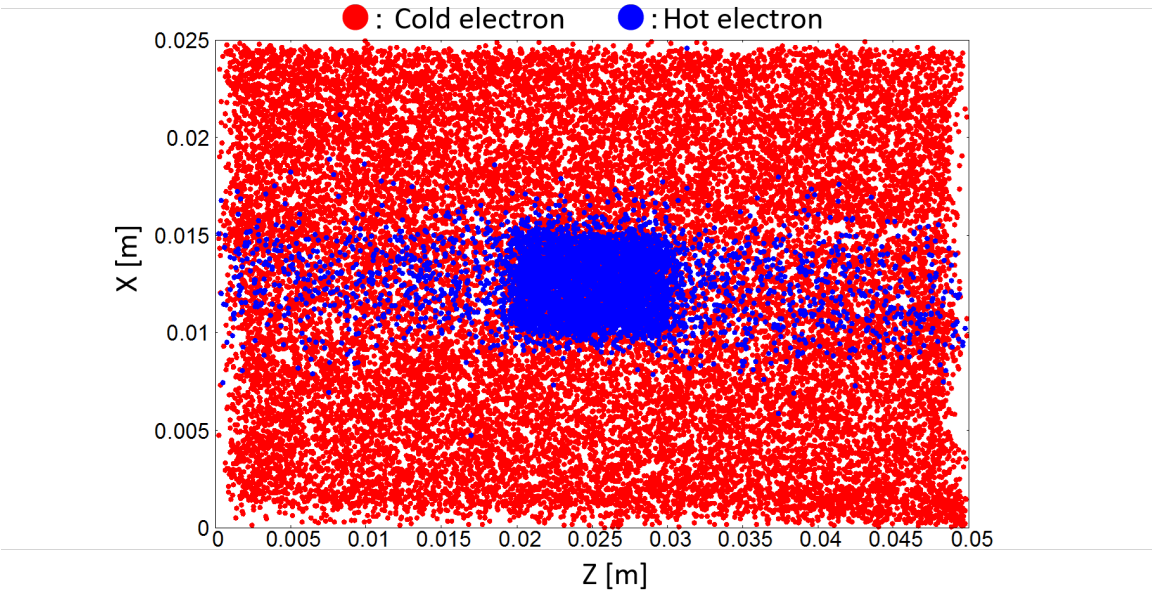

Figure 4.62: The spatial distributions of the electrons in the hot-dense region (blue) and in the background cold region (red) at $t \sim 0.032$ [μs].

From Figs. 4.57-4.62, one can understand the above result by the following particle transport mechanism: 1. The hot energetic electrons diffuse freely in the axial direction, 2. The absence of the electrons creates the net positive charge in the hot-dense region, 3. The potential difference between the hot-dense region and the background cold region generates the static electric field, and 4. The generated electric field collects the cold electrons from the background into the hot-dense region in order to keep the charge neutrality. When comparing the electron temperature profile in the PIC-MCC model (Fig. 4.56) with that in the full fluid model (Fig. 4.52), there remains a trace of the hot region in the PIC-MCC model, while the electron temperature is almost uniform in the full fluid model, that is due to the Maxwellian velocity distribution of electrons used in the PIC-MCC model (some particles which have low energy are confined by the potential wall). The above fast energy transport mechanism is clearly not the classical ambipolar diffusion that restricts the axial diffusion of electrons, and this energy transport can always occurs if there are density gradi-

ent and some energetic thermal electrons. It is obvious that this energy transport strongly depends on the energy in the hot-dense region and the potential deference between the hot-dense region and the background cold region.

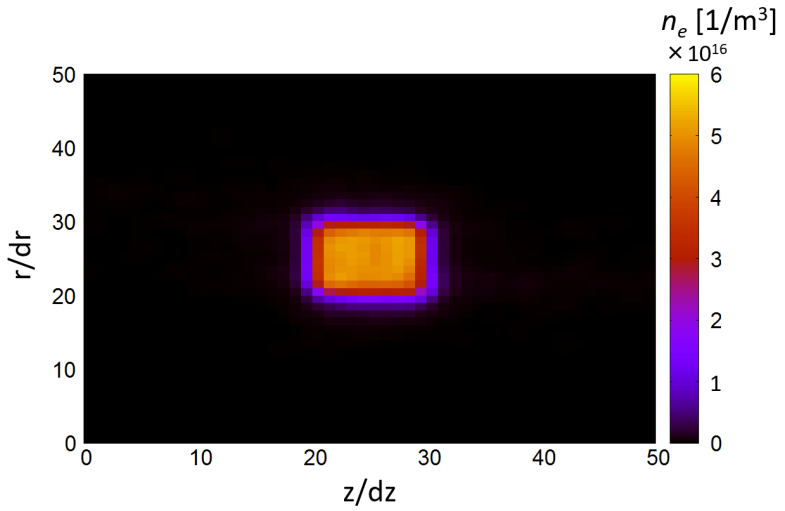

Figure 4.63: The hot electron density profile without the background cold electrons at $t \sim 0.032$ [μs].

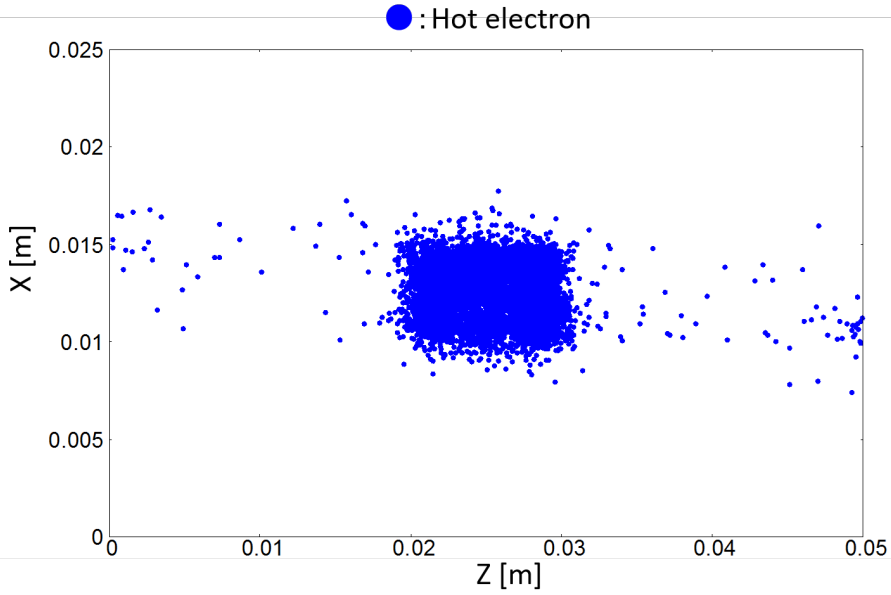

Figure 4.64: The spatial distributions of the hot electrons without the background cold electrons at $t \sim 0.032$ [μs].

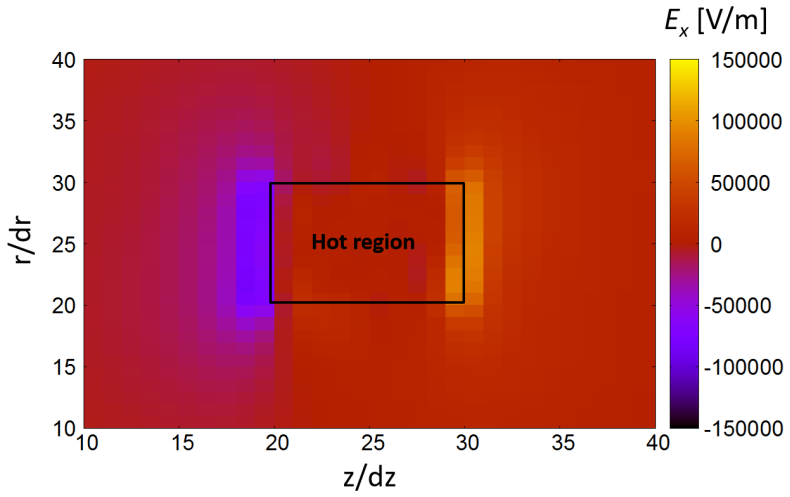

Figure 4.65: The electric field E_x profile at $t \sim 0.032$ [μs], which is generated by the potential difference between the hot-dense region and the vacuum region.

Figures 4.63-4.65 show the profiles of the hot electron density, the spatial distributions of the hot electrons, and the electric field, without background cold electrons (the vacuum region) at $t \sim 0.032$ [μs]. Comparing these figures with the previous ones, one can see that if there is no background cold electrons, the strong electric field is generated between the hot plasma region and the vacuum region when some energetic thermal electrons leave the plasma region, and that confine the electrons in the plasma region, thus the electrons can not diffuse freely in the axial direction. That is the classical ambipolar diffusion. Therefore, the background particles play the important role on the fast energy transport with keeping the charge neutrality in the hot-dense region.

4.8 Conclusion

We investigated the time evolution of the helicon discharge by the ambipolar diffusion model and the full fluid model. In the one-dimensional ambipolar diffusion model, we got the following characteristics of the helicon discharge.

◯ **The edge-localized power absorption by the TG wave leads to the edge localized profiles of the plasma density and the electron temperature**

This edge-localizations of the profiles of the plasma density and the electron temperature are due to the long time delay of the perpendicular ambipolar diffusion. The ambipoalr diffusion time scale of $t > 1$ [ms] is much longer than that of the density growth time scale of several tens of [μs] and the relaxation time scale of several hundreds of [μs].

◯ **When the plasma density reaches the upper limit density** $n_{up} \sim 1.6 \times 10^{16}$ **[1/m^3] for the** $N = 1$ **($k_z = 5$ [1/m]) mode, there is no discrepancy between the contributions of the helicon wave and the TG wave on the total power absorption.**

That is resulting from the merging of the branches of the helicon and the TG waves at above the upper limit density $n_{up} \sim 1.6 \times 10^{16}$ [1/m^3] for the $N = 1$ ($k_z = 5$ [1/m]) mode. However, since the one-dimensional model with the fixed axial mode does not includes the mode transition of the axial standing wave from the $N = 1$ ($k_z = 5$ [1/m]) mode to the $N = 3$ ($k_z = 15$ [1/m]) mode, which is observed at above the upper limit density $n_{up} \sim 1.6 \times 10^{16}$ [1/m^3] for the $N = 1$ ($k_z = 5$ [1/m]) mode in the experiment, the detail investigation should be made with the two-dimensional model.

◯ **The plasma density abruptly grows and the electron temperature abruptly decreases from some critical value of the plasma density**

The net power gain (the positive value of total power balance $P_{\rm abs} - P_{\rm loss}$) also abruptly increases from that critical density point, that leads to the increasing of the

internal energy, but the electron temperature decreases due to the abrupt density growth form that density point. That may related to the resonant excitation of the TG wave as discussed in chapter 2, but the detail analysis with the edge localized density and the electron temperature profiles is need.

◯ **The plasma density can not grow when the total power balance ($P_{\mathbf{abs}} - P_{\mathbf{loss}}$) is negative at the initial stage of the discharge**

In increasing the RF input power, there is some threshold value of the RF input power for the density growth, that leads to the discrepancy of the steady state density between the below and the above of this threshold power. This threshold value of the RF input power depends on the initial condition of the plasma density. When the initial density is $n = 10^{16}$ [1/m^3], the threshold value of the RF input power exists between $J_{\rm ext} = 2.88$ and $J_{\rm ext} = 2.86$ [A/m^2], and when the initial density is $n = 10^{15}$ [1/m^3], the threshold value of the RF input power exists between $J_{\rm ext} = 3.8$ and $J_{\rm ext} = 3.0$ [A/m^2]. However, since the axial energy loss is not included in this one-dimensional model, the total power balance should be discussed with the two-dimensional model.

Although the above results can explain the centrally peaked density profile and the density jumps observed in the experiment, the basic characteristics of the helicon discharge, and some problems that should be improved for the future self-consistent discharge model, are cleared. First, as Chen *et al* [85] pointed out, the centrally peaked density profile can not be explained by the classical ambipolar diffusion, thus some idea is need to explain the centrally peaked density profile. Second, the one-dimensional model cannot explain the density jumps, so the total power balance should be discussed in the two-dimensional model, that includes the axial energy loss toward the wall.

In the two-dimensional model, the RF input power is not realistic, so the time scale of the density growth is much faster ($t < 1$ [μs]) than that of several tens of

[μs] in the experiment. We did that in order to reduce the computational loading in calculating the time integration of the electron continuity, the electron momentum, the electron energy balance, and the Poisson's equation, explicitly. When calculating these equations explicitly, the time step is strongly limited by 4.97, so some implicit method to calculate time integration of these equations should be applied in order to discuss the steady state of the helicon discharge in the future works. However, we got the following conclusions by the two-dimensional wave excitation tests with three uniform plasma density ($n = 10^{16}, 5 \times 10^{18}$ and 5×10^{19} [1/m^3]) with a finite collision frequency ($\nu_e/\omega = 0.1$), the two-dimensional model self-consistent with taking the tiny time step which satisfies 2.97, and the two-dimensional diffusion tests:

◯ **The power absorption by the TG wave can play dominant role on the total power absorption even at the low-density mode (under the cut-off density $n_{\mathbf{low}} \sim 1.3 \times 10^{18}$ [1/m^3] for the $N = 1$ mode)**

By investigating the excited wave profiles at the low plasma density $n = 10^{16}$ [1/m^3], we found that the E_r and E_z components of the TG wave are dominant for the power absorption, and the E_θ component of the non-propagating helicon wave is miner for the power absorption. That is remarkable result, since the low-density mode can be generated by the TG wave, so the low-density mode is not the ICP mode but the low-density helicon mode. That argument is consistent with Chen's one [41]. However, the density jump from the low-density mode $n \sim 10^{17}$ [1/m^3] to the intermediate density $n \sim 7.0 \times 10^{18}$ [1/m^3] mode observed in the experiment should be explained by the self-consistent model.

◯ **The axial heat flux transfer is much faster than the classical ambipolar diffusion. and that leads to the axial broad plasma density profile.**

The antenna-localized electron temperature and the plasma density profiles are obtained in the ambipolar diffusion model, while the axial broad ones are obtained in the full fluid model. That is resulting from the fast heat transfer in the full fluid model.

This fast heat transfer mechanism is investigated by the diffusion test. The mechanism is as follows; 1. The hot energetic electrons diffuse freely in the axial direction, 2. The absence of the electrons creates the net positive charge in the hot-dense region, 3. The potential difference between the hot-dense region and the background cold region generates the static electric field, and 4. The generated electric field collects the cold electrons from the background into the hot-dense region in order to keep the charge neutrality. In this mechanism, unlike the classical ambipolar diffusion, the charge neutrality is conserved over the entire regions of the hot plasma and the background cold plasma by adjusting the number of particles each other, and that enables hot thermal electrons move freely in the axial direction.

CHAPTER V

Conclusion, future works and most outstanding issues

5.1 Conclusion and future works

In this thesis, we obtained the results of the each subjects, that are introduced in the introduction.

(a) The importance of the bulk mode conversion

Our results showed the relative importance of the bulk mode conversion in the power absorption. The efficiency of the bulk mode conversion strongly depends on the collision frequency. i) When the collision frequency is sufficiently small (case 1: $\nu/\omega < 0.01$), highly efficient bulk mode conversion occurs. The contribution of the bulk mode conversion on the power absorption is comparable to that of the surface mode conversion. ii) When the collision frequency has moderate value (case 2: $0.01 < \nu/\omega < 0.06$), the bulk mode conversion is not as evident as case 1, but still important for the power absorption, while the central heating by the helicon wave is most dominant. iii) When the collision frequency is large (case 3: $0.06 < \nu/\omega$), that is the case for typical laboratory experiments, the bulk mode conversion is not dominant, the input helicon energy directly dissipates and the power absorption by the surface mode conversion becomes more dominant at the plasma edge as the collision frequency

increases. Since the cases (cases 1 and 2) when the bulk mode conversion becomes important can occur when the collision frequency between the electrons and neutrals becomes small due to the effect of the neutral depletion, we have to investigate the above conclusion in the self-consistent discharge model, that includes the effect of the neutral dynamics.

(b) The time evolution of the plasma density and the electron temperature profiles and their maximum values.

Our results presents the first report on the time evolution of the plasma density and the electron temperature profiles and their maximum values. The edge-localized power absorption by the TG wave leads to the edge localized profiles of the plasma density and the electron temperature due to the long time delay of the classical ambipolar diffusion. From the crude estimation, one can see in the helicon discharge, that the electron temperature increases and the density grows within several tens of [μs], and relaxes to the steady state within several hundreds of [μs]. On the other hand, the time scale of the ambipolar diffusion is $t > 1$ [ms], that is much longer than the relaxation time scale.

The time evolution of the maximum plasma density and the electron temperature shows that the plasma density abruptly grows and the electron temperature abruptly decreases within several tens of [μs] from some critical value of the plasma density. The net power gain (the positive value of total power balance $P_{\rm abs} - P_{\rm loss}$) also abruptly increases from that critical density point, that leads to the increasing of the internal energy, but the electron temperature decreases due to the abrupt density growth form that density point. The time sale and the tendency of the time evolution of the plasma density and the electron temperature are consistent with the experiment by Shinohara as shown in Fig. 5.1 [110]. However, since the experimental conditions are different from the our model, the more detail investigation is required to compare our results with the laboratory experiments.

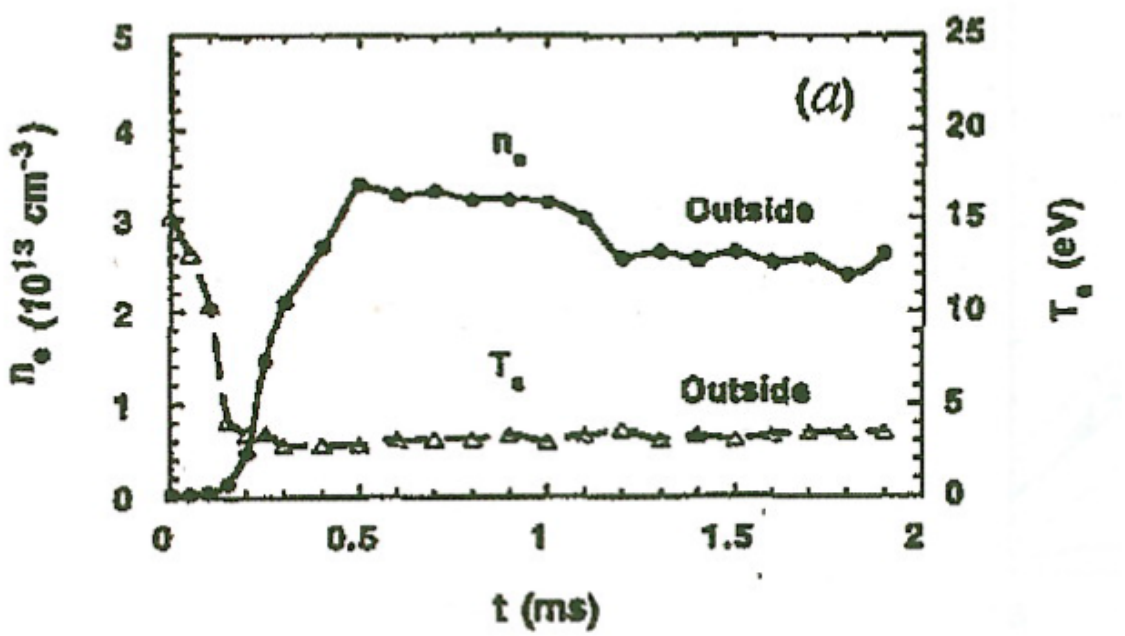

Figure 5.1: Time evolution of the electron density and the electron temperature, measured in the experiment by Shinohara *et al* [110].

In our results, although we found threshold values of the RF input power for the density growth, the density jumps can not be seen. That is due to the ignoring the axial energy loss and the mode transition of the axial standing wave in our 1 dimensional model. Furthermore, although the observed maximum density is $n \sim 1.5 \times 10^{19}$ [1/m^3] (Fig. 2.15) in the experiment by Nisoa *et al* [2], the maximum density reaches up to $n > 10^{20}$ [1/m^3] in our model. That is due to the ignoring of the effects of neutral depletion, that is considered to limit the plasma density in the helicon discharge.

We have to introduce some efficient perpendicular diffusion effect and neutral dynamics in our model, in order to demonstrate the centrally peaked density profile and the density jump.

(c) The wave excitation in the two-dimensional cylinder

We found that, in the low-density mode (under the cut-off density $n_{\rm low} \sim 1.3 \times 10^{18}$ [1/m^3] for the $N = 1$ mode), the E_r and E_z components of the TG wave are dominant

for the power absorption, and the E_θ component of the non-propagating helicon wave is miner for the power absorption. That is remarkable result, since the low-density mode can be generated by the TG wave as observed in the Lho's experiment [90], so the low-density mode is not the ICP mode but the low-density helicon mode. That argument is consistent with Chen's one [41].

It is necessary to demonstrate the steady-state of the low density mode, and the density jump from the low-density mode $n \sim 10^{17}$ [1/m^3] to the intermediate density $n \sim 7.0 \times 10^{18}$ [1/m^3] mode.

(d) The comparison between the ambipolar diffusion model and the full fluid model

The antenna-localized electron temperature and the plasma density profiles are obtained in the ambipolar diffusion model, while the axial broad ones are obtained in the full fluid model. That is resulting from the fast heat transfer in the full fluid model. Since the RF input power is not realistic (about ten times larger than that of the experiment) in our model, so the time scale of the density growth is much faster ($t < 1$ [μs]) than that of several tens of μs in the experiment.

The more realistic parameters should be used by introducing the implicit method for calculating the time integration of governing equations of background electrons.

(e) The the fast heat transfer mechanism along the magnetic field

This fast heat transfer mechanism is investigated by the diffusion test. The mechanism is as follows; 1. The hot energetic electrons diffuse freely in the axial direction, 2. The absence of the electrons creates the net positive charge in the hot-dense region, 3. The potential difference between the hot-dense region and the back ground cold region generates the static electric field, and 4. The generated electric field collects the cold electrons from the back ground into the hot-dense region in order to keep the charge neutrality. In this mechanism, unlike the classical ambipolar diffusion, the charge neutrality is conserved over the entire regions of the hot plasma and the back

ground cold plasma by adjusting the number of particles each other, and that enables hot thermal electrons move freely in the axial direction.

It is necessary to develop the PIC-MCC discharge model, in order to include the wave-particle interaction (the ion heating by the TG wave) and the wave-wave (parametric decay instability) interaction.

5.2 Most outstanding issues

◯ **Why the density profile relaxes to the central high profile ?**

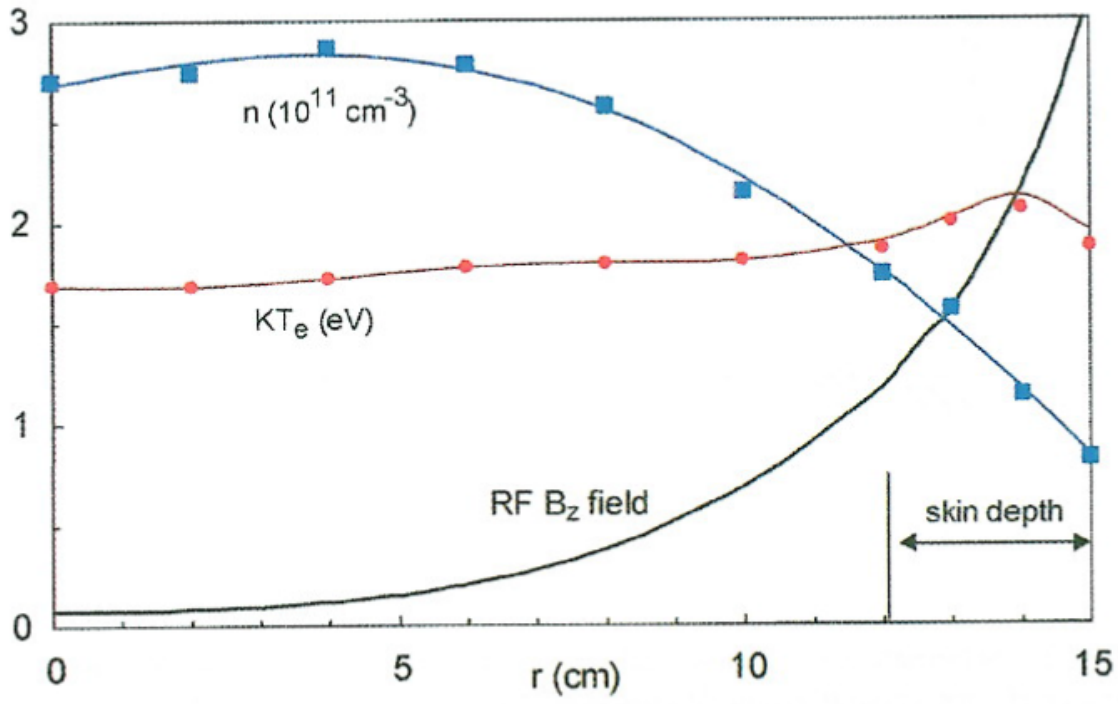

Figure 5.2: Radial profile of density, electron temperature, and the RF B_z field in ICP discharge [111].

In helicon discharge, most of the RF power is absorbed by excitation of the TG mode in a thin layer of the edge boundary. Nevertheless, plasma density peaked on axis is usually observed, and never shows the hollow profile. This central density problem is also arisen in ICP discharge when the RF sikin depth is much smaller

than the device scale as shown in Fig. 5.2 [111]. The RF field decays inward with the expected e folding distance, and electron temperature peaks in the skin layer, as expected. However, the density has a minimum in the skin layer and peaks near the center. This problem has been known for many years since it was reported by Demirkhanov *et al* [111], Kofoid and Dawson [112], and later by Joye and Schneider [113]. Weibel [114] and Sayasov [115] proposed theoretically that electron thermal motions could transport RF energy past the skin layer. Godyak *et al* [116] have discovered the nonlinear effects in ICPs. When the electron mean free path is about the size of the discharge, the current induced by the field at one point can be transfered by thermal electron motion to another point and produce there an additional field interfering with local field. The field and current become independent to some extent, that is called the anomalous skin effect [111,114,117]. The RF current transferred by thermal electron motion can be opposite in phase to the local electric field resulting in a local negative energy transfer from RF field to electrons. In an ICP reactor, the relation between the current density and the electric field with the assumption of the cold-electron plasma approximation can be obtained as

$$\boldsymbol{J}_e = \sigma \boldsymbol{E}, \tag{5.1}$$

$$\sigma(\boldsymbol{r}) = \frac{e^2 n_e(\boldsymbol{r})}{m_e \left[\nu_m(\boldsymbol{r}) + i\omega\right]}. \tag{5.2}$$

where, $\boldsymbol{J}_e$, σ, e, m_e, n_e, and ν_m, respectively, designate the electron current density, conductivity, electron charge, electron mass, electron density, and electron momentum transfer collision frequency. One typically ignores ion current due to the low ion mobility. The use of the cold-electron approximation has several implications. First, the only mechanism available for conversion of wave energy to random electron thermal energy is electron collisions with background heavy particles. Second, 5.2 implies that current at a particular location in the plasma depends only on the

local electromagnetic fields and plasma parameters. If the electron mean free path is sufficiently long that the electron crosses into a region having a different electric field or plasma density, that is, thermal effects are important, and 5.2 is no longer valid.

Figure 5.3 shows the axial distributions and phase distributions of the azimuthal RF electric field and current density in Godyak experiment [118] (Fig. 5.5). The slower spatial decay of the current density distribution than that of the electric field demonstrates the effect of the RF current diffusion due to thermal electron motion. The phase distribution profiles are also different for the electric field and current density and suggest the different mechanisms of propagation of electric field and current. In the normal skin effect with the cold-electron approximation, the field and the current phase distributions are similar and just shifted by $\Delta\phi = \arctan(\omega/\nu)$ which is always less than 90°. However, as one can see in the bottom panel of Fig. 5.3, the phase difference in the measured phase distributions at some distance from the glass window exceeds 90°, indicating the presence of negative power absorption. The distributions of the RF power absorption along its propagation in the axial direction calculated as $P = EJcos\Delta\phi$ are shown in Fig. 5.4 for different drive frequencies with a fixed discharge power of 100 W. As expected, the RF power is mainly absorbed in the skin layer near the window and decays faster for higher frequency. Deeper into the plasma the power absorption changes sign and becomes negative. Godyak compared these experimental results with theoretical calculations and got good agreement [118].

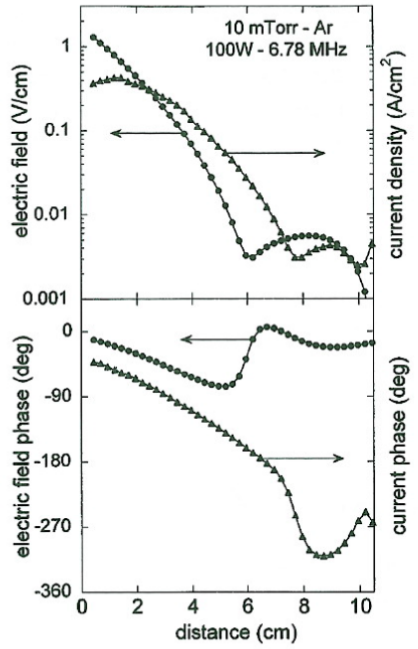

Figure 5.3: Axial distribution of the measured RF electric field and current [118].

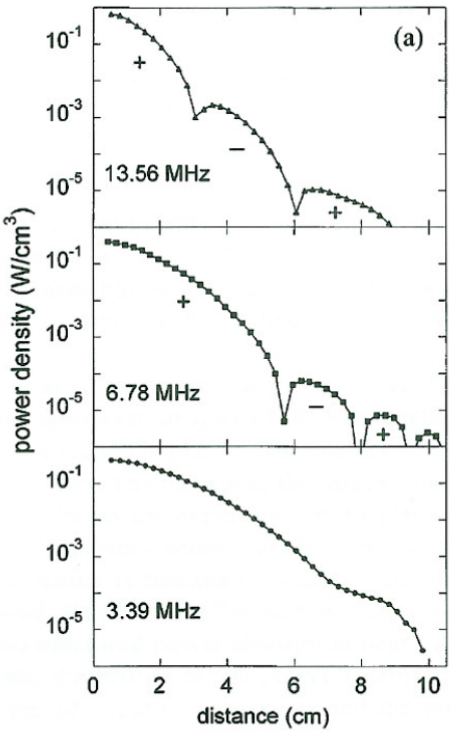

Figure 5.4: Experimental power absorption profile [118].

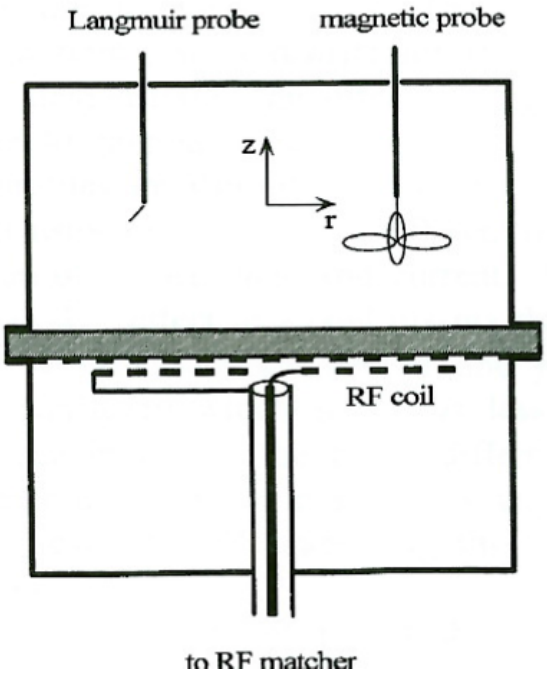

Figure 5.5: Experimental ICP discharge chamber [118].

A spatially non-uniform electric field by itself might lead to electron heating, even in the absence of collision, if the electrons have thermal velocities sufficient to sample the field inhomogeneity. This phenomenon has been well-known in plasma physics since Landau demonstrated the collisionless damping of an electrostatic wave in a warm plasma [119, 120]. The spatial distribution of conductivity caused by the anomalous skin effect also leads to collisionless power dissipation in the skin layer. This collisionless power absorption in ICPs has been widely accepted [121–127], and experimental evidence was reported by Godyak [128]. Furthermore, the ponderomotive force was found to generate 2ω oscillations [129, 130] at twice the RF frequency, as well as a nonlinear dc force [131–133]. Chen showed the non-linear effect on the particle trajectory during the several RF cycles, and he found that the non-linear force allows electrons to travel to the deep interior of plasma [98].

In recent study, Chen suggested the mechanism that the sheath adjustments at the end plates allow electrons to effectively move across the magnetic field [134], that has been known as the "Short-circuit effect" in a finite cylinder [135]. Lafleur *et al* [86] showed the existence of the non-ambipolar diffusion across the magnetic field by a two-dimensional PIC-MCC simulation. Two models are used in their simulation as shown in Fig. 5.6. With a Cartesian geometry (system length of $L_x = 10$ [cm] and $L_y = 5$ [cm]), a uniform magnetic field ($B_0 = 0$ and $B_0 = 5$ [mTesla]) is applied in the x-direction (the axial direction), they studied the periodic boundary discharge (configuration 1 in Fig. 5.6) and the axial bounded (conductor wall) discharge (configuration 2 in Fig. 5.6) (the y-direction is bounded in both configurations), by applying the uniform oscillating E_z field.

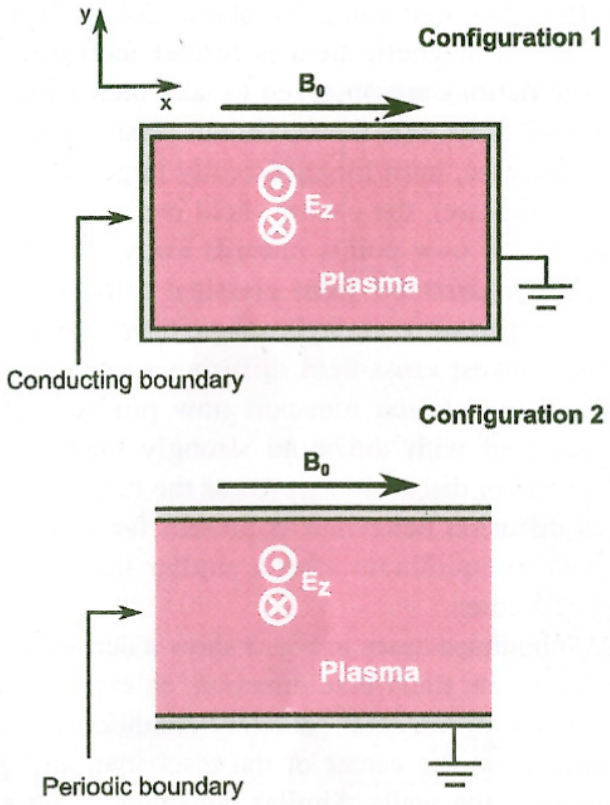

Figure 5.6: Schematic of the PIC model indicating the two simulation configurations used. The applied magnetic field is spatially uniform, and the heating field E_z, varies with time in the z-direction [86].

Figure 5.7 shows the time-averaged particle fluxes of the ions (the dashed lines) and the electrons the solid lines) along the transverse and axial walls for the periodic and bounded 0 [mTesla] and 5 [mTesla] test cases. For both unbounded cases, the time-averaged electron and ion current densities are spatially uniform, and approximately equal. This demonstrates the classical ambipolar diffusion. For the case of bounded discharge with 5 [mTesla], one can see that the ion flux to the transverse wall is significantly higher than the electron flux, while on the axial walls, the electron flux is larger than the ion flux. The sum of electron and the ion fluxes over all walls is however equal (the global charge neutrality is thus conserved). This presents clear evidence of the non-ambipolar diffusion; ion diffusion to the transverse walls is non-ambipolar, while the electrons are preferentially lost to the axial walls, verifying

the hypotheses of Simon [135].

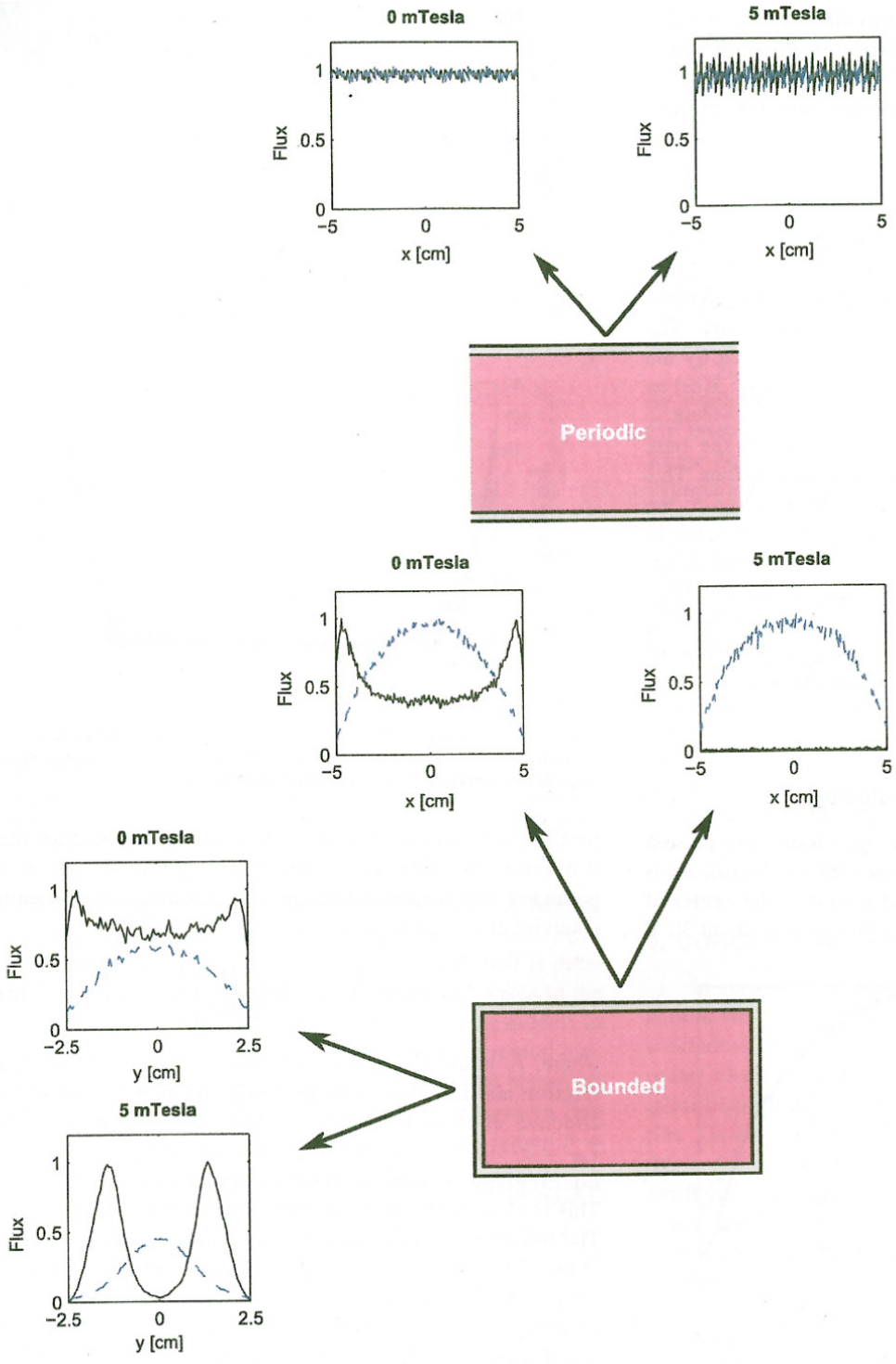

Figure 5.7: Time-averaged particle fluxes along transverse and axial walls for the periodic and bounded 0 [mTesla] and 5 [mTesla] test cases. The dashed line show the ion flux, while the solid line show the electron flux [86].

The above results demonstrate the importance of axial boundaries in magnetized discharges and show that in general, the diffusion needs not be ambipolar; short-circuit currents can play a significant role and change the overall transport behavior. Therefore, this enhanced transverse diffusion mechanism is the most influential theory to explain the center peaked density profile in the helicon discharge.

◯ **What determines the density limit?**

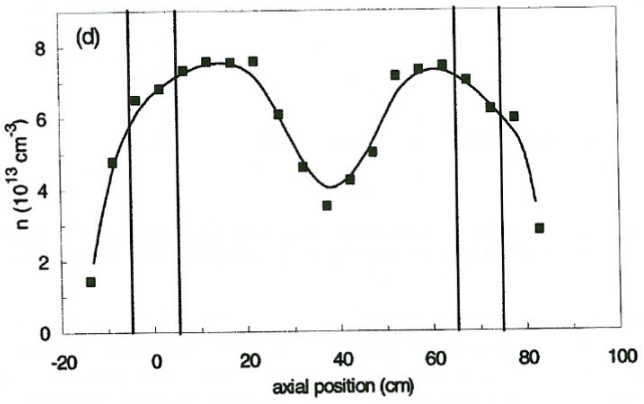

Figure 5.8: Axial profile of the density.The ends of the antenna are indicated by the vertical bars [136].

The suitability of helicon discharges for producing high density plasmas for various applications gas been known. It is difficult, however, to create plasmas with density over 10^{20} [1/m^3]. In 1998, Miljak and Chen [136] investigated the density limit by exciting $m = 1$ waves with two helical antennas. By applying 2 [kW] of RF power to two helicon antennas, a plasma of 8×10^{19} [1/m^3] density was generated (Fig. 5.8) in 63 [mTorr] of argon with 1.2 [kG] magnetic field. Attempts to increase the density by increasing the pressure failed because of the depletion of neutral gas. The effect of the neutral depletion has been known and studied by Fruchman and Raimbault *et al* [137–139] theoretically, and it has been shown both theoretically and experimentally that neutral depletion in low temperature RF plasmas can lead to an increase in plasma transport, resulting in a decreasing plasma density with increasing input power. This result can be understood as follows [89] : as the input power is

increased, ionization increases plasma density at the expense of neutral density. But as the neutral density decreases, the neutral drag on ions also decreases, and ions are able to escape the plasma volume more quickly.

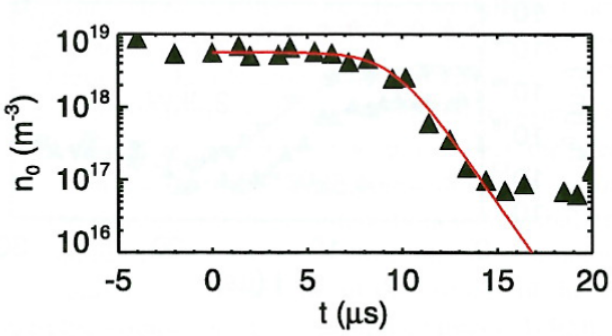

Figure 5.9: The neutral density in a 4.5 [kW] plasma measured in the source. The RF power is turned on at $t = 0$. The solution to the coupled differential equations described in the text is overlaid in red [89].

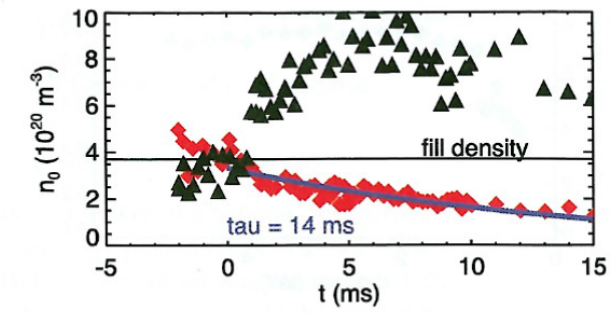

Figure 5.10: The neutral density measured in the expansion chamber as a function of time.The red diamonds are the data taken from $r = 0$ [cm] (the core) and the black triangles from $r = 6.7$ [cm] (the edge). The blue curve is the result of fitting the data to a simple exponential [89].

Magee *et al* [89] measured the density of the neutral gas at and downstream from the rf antenna. The results showed the much faster depletion (within 15 [μs]) near the antenna (Fig. 5.9), and much slower depletion (requiring 14 [ms]) at the downstream (Fig. 5.10) than the expected amount calculated from the ionization rate with electron temperature measured at the downstream. They mentioned the fast depletion near the antenna is due to the ionization by a small population of very energetic electrons,

or that the upstream and downstream electron energy distributions are different and kept from achieving thermal equilibrium. They also concluded the slow depletion at the downstream is due not to the ionization but to the neutral expulsion. The detailed physics of the neutral depletion which limits the density in the helicon discharge has not been cleared, it is therefore need to investigate the neutral dynamics in the self-consistent model.

APPENDICES

APPENDIX A

Finite Difference Time Domain (FDTD) method

In the FDTD calculation, Maxwell's equations are discretized using central-difference approximations to space and time partial derivatives. The resulting finite-difference equations are solved in a leap frog manner: the electric field vector components in a volume of space are solved at a given instant in time; then the magnetic field vector components in the same spatial volume are solved at the next instant in time; and the process is repeated over and over again until the desired transient or steady-state electromagnetic field behavior is fully evolved. In one-dimensional Cartesian coordinate with fixed k_y, discretized equations are given as follows: for magnetic fields,

$$B_{x_{j+1/2}}^{\ i+1/2} = B_{x_{j+1/2}}^{\ i-1/2} - dtik_y \left(E_{z_{j+1}}^{\ i} + E_{z_j}^{\ i}\right)/2, \tag{A.1}$$

$$B_{y_{j+1/2}}^{\ i+1/2} = B_{y_{j+1/2}}^{\ i-1/2} + dt \left(E_{z_{j+1}}^{\ i} - E_{z_j}^{\ i}\right)/dx, \tag{A.2}$$

$$B_{z_{j+1/2}}^{\ i+1/2} = B_{z_{j+1/2}}^{\ i-1/2} - dt \left(E_{y_{j+1}}^{\ i} - E_{y_j}^{\ i}\right)/dx + dtik_y \left(E_{x_{j+1}}^{\ i} + E_{x_j}^{\ i}\right)/2, \tag{A.3}$$

and for electric fields,

$$E_{x_j}^{\ i+1} = E_{x_j}^{\ i} + c^2 dtik_y \left(B_{z_{j+1/2}}^{\ i+1/2} + B_{z_{j-1/2}}^{\ i+1/2}\right)/2 - c^2\mu_0 J_{x_j}^{\ i+1/2}, \tag{A.4}$$

$$E_{y_j}^{i+1} = E_{y_j}^{i} - c^2 dt \left(B_{z_{j+1/2}}^{i+1/2} - B_{z_{j-1/2}}^{i+1/2} \right) / dx - c^2 \mu_0 J_{y_j}^{i+1/2}, \tag{A.5}$$

$$E_{z_j}^{i+1} = E_{z_j}^{i} + c^2 dt \left(B_{y_{j+1/2}}^{i+1/2} - B_{y_{j-1/2}}^{i+1/2} \right) / dx - c^2 dt i k_y \left(B_{x_{j+1/2}}^{i+1/2} + B_{x_{j-1/2}}^{i+1/2} \right) / 2 - c^2 \mu_0 J_{z_j}^{i+1/2}. \tag{A.6}$$

where superscript i and subscript j represent the temporal and the spatial grid numbers respectively and normal script i is the complex umber.

In one-dimensional cylindrical coordinate with fixed k_z, discretized equations are given as follows: for magnetic fields,

$$B_{r_{j+1/2}}^{i+1/2} = B_{r_{j+1/2}}^{i-1/2} + dt i k_z \left(E_{\theta_{j+1}}^{i} + E_{\theta_j}^{i} \right) / 2, \tag{A.7}$$

$$B_{\theta_{j+1/2}}^{i+1/2} = B_{\theta_{j+1/2}}^{i-1/2} - dt i k_z \left(E_{r_{j+1}}^{i} + E_{r_j}^{i} \right) / 2 + dt \left(E_{z_{j+1}}^{i} - E_{z_j}^{i} \right) / dr, \tag{A.8}$$

$$B_{z_{j+1/2}}^{i+1/2} = B_{z_{j+1/2}}^{i-1/2} - dt \left(E_{\theta_{j+1}}^{i} - E_{\theta_j}^{i} \right) / dr - dt \left(E_{\theta_{j+1}}^{i} + E_{\theta_j}^{i} \right) / 2r, \tag{A.9}$$

and for electric fields,

$$E_{r_j}^{i+1} = E_{r_j}^{i} - c^2 dt i k_z \left(B_{\theta_{j+1/2}}^{i+1/2} + B_{\theta_{j-1/2}}^{i+1/2} \right) / 2 - c^2 \mu_0 J_{r_j}^{i+1/2}, \tag{A.10}$$

$$E_{\theta_j}^{i+1} = E_{\theta_j}^{i} - c^2 dt \left(B_{z_{j+1/2}}^{i+1/2} - B_{z_{j-1/2}}^{i+1/2} \right) / dr + c^2 dt i k_z \left(B_{r_{j+1/2}}^{i+1/2} + B_{r_{j-1/2}}^{i+1/2} \right) / 2 + c^2 \mu_0 J_{\theta_j}^{i+1/2}, \tag{A.11}$$

$$E_{z_j}^{i+1} = E_{z_j}^{i} + c^2 dt \left(B_{\theta_{j+1/2}}^{i+1/2} - B_{\theta_{j-1/2}}^{i+1/2} \right) / dr + c^2 dt \left(B_{\theta_{j+1/2}}^{i+1/2} + B_{\theta_{j-1/2}}^{i+1/2} \right) / 2r - c^2 \mu_0 J_{z_j}^{i+1/2}. \tag{A.12}$$

In two-dimensional cylindrical coordinate, discretized equations are given by replacing ik_z to the central-difference in z direction in A.7-A.12.

BIBLIOGRAPHY

BIBLIOGRAPHY

[1] M. Nisoa, Y. Sakawa, and T. Shoji. Compact high-density plasma source produced by using standing helicon waves. *Jpn. J. Appl. Phys.*, Vol. 38, p. L777, 1999.

[2] M. Nisoa, Y. Sakawa, and T. Shoji. Characterization of plasma production by $m = 0$ standing helicon waves. *Jpn. J. Appl. Phys.*, Vol. 40, p. 3396, 2001.

[3] M. Nisoa, Y. Sakawa, and T. Shoji. Plasma production by m=0 standing helicon waves. *Jpn. J. Appl. Phys.*, Vol. 39, p. L429, 2000.

[4] P. Aigrain. Les 'helicons' dans les semiconducteurs. *Proc. Intl. Conf. on Semiconductor Physics*, p. 224, 1960.

[5] R. Bowers, C. Legendy, and F. Rose. Oscillatory galvanomagnetic effect in metallic sodium. *Phys. Rev. Lett.*, Vol. 7, p. 339, 1961.

[6] C. R. Legendy. Macroscopic theory of helicons. *Phys. Rev. A*, Vol. 135, p. A1713, 1964.

[7] C. R. Legendy. Existence of proper modes of helicon oscillations. *J. Math Phys.*, Vol. 6, p. 153, 1965.

[8] J. P. Klozenberg, B. McNamara, and P. C. Thonemann. The dispersion and attenuation of helicon waves in a uniform cylindrical plasma. *J. Fluid. Mech.*, Vol. 21, p. 545, 1965.

[9] J. L. Lehane and P. C. Thonemann. An experimental study of helicon wave propagation in a gaseous plasma. *Proc. Phys. Soc.*, Vol. 85, p. 301, 1965.

[10] T. A. Facey and G. N. Harding. *Culham Laboratory, Rep. CLM-R66*, 1966.

[11] R. W. Boswell. Plasma production using a standing helicon wave. *Phys. Lett. A*, Vol. 33, p. 457, 1970.

[12] F. F. Chen. Helicon plasma sources. *"High Density Plasma Sources", ed. by Oleg A. Popov (Noyes Publications, Park Ridge, NJ)*, p. Chap 1, 1995.

[13] F. F. Chen. Experiments on helicon plasma sources. *J. Vac. Sci. Technol. A*, Vol. 10, p. 1389, 1992.

[14] R. W. Boswell. Very efficient plasma generation by whistler waves near the lower hybrid frequency. *Plasma Phys. Control. Fusion*, Vol. 26, p. 1162, 1984.

[15] A. W. Degeling and R. W. Boswell. Modeling ionization by helicon waves. *Phys. Plasmas.*, Vol. 4, p. 2748, 1997.

[16] F. F. Chen. Plasma ionization by helicon waves. *Plasma Phys. Control. Fusion*, Vol. 33, p. 339, 1990.

[17] P. K. Loewenhardt, B. D. Blackwell, R. W. Boswell, G. D. Conway, and S. M. Hamberger. Plasma production in a toroidal helic by helicon waves. *Phys. Rev. Lett.*, Vol. 67, p. 279, 1991.

[18] P. Zhu and R. W. Boswell. Observation of nonthermal electron tails in an rf excited argon magnetoplasma. *Phys. Fluids. B*, Vol. 3, p. 869, 1991.

[19] A. R. Ellingboe, R. W. Boswell, J. P. Booth, and N. Sadeghi. Electron beam pulses produced by helicon]wave excitation. *Phys. Plasmas.*, Vol. 2, p. 1807, 1995.

[20] A. W. Molvik, A. R. Ellingboe, and T. D. Rognlien. Hot-electron production and wave structure in a helicon plasma source. *Phys. Rev. Lett.*, Vol. 79, p. 233, 1997.

[21] F. F. Chen and D. D. Blackwell. Upper limit to landau damping in helicon discharges. *Phys. Rev. Lett.*, Vol. 82, p. 2677, 1991.

[22] L. Spitzer. *Physics of Fully Ionized Gases (Inter-science: New York)*, 1962.

[23] B. Davis. Helicon wave propagation: Effect of electron inertia. *J. Plasma Phys.*, Vol. 4, p. 43, 1970.

[24] A. W. Trivelpiece and R. W. Gould. Space charge waves in cylindrical plasma columns. *J. Appl. Phys.*, Vol. 30, p. 1784, 1959.

[25] R. W. Boswell. Dependence of helicon wave radial structure on electron inertia. *Aust. J. Phys.*, Vol. 25, , 1972.

[26] K. P. Shamrai and V. B. Taranov. Volume and surface rf power absorption in a helicon plasma source. *Plasma Sources Sci. Technol.*, Vol. 5, p. 474, 1996.

[27] G. G. Borg and R. W. Boswell. Power coupling to helicon and trivelpiece-gould modes in helicon sources. *Phys. Plasmas.*, Vol. 5, p. 564, 1998.

[28] F. F. Chen and D. Arnush. Generalized theory of helicon waves. i. normal modes. *Phys. Plasmas.*, Vol. 4, p. 3411, 1997.

[29] D. D. Blackwell, T. G. Madziwa, D. Arnush, and F. F. Chen. Evidence for trivelpiece-gould modes in a helicon discharge. *Phys. Rev. Lett.*, Vol. 88, p. 145002, 2002.

[30] K. K. Chi, T. E. Sheridan, and R. W. Boswell. Resonant cavity modes of a bounded helicon discharge. *Plasma Sources Sci. Technol.*, Vol. 8, p. 421, 1999.

[31] A. R. Ellingboe and R. W. Boswell. Capacitive, inductive and helicon-wave modes of operation of a helicon plasma source. *Phys. Plasmas.*, Vol. 3, p. 2797, 1996.

[32] V. A. Godyak and R. B. Piejak. Observation of the ponderomotive effect in an inductive plasma. *Phys. Rev. Lett.*, Vol. 65, p. 996, 1990.

[33] N. S. Yoon, B. C. Kim, J. G. Yang, and S. M. Hwang. A theoretical formula of e-h discharge transition power in a transformer-coupled discharge. *IEEE trans. plasma. sci.*, Vol. 26, p. 190, 1998.

[34] C. W. Chung and H. Y. Chang. Heating-mode transition in the capacitive mode of inductivelycoupled plasmas. *Appl. Phys. Lett.*, Vol. 80, p. 1725, 2002.

[35] P. Chabert and N. Braithwaite. Physics of radio-frequency plasmas. *Cambridge University Press*, 2011.

[36] K. P. Shamrai and V. B. Tananov. Resonances and anti-resonances of a plasma column in a helicon plasma source. *Phys. Lett. A*, Vol. 204, p. 139, 1995.

[37] K. P. Shamrai. Stable modes and abrupt density jumps in a helicon plasma source. *Plasma Sources Sci. Technol.*, Vol. 7, p. 499, 1998.

[38] D. Arnush and F. F. Chen. Generalized theory of helicon waves. ii. excitation and absorption. *Phys. Plasmas.*, Vol. 5, p. 1239, 1998.

[39] S. Shinohara and K. P. Shamrai. Direct comparison of experimental and theoretical results on the antenna loading and density jumps in a high pressure helicon source. *Plasma Phys. Control. Fusion*, Vol. 42, p. 865, 2000.

[40] D. Arnush. The role of trivelpiece-gould waves in antenna coupling to helicon waves. *Phys. Plasmas.*, Vol. 7, p. 3042, 2000.

[41] F. F. Chen and H. Torreblanca. Density jump in helicon discharge. *Plasma Sources Sci.*, Vol. 16, p. 593, 2007.

[42] J. L. Kline, E. E. Scime, R. F. Boivin, A. M. Keesee, X. Sun, and V. S. Mikhailenko. Rf absorption and ion heating in helicon sources. *Phys. Rev. Lett.*, Vol. 88, p. 195002, 2002.

[43] M. M. Balkey, R. Boivin, J. L. Kline, and E. E. Scime. Ion heating and density production in helicon sources near the lower hybrid frequency. *Plasma Sources Sci. Technol.*, Vol. 10, p. 284, 2001.

[44] I. D. Sudit and F. F. Chen. Rf compensated probes for high-density discharges. *Plasma Sources Sci. Technol.*, Vol. 3, p. 162, 1994.

[45] E. E. Scime, R. F. Boivin, J. L. Kline, and M. M. Balkey. Microwave interferometer for steady-state plasmas. *Rev. Sci. Instrum*, Vol. 72, p. 1672, 2001.

[46] E. E. Scime, P. A. Keiter, M. W. Zintl, M. M. Balkey, J. L. Kline, and M. E. Koepke. Control of ion temperature anisotropy in a helicon plasma. *Plasma Sources Sci. Technol.*, Vol. 7, p. 186, 1998.

[47] T. Sheridan and J. Goree. Langmuir-probe characteristic in the presence of drifting electrons. *Phys. Rev. E*, Vol. 50, p. 2991, 1994.

[48] M. Kr*ddota*mer, Yu. M. Aliev, A. B. Altukhov, A. D. Gurchenko, E. Z. Gusakov, and K. Niemi. Anomalous helicon wave absorption and parametric excitation of electrostatic fluctuations in a helicon-produced plasma. *Plasma Phys. Control. Fusion*, Vol. 49, p. A167, 2007.

[49] B. Lorenz, M. Kr*ddota*mer, V. L. Selenin, and Yu. M. Aliev. Anomalous helicon wave absorption and parametric excitation of electrostatic fluctuations in a helicon-produced plasma. *Plasma Sources Sci. Technol.*, Vol. 14, p. 623, 2005.

[50] F. F. Chen. Helicon discharge and sources: a review. *Plasma Sources Sci. Technol.*, Vol. 24, p. 014001, 2015.

[51] C. K. Birdsall and A. B. Langdon. Plasma physics via computer simulation. *John Wiley & Sons, New York*, 1994.

[52] F. F. Chen. Helicon discharges and sources: a review. *Plasma Sources Sci. Technol.*, Vol. 24, p. 014001, 2015.

[53] N. M. P. Benjamin, B. N. Chapman, and R. W. Boswell. Progress of an advanced diffusion source plasma reactor. *Proc. SPIE*, Vol. 95, p. 1392, 1991.

[54] I. Tepermeister1, N. Blayo1, F. P. Klemens, D. E. Ibbotson, R. A. Gottscho, J. T. C. Lee, and H. H. Sawin. Comparison of advanced plasma sources for etching applications. i. etching rate, uniformity, and profile control in a helicon and a multiple electron cyclotron resonance source. *J. Vac. Sci. Technol. B*, Vol. 12, p. 2310, 1994.

[55] I. Tepermeister, D. E. Ibbotson, J. T. C. Lee, and H. H. Sawin. Comparison of advanced plasma sources for etching applications. ii. langmuir probe studies of a helicon and a multipole electron cyclotron resonance source. *J. Vac. Sci. Technol. B*, Vol. 12, p. 2322, 1994.

[56] G. W. Gibson Jr., H. H. Sawin, I. Tepermeister, D. E. Ibbotson, and J. T. C. Lee. Comparison of advanced plasma sources for etching applications. iii. ion energy distribution functions for a helicon and a multipole electron cyclotron resonance source. *J. Vac. Sci. Technol. B*, Vol. 12, p. 2333, 1994.

[57] G. R. Tynan, A. D. Bailey III, G. A. Campbell, R. Charatan, A. de Chambrier, G. Gibson, D. J. Hemker, K. Jones, A. Kuthi, C. Lee1, T. Shoji, and M. Wilcoxson. Characterization of an azimuthally symmetric helicon wave high density plasma source. *J. Vac. Sci. Technol. A*, Vol. 12, p. 288, 1997.

[58] F. F. Chen. Performance of a permanent-magnet helicon source at 27 and 13 mhz. *Phys. Plasmas*, Vol. 19, p. 093509, 2012.

[59] M. Yano and M. L. R. Walker. Plasma ionization by annularly bounded helicon waves. *Phys. Plasmas*, Vol. 14, p. 033510, 2006.

[60] F.R. Chang Diaz, J.P. Squire, R.D. Bengtson, B.N. Breizman, F.W. Baity, and M.D. Carter. The physics and engineering of the vasimr engine. *36th AIAA/ASME/SAE/ASEE Joint Propulsion Conference*, pp. AIAA 2000–3756, 2000.

[61] T. M. Ziemba, R. M. Winglee, P. Euripides, and J. Slough. Parameterization of the laboratory performance of the mini-magnetospheric plasma propulsion (m2p2) prototype. *27th International Electric Propulsion Conference*, pp. IEPC–01–201, 2001.

[62] K. P. Shamrai, A. Aleksandrov, G. Bougrov, V. Virko, V. Katiukha, S. Koh, E. Kralkina, G. Kirichenko, and A. Rukhadze. Quasistatic plasma sources: physical principles, modelling experiments, application aspects. *Journal de Physique IV, Colloque C4, Supplement au Journal de Physique III*, Vol. 7, p. 365, 2006.

[63] T. W. Glover M. D. Carter L. D. Cassady W. J. Chancery V. T. Jacobson G. E. McCaskill C. S. Olsen E. A. Bering M. S. Brukardt J. P. Squire, F. R. Chang-Diaz and B. W. Longmier. Vasimr performance measurements at powers exceeding 50 kw and lunar robotic mission applications. *International Interdisciplinary Symposium on Gaseous and Liquid Plasmas (ISGLP)*, 2008.

[64] K. Toki, S. Shinohara, T. Tanikawa, I. Funaki, and K. P. Shamrai. Preliminary investigation of helicon plasma source for electric propulsion applications. *28th Int. Electric Propul. Conf.*, Vol. 12, pp. IEPC 03–0168, 2003.

[65] K. Takahashi, T. Lafleur, C. Charles, P. Alexander, and R. W. Boswell. Direct thrust measurement of a permanent magnet helicon double layer thruster. *Appl. Phys. Lett.*, Vol. 98, p. 141503, 2011.

[66] K. Takahashi, T. Lafleur, C. Charles, P. Alexander, and R. W. Boswell. Electron diamagnetic effect on axial force in an expanding plasma: experiments and theory. *Phys. Rev. Lett.*, Vol. 107, p. 235001, 2011.

[67] K. Takahashi, T. Lafleur, C. Charles, P. Alexander, and R. W. Boswell. Approaching the theoretical limit of diamagnetic-induced momentum in a rapidly diverging magnetic nozzle. *Phys. Rev. Lett.*, Vol. 110, p. 195003, 2013.

[68] T. Nakamura, H. Nishida, S. Shinohara, I. Funaki, and T. Hada. Preliminary investigation of electromagnetic thrust characteristics in electrodeless compact helicon plasma thruster. *Trans. JSASS Aerospace Tech. Japan*, Vol. 12, p. Po 11, 2014.

[69] T. Matsuoka, I. Funaki, T. Nakamura, K. Yokoi, and H. Nishida. Scaling laws of lissajous acceleration for electrodeless helicon plasma thruster. *Plasma Fus. Res.*, Vol. 6, p. 2406103, 2011.

[70] S. Satoh, T. Matsuoka, T. Fujino, and I. Funaki. A theoretical analysis for electrodeless lissajous acceleration of helicon plasmas. *42th AIAA Plasmadynamics and Lasers Conf.*, pp. AIAA–2011–4008, 2011.

[71] H. Nishida, T. Nakamura, S. Shinohara, and T. Matsuoka. Study on helicon plasma lissajous acceleration for electrodeless electric propulsion. *Trans. JSASS Aerospace Tech. Japan*, p. Tb 17, 2012.

[72] S. Shinohara, H. Nishida, K. Yokoi, T. Nakamura, and T. Tanikawa. Research and development of electrodeless plasma thrusters using high-density helicon sources: The heat project. *32nd Int. Electric Propul. Conf.*, p. 056, 2011.

[73] S. Shinohara, H. Nishida, T. Tanikawa, T. Hada, I. Funaki, IEEE Member, and K. P. Shamrai. Development of electrodeless plasma thrusters with high-density helicon plasma sources. *IEEE Trans. Plasma, Sci.*, Vol. 42, p. 1245, 2014.

[74] S. Otsuka, K. Takizawa, Y. Tanida, D. Kuwahara, and S. Shinohara. Study on plasma acceleration in completely electrodeless electric propulsion system. *Plasma Fusion Res.*, Vol. 9, p. 3401026, 2015.

[75] S. Otsuka-N. Teshigahara H. Fujitsuka S. Waseda D. Kuwahara T. Ishii, H. Ishii and S. Shinohara. Study on electrodeless electric propulsion in high-density helicon plasma with permanent magnets. *JPS Conf. Proc.*, Vol. 1, p. 015047, 2014.

[76] S. Shinohara, H. Nishida, T. Tanikawa, T. Hada, I. Funaki, IEEE Member, and K. P. Shamrai (deceased). Development of electrodeless plasma thrusters with high-density helicon plasma sources. *IEEE Trans. Plasma, Sci.*, Vol. 42, p. 1245, 2014.

[77] F. Otsuka, T. Hada, S. Shinohara, T. Tanikawa, and T. Matsuoka. Numerical modeling of electrodeless electric thruster by ion cyclotron resonance/ponderomotive acceleration. *Plasma and Fusion Research*, Vol. 8, pp. 2406067–1, 2013.

[78] A. Fruchman. Electric field in a double layer and the imparted momentum. *Phys. Rev. Lett.*, Vol. 96, p. 065002, 2006.

[79] E. Ahedo and M. Merino. Two-dimensional supersonic plasma acceleration in a magnetic nozzle. *Phys. Plasmas*, Vol. 17, p. 073501, 2010.

[80] I. Y. Dodin, N. J. Fisch, and J. M. Rax. Ponderomotive barrier as a maxwell demon. *Phys. Plasmas.*, Vol. 11, p. 5046, 2004.

[81] G. Emsellem. Development of a high power electrodeless thruster. *IEPC-2005-156*, 2005.

[82] R. L. Kinder, A. R. Ellingboe, and M. J. Kushner. H- to w-mode transitions and properties of a multimode helicon plasma reactor. *Plasma Sources Sci. Technol.*, Vol. 12, p. 561, 2003.

[83] D. Bose, T. R. Govindan, and M. Meyyappan. Modeling of a helicon plasma source. *IEEE Trans. on Plasma Sci*, Vol. 31, p. 464, 2003.

[84] S. Cho and M. A. Liberman. Self-consistent discharge characteristics of collisional helicon source. *Phys. Plasmas.*, Vol. 31, p. 882, 2003.

[85] G. Chen. A self-consistent model of helicon discharge. *Ph.D. theses, University of Texas at Austin*, 2008.

[86] T. Lafleur and R. W. Boswell. Particle-in-cell simulations of ambipolar and non-ambipolar diffusion in magnetized plasmas. *Phys. Plasmas*, Vol. 19, p. 053505, 2012.

[87] Yu. M. Aliev and M. Krämer. Mode conversion of nonaxisymmetric modes in strongly nonuniform helicon-sustained plasma. *Phys. Plasmas*, Vol. 15, p. 104502, 2008.

[88] S. H. Kim and Y. H. Hwang. Collisional power absorption near mode conversion surface in helicon plasmas. *Plasma Phys. Control. Fusion*, Vol. 50, p. 035007, 2008.

[89] R. M. Magee, M. E. Galante, J. Carr Jr., G. Lusk, D. W. McCarren, and E. E. Scime. Neutral depletion and the helicon density limit. *Phys. Plasmas*, Vol. 20, p. 123511, 2013.

[90] J. Miller-W. Steer T. Lho, N. Hershkowitz and G. H. Kim. Azimuthally symmetric pseudosurface and helicon wave propagation in an inductively coupled plasma at low magnetic field. *Phys. Plasmas*, p. 3135, 1998.

[91] V. Vahedi and M. Surendra. A monte carlo collision model for the particle-in-cell method: applications to argon and oxygen discharges. *Computer Physics Communications*, Vol. 87, p. 179, 1995.

[92] K. P. Shamrai, V. P. Pavlenko, and V. B. Taranov. Excitation, conversion and damping of waves in a helicon plasma source driven by an $m = 0$ antenna. *Plasma Phys. Control. Fusion*, Vol. 39, p. 505, 1997.

[93] A. Fukuyama and Y. Ichida. *Proc. 1996 Int. Conf. Plasma Physics, Nagoya 1996*, Vol. 2, p. 1342, 1996.

[94] M. J. Hsieh F. F. Chen and M. Light. Helicon waves in a non-uniform plasma. *Plasma Sources Sci. Technol.*, Vol. 3, p. 49, 1994.

[95] K. P. Shamrai, V. P. Pavlenko, and V. B. Taranov. Spectral and spatial characterization of a radio frequency power absorption in high pressure helicon plasmas. *Phys. Plasmas*, Vol. 8, p. 4659, 2001.

[96] S. H. Stix. Theory of plasma waves.

[97] D. A. Gurnet and A. Bhattacharjee. Introduction to plasma physics, with space and laboratory applications. *United Kingdomat the University Press, Cambridge*, 2005.

[98] F. F. Chen. Nonlinear effects and anomalous transport in rf plasmas. *IEEE Trans. Plasma. Sci.*, Vol. 34, p. No. 3, 2012.

[99] D. B. Graves. Fluid model simulations of a 13.56 mhz rf discharge: Time and space dependence ofrates of electron impact excitation. *J. Appl. Phys.*, Vol. 62, p. 88, 1987.

[100] D. B. Graves and K. F. Jensen. A continuum model of dc and rf discharges. *IEEE Trans. Plasma, Sci.*, Vol. 14, p. 78, 1987.

[101] M. J. Kushner. Advances in plasma equipment modeling. *Solid State Technol.*, Vol. 135, p. 39, 1996.

[102] T. E. Nitschke and D. B. Graves. A comparison of particle in cell and fluid model simulations of low-pressure radio frequency discharges. *J. Appl. Phys.*, Vol. 5646, p. 76, 1994.

[103] M. S. Barnes, T. J. Colter, and M. E. Elta. Large-single time-domain modeling of low-pressure rf grow discharges. *J. Appl. Phys.*, Vol. 61, p. 81, 1987.

[104] E. P. Hammond, K. Mahesh, and P. Moin. A numerical method to simulate radio-frequency plasma discharges. *J. Comp. Phys.*, Vol. 176, p. 402, 2002.

[105] J. D. Callen. Fundamental of plasma physics. *Lecture note at CEMRACS 2014 Summer School*, 2014.

[106] M. Surendra, D. B. Graves, and G. M. Jellum. Self-consistent model of a direct-current glow discharge: Treatment of fast electrons. *Phys. Rev. A*, Vol. 41, p. 1112, 1990.

[107] S. N. Nahar. Electron-ion recombination rate coefficients and photoionization cross sections for astrophysically abundant elements. viii. ar xiii with new features. *Astrophysical Journal Supplement Series*, Vol. 156, p. 93, 2005.

[108] W. H. Cramer. Elastic and inelastic scattering of low-velocity ions: Ne+ in a, a+ in ne, and a+ in a. *J. Chem. Phys*, Vol. 30, p. 641, 1959.

[109] I. Hutchinson. Chap. 3: Collisions in plasmas. *Lecture Notes of MIT open course*, p. 40, 2003.

[110] S. Shinohara, Y. MIyauchi, and Y. Kawai. Dynamic plasma behavior excited by $m = \pm 1$ helicon wave. *Plasma Phys. Control. Fusion*, Vol. 37, p. 1015, 1995.

[111] R. A. Demirkhanov, I. Y. Kadysh, and Y. S. Khodyrev. Skin effect in a high frequency ring discharge. *Soviet Phys. JETP*, Vol. 19, p. 791, 1964.

[112] M. J. Kofoid and J. M. Dawson. Anomalous skin depth in a gaseous plasma. *Phys. Rev. Lett.*, Vol. 17, p. 1086, 1966.

[113] B. Joye and H. Schneider. *Helv. Phys. Acta*, Vol. 51, p. 804, 1978.

[114] E. S. Weibel. Anomalous skin depth in a gaseous plasma. *Phys. Plasmas*, Vol. 10, p. 741, 1967.

[115] Y. S. Sayasov. *Helv. Phys. Acta*, Vol. 52, p. 288, 1979.

[116] V. A. Godyak and V. I. Kolobov. Plasma phenomena in inductive discharges. *Phys. Control Fusion*, Vol. 79, p. 4589, 1997.

[117] S. Ichimaru. Basic principles of plasma physics: A statistical approach. *Frontiers in Physics*, Vol. 41, p. A339, 1973.

[118] V. A. Godyak and V. I. Kolobov. Negative power absorption in inductively coupled plasma. *Phys. Rev. Lett.*, Vol. 45, p. A339, 2003.

[119] L. D. Landau and E. M. Lifshitz. Electrodynamics of continuous media. 1960.

[120] L. D. Landau. On the vibration of the electronic plasma. *J. Phys. USSR*, Vol. 25, p. 10, 1946.

[121] V. Vahedi, M. A. Lieberman, G. Dipeso, T.D. Rognlien, and D. Hewett. Analytic model of power deposition in inductively coupled plasma sources. *J. Appl. Phys.*, Vol. 78, p. 1446, 1995.

[122] N. S. Yoon, S. S. Kim, C. S. Chang, and Duk-In Choi. One-dimensional solution for electron heating in an inductively coupled plasma discharge. *Phys. Rev. E*, Vol. 54, p. 757, 1996.

[123] V. I. Kolobov and D. J. Economou. The anomalous skin effect in gas discharge plasmas. *Plasma Sources Sci. Technol.*, Vol. 6, p. R1, 1997.

[124] Yu. M. Aliev, I. D. Kaganovich, and H. Schlüter. Quasilinear theory of collisionless electron heating in radio frequency gas discharges. *Plasma Sources Sci. Technol.*, Vol. 4, p. 2413, 1997.

[125] M. M. Turner. Collisionless electron heating in an inductively coupled discharge. *Phys. Rev. Lett.*, Vol. 71, p. 1844, 1993.

[126] V. A. Godyak, R. B. Piejak, and B. M. Alexandrovich. Electrical characteristics and electron heating mechanism of an inductively coupled argon discharge. *Plasma Sources Sci. Technol.*, Vol. 3, p. 169, 1994.

[127] S. Rauf and M. J. Kushner. Model for noncollisional heating in inductively coupled plasma processing sources. *J. Appl. Phys.*, Vol. 81, p. 5966, 1997.

[128] V. A. Godyak, R. B. Piejak, B. M. Alexandrovich, and V. I. Kolobov. Experimental evidence of collisionless power absorption in inductively coupled plasmas. *Phys. Rev. Lett.*, Vol. 80, p. 3264, 1998.

[129] V. A. Godyak, R. B. Piejak, and B. M. Alexandrovich. Observationof second harmonic currents in inductively coupled plasmas. *Phys. Rev. Lett.*, Vol. 83, p. 1610, 1999.

[130] V. A. Godyak, R. Piejak, B. Alexandrovich, and A. Smolyakov. Nonlinear radio-frequency potential in an inductive plasma. *Plasma Sources Sci. Technol.*, Vol. 9, p. 541, 2000.

[131] V. A. Godyak, R. Piejak, B. Alexandrovich, and A. Smolyakov. Observation of the ponderomotive effect in an inductive plasma. *Plasma Sources Sci. Technol.*, Vol. 10, p. 459, 2001.

[132] A. I. Smolyakov, V. A. Godyak, and Y. O. Tyshetskiy. Effect of the electron thermal motion on the ponderomotive force in inductive plasma. *Plasma Sources Sci. Technol.*, Vol. 8, p. 3857, 2001.

[133] A. I. Smolyakov, V. A. Godyak, and Y. O. Tyshetskiy. Nonlinear effects in inductively coupled plasmas. *Phys. Plasmas*, Vol. 10, p. 2108, 2003.

[134] F. F. Chen and D. Curreli. Central peaking of magnetized gas discharges. *Phys. Plasmas*, Vol. 20, p. 057102, 2013.

[135] A. Simon. Ambipolar diffusion in a magnetic field. *Phys. Rev.*, Vol. 98, p. 317, 1955.

[136] D. G. Miljak and F. F. Chen. Density limit in helicon discharges. *Plasma Sources Sci. Technol.*, Vol. 7, p. 537, 1998.

[137] A. Fruchman, G. Makrinich, P. Chabert, and J. M. Rax. Enhanced plasma transport due to neutral depletion. *Phys. Rev. Lett.*, Vol. 95, p. 115002, 2005.

[138] J.-L. Raimbault, L. Liard, J.-M. Rax, P. Chabert, A. Fruchtman, and G. Makrinich. Steady-state isothermal bounded plasma with neutral dynamics. *Phys. Plasmas*, Vol. 14, p. 013503, 2007.

[139] L. Liard, J. L. Raimbault, J. M. Rax, and P. Chabert. Plasma transport under neutral gas depletion conditions. *J. Phys. D: Appl. Phys.*, Vol. 40, p. 5192, 2007.